UNIVERSITE DE LILLE 1 - IMCCE

THESE D'HABILITATION A DIRIGER DES RECHERCHES

par

Marc Fouchard

Dynamique des comètes du nuage de Oort

Soutenue publiquement le 10 Décembre 2013 à l'observatoire
de Lille devant le jury composé de :

Julio Fernandez	*Facultad de Ciencias, Montevideo, Uruguay*	Rapporteur
Giovanni Gronchi	*Università di Pisa, Pise, Italie*	Rapporteur
François Mignard	*Observatoire de la côte d'Azur*	Rapporteur
Hans Rickman	*Centre de recherche spatiale, Varsovie, Pologne*	Examinateur
Charles Suquet	*Universié Lille 1*	Président
Alain Vienne	*LAL-Université de Lille 1 / IMCCE*	Garant

Table des matières

Introduction **1**

1 Tout ce que vous avez toujours voulu savoir sur le nuage de Oort sans jamais avoir osé le demander **3**
- 1.1 La dynamique 3
  - 1.1.1 Les premiers pas, avec les étoiles 3
  - 1.1.2 La Galaxie 5
  - 1.1.3 La synergie 7
  - 1.1.4 Et les planètes 8
- 1.2 Les questions ouvertes 10
  - 1.2.1 Taille, forme, population et masse 10
  - 1.2.2 Formation 14
  - 1.2.3 “Fading problem” et origine des comètes de type Halley 17

2 Le modèle dynamique **21**
- 2.1 Construction du modèle de Marées Galactiques 21
  - **Article 1 : Methods for the Study of the Dynamics of the Oort Cloud Comets II : Modelling the Galactic Tide** 22
- 2.2 Construction du modèle de perturbations stellaires 46
  - **Article 2 : Methods for the Study of the Dynamics of the Oort Cloud Comets I : Modelling the Stellar Perturbations** 47
- 2.3 Construction du modèle de perturbations planétaires 63
  - **Article 3 : Planetary perturbations for Oort Cloud comets. I. Distributions and dynamics** 64

3 Résultats **77**
- 3.1 Synergie entre les perturbations stellaires et les marées galactiques 77
  - 3.1.1 Synergie à long terme 77

Article 4 : Injection of Oort Cloud Comets : The Fundamental Role of Stellar Perturbations 79
Article 5 : The key role of massive stars in Oort cloud comet dynamics 101
3.1.2 Synergie à court terme 115
Article 6 : The last revolution of new comets : the role of stars and their detectability 116
3.2 Interaction entre les perturbateurs galactiques et les perturbations planétaires 129
3.2.1 Implications sur le flux de comètes observables 129
Article 7 : Planetary perturbations for Oort cloud comets : II. Implications for the origin of observable comets 130
3.2.2 Implications sur la production à long terme d'objets du disque étendu 142
Article 8 : Planetary perturbations for Oort cloud comets : III. Evolution of the cloud and production of centaurs and Halley type comets . . . 144

4 Conclusion et perspectives **155**

A Autres travaux de recherche et publications **157**
A.1 Un modèle statistique de perturbations planétaires 157
A.2 Satellites irréguliers de Jupiter 160
A.3 Travaux de recherche reliés à la genèse du modèle dynamique pour les comètes du nuage de Oort 162
A.4 Résultats complémentaires autour des comètes du nuage de Oort 167
A.4.1 Complément sur la dynamique générée par les marées seules 167
A.4.2 Complément sur la synergie à court terme 167
A.5 Cours ou article de revue 168
A.6 Activité de recherche sur les indicateurs de chaoticité 170

B Curriculum vitae **173**

Introduction

Il n'est pas facile d'écrire un document supposé résumer plus de 10 ans d'activité de recherche. Je vais profiter de cette introduction pour faire une rapide présentation des différents domaines de recherche auxquels j'ai été confronté depuis le début de ma thèse pour ensuite expliquer mes choix pour la rédaction de ma HDR.

En début de ma thèse, dirigée par Christiane Froeschlé et Giovanni Valsecchi, j'ai commencé par étudier les indicateurs de stochasticité ce qui a fait l'objet d'une publication sur les indicateurs rapides de Lyapunov pour des systèmes dynamiques continus (voir l'annexe A.6). Cette activité m'a permis d'acquérir une certaine expertise sur l'étude de la stabilité numérique de systèmes dynamiques, ce qui m'a été très utile à plusieurs reprises par la suite.

Je me suis aussi consacré, toujours dans le cadre de ma thèse, à l'applicabilité des méthodes de Monte Carlo pour modéliser la dynamique des comètes de la famille de Jupiter. Ce travail montrait essentiellement l'inapplicabilité d'une telle méthode dans ce cadre . L'obtention d'un poste de maître de conférences à l'université de Lille 1 dans un département de Mathématiques m'a conduit à collaborer avec Radu S. Stoica sur l'utilisation de méthodes statistiques pour la modélisation des perturbations planétaires sur des comètes se trouvant sur des trajectoires quasi-paraboliques (voir l'annexe A.1).

Après mon arrivée à l'université de Lille 1, j'ai également co-encadrer avec Alain Vienne, la thèse de doctorat effectuée par Julien Frouard, sur la stabilité à long terme des satellites lointains de Jupiter (voir l'annexe A.2).

C'est donc en 2004, que je suis tombé dans la "marmite" de la dynamique des comètes du nuage de Oort. Depuis cette date, ce sujet est devenu mon activité de recherche principale et c'est pourquoi j'ai choisi de rédiger ma HDR autour de ce sujet. J'ai choisi aussi d'insérer des articles publiés dans des revues internationales avec comité de lecture pour mettre en valeur ma recherche dans ce domaine en choisissant les articles qui la synthétisent au mieux et qui contiennent les résultats principaux. Les autres articles sont rapidement présentés dans les annexes A.3 pour ce qui concerne le modèle et A.4 pour les résultats complémentaires dans ce domaine.

Le chapitre 1 consiste en une présentation du nuage de Oort avec d'une part la dynamique (section 1.1) et d'autre part les questions encore ouvertes qui lui sont reliées (section 1.2).

Le chapitre 2 est consacré à la présentation du modèle dynamique que j'ai conçu. Le modèle des marées galactiques est présenté dans la partie 2.1, celui des étoiles dans la partie 2.2 et celui des perturbations planétaires dans la partie 2.3.

Le chapitre 3 présente les principaux résultats obtenus à partir ce modèle pour ce qui concerne la synergie entre les marées galactiques et les passages stellaires (section 3.1) et les interactions avec les perturbations planétaires (section 3.2).

On trouvera enfin dans le chapitre 4 les conclusions et perspectives.

Chapitre 1

Tout ce que vous avez toujours voulu savoir sur le nuage de Oort sans jamais avoir osé le demander

1.1 La dynamique

1.1.1 Les premiers pas, avec les étoiles

Tout a commencé en 1932, quand Öpik (1932) mit en évidence que les perturbations stellaires sur les trajectoires presque paraboliques de comètes ou de météores avaient pour effet d'accroître considérablement la distance périhélique[1]. Ainsi ces objets se retrouvaient sur des orbites d'où seules d'autres étoiles pouvaient les éjecter. Öpik en conclut qu'il devait exister un nuage d'objets se trouvant à plus de 10 000 UA du Soleil. Cependant, pour lui, les objets de ce nuage étaient essentiellement inobservables puisque les perturbations stellaires étaient efficaces pour augmenter les distances périhéliques mais pas pour les réduire.

En 1950, Oort (1950) observa, à partir de la distribution de 19 comètes à longue période connues à cette époque, que la distribution de l'énergie orbitale originale[2] de ces comètes montrait un “pic” vers les très petites valeurs,

---

[1] Ces perturbations stellaires sont dues à des passages d'étoiles au voisinage du Soleil. Il faut remarquer que les étoiles ont des vitesses relatives au Soleil de l'ordre de la dizaine de kilomètres par seconde, alors qu'une comète se trouvant à 10 000 UA du Soleil sur une orbite presque parabolique a une vitesse de l'ordre du décimètre par seconde.

[2] Dans la suite, les paramètres originaux d'une trajectoire se réfèrent aux éléments orbitaux avant que la trajectoire ne soit affectée par les planètes

c'est-à-dire que leur demi-grand axe se trouvait entre 25 000 et 75 000 UA. Ce pic prit le nom de *pic de Oort*. Oort remarqua qu'en revanche le pic ne résistait pas aux perturbations planétaires. Ainsi, il n'apparaissait pas sur la distribution des énergies orbitales une fois l'effet des planètes pris en compte.

Ces comètes devaient donc venir dans la région planétaire du système solaire pour la première fois. La valeur de leur demi-grand axe conduit Oort à émettre l'hypothèse d'une région se trouvant entre 10 000 et 100 000 UA, contenant un grand nombre de comètes. Cette région prit le nom de *nuage de Oort*.

Comme Öpik, Oort prit aussi en compte les effets des passages d'étoiles au voisinage du Soleil. Mais c'est en considérant que ces effets pouvaient se traduire *aussi* par une réduction de la distance périhélique qu'il expliqua pourquoi des comètes du nuage de Oort pouvaient devenir observables.

A la suite de ces premiers travaux de Oort, les chercheurs ont essayé de comprendre et de modéliser le mieux possible comment une comète se trouvant dans le nuage pouvait devenir observable. Pour cela, le concept de *loss cone* (cône de perte), déjà introduit par Oort, a été utilisé (voir Weissman, 1980; Fernandez, 1981, entre autre, pour une illustration de ce concept). Ce concept repose sur le fait que, statistiquement, les effets des planètes géantes sur une trajectoire augmentent lorsque le moment angulaire diminue. Pour une comète se trouvant sur une orbite presque parabolique ce moment angulaire est proportionnelle à $\sqrt{q}$, où q est la distance périhélique. Donc plus la distance périhélique est petite, plus les effets des planètes sont statistiquement importants. Comme une comète du nuage de Oort a une énergie orbitale[3] de l'ordre de $-10^{-4}\,\mathrm{UA}^{-1}$, dès que la perturbation caractéristique des planètes sur l'énergie orbitale dépasse $10^{-4}\,\mathrm{UA}^{-1}$ en valeur absolue, on peut supposer que la comète est éjectée du nuage de Oort (on verra dans quelle mesure cette idée ne correspond pas à la réalité dans la section 2.3).

D'après différentes simulations (en particulier Fernandez, 1981), le seuil de $10^{-4}\,\mathrm{UA}^{-1}$ est atteint dès que la distance périhélique passe en dessous de 10$\sim$15 UA. Ainsi, si une comète du nuage de Oort se trouve à une distance héliocentrique inférieure à 15 UA par exemple (voir Matese et Whitman, 1992), alors elle est éjectée du nuage de Oort, sinon sa trajectoire n'est pas affectée par les planètes. La région qui contient les comètes du nuage de Oort ayant une distance périhélique inférieure à 15 UA correspond au loss cone. On appelle aussi cette région la barrière de Jupiter-Saturne puisque ce sont essentiellement ces deux planètes qui sont responsables de l'éjection des comètes. Le flux de comètes observables venant du nuage de Oort peut

---

[3] On utilisera la quantité $z = -1/a$, où a est le demi-grand axe de la trajectoire de la comète, comme représentative de l'énergie orbitale.

alors être étudié en regardant les comètes du loss cone se trouvant à moins de 5 UA du Soleil.

Jusque dans les années 80, seules les perturbations stellaires étaient considérées comme capables de remplir de manière efficace le loss cone (voir par exemple Rickman, 1976; Weissman, 1979; Fernández, 1980; Hills, 1981; Remy et Mignard, 1985). Les nuages moléculaires ont aussi été considérés, et le sont encore dans quelques travaux (Jakubík et Neslušan, 2008, par exemple). Cependant leurs effets, bien que pouvant être dévastateurs (Biermann, 1978; Napier, W.M., and Staniucha, M., 1982; Clube et Napier, 1982; Bailey, 1983), sont tellement difficiles à paramétrer d'une part, et que de telles rencontres sont probablement très rares d'autre part, qu'ils ne sont généralement pas pris en considération dans les études actuelles.

Pour ce qui concerne les effets des étoiles, il ressort que le flux de comètes observables dû aux passages d'étoiles peut être divisé en deux parties (voir en particulier Heisler et al., 1987). La première consiste en un flux de fond, pratiquement constant dans le temps venant de la partie externe du nuage de Oort, c'est-à-dire celle dont les comètes ont un demi-grand axe supérieur à 20 000 UA. La deuxième, principalement mise en évidence par Hills (1981), consiste en un flux sporadique pouvant être plusieurs ordres de grandeur plus important que le flux de fond, mais de courte durée et qui contient surtout des comètes venant de la partie interne du nuage de Oort (demi-grand axe inférieur à 20 000 AU). On parle alors de *douche cométaire*. Cette douche est provoquée par le passage d'une étoile passant très près du Soleil. D'après Dybczyński (2002), la géométrie de la trajectoire de l'étoile va influencer la distribution de la direction des aphélies des comètes à longue période rendues observables lors de la douche. Or on ne distingue pas de tel signe dans la distribution des comètes à longue période observées, ce qui permet d'exclure l'hypothèse que nous sommes actuellement en train d'observer une forte douche cométaire. Cependant d'après Rickman et al. (2008) on ne peut pas exclure une douche cométaire modérée.

1.1.2 La Galaxie

Suite aux travaux précurseurs de Chebotarev (1966); Smoluchowski et Torbett (1984); Byl (1983), les effets de la Galaxie sur la dynamique des comètes du nuage de Oort ont commencé à être pris en considération. Cependant, si dans ces travaux la Galaxie n'était modélisée que par une masse ponctuelle, ce n'est que dans les années 80, lorsque le disque galactique fut modélisé (voir en particulier Byl, 1986; Heisler et Tremaine, 1986; Duncan et al., 1987) que la Galaxie obtient toute l'importance qu'elle a aujourd'hui dans la dynamique des comètes du nuage de Oort.

Les effets de la Galaxie sur une comète du nuage de Oort est une conséquence de la très grande distance entre la comète et le Soleil, de telle sorte que la force gravitationnelle de la Galaxie sur le Soleil est significativement différente de celle de la Galaxie sur la comète. En ce sens on parle de force de marées galactiques, que l'on a l'habitude de décomposer en une composante normale au plan de la Galaxie induite par le disque galactique, et une composante radiale se trouvant dans le plan de la Galaxie induite par le bulbe galactique et le halo. L'estimation des paramètres intervenant dans le calcul de ces marées montrent que la composante normale est près d'un ordre de grandeur plus grande que la composante radiale (Levison et al., 2001).

En négligeant la composante radiale et en moyennant les équations par rapport au mouvement moyen de la comète (les marées engendrent des effets à très long terme), alors on obtient un système qui est complètement intégrable (Heisler et Tremaine, 1986). La dynamique induite par un tel système se résume alors en un mouvement périodique de l'excentricité et de l'argument du périhélie alors que le demi-grand axe reste constant. L'inclinaison par rapport au disque galactique subit aussi des oscillations de telle sorte que la troisième composante du moment angulaire de la comète $\sqrt{a(1-e^2)}\cos i$ reste constante.

La période du cycle de l'excentricité est inversement proportionnelle à la période orbitale de la comète. Ainsi, plus le demi-grand axe est grand plus la période de ce cycle diminue (mais son amplitude reste constante). Ceci montre que la moyennisation effectuée pour obtenir le système intégrable va atteindre sa limite de validité lorsque le demi-grand axe deviendra trop important (on verra dans les articles publiés que celle limite se trouve aux alentours de 50 000 UA).

Lorsqu'on utilise le concept de loss cone, pour qu'une comète soit observable elle doit passer la barrière de Jupiter-Saturne en une seule période orbitale et être injectée directement dans la région observable (typiquement moins de 5 UA du Soleil). Or la variation de la distance périhélique augmente avec le demi-grand axe, ainsi dans un modèle dynamique ne contenant que les marées galactiques et utilisant le concept de loss cone, seules des comètes ayant un demi-grand axe supérieur à $\approx 23\,000$ UA pourront devenir observables (Fouchard et al., 2011b).

Le modèle intégrable de marées a permis de montrer que la direction des périhélies des comètes à longue période observées était une conséquence de l'influence de la composante normale des marées galactiques sur leur observabilité (Delsemme, 1987). A la même époque, Duncan et al. (1987) ont montré de manière convaincante que les échelles de temps pour rendre observable une comète du nuage de Oort sont beaucoup plus courtes pour les marées galactiques que pour les effets des étoiles passantes.

Ainsi, dans les années 1990 et 2000, les marées s'imposèrent au détriment de l'influence des étoiles. Cependant, c'est justement la quasi-intégrabilité des marées galactiques qui constitue leur première faiblesse, comme on va le voir.

1.1.3 La synergie

Du fait de la quasi-intégrabilité de la dynamique générée par les marées galactiques, les régions du nuage de Oort à partir desquelles une comète peut devenir observable (appelées TAZ, pour Tidal Active Zone) sous l'effet des marées possèdent une frontière pratiquement infranchissable. Ces régions vont donc se vider sans qu'aucun mécanisme ne puisse efficacement les remplir. Le flux de comètes observables va donc diminuer fortement pour atteindre un niveau où les injections ne sont dues qu'à la faible perméabilité de la TAZ ou à un problème de synchronisation qui veut que pour qu'une comète soit observable elle doit se trouver au voisinage de son périhélie au moment où son périhélie est dans la région d'observabilité. La probabilité de ce dernier événement est proportionnelle à l'inverse du carré de la période orbitale (Fouchard et al., 2010). Finalement on atteindra un flux résiduel en moins de 2 milliards d'années (Rickman et al., 2008; Fouchard et al., 2011a).

La présence des étoiles change drastiquement la situation. En effet une très forte synergie existe entre les effets des marées galactiques et ceux des étoiles (Rickman et al., 2008; Fouchard et al., 2011a,b; Rickman et al., 2012). Cette synergie peut se décomposer en deux parties : une à long terme directement reliée au remplissage de la TAZ, et une à court terme due à une interférence constructive entre les perturbations galactiques et les perturbations stellaires.

La synergie à long terme peut se résumer aux deux points suivants.

- les étoiles garantissent un remplissage de la TAZ de l'ordre de 70% même sur 5 milliards d'années. Ainsi le flux résiduel n'est jamais atteint.
- le passage d'une unique étoile, préférentiellement massive, est capable de remplir complètement la TAZ, générant une augmentation du flux de comètes observables pendant plusieurs centaines de millions d'années. On parle de bruine cométaire, dans le sens que l'augmentation est modérée mais de longue durée.

Pour ce qui est de la synergie à court terme, il s'agit d'une synergie qui a lieu en dehors de tout passage stellaire pouvant induire des douches cométaires, même modérées. Il s'ensuit que les injections sont donc principalement dues aux marées galactiques. Les interférences entre les effets des marées et des étoiles peuvent être autant constructives (les effets vont dans le même sens) que destructives (les effets sont de sens contraire), mais il se trouve que le cas constructif domine sur celui destructif, pourvu que la distribution des énergies orbitales des comètes considérées soit pas trop éloignée d'une distribution uniforme (Rickman et al., 2008; Fouchard et al., 2011b), ce qui est en général le cas.

Ainsi la présence de perturbations stellaires permet de changer certaines caractéristiques du flux même sur du court terme, c'est-à-dire sur la dernière période orbitale avant l'observabilité. Ces changements peuvent se résumer aux 2 points suivants.

- Une augmentation globale du flux de l'ordre de 30%, qui est directement reliée aux interférences constructives.
- La région observable du nuage de Oort, et en particulier le pic de Oort, sont déplacés vers des valeurs plus petites du demi-grand axe (de $\approx$ 23 000 UA à $\approx$ 20 000 UA pour le bord interne, et de $\approx$ 48 000 UA à $\approx$ 34 000 UA pour le maximum du pic de Oort).

Il faut souligner ici, qu'en considérant une orbite du système solaire autour du centre de la Galaxie plus réaliste que la trajectoire uniforme et circulaire, conduit à des marées galactiques qui dépendent du temps. Par exemple dans Gardner et al. (2011), cette variation périodique des marées induit une variation du flux de comètes observables de l'ordre aussi de 30%.

1.1.4 Et les planètes

Lorsque les comètes à longue période passent dans la région planétaire du système solaire, elles subissent les effets des planètes géantes. Une modélisation précise de ces perturbations est très coûteuse en temps de calcul nécessitant l'utilisation de méthodes plus rapides mais aussi moins précises. Avant les années 90, ces perturbations étaient préférentiellement modélisées par une marche aléatoire en énergie orbitale comme dans Duncan et al. (1987), ou en utilisant des méthodes de Monte Carlo (Everhart, 1972; Stagg et Bailey, 1989). Le concept de loss cone a aussi été largement utilisé (voir Heisler et Tremaine, 1986; Matese et Whitman, 1992, entre autres).

A la fin des années 90, les capacités des ordinateurs ont permis de faire une modélisation plus précise des perturbations planétaires sur les comètes du nuage de Oort. Wiegert et Tremaine (1999) ont été les premiers à le faire de manière précise. Mais leur recherche était principalement consacrée au "fading problem" (voir la partie 1.2.3 consacrée à ce problème).

La première modélisation complète de la dynamique des comètes du nuage de Oort sur l'âge du système solaire tenant en compte les 3 principaux perturbateurs (marées galactiques, passages stellaires et les planètes) a été faite par Emel'yanenko et al. (2007). Leurs travaux ont permis de mettre en évidence que l'introduction des perturbations planétaires conduisait à une efficacité plus élevée pour rendre une comète du nuage de Oort observable. Mais les auteurs n'ont pas poussé plus loin leur analyse.

Ce n'est qu'avec les travaux de Kaib et Quinn (2009) que le rôle des perturbations planétaires, et plus particulièrement de leur interaction avec les perturbations galactiques, a pu être mis en évidence.

Dans cet article, les auteurs illustrent le chemin typique d'une comète du nuage de Oort devenant observable par une comète du nuage de Oort interne ($a < 20\,000$ UA) qui pénètre la région planétaire du système solaire, à ce point une perturbation planétaire envoie la comète dans le nuage externe ou central ($a > 20\,000$ UA), région à partir de laquelle les marées galactiques peuvent facilement rendre la comète observable. Les auteurs montrent que plus de la moitié des comètes observables suivent une telle route. Ce scénario avait déjà été mis en valeur par Levison et al. (2006) mais dans le cadre de l'origine des comètes de type Halley.

Cependant, le modèle de Kaib et Quinn (2009) ne tient pas compte des perturbations stellaires en fin d'intégration alors qu'on a montré dans Fouchard et al. (2011b); Rickman et al. (2012) qu'elles sont importantes lors de la dernière période orbitale précédant l'observabilité. Enfin, il existe d'autres routes conduisant à l'observabilité que l'introduction des perturbations planétaires rend possible mais qui ne sont pas discutées dans Kaib et Quinn (2009). Cette étude approfondie a été l'objectif de l'article Fouchard et al. (2013). Les résultats de Kaib et Quinn (2009) sont confirmés, mais l'introduction de nouvelles routes permet de préciser comment les planètes agissent en interaction avec les marées et les étoiles.

Ces résultats montrent que la composante interne du nuage de Oort, longtemps considérée comme non-observable, est en fait la principale source des comètes à longue période observables.

Pour finir cette partie sur les perturbateurs des comètes du nuage de Oort, il faut mentionner l'hypothèse qui stipule qu'il existe une planète dans la partie interne du nuage de Oort. D'après Matese et Whitmire (2011), le flux de comètes du nuage de Oort observé est statistiquement consistant avec la présence d'une planète d'une à quatre masses joviennes et orbitant à moins de 10 000 UA du Soleil. Cependant l'observation d'une telle planète est encore difficile de nos jours. D'autre part, il faudrait expliquer l'origine d'une telle planète dans notre système solaire.

1.2 Les questions ouvertes

1.2.1 Taille, forme, population et masse

Taille et forme

Si on pense au nuage de Oort comme une région du système solaire alors forcément il existe et correspond à la sphère d'influence gravitationnelle du Soleil qui s'étend environ jusqu'à 200 000 UA du Soleil (Heisler et Tremaine, 1986) à laquelle on a retiré sa partie la plus interne à moins de quelques milliers d'UA du Soleil. Mais l'étude du nuage de Oort n'a de sens que si il contient des objets, et c'est là que les problèmes se posent. Les objets supposés se trouver dans cette région sont complètement inaccessibles aux observations. En effet leur présence dans le nuage n'est déduite que de la forme du pic de Oort, c'est-à-dire de la valeur très élevée du demi-grand axe d'une grande partie des comètes à longue période.

En conséquence l'objet de pratiquement toutes les études sur la dynamique du nuage de Oort, est de pouvoir répondre aux questions suivantes : que contient-il ? quelle forme a-t-il ? quelle dimension a-t-il ? Pour le moment, c'est-à-dire tant que ces objets ne sont pas observables dans le nuage de Oort, le seul moyen que l'on a pour essayer de répondre à ces questions c'est la modélisation de la dynamique et la confrontation des résultats avec les comètes à longue période observées. Ceci implique une première limitation aux réponses que l'on peut donner : on ne peut déduire de l'information que sur la partie du nuage de Oort qui est capable de produire des comètes observables.

En fait la seule quantité sur laquelle il y a un bon accord mais qui n'engage pratiquement à rien est relative à la frontière externe du nuage. La valeur de 200 000 UA (Heisler et Tremaine, 1986) est généralement admise. Pour ce qui est du bord interne, les choses commencent déjà à se compliquer. En effet, la plupart des études placent ce bord à 3 000 UA suite à l'article de Duncan et al. (1987).

Dans cette étude, ils ont montré qu'au voisinage de 3 000 UA l'échelle de temps nécessaire aux marées pour changer la distance périhélique d'une comète est comparable à l'échelle de temps nécessaire aux planètes pour changer l'énergie orbitale de cette comète. Cependant une composante très interne du nuage peut aussi être considérée et contient très probablement des objets, faisant le lien avec le disque étendu[4] (Brasser, 2008).

Mis à part cette partie très interne du nuage de Oort, celui-ci peut ensuite être divisé en 3 parties.

- La *partie interne* contenant les comètes ayant un demi-grand axe inférieur à 20 000 AU. Cette partie ne produit pas directement de comète observable, mis à part un flux très faible (Fouchard et al., 2011b) ou pendant les douches cométaires provoquées par le passage très proche d'une étoile (Hills, 1981).
- La *partie centrale* contenant les comètes ayant un demi-grand axe compris entre 20 000 et 50 000 AU. C'est la partie d'où proviennent la majorité des comètes observables. Les marées galactiques y sont très efficaces et de plus l'approximation de quasi-intégrabilité de la dynamique générée par les marées est fiable dans cette région. Ceci permet d'étudier les propriétés quantitatives du flux de manière presque analytique (Fouchard et al., 2011a).
- La *partie externe* qui contient toutes les comètes se trouvant au-delà de la partie centrale. Dans cette région l'hypothèse de quasi-intégrabilité de la dynamique générée par les marées n'est plus valable. Les marées et les étoiles sont paradoxalement moins efficaces que dans la partie centrale pour rendre des comètes de cette région observables. Ceci est dû à un problème de synchronisation entre le moment où le périhélie de la trajectoire des comètes se trouve dans la région observable et la position de la comète sur sa trajectoire. On a vu que la probabilité d'un tel événement sur un intervalle de temps donné est proportionnel à l'inverse du carré de la période orbitale de la comète (Fouchard et al., 2010).

Pour ce qui est de la forme du nuage, il semblerait qu'au delà de 10 000 UA la direction des vitesses héliocentriques des comètes du nuage doit adopter une distribution isotropique conduisant à une distribution isotropique de la direction des périhélies et une distribution des excentricités proportionnelle au carré de l'excentricité (Oort, 1950; Hills, 1981; Yabushita et al., 1982). Pour des valeurs du demi-grand axe plus petites, les plans orbitaux des comètes du nuage se concentrent vers l'écliptique, gardant une certaine mémoire de leur plan d'origine (Levison et al., 2001; Emel'yanenko et al., 2007). D'après Levison et al. (2001) la transition devrait se trouver à 3 000 UA.

Le profil de densité des distances héliocentriques est généralement un

---

[4] Ce disque correspond à des objets se trouvant sur des orbites très excentriques avec un périhélie proche de Neptune. Leur demi-grand axe peut aller jusqu'à la limite interne du nuage de Oort. Dynamiquement les objets du disque étendu ont leur demi-grand axe significativement affecté par Neptune (Gladman et al., 2008).

résultat de simulations numériques. Actuellement, un profil $n(r) \propto r^{-3.5}$ est souvent considéré dans les études à long terme du nuage (Duncan et al., 1987; Dones et al., 2004; Brasser et al., 2006; Emel'yanenko et al., 2007). Cependant il semble que dans des simulations à long terme la distribution se rapproche d'une distribution uniforme en énergie orbitale (Rickman et al., 2008; Fouchard et al., 2014b).

Ainsi, l'étude du flux de comètes observables permet surtout d'avoir des informations sur la partie centrale du nuage de Oort. L'amélioration de la détermination du demi-grand axe original des comètes observées a conduit à une modification de la localisation du pic de Oort. Pour Oort il se trouvait entre 25 000 et 75 000 UA (pour le demi-grand axe), puis la modélisation des forces non gravitationnelles ont permis de le situer plutôt vers 25 000 UA (Marsden et Sekanina, 1973), et même 17 000 UA (Królikowska, 2006).

On voit que cette dernière valeur est à l'intérieur de la partie centrale. En effet, les travaux de Kaib et Quinn (2009) ont montré qu'une majorité des comètes observables venant de la partie centrale (ou externe) se trouvait dans la partie interne une période orbitale avant leur injection. Ces résultats, confirmés par Fouchard et al. (2014a), montrent que la partie "observable" du nuage de Oort s'étend significativement à la partie interne.

D'autre part, Królikowska et Dybczyński (2010); Dybczyński et Królikowska (2011) ont montré qu'une large proportion des comètes observables considérées comme nouvelles, c'est-à-dire n'ayant jamais visité la région planétaire du système solaire, se trouvaient en fait à moins de 15 UA du Soleil lors de leur précédent passage au périhélie. Ce résultat remet en discussion le fait que les comètes du pic de Oort sont nouvelles, puisqu'elles sont déjà passées dans la région planétaire du système solaire. Lors de ce précédent passage, elles ont pu subir une perturbation planétaire augmentant le demi-grand axe permettant alors aux marées galactiques de rendre ces comètes observables (scénario de Kaib et Quinn, 2009), soit elle n'ont pas reçu de perturbation planétaire significative mais la distance périhélique a continué à décroître sous l'effet des marées galactiques rendant ces comètes observables. Ce deuxième scénario est possible puisque les planètes n'éjectent pas toutes les comètes se trouvant à moins de 15 UA du Soleil, contrairement à ce qui est considéré dans le concept de loss cone comme on l'a vu dans Fouchard et al. (2013). D'autre part ce scénario a été mis en évidence dans Fouchard et al. (2014a).

Ainsi, on voit que notre idée sur la forme du pic de Oort se précise, même si il faudra probablement attendre les données de la mission GAIA sur le voisinage stellaire du Soleil, pour effectuer une reconstruction réaliste du pic de Oort (Fouchard et al., 2011a; Rickman et al., 2012).

Population et masse

Ce sont les paramètres clef. En effet la population des comètes du nuage de Oort est une contrainte très forte pour les modèles de formation du système solaire. Le nombre de comètes dans le nuage de Oort se fait en comparant les résultats de modèles numériques avec le flux de comètes à longue période observé. La détermination même de ce flux n'est pas évidente. Everhart (1967) estime qu'on a 63 comètes nouvelles par an pour des distances périhéliques inférieures à 4 UA et une magnitude absolue inférieure à 10.9 . Hughes (2001) estime un flux de 0.53 comètes par an et par unité astronomique ayant une magnitude absolue inférieure à 6.5. La différence entre ces deux estimations du flux est significative. D'autant plus que Everhart (1967) a considéré une incomplétude des comètes observées très forte pour les magnitudes élevées, alors qu'il semble qu'il existe des ruptures dans la courbe des populations des comètes existantes pour des magnitudes absolues égales à 6 et 8.6 (Fernández et Sosa, 2012).

Cependant c'est souvent le flux estimé par Everhart (1967) qui est utilisé comme base de comparaison. Les estimations donnent alors entre 5×10^{11} à 5×10^{12} comètes dans le nuage central et externe d'après Emel'yanenko et al. (2007) et Weissman (1996), et une partie interne étant d'une (Dones et al., 2004) à quatre (Duncan et al., 1987) fois plus massive que les parties centrale et externe.

Plus récemment Francis (2005) a estimé le nombre de comètes dans la partie externe du nuage de Oort égale à 5×10^{11} en se basant cette fois sur le flux estimé par Hughes (2001). Alors que le modèle de Kaib et Quinn (2009) donne un nuage interne contenant au plus 10^{12} comètes en considérant que toutes les comètes observées étaient initialement dans la partie interne du nuage. En utilisant les mêmes estimations que Francis (2005), on a estimé dans Fouchard et al. (2014a) une population totale du nuage de Oort au environ de 10^{12} comètes.

Il est délicat de convertir ensuite ce nombre de comètes en masse. En effet ceci nécessite de faire une estimation de la taille et de la densité des comètes à longue période, ce qui est particulièrement difficile étant donné que ces comètes n'ont été observées qu'une seule fois.

En utilisant une masse moyenne de comète de 4×10^{16} g, Weissman (1996) estime la masse initiale du nuage de Oort égale à 6-7 masses terrestres. Mais Francis (2005), en utilisant différentes approximations, montre que cette masse se trouve entre 2 et 40 masses terrestres.

1.2.2 Formation

Les comètes du nuage de Oort ne se sont clairement pas formées sur place, la densité de matière y étant beaucoup trop faible. Elles se sont formées à partir du disque protoplanétaire dans une région se trouvant entre 5 et 40 UA (Charnoz et Morbidelli, 2007). Les perturbations des planètes géantes sur la trajectoire des jeunes comètes ont eu pour effet d'augmenter considérablement leur énergie orbitale, éjectant une partie des comètes dans le milieu interstellaire mais aussi en injectant une partie d'entre elles dans ce qui deviendra le nuage de Oort. Les étoiles passantes et les marées galactiques ont ensuite déplacé le périhélie de ces comètes à l'extérieur de la région d'influence des planètes géantes permettant à ces comètes de rester dans le nuage pendant des milliards d'années jusqu'à ce que les marées ou les étoiles réinjectent de nouveau le périhélie dans la région planétaire du système solaire.

Ceci correspond aux grandes lignes de la formation et de la dynamique du nuage de Oort généralement acceptées. Mais dès qu'on cherche à modéliser les choses et donc à comprendre en détail ce qui se passe les choses se compliquent considérablement.

Par exemple, si le périhélie d'une comète se trouve dans la région de Jupiter et Saturne, alors les perturbations de ces planètes sont telles qu'elles vont éjecter la majorité des comètes, laissant un nuage de Oort pratiquement vide. Fernández (1980) a montré que Uranus et Neptune sont bien plus efficaces pour placer une comète dans le nuage de Oort mais son modèle favorisait aussi un tel effet. Ces travaux mettaient déjà en lumière le problème de la formation du nuage.

La première simulation numérique de la formation du nuage de Oort a été faite par Duncan et al. (1987). C'est cette simulation qui a amené à considérer une frontière interne du nuage de Oort au voisinage de 3 000 UA et à un profil de densité proportionel à $r^{-3.5}$ (où r est la distance héliocentrique). Dans ce travail aussi, les auteurs montrent que le rôle d'Uranus et Netpune est plus important que le rôle de Jupiter et Saturne pour former le nuage de Oort. Cependant les conditions initiales choisies, avec des comètes sur des orbites très excentriques, accentuent l'influence d'Uranus et Neptune, mettant en doute l'efficacité réelle de ces planètes pour la formation le nuage (Dones et al., 2004).

Dones et al. (2004) ont montré que si les excentricités initiales des orbites cométaires, se trouvant dans la région des planètes géantes, sont faibles alors l'efficacité des planètes à construire le nuage de Oort est 3 ordres de grandeur plus faible que dans Duncan et al. (1987) pour le nuage centrale et externe et 1 ordre de grandeur plus faible pour la partie interne. Ceci s'explique par le fait que la majorité des comètes évoluant dans la région d'Uranus et

Neptune passe en fait dans la région de Jupiter et Saturne qui les éjectent complètement. Ils obtiennent une efficacité de formation du nuage par les planètes égale à 5% seulement.

Si les planètes géantes sont aussi peu efficaces pour remplir le nuage de Oort, alors il devient nécessaire d'avoir un disque protoplanétaire très massif, bien plus que la masse minimale habituellement considérée pour la formation de notre système solaire, afin de pouvoir obtenir un nuage avec suffisamment de comètes permettant d'expliquer le flux actuel de comètes à longue période observé. Mais si le disque protoplanétaire est trop massif alors on obtient un migration excessive des planètes ou la formation de planète supplémentaire (Hahn et Malhotra, 1999).D'autre part, le modèle de Dones et al. (2004) prévoit une population du disque étendu de l'ordre de 10% de celle du nuage de Oort, alors que la population de ce disque à partir du flux de comètes de la famille de Jupiter est supposée de 150 à 750 fois moindre que celle du nuage de Oort d'après les estimations de Duncan et Levison (1997); Levison et al. (2008).

Afin de construire des modèles plus réalistes, les modèles de formation ont commencé à prendre en compte le milieu dans lequel se trouvait le système solaire au moment de la formation du nuage. Ainsi, Fernandez (1997); Fernández et Brunini (2000) ont étudié la formation d'un nuage de Oort alors que le Soleil se trouvait encore dans l'amas d'étoiles dans lequel il est né. Ils ont montré qu'un environnement galactique dense favorisait la formation d'un noyau interne du nuage de Oort à moins de 1000 UA. Ce modèle dépend de plusieurs hypothèses sur les échelles de temps de formation des planètes géantes et de dissipation de l'amas : l'amas doit se dissiper suffisamment lentement pour permettre aux planètes géantes de se former et d'éjecter des planétésimaux dans le nuage de Oort. Mais cette dissipation doit être suffisamment rapide pour ne pas détruire le noyau de nuage de Oort construit.

Cependant, en prenant en compte un environnement primordial plus réaliste, c'est-à-dire une amas ouvert plongé dans un nuage moléculaire, Kaib et Quinn (2008) ont montré qu'il est relativement facile de construire un noyau interne et même d'obtenir des objets comme Sedna. En revanche il est plus difficile d'obtenir un nuage suffisamment peuplé au-delà de 10 000 UA. Des résultats similaires ont été obtenus par Brasser et al. (2006) et Brasser et al. (2008), montrant qu'un environnement galactique initialement dense permet la formation d'un noyau très interne du nuage de Oort, mais qu'il reste difficile de construire la partie externe du nuage, même après 4 milliards d'années. Une solution envisagée par Levison et al. (2010) était de considérer que des comètes, formées autour d'autres étoiles de l'amas, ont pu avoir été capturées par le Soleil.

Mais, comme ceci aussi à lieu pendant la phase initiale de la formation du système solaire, on doit tenir compte le frottement induit par le gaz encore présent. Dans ce cas, les perturbations planétaires n'arrivent à placer dans le nuage de Oort que des objets massifs qui ne ressentent pas les effets du frottement (Brasser et al., 2007).

Ainsi, il semble que la partie externe du nuage doit se former après la dissipation du gaz. Le modèle de Nice (Gomes, 2005) qui permet d'expliquer le bombardement tardif des planètes telluriques, pourrait être alors le maillon manquant à la formation de la partie externe du nuage de Oort.

Dans ce modèle, le bombardement tardif s'explique par une migration des planètes géantes à partir de positions plus proches du Soleil que leur position actuelle sous l'effet d'interaction avec un disque de planétésimaux se trouvant juste au delà de l'orbite de Neptune. Lors de la migration Jupiter et Saturne traversent la résonance 2 :1 provoquant une forte instabilité du disque de planétésimaux.

Ainsi, le nuage de Oort se serait formé en deux étapes : la première lorsque le Soleil se trouvait encore dans l'amas l'ayant vu naître et en présence du gaz, étape pendant laquelle un noyau très interne se serait formé ; et la deuxième à partir du bombardement tardif, donc une fois l'amas et le gaz dissipé, ayant permis la formation du nuage au-delà de 10 000 UA. Cette approche a été celle suivie par Brasser (2008).

En se focalisant sur la deuxième étape, Brasser et Morbidelli (2013) montrent que l'excentricité initialement plus élevée de Uranus et Neptune, permet à ces planètes d'avoir un contrôle plus solide sur la dynamique des objets dans leur voisinage, leur permettant de placer ces objets dans le nuage de Oort plutôt que de les envoyer sous le contrôle de Jupiter et Saturne qui les éjectent. Ainsi, l'efficacité des planètes à construire un nuage de Oort externe au bout de 4 milliards d'années passe à 7% et le rapport entre la population du nuage de Oort et celle du disque étendu est voisin de 12. D'autre part, en estimant au mieux le flux de comètes nouvelles venant du nuage de Oort et le flux de comètes de la famille de Jupiter venant du disque étendu pour des magnitudes totales supposées correspondre à des objets de taille similaire (pour une même taille, une comète de la famille de Jupiter à une magnitude totale plus faible qu'une comète à longue période (Fernández et al., 1999; Sosa, 2011)) Brasser et Morbidelli (2013) obtiennent un rapport de population entre le nuage de Oort et le disque étendu se trouvant entre 10 et 98, avec une valeur nominale égale à 44. Près d'un facteur 4 plus grand que le facteur 12 trouvé à partir des simulations mais dont les barres d'erreur contiennent ce facteur 12.

Le problème n'est donc pas encore résolu, même si cette formation en deux étapes donne des résultats prometteurs. L'amélioration des modèles ainsi que la réduction des barres d'erreur par de futures observations permettront probablement de préciser le scénario ayant mené à un nuage de Oort tel qu'on le suppose aujourd'hui.

1.2.3 "Fading problem" et origine des comètes de type Halley

Fading problem

Oort (1950) avait remarqué que pour reproduire, à partir d'un modèle, une distribution en énergie orbitale des comètes à longue période qui soit similaire à celle observée alors il était confronté à deux problèmes : *(i)* il devait considérer une probabilité *ad hoc* de désintégration d'une comète à chaque passage au périhélie égale à 0.014, *(ii)* il y avait 5 fois trop de comètes dans le fameux pic de Oort. Il stipula que les comètes du pic de Oort sont des comètes qui viennent pour la première fois au voisinage du Soleil. Ainsi leur capacité de dégazage n'a pas encore été altérée par des passages précédents. La diminution du dégazage lors des passages suivants peut être due à plusieurs facteurs : rupture ou désintégration de la comète, disparition de la matière volatile, formation d'une croûte, etc.. La conséquence est que lors des passages au périhélie suivants, les comètes deviennent plus difficilement détectables. C'est ce qu'on appelle le "fading problem" ou le problème de l'extinction.

Wiegert et Tremaine (1999) ont essayé de trouver une loi d'extinction en cherchant à faire correspondre au mieux les distributions des élément orbitaux des comètes observables obtenues à partir d'un modèle numérique avec la distribution des comètes observées. Ils obtiennent la meilleure correspondance entre les deux distributions en considérant une loi d'extinction telle que la proportion de comètes encore observables après m passages au périhélie est proportionnelle à $m^{-0.6}$.

Cependant, une telle loi est obtenue en essayant de faire correspondre le résultat de simulations numériques avec les observations. Elles ne sont donc pas forcément représentatives de l'évolution physique des comètes en regroupant sous le même phénomène de fading des évolutions pouvant être très différentes.

Weissman (2011) montre justement que le mécanisme dominant de fading est une destruction du noyau cométaire (destruction pas encore bien comprise d'ailleurs). La formation de croûte à la surface de la comète semble aussi avoir un rôle assez important mais moindre.

Ce problème reste encore ouvert faute en particulier d'informations physiques fiables sur les comètes à longue période.

Origine des comètes de type Halley

Les comètes de type Halley font partie des comètes à courte période (période inférieure à 200 ans). Cette classe de comètes est ensuite divisée en deux classes, les comètes de la famille de Jupiter ayant un paramètre de Tisserand[5] par rapport à Jupiter supérieur à 2, et les autres comètes qui sont dites de type Halley. Cette séparation suivant le paramètre de Tisserand est proche d'une séparation suivant la période orbitale (≈20 ans) mais elle permet en plus de souligner l'importance de Jupiter pour les comètes de la famille de Jupiter (Carusi et al., 1987).

Si on considère une origine commune pour ces deux familles à partir d'orbites presque paraboliques, alors on obtient une proportion de comètes de type Halley beaucoup plus grande que celle de la famille de Jupiter ; ce qui est en contradiction avec les observations.

Ainsi, une origine différente a été supposée pour les comètes de type Halley, et pour les comètes de la famille de Jupiter. Il est maintenant bien accepté que les comètes de la famille de Jupiter viennent du disque étendu (Duncan et Levison, 1997). En revanche, l'origine des comètes de type Halley reste une question ouverte. Une origine dans le nuage de Oort pose problème du fait de la distribution des inclinaisons. En effet la distribution des comètes dans le nuage est isotrope. Ensuite, pour qu'une comète du nuage de Oort devienne une comète de type Halley elle doit interagir avec les planètes géantes sans être éjectée. Ainsi, une telle origine devrait produire une majorité de comète rétrograde, alors que c'est l'inverse qui est observée(Levison et al., 2001). Une hypothèse a été d'introduire de nouveau des lois de fading, mais sans solution satisfaisante. Levison et al. (2001) ont alors montré que ces comètes pouvaient venir d'une composante interne du nuage de Oort aplatie sur l'écliptique permettant alors d'obtenir une distribution d'inclinaison similaire à celle des comètes de type Halley connues.

Cependant, Levison et al. (2006) montrent qu'en fait ce scénario n'est pas satisfaisant. En effet, cette composante interne du nuage de Oort aplatie sur l'écliptique doit se trouver à moins de 3 000 UA du Soleil pour que la structure de disque ne soit pas détruite par les marées galactiques. Mais à de telles distances les marées sont aussi très inefficaces pour réduire la distance

---

[5] Ce paramètre est une approximation de la constante de Jacobi du problème de deux corps restreint et circulaire. Il est égale à

$$T = \frac{a_J}{a} + 2\sqrt{\frac{a}{a_J}(1-e^2)}\cos i$$

, où a, e, i sont respectivement le demi-grand axe, l'excentricité et l'inclinaison de l'orbite de la comète par rapport à l'écliptique, et a_J est le demi-grand axe de Jupiter.

périhélique d'un comète suffisamment rapidement pour qu'elle puisse devenir une comète de type Halley avant que Neptune ou Uranus ne l'éjecte.

Un autre scénario a été proposé par Levison et al. (2006) : les comètes de type Halley viendraient en fait du bord externe disque étendu. Le demi-grand axe de ces comètes augmente sous l'influence des planètes, à tel point que les marées galactiques deviennent suffisamment importantes pour réduire la distance périhélique de la comète jusque dans la région des planètes géantes. A ce point, une perturbation planétaire réduit considérablement le demi-grand axe permettant ainsi d'obtenir une comète de type Halley. D'après Levison et al. (2006) 0.01% des comètes du bord externe du disque étendu deviennent des comètes de type Halley.

Le point faible de ce scénario est qu'il conduit à une ré-évaluation de la population du disque étendu rentrant en contradiction avec les observations et avec les estimations basées sur le flux de comètes de la famille de Jupiter. Cependant, comme ces comètes de types Halley viendraient du bord externe du disque étendu qui est moins assujetti à ces contraintes, il semble que ce scénario reste possible.

D'autre part, il est dans tous les cas possible de produire des comètes de type Halley directement à partir du nuage de Oort. Et ce flux supplémentaire doit être pris en considération pour estimer finalement la structure initiale du disque étendu et du nuage de Oort. D'autant plus qu'une partie significative des centaures, et en particulier ceux ayant une grande inclinaison, viennent très probablement du nuage de Oort. Or, les centaures représentent une population d'objets dynamique transitoire, entre le lieu d'origine et les comètes à courte période (de type Halley ou de la famille de Jupiter).

Quoiqu'il en soit, le faible nombre de comète de type Halley observées par rapport au nombre de comètes de la famille de Jupiter constitue un problème similaire à celui du fading problème pour les comètes à longue période : une comète de type Halley devant s'éteindre beaucoup plus rapidement qu'une comète de la famille de Jupiter. Pour résoudre ce problème, Emel'yanenko et al. (2013) proposent une origine commune aux comètes de type Halley et aux comètes de la famille de Jupiter. Les comètes de type Halley et la moitié des comètes de la famille de Jupiter seraient passées par le nuage de Oort, avec une distance périhélique initiale fortement concentrée vers la zone externe de la région planétaire du système solaire et une activité actuelle étant d'autant pus importante que la distance périhélique initiale était élevée.

Ce modèle permettrait aussi de mettre en évidence qu'une grande partie des centaures viendraient du nuage de Oort. Ce qui a aussi été montré par Brasser et al. (2012) pour les centaures ayant une inclinaison élevée.

Chapitre 2

Le modèle dynamique

2.1 Construction du modèle de Marées Galactiques

Le modèle de marées galactiques est un modèle hybride constitué :

(i) d'un mapping, dont le domaine de validation est limité en demi-grand axe et excentricité suivant la précision souhaitée ;

(ii) d'un intégrateur simplectique, dont le domaine de validation a été limité pour des problèmes de convergence ;

(iii) d'un intégrateur numérique classique à pas variable (RADAU 15, Everhart, 1985) qui est utilisé pour les cas limites (orbite pratiquement parabolique, voire hyperbolique).

La construction du modèle est faite dans l'article Breiter et al. (2007) et son implémentation dans le modèle final dans Fouchard et al. (2007a) inséré ci-après.

10

Methods for the Study of the Dynamics of the Oort Cloud Comets II: Modelling the Galactic Tide

Marc Fouchard[1,2,5], Christiane Froeschlé[3], Sławomir Breiter[4],
Roman Ratajczak[4], and Giovanni B. Valsecchi[5] and Hans Rickman[6]

[1] Laboratoire d'Astronomie de Lille/Université de Lille,
1 impasse de l'Observatoire 59000 Lille, France
[2] Institut de Mécanique Céleste et de Calcul d'Ephémérides, UMR 8028 du CNRS, 75014 Paris, France
`fouchard@imcce.fr`
[3] Laboratoire Cassiopée, Université de Nice, CNRS, Observatoire de la Côte d'Azur, BP 4229, FR–06304 Nice, France
`froesch@obs-nice.fr`
[4] Astronomical Observatory of A. Mickiewicz University,
Słoneczna 36, Poznań 60-286, Poland
`breiter@amu.edu.pl,astromek@amu.edu.pl`
[5] INAF-IASF, Via Fosso dell Cavaliere 100, 00133 Roma, Italy
`giovanni@iasf-roma.inaf.it`
[6] Uppsala Astronomical Observatory, Box 515, SE-75120 Uppsala, Sweden
`hans@astro.uu.se`

Abstract. In this paper we present several fast integrators and mappings which model the orbital perturbations of Oort cloud comets, caused by the Galactic tide. The perturbations computed with these models are compared with those obtained using an accurate numerical integration using Everhart's RA15 code. In order to have the best compromise between the computing velocity and precision, it is shown that it is necessary to use a **hybrid model** i.e. a combination of two algorithms, according to the values of the semimajor axe a and the eccentricity-e of the considered comet.

10.1 Introduction

The present paper follows the accompanying Chap. 9, in which we investigated different algorithms to compute the orbital perturbations of Oort cloud comets caused by passing stars. In this chapter, we present several fast integrators and mappings which modelise the effects of the galactic tide. The results computed with these methods are compared with those obtained using a numerical integration of the equations of motion.

M. Fouchard et al.: *Methods for the Study of the Dynamics of the Oort Cloud Comets II*,
Lect. Notes Phys. **729**, 273–296 (2008)
DOI 10.1007/978-3-540-72984-6_10

To model the normal and radial components, with respect to the galactic plane, of the galactic tide different methods and mappings are developed in Sect. 10.2. First of all in Sect. 10.2.1 we give the equations of motion of a comet perturbed by the galactic tide. Then the following models are described, namely:

- A symplectic and regularised integrator (Sect. 10.2.2)
- Some averaged Hamiltonian models using, according to the value of the orbital eccentricity e, either the Delaunay elements or the "Matese elements" and, for each model, mappings based on the respective Taylor development (Sect. 10.2.3);
- A Lie–Poisson averaged model (Sect. 10.2.4).

In Sect. 10.3 the results of calculations performed using the different models are compared to those obtained by numerical integrations. This comparison allows us to build models which use a composition of two different kinds of integrators in order to increase the velocity of the integrations minimising the loss of accuracy (Sect. 10.4). Section 10.5 is devoted to the conclusions.

10.2 Models of Galactic Tide Effects on Cometary Orbits

10.2.1 The Cartesian Model

To establish the equations of motion, we consider two different heliocentric frames. The first one is a *rotating frame* with the $\hat{x}'$–axis in the radial direction pointing towards the galactic centre, the $\hat{y}'$-axis pointing transversely along the local circular velocity and $\hat{z}$ completing a right-handed system. The *fixed frame* $(\hat{x}, \hat{y}, \hat{z})$ is such that it coincides with the rotating frame $(\hat{x}', \hat{y}', \hat{z})$ at time $t = 0$ while keeping its axial directions fixed (see Fig. 1 of [8]).

Let us define Ω_0 as the angular velocity about the galactic centre, assuming the Sun to follow a circular orbit (since the motion of the Sun around the galaxy is clockwise in both our frames, Ω_0 is negative, i.e. the vector is directed along $-\hat{z}$). If ϕ_{r} is an angle in the galactic plane measured in the rotating frame from $\hat{x}'$, and ϕ the corresponding angle measured in the fixed frame from $\hat{x}$ at time t, we have the relation: $\phi = \phi_{\mathrm{r}} + \Omega_0 t$ (see Fig. 1 of [8]). All the final results will be presented in the fixed frame.

The force $\mathbf{F}$ per unit of mass acting on a test particle orbiting the Sun under the influence of the galactic tide is given by (see [10]):

$$\begin{aligned}\mathbf{F} = &-\frac{\mu M_\odot}{r^3}\mathbf{r} + (A-B)(3A+B)x'\hat{x}' - (A-B)^2 y'\hat{y}' \\ &-[4\pi\mu\rho_\odot - 2(B^2 - A^2)]z\hat{z}\ , \end{aligned} \tag{10.1}$$

where x', y', z are the coordinates of the comet in the rotating frame, $\mathbf{r}$ is the Sun–comet vector of length r, A and B are the Oort constants and $\rho_\odot$ is the local density of the galactic disk in the solar neighbourhood. In the remaining part of the paper we will assume $\rho_0 = 0.1 M_\odot\,\mathrm{pc}^{-3}$ [12] and an angular velocity of the Sun around the galactic centre $\Omega_0 = B - A = -26\,\mathrm{km\,s^{-1}kpc^{-1}}$, with the approximation $A = -B$.

The unit of mass is the solar mass ($M_\odot = 1$), the unit of time is the year, and the unit of length is the astronomical unit (AU). As a consequence, the gravitational constant μ is equal to $4\pi^2$.

Let $\mathcal{G}_1$, $\mathcal{G}_2$ and $\mathcal{G}_3$ be defined by

$$\begin{aligned}\mathcal{G}_1 &= -(A-B)(3A+B)\\ \mathcal{G}_2 &= (A-B)^2\\ \mathcal{G}_3 &= 4\pi\mu\rho_\odot - 2(B^2 - A^2)\ .\end{aligned} \tag{10.2}$$

Then, with the chosen values of A, B and ρ_0, one has

$$\begin{aligned}&\mathcal{G}_2 = -\mathcal{G}_1 = 7.0706 \times 10^{-16}\,\mathrm{yr}^{-2}\ ,\\ &\mathcal{G}_3 = 5.6530 \times 10^{-15}\,\mathrm{yr}^{-2}\ ,\\ &\Omega_0 = -\sqrt{\mathcal{G}_2}\ .\end{aligned} \tag{10.3}$$

One may note that the relation $\mathcal{G}_2 = -\mathcal{G}_1$ is a particular case which corresponds to a flat rotation curve of the galaxy, i.e. to a constant tangential velocity of the stars around the galactic centre whatever the star distance to the galactic centre. Numerical experiments have shown that another choice of Oort constants A and B consistent with the observations does not affect the long-term dynamics of the Oort cloud comets [9]. Consequently, some of the models presented here will use the relation $\mathcal{G}_2 = -\mathcal{G}_1$ in order to simplify the equations.

The general equations of motion in Cartesian coordinates are

$$\begin{aligned}\frac{\mathrm{d}^2x}{\mathrm{d}t^2} &= -\frac{\mu M_\odot}{r^3}x - \mathcal{G}_1 x'\cos(\Omega_0 t) + \mathcal{G}_2 y'\sin(\Omega_0 t)\\ \frac{\mathrm{d}^2y}{\mathrm{d}t^2} &= -\frac{\mu M_\odot}{r^3}y - \mathcal{G}_1 x'\sin(\Omega_0 t) - \mathcal{G}_2 y'\cos(\Omega_0 t)\\ \frac{\mathrm{d}^2z}{\mathrm{d}t^2} &= -\frac{\mu M_\odot}{r^3}z - \mathcal{G}_3 z\ ,\end{aligned} \tag{10.4}$$

where x, y, z are the coordinates of the comet in the fixed frame [thus $x' = x\cos(\Omega_0 t) + y\sin(\Omega_0 t)$ and $y' = -x\sin(\Omega_0 t) + y\cos(\Omega_0 t)$]. Equations (10.4) will be referred to as the Cartesian model, also denoted RADAU. The RADAU integrator described by [7] is used at the 15th order, with LL = 12, to integrate (10.4). This integrator was chosen because it is fast, reliable and accurate compared to other non-symplectic integrators.

10.2.2 Regularised Symplectic Integrator

This method was first introduced in [5]. For a detailed description of the method one should read the original paper, only the key points are presented here. In the following we recall the key steps.

Hamiltonian in Cartesian Variables

From (10.1) the complete Hamiltonian is given by

$$\mathcal{H} = \mathcal{H}_0 + \mathcal{H}_1 \tag{10.5}$$

$$\mathcal{H}_0 = \tfrac{1}{2}\left(X^2 + Y^2 + Z^2\right) - \frac{\mu}{r}\,, \tag{10.6}$$

$$\mathcal{H}_1 = \tfrac{1}{2}\left(\mathcal{G}_1 x'^2 + \mathcal{G}_2 y'^2 + \mathcal{G}_3 z^2\right)\,, \tag{10.7}$$

where $(X, Y, Z)^{\mathrm{T}}$ is the velocity vector of the comet in the fixed frame.

Introducing the first equation of system (10.3) explicitly, we can rewrite $\mathcal{H}_1$ as

$$\mathcal{H}_1(x, y, z, t) = \tfrac{1}{2}\,\mathcal{G}_2\left[(y^2 - x^2)C - 2xyS\right] + \tfrac{1}{2}\,\mathcal{G}_3 z^2\,, \tag{10.8}$$

where

$$C = \cos(2\,\Omega_0 t), \qquad S = \sin(2\,\Omega_0 t)\,. \tag{10.9}$$

It is well known that in cometary problems one cannot expect to meet moderate eccentricities of orbits; some kind of regularisation will become unavoidable if a fixed step integrator is to be applied. One of the standard regularising tools is the application of the so-called Kuustanheimo–Stiefel (KS) transformation that turns a Kepler problem into a harmonic oscillator at the expense of increasing the number of degrees of freedom [16]. The approach of [6] is used to set the KS variables in the canonical formalism.

KS Variables

Leaving aside the in-depth quaternion interpretation of the KS transformation given in [6], we restrict ourselves to the basic set of transformation formulae, treating the KS variables as a formal column vector. In the phase space of the KS coordinates $\mathbf{u} = (u_0, u_1, u_2, u_3)^{\mathrm{T}}$ and KS momenta $\mathbf{U} = (U_0, U_1, U_2, U_3)^{\mathrm{T}}$, the former are defined by means of the inverse transformation

$$\begin{aligned} x &= (u_0^2 + u_1^2 - u_2^2 - u_3^2)/\alpha, \\ y &= 2\,(u_1 u_2 + u_0 u_3)/\alpha\,, \\ z &= 2\,(u_1 u_3 - u_0 u_2)/\alpha\,, \end{aligned} \tag{10.10}$$

where α is an arbitrary parameter with the dimension of a length. A dimension raising transformation cannot be bijective, so the inverse of (10.10) is to some extent arbitrary. Following [6] we adopt

$$\mathbf{u} = \sqrt{\frac{\alpha}{2\,(r + x)}}\;(0,\, r + x,\, y,\, z)^{\mathrm{T}}\,, \tag{10.11}$$

for $x \geq 0$, and

$$\mathbf{u} = \sqrt{\frac{\alpha}{2\,(r - x)}}\;(-z,\, y,\, r - x,\, 0)^{\mathrm{T}}\,, \tag{10.12}$$

otherwise. A remarkable property of this transformation is that the distance r becomes a quadratic function of u_i, namely

$$r = \sqrt{x^2 + y^2 + z^2} = \frac{u_0^2 + u_1^2 + u_2^2 + u_3^2}{\alpha} = \frac{\mathbf{u}^2}{\alpha} \; . \tag{10.13}$$

The momenta conjugate to $\mathbf{u}$ are defined as

$$\mathbf{U} = \frac{2}{\alpha} \begin{pmatrix} u_0 X + u_3 Y - u_2 Z \\ u_1 X + u_2 Y + u_3 Z \\ -u_2 X + u_1 Y - u_0 Z \\ -u_3 X + u_0 Y + u_1 Z \end{pmatrix} \; . \tag{10.14}$$

The inverse transformation, allowing the computation of $\mathbf{R} = (X, Y, Z)^{\mathrm{T}}$,

$$\mathbf{R} = \frac{1}{2\,r} \begin{pmatrix} u_0 U_0 + u_1 U_1 - u_2 U_2 - u_3 U_3 \\ u_3 U_0 + u_2 U_1 + u_1 U_2 + u_0 U_3 \\ -u_2 U_0 + u_3 U_1 - u_0 U_2 + u_1 U_3 \end{pmatrix} \; , \tag{10.15}$$

can be supplemented with the identity

$$u_1 U_0 - u_0 U_1 - u_3 U_2 + u_2 U_3 = 0 \; . \tag{10.16}$$

In order to achieve the regularisation without leaving the canonical formalism, we have to change the independent variable from t to a fictitious time s and consider the extended phase space of dimension 10, with a new pair of conjugate variables (u^*, U^*). Thus, in the extended set of canonical KS variables, the motion of a comet is governed by the Hamiltonian function

$$\mathcal{M} = \frac{4\,\mathbf{u}^2}{\alpha^2} \left(\mathcal{K}_0 + U^* + \mathcal{K}_1 \right) = 0 \; , \tag{10.17}$$

where $\mathcal{K}_0$ and $\mathcal{K}_1$ stand for $\mathcal{H}_0$ and $\mathcal{H}_1$ expressed in terms of the extended KS variables set. The transformation just presented is univalent, hence the respective Hamiltonians will have different functional forms, but equal values: $\mathcal{H}_0 = \mathcal{K}_0$, $\mathcal{H}_1 = \mathcal{K}_1$. Restricting the motion to the manifold of $\mathcal{M} = 0$ is of fundamental importance to the canonical change of independent variable; in practical terms we achieve it by setting

$$U^* = -\mathcal{K}_0 - \mathcal{K}_1 \; , \tag{10.18}$$

at the beginning of the numerical integration.

Splitting the Hamiltonian function $\mathcal{M}$ into the sum of the principal term $\mathcal{M}_0$ and of a perturbation $\mathcal{M}_1$, we have

$$\mathcal{M}_0 = \tfrac{1}{2}\, \mathbf{U}^2 + (4U^*/\alpha^2)\, \mathbf{u}^2 \; , \tag{10.19}$$

$$\mathcal{M}_1 = \frac{4\,\mathbf{u}^2}{\alpha^2} \mathcal{H}_1(x, y, z, t) \; . \tag{10.20}$$

Although nothing prohibits u^* and t from differing by an additive constant, we do not take advantage from this freedom and will therefore use the symbol t in most instances instead of the formal u^*. In the next section we provide equations of motion generated by $\mathcal{M}_0$ and $\mathcal{M}_1$ alone; the complete equations of motion can be quickly obtained by adding the respective right-hand sides.

Keplerian Motion

The principal virtue of the KS variables consists in their ability to transform the Kepler problem into a four-dimensional oscillator with a constant frequency

$$\omega = 2\,\frac{\sqrt{2U^*}}{\alpha}\,. \tag{10.21}$$

In addition one gets the equation for the fictitious time s, that may be written as:

$$\frac{\mathrm{d}s}{\mathrm{d}t} = \frac{\alpha}{4\,r}\,. \tag{10.22}$$

Thanks to the introduction of α, the fictitious time s has the dimension of time and if we assume

$$\alpha = \frac{2\,\mu}{|U^*|}\,, \tag{10.23}$$

orbital periods in s and t will be equal.

For $U^* > 0$, the map Φ_0 representing the solution of the Keplerian motion can be directly quoted from [2]. If Δ is the fictitious time step, then

$$\Phi_{0,\Delta}:\ \begin{pmatrix} \mathbf{u} \\ \mathbf{U} \\ U^* \end{pmatrix} \to \begin{pmatrix} \mathbf{u}\cos\omega\Delta + \mathbf{U}\omega^{-1}\sin\omega\Delta \\ -\mathbf{u}\,\omega\sin\omega\Delta + \mathbf{U}\cos\omega\Delta \\ U^* \end{pmatrix}\,. \tag{10.24}$$

Moreover, if $\mathbf{v} = \Phi_{0,\Delta}\mathbf{u}$ and $\mathbf{V} = \Phi_{0,\Delta}\mathbf{U}$ are the final values of variables,

$$\Phi_{0,\Delta}:\ t \to t + \frac{2\,\Delta}{\alpha^2}\left(\boldsymbol{u}^2 + \frac{\boldsymbol{U}^2}{\omega^2}\right) + 2\,\frac{\boldsymbol{u}^{\mathrm{T}}\boldsymbol{U} - \boldsymbol{v}^{\mathrm{T}}\boldsymbol{V}}{\alpha^2\omega^2}\,. \tag{10.25}$$

One may easily check that the sum $\mathbf{u}^2 + \mathbf{U}^2\omega^{-2}$ is invariant under Φ_0 and it can be replaced by $\mathbf{v}^2 + \mathbf{V}^2\omega^{-2}$ in practical computations of the Kepler equation (10.25).

It may happen, however, that $U^* < 0$ (when the motion is hyperbolic for instance). A simple modification of Φ_0 in that case amounts to take

$$\omega = 2\frac{\sqrt{-2\,U^*}}{\alpha}\,, \tag{10.26}$$

and replacing (10.24) and (10.25) by

$$\Phi_{0,\Delta}: \begin{pmatrix} \mathbf{u} \\ \mathbf{U} \\ U^* \end{pmatrix} \to \begin{pmatrix} \mathbf{u} \cosh \omega\Delta + \mathbf{U}\omega^{-1} \sinh \omega\Delta \\ \mathbf{u}\, \omega \sinh \omega\Delta + \mathbf{U} \cosh \omega\Delta \\ U^* \end{pmatrix} , \qquad (10.27)$$

and

$$\Phi_{0,\Delta}: \ t \to t + \frac{2\,\Delta}{\alpha^2} \left(\boldsymbol{u}^2 - \frac{\boldsymbol{U}^2}{\omega^2} \right) - 2\, \frac{\boldsymbol{u}^{\mathrm{T}} \mathbf{U} - \boldsymbol{v}^{\mathrm{T}} \mathbf{V}}{\alpha^2 \omega^2} . \qquad (10.28)$$

Similarly to the elliptic case, $\mathbf{u}^2 - \mathbf{U}^2/\omega^2$ is invariant under Φ_0.

Galactic Tide

The Hamiltonian $\mathcal{M}_1$ has the nice property of being independent of the momenta. Thus a half of the equations of motion have right-hand sides equal to zero, and the remaining right-hand sides are constant.

Accordingly, all KS coordinates are constant, the physical time t does not flow, and the momenta are subjected to a linear "kick":

$$\Phi_{1,\Delta}: \begin{pmatrix} \mathbf{u} \\ t \\ \mathbf{U} \\ U^* \end{pmatrix} \to \begin{pmatrix} \mathbf{u} \\ t \\ \mathbf{U} - \Delta\, \mathbf{F}(\mathbf{u}, t) \\ U^* - \Delta\, F^*(\mathbf{u}, t) \end{pmatrix} . \qquad (10.29)$$

Mixing Cartesian and KS variables for the sake of brevity, we can represent $\mathbf{F}$ and F^* as

$$\mathbf{F} = \frac{8\,\mathcal{H}_1}{\alpha^2}\, \boldsymbol{u} + \frac{4\boldsymbol{u}^2}{\alpha^2} \frac{\partial \mathcal{H}_1}{\partial \boldsymbol{u}} \qquad (10.30)$$

$$F^* = \frac{4\,\boldsymbol{u}^2}{\alpha^2}\, \Omega_0\, \mathcal{G}_2 \xi_3 , \qquad (10.31)$$

where

$$\frac{\partial \mathcal{H}_1}{\partial \mathbf{u}} = -\mathcal{G}_2\, \xi_2 \frac{\partial x}{\partial \mathbf{u}} + \mathcal{G}_2\, \xi_1 \frac{\partial y}{\partial \mathbf{u}} + \mathcal{G}_3\, z \frac{\partial z}{\partial \mathbf{u}} \qquad (10.32)$$

$$\begin{aligned} \xi_1 &= yC - xS, \\ \xi_2 &= xC + yS, \\ \xi_3 &= (x^2 - y^2)\, S - 2\, x\, y\, C . \end{aligned} \qquad (10.33)$$

Symplectic Corrector

One of the advantages offered by the integrators introduced in [11] is a simple definition of a symplectic corrector—an extra stage that improves the accuracy in perturbed motion problems. The symplectic corrector is defined as a solution of the equations of motion generated by

$$\mathcal{M}_{\mathrm{c}} = \left\{ \left\{ \mathcal{M}_0, \mathcal{M}_1 \right\}, \mathcal{M}_1 \right\} , \qquad (10.34)$$

where $\{\ ,\ \}$ is the canonical (or "symplectic") Poisson bracket in the phase space spanned by $\mathbf{u}, t, \mathbf{U}, U^*$. Observing that $\mathcal{M}_0$ is quadratic in $\mathbf{U}$ and linear in U^*, we easily obtain

$$\mathcal{M}_{\mathrm{c}}(\boldsymbol{u}, t) = \sum_{i=0}^{3} \left(\frac{\partial \mathcal{M}_1}{\partial u_i} \right)^2 = \mathbf{F}^2 \,. \tag{10.35}$$

The solution of the equations of motion derived from $\mathcal{M}_{\mathrm{c}}$ results in

$$\Phi_{\mathrm{c},\Delta} : \begin{pmatrix} \mathbf{u} \\ t \\ U_j \\ U^* \end{pmatrix} \to \begin{pmatrix} \mathbf{u} \\ t \\ U_j - 2\,\Delta \left(\frac{\partial \mathbf{F}}{\partial u_j} \right) \cdot \mathbf{F} \\ U^* - 2\,\Delta \left(\frac{\partial \mathbf{F}}{\partial t} \right) \cdot \mathbf{F} \end{pmatrix} . \tag{10.36}$$

In spite of a formally simple form, (10.36) involve rather complicated expressions for the second derivatives of $\mathcal{M}_1$, because

$$\frac{\partial \mathbf{F}}{\partial u_j} \cdot \mathbf{F}(\mathbf{u}, t) = \sum_{i=0}^{3} \frac{\partial^2 \mathcal{M}_1}{\partial u_i \partial u_j} \frac{\partial \mathcal{M}_1}{\partial u_i} , \tag{10.37}$$

$$\frac{\partial \mathbf{F}}{\partial t} \cdot \mathbf{F}(\mathbf{u}, t) = \sum_{i=0}^{3} \frac{\partial^2 \mathcal{M}_1}{\partial u_i \partial t} \frac{\partial \mathcal{M}_1}{\partial u_i} \,. \tag{10.38}$$

One may find a detailed method to compute the Hessian matrix of $\mathcal{M}_1$ in [5].

Laskar–Robutel Integrators

The composition methods of [11] differ from usual recipes because, regardless of the number of "stages" involved in one step, they all remain second-order integrators according to the formal estimates. However, if the Hamiltonian has been split into a leading term and a perturbation having a small parameter ε as a factor, the truncation error of the integrator is $\max(\varepsilon^2\, h^3, \varepsilon\, h^m)$ where m is the number of stages involved in one step. The second term of this sum is similar to classical composition methods errors, and the first can be quite small for weakly perturbed problems. At the expense of the $\varepsilon^2\, h^3$ term in the error estimate, the authors were able to avoid backward stages that degrade numerical properties of usual composition methods. The use of a corrector improves the integrator by reducing the truncation error: its first term drops to $\varepsilon^2\, h^5$.

Following the recommendation of [11], and after having performed numerical tests (see [5]), the best integrator is obtained using the following composition for each single step of size h:

$$\begin{aligned}\Phi_h = \Phi_{c,q} \circ \Phi_{1,d_1} \circ \Phi_{0,c_2} \circ \Phi_{1,d_2} \circ \Phi_{0,c_3} \circ \\ \circ \Phi_{1,d_2} \circ \Phi_{0,c_2} \circ \Phi_{1,d_1} \circ \Phi_{c,q} \;,\end{aligned} \tag{10.39}$$

where

$$\begin{aligned} &d_1 = h/12, && d_2 = (5/12)\,h \;, \\ &c_2 = (1/2 - \sqrt{5}/10)\,h, && c_3 = h/\sqrt{5} \;, \\ &q = -h^3(13 - 5\sqrt{5})/288 \;. \end{aligned} \tag{10.40}$$

This integrator will be referred as LARKS.

LARKS Step Size Choice

The Hamiltonian error of LARKS, based on the above composition, is proportional to $\varepsilon^2 h^4$ (see [5]). Observing that $\varepsilon \propto ar^2$, where a is the semi-major axis of a comet, and r is the Sun–comet distance, we look for the step size selection rule that gives a similar precision for a wide range of initial conditions. This can be achieved if the product

$$K = \varepsilon^2 h^4 \tag{10.41}$$

has similar values for all comets to be studied. Thus, finding some optimum step size h_o for a given semi-axis a_o, and then launching the integration for a different semi-axis a_1, we adjust the step size and use

$$h_1 = h_\mathrm{o} \left(\frac{a_\mathrm{o}}{a_1}\right)^{3/2} \;, \tag{10.42}$$

when the orbit is elliptic ($a_1 > 0$) and using a_1 instead of r. For a hyperbolic orbit the step size is adjusted through

$$h_1 = h_\mathrm{o} \left(\frac{a_\mathrm{o}^{3/2}}{|a_1|^{1/2} r}\right) \;. \tag{10.43}$$

In the test described in this section, we set h_o as 1/20 of the Keplerian period implied by $a_\mathrm{o} = 50,000$ AU and adjusted the step according to (10.42) or (10.43) for other orbits. For elliptical orbits, in order to avoid numerical resonance between the step size and the orbital period [19], we do not use a step size larger than 1/20 of the Keplerian period, even if it might be allowed by (10.42).

Stop Time for LARKS

The fact that the fictitious time s is the independent variable is an inevitable issue associated with the use of the KS variables regularisation. What happens if one wants to obtain the state of a comet at some particular final epoch of the physical time t? This problem appears if one wants to stop the integration as close as possible to a precise value T_f of the real time.

A method which turns out to be effective, whatever the dynamics, is the following. Let f be the function defined by $f(s) = t - T_f$. Thus the problem is to solve $f(s) = 0$. Let f_p and s_p be the values of f and s before some step, and f_a and s_a be the values after this step. The integration stops as soon as $f_\mathrm{a} > 0$. From this point, the method is built according to an iterative process which evaluates $f_\mathrm{p}, s_\mathrm{p}$ and $f_\mathrm{a}, s_\mathrm{a}$, such that the solution s_s is always between s_p and s_a.

For each step, one computes the derivatives $\mathrm{d}f_\mathrm{p}$ and $\mathrm{d}f_\mathrm{a}$ of f in s_p and s_a, respectively, using (10.22) and (10.13). Consequently, one can easily compute the equation of the tangent to f in s_p and s_a. Let s_m be the value of s for which the two tangents intersect. If s_m is not between s_p and s_a, the next guess s_g of the solution s_s is computed using a linear approximation of f or a bisection method between s_p and s_a. The choice is made according to the method which makes the most important reduction of the interval $[s_\mathrm{p}, s_\mathrm{a}]$. Otherwise, if s_m is between s_p and s_a, then the next guess s_g is given by the intersection of the tangent at f in s_p (resp. in s_a) with the abscissa axis if it lies between s_p and s_m (resp. between s_m and s_a).

One stops the iterative process as soon as $f(s_\mathrm{g})$ is close enough to 0, that is $t_\mathrm{g} - T_f \approx 0$, where t_g is the value of the real time obtained for s_g.

Stop at Perihelion for LARKS

In the framework of Oort cloud comets dynamics, it may be necessary to suspend the integration of a comet at its perihelion. When an integrator like RADAU is used, then the step size is very small when the comet passes through its perihelion, thus it is quite easy to stop at the cometary perihelion only by checking the evolution of the Sun–comet distance. This is not the case for LARKS, which may have a large step size even when the comet is at its perihelion, hence the evolution of the Sun–comet distance is not sufficient.

However, when a comet is near its perihelion, one may neglect the perturbative part due to the galactic tide. Consequently, as it has been already noted, the motion in the KS variables is simply a harmonic oscillator. Using this property it is very easy to stop the integration exactly at the cometary perihelion. Indeed, if $(\mathbf{u}, \mathbf{U})$ are the KS variables of a comet, then $\mathbf{u} \cdot \mathbf{U} = 0$ when the comet is at its perihelion. Thus, let $(\mathbf{u}_\mathrm{p}, \mathbf{U}_\mathrm{p})$ be the KS variables before some step and $(\mathbf{u}_\mathrm{a}, \mathbf{U}_\mathrm{a})$ after this step. When $\mathbf{u}_\mathrm{p} \cdot \mathbf{U}_\mathrm{p} < 0$ and $\mathbf{u}_\mathrm{a} \cdot \mathbf{U}_\mathrm{a} > 0$ it means that the comet went through its perihelion during the step. When $U^* > 0$, using (10.24), the step length h which should be performed from $(\mathbf{u}_\mathrm{p}, \mathbf{U}_\mathrm{p})$ to the exact perihelion is given by

$$h = \frac{1}{2\omega} \tan^{-1} \left(\frac{2\omega \mathbf{u}_\mathrm{p} \cdot \mathbf{U}_\mathrm{p}}{\omega^2 u_\mathrm{p}^2 - U_\mathrm{p}^2} \right) . \qquad (10.44)$$

When $U^* < 0$, using (10.25), the step length is given by

$$h = \frac{1}{4\omega} \log\left(\frac{1+X}{1-X}\right) , \tag{10.45}$$

where

$$X = \frac{2\omega \mathbf{u}_\mathrm{p} \cdot \mathbf{U}_\mathrm{p}}{\omega^2 u_\mathrm{p}^2 + U_\mathrm{p}^2} . \tag{10.46}$$

10.2.3 The Hamiltonian Models

In this section we will give the Hamiltonian equations of motion derived from the average Hamiltonian, using two sets of variables according to the value of the orbital eccentricity e (see [9]).

The Hamiltonian Model with Delaunay Variables

The complete Hamiltonian given by

$$\mathcal{H} = -\frac{\mu}{2a} + \mathcal{G}_1 \frac{x'^2}{2} + \mathcal{G}_2 \frac{y'^2}{2} + \mathcal{G}_3 \frac{z^2}{2} \tag{10.47}$$

may be written using the Delaunay's variables: $L = \sqrt{\mu a}$, $G = \sqrt{\mu a(1-e^2)}$, $H = G \cos i$, $\ell = M$, $g = \omega$ and $h = \Omega$, where a, e, i, M, ω, are the cometary semi-major axis, eccentricity, inclination, mean anomaly, argument of perihelion and longitude of node (all the angles being measured in the fixed galactic frame). The mean anomaly being a fast variable with respect to the other ones, the Hamiltonian is averaged over ℓ.

Then, one writes the averaged Hamiltonian equations of motion, which gives:

$$\left\langle \frac{\mathrm{d}L}{\mathrm{d}t} \right\rangle = 0 \tag{10.48}$$

$$\begin{aligned}\left\langle \frac{\mathrm{d}G}{\mathrm{d}t} \right\rangle = & -\frac{5L^2}{2\mu^2}(L^2 - G^2)\Big\{ \cos g \sin g \Big[\mathcal{G}_3 \Big(1 - \frac{H^2}{G^2}\Big) \\ & + (\mathcal{G}_1 \sin^2 h_\mathrm{r} + \mathcal{G}_2 \cos^2 h_\mathrm{r}) \frac{H^2}{G^2} - \mathcal{G}_1 \cos^2 h_\mathrm{r} \\ & - \mathcal{G}_2 \sin^2 h_\mathrm{r} \Big] - (\mathcal{G}_1 - \mathcal{G}_2)(\cos^2 g - \sin^2 g) \cos h_\mathrm{r} \sin h_\mathrm{r} \frac{H}{G} \Big\}\end{aligned} \tag{10.49}$$

$$\begin{aligned}\left\langle \frac{\mathrm{d}H}{\mathrm{d}t} \right\rangle = & \frac{L^2}{2\mu^2}(\mathcal{G}_1 - \mathcal{G}_2)\Big\{ 5(L^2 - G^2)\frac{H}{G} \cos g \sin g (\cos^2 h_\mathrm{r} - \sin^2 h_\mathrm{r}) \\ & + \sin h_\mathrm{r} \cos h_\mathrm{r} \\ & \cdot \Big[G^2 - H^2 + 5(L^2 - G^2)\Big(\cos^2 g - \sin^2 g \frac{H^2}{G^2} \Big) \Big] \Big\}\end{aligned} \tag{10.50}$$

$$\begin{aligned}\left\langle\frac{\mathrm{d}g}{\mathrm{d}t}\right\rangle = \frac{L^2G}{2\mu^2}\Big\{&\mathcal{G}_3\Big[1-5\sin^2 g\Big(1-\frac{L^2H^2}{G^4}\Big)\Big]\\ &+(\mathcal{G}_1\cos^2 h_\mathrm{r}+\mathcal{G}_2\sin^2 h_\mathrm{r})(1-5\cos^2 g)\\ &-5(\mathcal{G}_1\sin^2 h_\mathrm{r}+\mathcal{G}_2\cos^2 h_\mathrm{r})\frac{L^2H^2}{G^4}\sin^2 g\\ &+5(\mathcal{G}_1-\mathcal{G}_2)\cos g\sin g\cos h_\mathrm{r}\sin h_\mathrm{r}(G^2+L^2)\frac{H}{G^3}\Big\}\end{aligned} \tag{10.51}$$

$$\begin{aligned}\left\langle\frac{\mathrm{d}h}{\mathrm{d}t}\right\rangle = \frac{L^2}{2G\mu^2}\Big\{&(\mathcal{G}_1\sin^2 h_\mathrm{r}+\mathcal{G}_2\cos^2 h_\mathrm{r}-\mathcal{G}_3)\\ &[G^2+5(L^2-G^2)\sin^2 g]\frac{H}{G}-5(\mathcal{G}_1-\mathcal{G}_2)\\ &(L^2-G^2)\cos g\sin g\cos h_\mathrm{r}\sin h_\mathrm{r}\Big\},\end{aligned} \tag{10.52}$$

where $h_\mathrm{r} = h - \Omega_0 t$ at time t.

The quantity L, i.e. the semi-major axis, is obviously conserved since the mean anomaly does not appear in the averaged Hamiltonian. Furthermore, one may note that, when the radial component of the tide is neglected, i.e. when $\mathcal{G}_1 = \mathcal{G}_2 = 0$, then H is conserved. In this case the dynamics is completely integrable. Many papers were devoted to this peculiar case: for instance [1, 3, 10, 14, 15].

The Hamiltonian Model with Matese Elements

When $e \simeq 1$, (10.49)–(10.52) become singular. In order to remove this singularity, we adopt the variables: L, $\Theta = H_b$, H, M, $\theta = b$ and $\lambda = l$, with $H_\mathrm{b} = -\sqrt{\mu a(1-e^2)}\cos\alpha$ and $H = \sqrt{\mu a(1-e^2)}\cos i$. Here b and l are the latitude and longitude of perihelion of the comet, and α is the angle between the orbital plane and the plane orthogonal to the galactic plane and passing through the perihelion and the galactic poles, measured from the south galactic pole to the cometary velocity (see Fig. 1 of [9]).

This set of elements will be referred to as Matese elements since it first appeared in [15]. Similar elements have been used elsewhere in the literature in order to remove the singularity at $e = 1$: see [18] for elliptic collision orbits and [17] for hyperbolic collision orbits. The Matese elements are slightly different from those used in the quoted papers, but the procedure to define them is similar. These can be shown to be canonical.

One substitutes x', y' and z by the Matese elements in (10.47), and averages with respect to the mean anomaly. Then, the Hamiltonian equations of motion are:

$$
\begin{aligned}
\left\langle \frac{\mathrm{d}L}{\mathrm{d}t} \right\rangle &= 0 \\
\left\langle \frac{\mathrm{d}\Theta}{\mathrm{d}t} \right\rangle &= \frac{L^2}{2\mu^2} \Big[\cos\theta \sin\theta (-4\Theta^2 + 5L^2)(\mathcal{G}_1 \cos^2\lambda_\mathrm{r} + \mathcal{G}_2 \sin^2\lambda_\mathrm{r}) \\
&\quad -\mathcal{G}_1 \left(\Theta\cos\theta\cos\lambda_\mathrm{r} + H\sin\lambda_\mathrm{r}\frac{\sin\theta}{\cos^2\theta} \right) \\
&\quad \cdot \left(\Theta\sin\theta\cos\lambda_\mathrm{r} + H\sin\lambda_\mathrm{r}\frac{1}{\cos\theta} \right) \\
&\quad -\mathcal{G}_2 \left(\Theta\cos\theta\sin\lambda_\mathrm{r} - H\cos\lambda_\mathrm{r}\frac{\sin\theta}{\cos^2\theta} \right) \\
&\quad \cdot \left(\Theta\sin\theta\sin\lambda_\mathrm{r} - H\cos\lambda_\mathrm{r}\frac{1}{\cos\theta} \right) \\
&\quad +\mathcal{G}_3 \frac{\sin\theta}{\cos^3 b}(5(\Theta^2 - L^2)\cos^4\theta + 4H^2) \Big] \\
\left\langle \frac{\mathrm{d}H}{\mathrm{d}t} \right\rangle &= \frac{L^2(\mathcal{G}_1 - \mathcal{G}_2)}{2\mu^2\cos^2\theta} \big[(-4\Theta^2\cos^2\theta - 4H^2 + 5L^2\cos^2\theta)\cos^2\theta\cos\lambda_\mathrm{r}\sin\lambda_\mathrm{r} \\
&\quad +(\Theta\cos\theta\sin\theta\sin\lambda_\mathrm{r} - H\cos\lambda_\mathrm{r})(\Theta\cos\theta\sin\theta\cos\lambda_\mathrm{r} + H\sin\lambda_\mathrm{r}) \big] \\
\left\langle \frac{\mathrm{d}\theta}{\mathrm{d}t} \right\rangle &= \frac{L^2}{2\mu^2\cos^2\theta} \big\{ -4\Theta\cos^4\theta \left(\mathcal{G}_1\cos^2\lambda_\mathrm{r} + \mathcal{G}_2\sin^2\lambda_\mathrm{r} \right) \\
&\quad +\mathcal{G}_1(\Theta\cos\theta\sin\theta\cos\lambda_\mathrm{r} + H\sin\lambda_\mathrm{r})\cos\theta\sin\theta\cos\lambda_\mathrm{r} \\
&\quad +\mathcal{G}_2(\Theta\cos\theta\sin\theta\sin\lambda_\mathrm{r} - H\cos\lambda_\mathrm{r})\cos\theta\sin\theta\sin\lambda_\mathrm{r} \\
&\quad +\mathcal{G}_3\Theta\cos^2\theta(1 - 5\sin^2\theta) \big\} \\
\left\langle \frac{\mathrm{d}\lambda}{\mathrm{d}t} \right\rangle &= \frac{L^2}{2\mu^2\cos^2\theta} \big\{ -4H\cos^2\theta \left(\mathcal{G}_1\cos^2\lambda_\mathrm{r} + \mathcal{G}_2\sin^2\lambda_\mathrm{r} \right) \\
&\quad +\mathcal{G}_1\sin\lambda_\mathrm{r}(\Theta\cos\theta\sin\theta\cos\lambda_\mathrm{r} + H\sin\lambda_\mathrm{r}) \\
&\quad -\mathcal{G}_2\cos\lambda_\mathrm{r}(\Theta\cos\theta\sin\theta\sin\lambda_\mathrm{r} - H\cos\lambda_\mathrm{r}) - 4\mathcal{G}_3 H\sin^2\theta \big\}
\end{aligned}
$$

The singularity at $\cos\theta = 0$ is evident, but these equations show that the singularity at $e = 1$ has indeed disappeared.

The Mappings

The two above averaged models are already faster than the Cartesian model (see [8]). However, in order to enhance their efficiency, one may consider the truncated Taylor development of their solution. More precisely, one writes any of the averaged models in the form:

$$
\frac{\mathrm{d}\mathbf{x}}{\mathrm{d}t} = \mathbf{f}(\mathbf{x}_\mathrm{r}) \, , \tag{10.53}
$$

where $\mathbf{x}$ is the vector defined by the Delaunay or the Matese elements, and the subscript r means that the longitude is measured in the rotating frame.

Then, the truncated Taylor development at order N of the solution of this equation is

$$\mathbf{x}(T+\Delta T)=\mathbf{x}(T)+\sum_{n=1}^{N}\left.\frac{\mathrm{d}^n\mathbf{x}}{\mathrm{d}t^n}\right|_T\frac{\Delta T^n}{n!}+\mathcal{O}(\varDelta T^{N+1})\ , \tag{10.54}$$

where the subscript T indicates that the quantities are computed at time T.

Taking ΔT equal to one orbital period of the comet (which is consistent with having averaged the Hamiltonian) this development provides us an easy way to derive mappings of different orders.

Experiments have shown (see [18]) that the mappings of order 3 give the best compromise between precision and velocity. However, one should be very careful in using these mappings, due to the singularities of the two averaged models. Indeed, the effects of the singularity when $e=1$ for the model using the Delaunay variables and the singularity when $\cos b = 0$ for the model using the Matese variables are enhanced when one uses the truncated Taylor development of their solution.

It turns out that the mapping using the Delaunay elements may be safely used for eccentricity smaller than 0.999, otherwise the mapping using the Matese elements is more precise. The composition of this two mappings will be referred as the MAPP model.

10.2.4 The Lie–Poisson Model

This model is described in detail in [5]. One should refer to this paper for a full description of the method.

Equations of Motion

The integrators presented in the previous sections solve the equations of motion in the fixed reference frame, where the radial component of the galactic tide is explicitly time-dependent. Our second method can be more conveniently discussed in the rotating heliocentric reference frame $(\hat{x}', \hat{y}', \hat{z})$. The present model uses also the first equation of (10.3) explicitly, which simplifies the results drastically.

The Hamiltonian function for a comet subjected to the galactic tide in the rotating frame is given by

$$\mathcal{H}=\mathcal{H}_0+\mathcal{H}_1\ , \tag{10.55}$$

$$\mathcal{H}_0=\frac{1}{2}\left(X'^2+Y'^2+Z^2\right)-\frac{\mu}{(x'^2+y'^2+z^2)^{1/2}}, \tag{10.56}$$

$$\mathcal{H}_1=\Omega_0\,(y'\,X'-x'\,Y')+\tfrac{1}{2}\left(\mathcal{G}_2\,(y'^2-x'^2)+\mathcal{G}_3\,z^2\right), \tag{10.57}$$

where (x', y', z) and (X', Y', Z) are the position and velocity of the comet in the rotating frame.

As in Sect. 10.2.3, one may average the Hamiltonian $\mathcal{H}$ with respect to the mean anomaly ℓ. The averaged Hamiltonian $\langle \mathcal{H}_1 \rangle$ is now expressed in terms of the Laplace vector $\mathbf{e}$ and a scaled angular momentum vector $\mathbf{h}$ instead of canonical elements as the Delaunay or the Matese ones. Their components are related to the Keplerian orbit elements

$$\mathbf{e} \equiv \begin{pmatrix} e_1 \\ e_2 \\ e_3 \end{pmatrix} = e \begin{pmatrix} \cos\omega \cos\Omega_\mathrm{r} - c \sin\omega \sin\Omega_\mathrm{r} \\ \cos\omega \sin\Omega_\mathrm{r} + c \sin\omega \cos\Omega_\mathrm{r} \\ s\, \sin\omega \end{pmatrix} , \tag{10.58}$$

$$\mathbf{h} \equiv \begin{pmatrix} h_1 \\ h_2 \\ h_3 \end{pmatrix} = \sqrt{1-e^2} \begin{pmatrix} s\, \sin\Omega_\mathrm{r} \\ -s\, \cos\Omega_\mathrm{r} \\ c \end{pmatrix} , \tag{10.59}$$

where e is the eccentricity, $s = \sin i$, $c = \cos i$. Recalling that in the rotating frame the momenta X' and Y' are not equal to velocities $\frac{\mathrm{d}x'}{\mathrm{d}t}$ and $\frac{\mathrm{d}y'}{\mathrm{d}t}$ (this fact can be immediately deduced from the canonical equations $\frac{\mathrm{d}x'}{\mathrm{d}t} = \partial\mathcal{H}/\partial X'$ and $\frac{\mathrm{d}y'}{\mathrm{d}t} = \partial\mathcal{H}/\partial Y'$), we assume that the usual transformation rules between Keplerian elements and position/velocity are used with the velocities directly substituted by the momenta. With this approach the Keplerian motion in the rotating frame is described by the means of orbital elements that are all constant except for Ω_r which reflects the frame rotation $\left(\frac{\mathrm{d}\Omega_\mathrm{r}}{\mathrm{d}t} = -\Omega_0\right)$.

Using the "vectorial elements" $\mathbf{h}$ and $\mathbf{e}$, letting n stand for

$$n = \sqrt{\frac{\mu}{a^3}} , \tag{10.60}$$

and changing the independent variable from time t to τ_1, such that

$$\frac{\mathrm{d}\tau_1}{\mathrm{d}t} = \frac{\mathcal{G}_3}{n} , \tag{10.61}$$

one obtains the averaged Hamiltonian $\langle \mathcal{H} \rangle$, given by

$$\begin{aligned} \langle \mathcal{H} \rangle = n\, a^2\, \Big[& \tfrac{5}{4}\, e_3^2 + \tfrac{1}{4} h_1^2 + \tfrac{1}{4} h_2^2 + \\ & + \nu \left(-\tfrac{5}{4}\, e_1^2 + \tfrac{5}{4}\, e_2^2 + \tfrac{1}{4} h_1^2 - \tfrac{1}{4} h_2^2 - n\, \Omega_0^{-1}\, h_3 \right) \Big] , \end{aligned} \tag{10.62}$$

where, all the constant terms have been dropped and, using the usual approximation $\Omega_0 = -\sqrt{\mathcal{G}_2}$, we introduced a dimensionless parameter

$$\nu = \frac{\Omega_0^2}{\mathcal{G}_3} = \frac{\mathcal{G}_2}{\mathcal{G}_3} . \tag{10.63}$$

The vectorial elements can be used to create a Lie–Poisson bracket

$$(f; g) \equiv \left(\frac{\partial f}{\partial \mathbf{v}} \right)^{\mathrm{T}} \mathbf{J}(\mathbf{v})\, \frac{\partial g}{\partial \mathbf{v}} , \tag{10.64}$$

with the structure matrix

$$\mathbf{J}(\mathbf{v}) = \begin{pmatrix} \hat{\mathbf{h}} & \hat{\mathbf{e}} \\ \hat{\mathbf{e}} & \hat{\mathbf{h}} \end{pmatrix} . \tag{10.65}$$

The "hat map" of any vector $\mathbf{x} = (x_1, x_2, x_3)^{\mathrm{T}}$ is defined as

$$\hat{\mathbf{x}} = \begin{pmatrix} 0 & -x_3 & x_2 \\ x_3 & 0 & -x_1 \\ -x_2 & x_1 & 0 \end{pmatrix} . \tag{10.66}$$

This matrix is known as the vector product matrix, because

$$\hat{\mathbf{x}}\,\mathbf{y} = \mathbf{x} \times \mathbf{y} . \tag{10.67}$$

Using the Lie–Poisson bracket (10.64) we can write equations of motion for the vectorial elements

$$\mathbf{v} = (h_1, h_2, h_3, e_1, e_2, e_3)^{\mathrm{T}} \tag{10.68}$$

in the non-canonical Hamiltonian form

$$\mathbf{v}' = (\mathbf{v}; \mathcal{K}) , \tag{10.69}$$

where derivatives with respect to τ are marked by the "prime" symbol and the scaled Hamiltonian

$$\mathcal{K} = -\frac{\langle \mathcal{H} \rangle}{n\,a^2} . \tag{10.70}$$

Writing (10.69) explicitly, we obtain

$$h_1' = -\frac{5}{2}(1-\nu)\,e_2\,e_3 + \frac{1-\nu}{2}\,h_2\,h_3 + \frac{n\,\nu}{\Omega_0}\,h_2 , \tag{10.71}$$

$$h_2' = \frac{5}{2}(1+\nu)\,e_1\,e_3 - \frac{1+\nu}{2}\,h_1\,h_3 - \frac{n\,\nu}{\Omega_0}\,h_1, \tag{10.72}$$

$$h_3' = \nu\,(h_1\,h_2 - 5\,e_1\,e_2), \tag{10.73}$$

$$e_1' = -\frac{4+\nu}{2}\,h_2\,e_3 + \frac{5}{2}\,\nu\,h_3\,e_2 + \frac{n\,\nu}{\Omega_0}\,e_2, \tag{10.74}$$

$$e_2' = \frac{4-\nu}{2}\,h_1\,e_3 + \frac{5}{2}\,\nu\,h_3\,e_1 - \frac{n\,\nu}{\Omega_0}\,e_1, \tag{10.75}$$

$$e_3' = \frac{1-4\,\nu}{2}\,h_1\,e_2 - \frac{1+4\,\nu}{2}\,h_2\,e_1. \tag{10.76}$$

Substituting $\nu = 0$, the readers may recover the correct form of the galactic disk tide equations published in [3, 4]. Equations (10.71)–(10.76) admit three integrals of motion: apart from the usual conservation of the time-independent Hamiltonian $\mathcal{K} = \mathrm{const}$, two geometrical constraints

$$\mathbf{h}\cdot\mathbf{e}=0, \qquad h^2+e^2=1\ , \tag{10.77}$$

are respected thanks to the properties of the Lie–Poisson bracket (10.64). Indeed, both quadratic forms are the Casimir functions of our bracket, i.e.

$$(\mathbf{h}\cdot\mathbf{e};\, f)=(h^2+e^2;\, f)=0\ , \tag{10.78}$$

for any function f, hence in particular for $f=\mathcal{K}$.

Lie–Poisson Splitting Method

The Hamiltonian $\mathcal{K}$ can be split into a sum of three non-commuting terms

$$\mathcal{K}=\mathcal{K}_1+\mathcal{K}_2+\mathcal{K}_3, \tag{10.79}$$

$$\mathcal{K}_1=\frac{5}{4}\,\nu\,e_1^2-\frac{1+\nu}{4}\,h_1^2\ , \tag{10.80}$$

$$\mathcal{K}_2=-\frac{5}{4}\,\nu\,e_2^2-\frac{1-\nu}{4}\,h_2^2\ , \tag{10.81}$$

$$\mathcal{K}_3=-\frac{5}{4}\,e_3^2+\frac{n\,\nu}{\Omega_0}\,h_3\ . \tag{10.82}$$

Each of the terms $\mathcal{K}_i$ is in turn a sum of two components that commute, because it can be easily verified that $(e_j;\, h_j)=0$ for all $j\in\{1,2,3\}$. In these circumstances, we can approximate the real solution

$$\mathbf{v}(\tau)=\exp\left(\tau\, L\right)\,\mathbf{v}(0)\ , \tag{10.83}$$

where $L\,f\equiv(f;\,\mathcal{K})$, using a composition of maps

$$\Psi_{i,\tau}:\quad \mathbf{v}(0)\rightarrow\mathbf{v}(\tau)=\exp\left(\tau\, L_i\right)\,\mathbf{v}(0)\ , \tag{10.84}$$

where $L_i\,f\equiv(f;\,\mathcal{K}_i)$ for $i=1,2,3$. Each $\Psi_{i,\tau}$ is in turn a composition of two maps

$$\Psi_{i,\tau}=E_{i,\tau}\circ H_{i,\tau}=H_{i,\tau}\circ E_{i,\tau}\ , \tag{10.85}$$

generated by the e_i and h_i related terms of $\mathcal{K}_i$.

The Contribution of $\mathcal{K}_1$

The two terms of $\mathcal{K}_1$ generate equations of motion

$$\mathbf{v}'=\left(\mathbf{v};\,\tfrac{5}{4}\,\nu\,e_1^2\right)=\tfrac{5}{2}\,e_1\,\nu\begin{pmatrix}\mathbf{0} & \mathbf{Y}_1\\ \mathbf{Y}_1 & \mathbf{0}\end{pmatrix}\mathbf{v}\ , \tag{10.86}$$

and

$$\mathbf{v}'=\left(\mathbf{v};\,-\tfrac{1}{4}(1+\nu)\,h_1^2\right)=-\tfrac{1}{2}\,h_1\,(1+\nu)\begin{pmatrix}\mathbf{0} & \mathbf{Y}_1\\ \mathbf{Y}_1 & \mathbf{0}\end{pmatrix}\mathbf{v}\ , \tag{10.87}$$

where

$$\mathbf{Y}_1 = \begin{pmatrix} 0 & 0 & 0 \\ 0 & 0 & -1 \\ 0 & 1 & 0 \end{pmatrix} . \tag{10.88}$$

The composition of these two maps results in

$$\Psi_{1,\tau} :\ \mathbf{v} \to \begin{pmatrix} \mathbf{M}_1 & \mathbf{N}_1 \\ \mathbf{N}_1 & \mathbf{M}_1 \end{pmatrix} \mathbf{v} , \tag{10.89}$$

where

$$\mathbf{M}_1 = \begin{pmatrix} 1 & 0 & 0 \\ 0 & c_{11}c_{12} & -c_{11}s_{12} \\ 0 & c_{11}s_{12} & c_{11}c_{12} \end{pmatrix} , \quad \mathbf{N}_1 = \begin{pmatrix} 0 & 0 & 0 \\ 0 & s_{11}s_{12} & s_{11}c_{12} \\ 0 & -s_{11}c_{12} & s_{11}s_{12} \end{pmatrix} . \tag{10.90}$$

$$\psi_{11} = \tfrac{5}{2}\, e_1\, \nu\, \tau \quad \text{and} \quad \psi_{12} = \tfrac{1}{2}\,(1+\nu)\, h_1\, \tau , \tag{10.91}$$

introducing

$$c_{ij} = \cos\psi_{ij}, \qquad s_{ij} = \sin\psi_{ij} . \tag{10.92}$$

The Contribution of $\mathcal{K}_2$

The equations of motion derived from the two terms of $\mathcal{K}_2$ are

$$\mathbf{v}' = \left(\mathbf{v};\, -\tfrac{5}{4}\,\nu\, e_2^2\right) = \tfrac{5}{2}\,\nu\, e_2 \begin{pmatrix} \mathbf{0} & \mathbf{Y}_2 \\ \mathbf{Y}_2 & \mathbf{0} \end{pmatrix} \mathbf{v} , \tag{10.93}$$

and

$$\mathbf{v}' = \left(\mathbf{v};\, -\tfrac{1}{4}(1-\nu)\, h_2^2\right) = \tfrac{1}{2}\,(1-\nu)\, h_2 \begin{pmatrix} \mathbf{0} & \mathbf{Y}_2 \\ \mathbf{Y}_2 & \mathbf{0} \end{pmatrix} \mathbf{v} , \tag{10.94}$$

where

$$\mathbf{Y}_2 = \begin{pmatrix} 0 & 0 & 1 \\ 0 & 0 & 0 \\ -1 & 0 & 0 \end{pmatrix} . \tag{10.95}$$

Composing the two maps we obtain

$$\Psi_{2,\tau} :\ \mathbf{v} \to \begin{pmatrix} \mathbf{M}_2 & \mathbf{N}_2 \\ \mathbf{N}_2 & \mathbf{M}_2 \end{pmatrix} \mathbf{v} , \tag{10.96}$$

where

$$\mathbf{M}_2 = \begin{pmatrix} c_{21}c_{22} & 0 & -c_{21}s_{22} \\ 0 & 1 & 0 \\ c_{21}s_{22} & 0 & c_{21}c_{22} \end{pmatrix} , \quad \mathbf{N}_2 = \begin{pmatrix} s_{21}s_{22} & 0 & c_{22}s_{21} \\ 0 & 0 & 0 \\ -c_{22}s_{21} & 0 & s_{21}s_{22} \end{pmatrix} , \tag{10.97}$$

$$\psi_{21} = \tfrac{5}{2}\,\nu\, e_2\, \tau \quad \text{and} \quad \psi_{22} = -\,\frac{h_2\,(1-\nu)}{2}\,\tau . \tag{10.98}$$

The Contribution of $\mathcal{K}_3$

The equations of motion derived from the two terms of $\mathcal{K}_3$ are

$$\mathbf{v}' = \left(\mathbf{v};\, -\tfrac{5}{4}\, e_3^2\right) = \tfrac{5}{2}\, e_3 \begin{pmatrix} \mathbf{0} & \mathbf{Y}_3 \\ \mathbf{Y}_3 & \mathbf{0} \end{pmatrix} \mathbf{v}\ , \tag{10.99}$$

and

$$\mathbf{v}' = \left(\mathbf{v};\, h_3\, n\, \nu\, \Omega_0^{-1}\right) = -\frac{n\,\nu}{\Omega_0} \begin{pmatrix} \mathbf{0} & \mathbf{Y}_3 \\ \mathbf{Y}_3 & \mathbf{0} \end{pmatrix} \mathbf{v}\ , \tag{10.100}$$

where

$$\mathbf{Y}_3 = \begin{pmatrix} 0 & -1 & 0 \\ 1 & 0 & 0 \\ 0 & 0 & 0 \end{pmatrix}\ . \tag{10.101}$$

Composing the two maps we obtain

$$\Psi_{3,\tau} :\ \mathbf{v} \to \begin{pmatrix} \mathbf{M}_3 & \mathbf{N}_3 \\ \mathbf{N}_3 & \mathbf{M}_3 \end{pmatrix} \mathbf{v}\ , \tag{10.102}$$

where

$$\mathbf{M}_3 = \begin{pmatrix} c_{31}c_{32} & c_{31}s_{32} & 0 \\ -c_{31}s_{32} & c_{31}c_{32} & 0 \\ 0 & 0 & 1 \end{pmatrix}\ , \quad \mathbf{N}_3 = \begin{pmatrix} s_{31}s_{32} & -c_{32}s_{31} & 0 \\ c_{32}s_{31} & s_{31}s_{32} & 0 \\ 0 & 0 & 0 \end{pmatrix}\ , \tag{10.103}$$

$$\psi_{31} = \frac{5}{2}\, e_3\, \tau \quad \text{and} \quad \psi_{32} = \frac{n\,\nu}{\Omega_0}\, \tau\ . \tag{10.104}$$

10.2.5 The Lie–Poisson Method of Order 2

The composition methods of [11] cannot be used for our Lie–Poisson splitting method, because the Hamiltonian function has been partitioned into three terms. Moreover, none of the terms can be qualified as a small perturbation. In these circumstances, the principal building block can be a "generalised leapfrog"

$$\Psi_\Delta = \Psi_{1,\Delta/2} \circ \Psi_{2,\Delta/2} \circ \Psi_{3,\Delta} \circ \Psi_{2,\Delta/2} \circ \Psi_{1,\Delta/2}\ . \tag{10.105}$$

This Lie–Poisson method, called LPV2, is a second-order method with a local truncation error proportional to the cube of the step size Δ^3. Although we use LPV2 as a final product in this paper, it can be used as a building block for higher-order methods. A collection of appropriate composition rules can be found in [13].

In practice, the step size Δ will be set equal to one orbital period.

10.3 Comparisons Between the Different Models

In order to compare the reliability and speed of the integrators we performed the following experiment: $400,000$ sets of initial orbital elements were randomly chosen in a specified range, under the condition that their respective distribution is uniform, i.e.

- The initial semi-major axes in the range $3000 \leq a_0 \leq 10^5$ AU, with distribution uniform in $\log_{10} a_0$
- The initial eccentricity in the range $0 \leq e_0 \leq 0.9999$, with a uniform distribution
- The initial inclination i_0 such that $-1 \leq \cos i_0 \leq 1$, with a uniform distribution
- The initial argument of the perihelion, the longitude of the ascending node and the initial mean anomaly (where needed) in the range from 0 to 2π, with a uniform distribution

Using this set of elements, we integrated the equations over one cometary period using LARKS, LPV2, MAPP and compared the results with those obtained with the Cartesian model.

For the stopping time in LARKS, the method described at the end of Sect. 10.2.2 until $|T_f - t| < 10^{-3}$ yr was used.

The relative error in the comet position E_{p} was defined as

$$E_{\mathrm{p}} = \left| \frac{q_{\mathrm{mod}} - q_{\mathrm{R}}}{q_0} \right| , \tag{10.106}$$

where q_{mod} and q_{R} denote the value of the perihelion distance at the end of the integration of one period computed by the tested integrator and by the RADAU, respectively, and q_0 is the initial value of the perihelion distance.

Then, the e_0–$\log_{10} a_0$ plane is divided into 60×70 cells. In each cell we record the maximum value E_{max} reached by the error E_{p} for the initial conditions belonging to the cell.

The results obtained for the three models are shown in Fig. 10.1. The MAPP and the LPV2 models, both used with a step size equal to the unperturbed Keplerian period, are equivalent as far as the accuracy is concerned. Indeed, the best analytical fit of the level curve $E_{\mathrm{p}} = 0.01$ is given by:

$$a_{\mathrm{c}} = 10^{4.748 \pm 0.004} (1 - e)^{0.182 \pm 0.006} , \tag{10.107}$$

for the MAPP model, and

$$a_c = 10^{4.751 \pm 0.003} (1 - e)^{0.185 \pm 0.005} , \tag{10.108}$$

for the LPV2 model. These two equations may be considered as identical within the error bounds of the exponents.

For both models the error is essentially due to the averaging of the equations of motion with respect to the mean anomaly. Conversely, the LARKS method is highly reliable in the whole phase space domain under study, since the error never exceed 0.01. The effect of the time step selection rule (10.42)

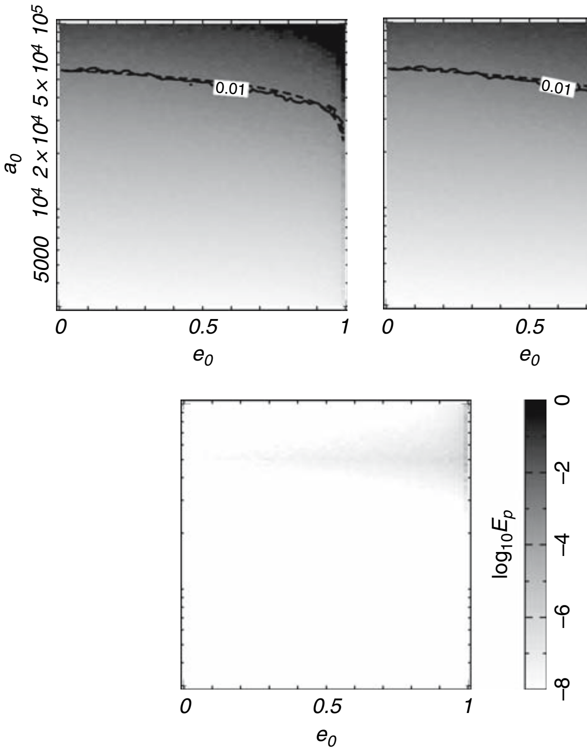

Fig. 10.1. Maximum error E_p [(see 10.106)] in each cell of the e_0–a_0 plane for the models MAPP (**top left**), LPV2 (**top right**) and LARKS (**bottom**). The *solid line curves* correspond to $E_\mathrm{p} = 0.01$ and the *dotted curves* are the best fits of the level curves

is clearly visible above $a_0 = 50,000$ AU; the reliability of LARKS is almost conserved when a_0 increases.

Speaking about the computation times required to perform all the integrations, the MAPP, LPV2 and LARKS needed 5.5, 1.8 and 99 s, whereas the RA15 integration took 1820 s. That is, LPV2 is three times faster than MAPP, and almost 40 times faster than LARKS, and LARKS is almost 20 times faster than RA15.

10.4 Hybrid Integrators

10.4.1 Definition

In order to have the best compromise between velocity and precision, one can consider hybrid models which use the fastest accurate model according to the values of the cometary eccentricity and semi-major axis.

In [9] the hybrid model MAPP + RADAU was introduced and applied to reproduce the effects of the galactic tide on the dynamics of 10^6 comets over 5 Gyr. This hybrid model was such that MAPP was used below the analytical fit of the $E_\mathrm{p} = 0.01$ level curve given by (10.107), otherwise RADAU was used.

This hybrid model became obsolete since [5] where LPV2 and LARKS have been introduced. Indeed, the hybrid model LPV2 + LARKS, where LPV2 is used below the analytical fit of the $E_\mathrm{p} = 0.01$ level curve given by (10.108), is much faster than MAPP + RADAU and has the same accuracy. In the special case of a galactic potential such that $A \neq -B$, i.e. $\mathcal{G}_2 \neq -\mathcal{G}_1$, LARKS is easily generalisable whereas LPV2 is not. Thus in such a case the hybrid model MAPP + LARKS may be used.

Let us consider the integration of a comet with a hybrid model, say LARKS + LPV2. The oscillation of the eccentricity with time may lead to repeating shifts between the use of LARKS and the use of LPV2. However, when LARKS is used the semi-major axis oscillates with a period equal to the orbital period of the comet (this may be easily understood from the fact that in the Hamiltonian formalism, the mean anomaly and $L = \sqrt{\mu a}$ are conjugate coordinates), whereas it is a constant of motion when LPV2 is used. Indeed, for the LPV2 model the mean anomaly cancels out.

Since LPV2 is applied for an integer number of orbital periods, one may just record the value of the mean anomaly at the beginning of a sequence where LPV2 is used, and restore the mean anomaly value at the end of the sequence. Consequently, when one shifts from LPV2 to LARKS, the memory of the original orbit is conserved, as far as the averaging is neglected.

However, a shift from LARKS to LPV2 occurs for an arbitrary value of the mean anomaly, thus it occurs for an arbitrary value of the semi-major axis in the interval of its oscillations. Consequently, from one such shift to another one, the LPV2 model will be applied to different averaged orbits since the semi-major axis is different. After many shifts, a drift on the semi-major axis value may be observed.

An easy way to remove this drift is to allow the shift between LARKS and LPV2 only when the comet is exactly at its perihelion. Indeed, in this way, the shift occurs always at a precise time of the semi-major axis oscillation, thus the memory of the real orbit may be conserved when many shifts from LARKS to LPV2 are performed.

10.5 Conclusion

Different models of the galactic tide have been presented. The first one, called LARKS, is a symplectic integrator which uses the Kuustanheimo–Stiefel (KS) transformation to regularise the equations of motion. This model turns out to be reliable over the whole phase space and almost 20 times faster than a non-symplectic integrator using Cartesian coordinates (RADAU). The two other models are based on the averaging of the equations of motion with respect to the mean anomaly. One, which is called MAPP, which uses the Taylor development at order three of the solutions of the averaged equations of motion. In this case the equations are written using the Hamiltonian formalism with two different sets of canonical variables according to the value of the eccentricity. The second averaged model, called LPV2, considers the equations of motion using the normalised Laplace and angular momentum vectors. Then a Lie–Poisson integrator of order 2 is used by splitting the Hamiltonian into three parts.

As regards the accuracy, these two models are equivalent, but they are reliable only in a limited domain of the phase space. These models are both faster than LARKS, but LPV2 is three times faster than MAPP and 40 times faster than LARKS. The main advantage of MAPP is that it is more didactic. MAPP is also more general since it may consider any kind of radial component of the tide—but with the assumption that the tide is axi-symmetric—whereas LPV2 requires $\mathcal{G}_2 = -\mathcal{G}_1$.

The best hybrid model can be defined as a combination between the use of LPV2 and LARKS according to the value of the cometary eccentricity and semi-major axis. For instance, if one wants a confidence level of 1% on the perihelion distance variation over one cometary period, one may use the analytical equation given by

$$a_{\rm c} = 10^{4.751}(1-e)^{0.185} \tag{10.109}$$

to define the upper frontier of the domain where LPV2 may be used.

If one wants a confidence level of 0.1% one may consider the value

$$a_{\rm c} = 10^{4.570}(1-e)^{0.176} \tag{10.110}$$

as the upper limit of the domain where LPV2 may be used. However, the use of (10.110) will slow down the integrations since it reduces the domain of application of LPV2. It may be also softer to use RADAU rather than LARKS for hyperbolic orbits or when the semimajor axis is greater than 100 000 all. Indeed the loss in computation time will be small whereas the accuracy of LARKS is less guaranteed. The above hybrid model may be used for any long-term simulations of the Oort cloud comets dynamics under the effects of the galactic tide.

References

1. Brasser, R., 2001. *MNRAS* **324**, 1109. 284
2. Breiter, S., 1998. *CeMDA* **71**, 229. 278
3. Breiter, S. and Ratajczak, R., 2005. *MNRAS* **364**, 1222. 284, 288
4. Breiter, S. and Ratajczak, R., 2006. *MNRAS* **367**, 1808. 288
5. Breiter, S., Fouchard, M., and Ratajczak, R., 2007. *MNRAS* **377**, 1151. 275, 280, 281, 286, 2
6. Deprit, A., Elipe, A., and Ferrer, S., 1994. *CeMDA* **58**, 151. 276

7. Everhart, E., 1985. In Carusi, A. and Valsecchi G. B. (eds), *Dynamics of Comets: Their Origin and Evolution*, Reidel, Dordrecht, p. 185. 275
8. Fouchard, M., Froeschle, Ch., Matese, J. J., and Valsecchi, G. B., 2005. *CeMDA* **93**, 231. 274, 285
9. Fouchard, M., Froeschle, Ch., Valsecchi, G. B., and Rickman, H., 2006. *CeMDA* **95**, 299. 275, 283, 284, 294
10. Heisler, J. and Tremaine, S., 1986. *Icarus* **65**, 13. 274, 284
11. Laskar, J. and Robutel, P., 2001. *CeMDA* **80**, 39. 279, 280, 291
12. Levison, H., Dones, L., and Duncan, M. J., 2001. *AJ* **121**, 2253. 275
13. McLachlan, R. I. and Quispel, G. R. W., 2002. *Acta Numer.* **11**, 341. 291
14. Matese, J. J. and Whitman, P. G., 1989. *Icarus* **82**, 389. 284
15. Matese, J. J. and Whitman, P. G., 1992. *CeMDA* **54**, 13. 284
16. Stiefel, E. L. and Scheifele, G., 1971. *Linear and Regular Celestial Mechanics*, Springer-Verlag, Berlin. 276
17. Tommei, G., 2006. *CeMDA* **94**, 176. 284
18. Tremaine, S., 2001. *CeMDA* **79**, 231. 284, 286
19. Wisdom, J. and Holman, M., 1992. *AJ* **104**, 2022. 281

2.2 Construction du modèle de perturbations stellaires

Les perturbations des étoiles passant au voisinage du Soleil sur les trajectoires des comètes, lorsque le demi-grand axe est significativement élevé, a été pris en compte par Öpik (1932), avant même que Oort (1950) ne fasse l'hypothèse de l'existence du nuage portant son nom. Sachant que les vitesses relatives des étoiles par rapport au Soleil sont bien plus élevées que les vitesses héliocentriques des comètes lorsqu'elles se trouvent à leur aphélie, les perturbations stellaires ont été modélisées en considérant : *(i)* les effets des étoiles se traduisent par une impulsion appliquée à la vitesse héliocentrique de la comète lorsque l'étoile passe à son périhélie ; *(ii)* on considère que les mouvements héliocentriques des étoiles sont rectilignes et uniformes ; *(iii)* et l'impulsion est calculée à partir d'une trajectoire infinie de l'étoile vers le passé et vers le futur.

Ces trois hypothèses conduisent à la construction de l'impulsion classique définie dans Rickman (1976). Ce modèle a été amélioré en suivant les propositions faites par Dybczynski (1994) qui supprime l'hypothèse de trajectoire rectiligne et uniforme et celle d'une impulsion calculée à partir d'une trajectoire infinie.

Le modèle construit dans Rickman et al. (2005) permet de tenir compte au mieux de la trajectoire de l'étoile. La perturbation est toujours modélisée sous forme d'une impulsion appliquée à la vitesse, et à la position de la comète dans ce cas, à l'instant du passage de l'étoile à son périhélie. Cette impulsion est calculée de manière séquentielle en utilisant un pas constant en anomalie vraie du corps le plus proche de l'étoile (Soleil ou comète). Ceci permet d'avoir un pas variable en temps, diminuant lorsque l'étoile se rapproche de l'un des deux objets.

Si la distance minimale entre l'étoile et le Soleil ou la comète devient trop petite, alors le calcul séquentiel devient très lent et le calcul de l'impulsion se fait alors en effectuant une intégration numérique avec l'intégrateur classique RADAU 15 (Everhart, 1985).

La mise en place du modèle ainsi que les tests sur son efficacité et fiabilité sont présentés dans l'article Rickman et al. (2005), et son implémentation dans le modèle final dans Fouchard et al. (2007b).

9

Methods for the Study of the Dynamics of the Oort Cloud Comets I: Modelling the Stellar Perturbations

Marc Fouchard[1,2,5], Christiane Froeschlé[3], Hans Rickman[4]
and Giovanni B. Valsecchi[5]

[1] Laboratoire d'Astronomie de Lille/Université de Lille,
1 impasse de l'Observatoire 59000 Lille, France
[2] Institut de Mécanique Céleste et de Calcul d'Ephémérides, UMR 8028 du CNRS, 75014 Paris, France
`fouchard@imcce.fr`
[3] Laboratoire Cassiopée, Université de Nice, CNRS, Observatoire de la Côte d'Azur, BP 4229, FR-06304 Nice, France
`froesch@obs-nice.fr`
[4] Uppsala Astronomical Observatory, Box 515, SE-75120 Uppsala, Sweden
`hans@astro.uu.se`
[5] INAF-IASF, Via Fosso dell Cavaliere 100, 00133 Roma, Italy
`giovanni@iasf-roma.inaf.it`

Abstract. In this chapter we present different approximate models of computing the perturbations on the Oort cloud comets caused by passing stars. All these methods are checked against an accurate numerical integration using Everhart's RA15 code. A random sample of stellar passages, simulating those suffered by the solar system, but extrapolated over a time of $10^{(10)}$ years, is created. For each model we measured the errors and their dependence on the encounter parameters.

9.1 Introduction

A good knowledge of the present structure of the Oort cloud is one of the clues to understand the formation of the solar system. There is a wide consensus on the fact that the Oort cloud was formed by the residual planetesimals scattered by the giant planets during the period of their formation. Moreover, it is important to follow carefully the history of comets which originated in the Oort cloud, to be able to estimate the total population and the mass of the entire cloud.

There are three major external perturbers which influence the Oort cloud comets and inject them into the planetary region. These are the stellar perturbations, the galactic tidal forces and giant molecular clouds (GMCs). Although

M. Fouchard et al.: *Methods for the Study of the Dynamics of the Oort Cloud Comets I*, Lect. Notes Phys. **729**, 257–272 (2008)
DOI 10.1007/978-3-540-72984-6_9

a penetrating encounter of the solar system with a GMC is a rare event, it may have considerable effects [18]. However, due to the rarity and the poor knowledge of the circumstances of such encounters [1], they are generally omitted from studies of Oort cloud dynamics.

We concentrate our study on the effects of the two other external perturbers, namely passing stars and the galactic tide. While stellar perturbations occur at random and may be treated as a stochastic process, the galactic tidal force is a quasi–integrable perturbation which acts continuously, changing the cometary orbital elements and in particular the perihelion distance. As shown by many authors [3, 9, 20] the fraction of the population of Oort cloud comets that can become observable would be very small if only the effect of the galactic tide was at work.

Passing stars can randomize the whole population and may cause strong temporary enhancements of the flux of observable comets called comet showers [15], while the galactic tide produces the main part of the steady flux of Oort cloud comets towards the observable region (e.g. [16, 21]). Thus for a general understanding of the origin of LP comets, both pertubers, i.e. passing stars and galactic tide must be modelled.

To get a realistic model of the Oort cloud it is necessary to follow the dynamics of a very large number of test particles ($\simeq 10^6$, to sample as well as possible the available parameter space), over time scales equal to the age of the solar system. Therefore, one has to develop reliable methods that model both the galactic tide and the stellar close encounters with the lowest possible computational cost.

In the present chapter we investigate different algorithms to compute the orbital perturbations of Oort cloud comets caused by passing stars. The reliability and validity of these methods are checked against pure numerical integrations. In an accompanying paper (Chap. 10) we present several fast integrators and mappings that model the effects of the galactic tide. Again, the results computed with those methods will be compared to those obtained using a numerical integration of the equations of motion.

9.2 Modelling the Stellar Pertubations

As underlined previously, passing stars may perturb the orbits of Oort cloud comets. Oort [24] considered stellar perturbations as the only source of perturbations that change cometary orbits and inject them into the observable region. However, it has later been shown that the galaxy is another major perturber of cometary orbits. According to Hills [15] stellar perturbations ensure a constant flux of comets with $a \geq 2 \times 10^4$ AU towards the planetary region. As found by Dybczyǹski [7], star perturbations through the Oort cloud may induce the asymmetry of the distribution of observable comets (see also [8] and citations therein). Moreover Hills [15] showed that a close or penetrating stellar passage through the Oort cloud may deflect large numbers of comets to orbits that enter the planetary region forming what are known as comet showers.

To estimate stellar perturbations Oort [24] used the so-called impulse approximation, introduced in [25] to investigate the influence of stellar encounters on a cloud of meteoroids or comets. This approximation allows to obtain analytical solutions using simplifying assumptions, namely:

- The star velocity is constant and the motion follows a straight line;
- The star velocity is large enough that the comet and the Sun can be considered to be at rest during the stellar passage.

This approximation was used in a large number of papers (e.g., [2, 15, 21, 27, 32]) and has been found to be useful as a quick estimator in numerical Monte Carlo simulations of cometary orbital evolutions (e.g., [5, 12, 13, 16, 17, 22, 26, 28, 31]).

However, some concern over the accuracy of the method arises from simple considerations. For instance, the particularly important, very large impulses tend to be associated with the slowest stellar encounters, for which the assumption of a high stellar speed is not verified, or with very close passages to either the Sun, in which case the neglect of the hyperbolic deflection may lead to large errors, or the comet, where the neglect of even a slight cometary motion may change the results considerably.

The impulse approximation was briefly discussed in [23] in a work that concerned planets rather than comets, and in which an improvement for the case of a very close encounter star–Sun, which took into account the hyperbolic deflection of the stellar trajectory, was introduced.

Later on, Dybczyński [6] introduced a new, improved variant of the impulse approximation that is applicable to any time interval and allows a higher accuracy by treating the stellar orbit exactly. The advantage over the classical impulse approximation was convincingly demonstrated, but there was no discussion of the errors arising from the neglect of the motion of the comet during the stellar passage.

Eggers and Woolfson [10] have shown that for comets moving relatively fast, the impulse approximation breaks down. They developed a sequential method, in which the star path is split up and several partial impulses are computed along the stellar orbit assumed to be rectilinear. The authors found that this method is in good agreement with numerical integrations and also 10–100 times faster; they also suggested that their method may be improved by applying a sequential treatment to Dybczyński's method.

In this chapter we present such a method, that was introduced for the first time in [29]; the comet moves along its changing orbit receiving several impulses from the star which describes a hyperbolic orbit. Our method, the classical impulse approximation, and Dybczyński's algorithm are studied by comparing their results with those obtained in purely numerical integrations of the motion equations for a random sample of stellar encounters, simulating the ones expected for the solar system during 10^{10} yr. Each star is allowed to interact with 40 comets placed on Oort cloud orbits with given semi-major axis (a_0) and perihelion distance (q_0).

In Sect. 9.3 we describe the sample of stellar encounters which may interact with the comets. Section 9.4 is devoted to present the different algorithms, while the results of the computations are presented in Sect. 9.5. Finally the conclusions are given in Sect. 9.6.

9.3 Stellar Encounters

Our purpose is to study the errors introduced by the different algorithms as a function of the encounter parameters. We use a distribution of stellar parameters that is as realistic as possible, and to this purpose we have created a random sample of stellar encounters experienced by the solar system during 10^{10} yr, according to the frequency distribution given in [14]. The upper limit for the solar impact parameter is 4×10^5 AU, and we use the 13 stellar categories listed in Table 9.1 of [28] with their corresponding data, for which the total encounter frequency is $10.525\,\pi^{-1}$ pc^{-2}Myr^{-1}. The total number of encounters in our random sample is thus 395,813.

The stellar speed of a given encounter is computed in the same fashion as in [28]. We combine the apex velocity vectorially with a peculiar velocity vector that is randomly chosen from a 3D gaussian distribution with the prescribed dispersion. The direction of motion of each star is distributed uniformly, since the Oort cloud may be modelled as spherically symmetric; in this way, with respect to a random orientation of the cometary orbit, the stellar encounters are always isotropically oriented. Figure 9.1 shows the frequency distribution of our encounter sample in the parametric plane of approach velocity V^* and solar impact parameter b^*.

Table 9.1. Computing time spent with different methods for calculating stellar perturbations

a_0 (AU)	10^4	3×10^4	10^5
IEM (s)	5×10^4	2.3×10^4	1.7×10^4
CIA (s)	44	45	44
DIA* (s)	37	37	37
DIA (s)	130	131	116
SIA50 (s)	7 646	8 246	9 172
SIA250 (s)	1 470	1 557	1 764
SIA500 (s)	779	932	912
SIA1000 (s)	476	476	500

The method used is indicated in the left column, and the four SIA calculations are distinguished by the choice of the initial time step. The three columns to the right correspond to different choices of the initial semi-major axis, as indicated in the top line.

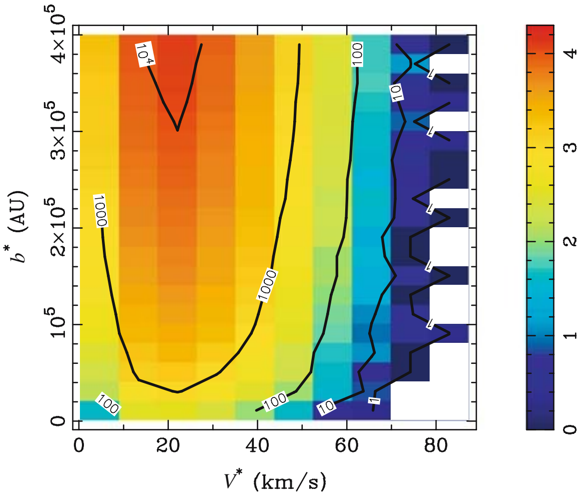

Fig. 9.1. The (V^*, b^*) plane is split into equal boxes, and the colour coding shows the number of stellar encounters in each box on a log scale as indicated to the right. Isodensity curves marked by the corresponding numbers are also shown

Our data set for each combination $(a_0,\ q_0)$ consists of 395,813 stellar encounters, experienced one by one by a sample of 40 comets. For each new star, each comet is put back into its initial orbit with the same starting value of the mean anomaly. The random timing of the encounters means that, each time, the comets find themselves at random orbital positions as the star passes.

9.4 The Dynamical Models

In order to estimate the errors of the different methods of computing stellar pertubations we have to compare their results with those obtained with an accurate numerical integration. To this purpose, the Newtonian equations of motion of the comet and the star are integrated in a heliocentric reference frame, using the RA15 [7] integrator. RA15 is a variable step integrator with an external control of the accuracy specified as an input parameter (LL). The value LL = 12 was found sufficient to guarantee a high accuracy of the resulting stellar perturbations.

As explained in [29], since our numerical integration is not extended over an infinite path before and after closest approach, we have performed numerical experiments in order to find the optimal choice of the limiting start and end distance d_{lim}. We found that $d_{\mathrm{lim}} = \sqrt{b^{*2} + r_{\mathrm{lim}}^2}$ with $r_{\mathrm{lim}} = 1.0 \times 10^6$ AU is large enough to define the limiting distance in our study of different dynamical models [29]. In the remainder of this paper, the reference model to compute stellar perturbations, denoted by IEM (integration of the equations of motion), consists of an integration using RA15 with LL = 12 that starts and ends when the Sun–star distance is equal to d_{lim}.

9.4.1 The Classical Impulse Model

In this case, which we hereafter denote by CIA (classical impulse approximation), the comet is held fixed with respect to the Sun, while the star passes with constant velocity along the straight line defined by the impact parameter b^*, a unit vector $\hat{\mathbf{b}}^*$ that defines the direction of closest approach and the velocity vector $\mathbf{V}^*$ of the star with respect to the Sun. The impulse of the comet relative to that of the Sun caused by the time-integrated stellar attraction is computed from

$$\Delta\mathbf{v} = \frac{2GM_*}{V^*}\left\{\frac{\hat{\mathbf{b}}_{\mathrm{c}}}{b_{\mathrm{c}}} - \frac{\hat{\mathbf{b}}^*}{b^*}\right\} \; ; \tag{9.1}$$

adding this value of $\Delta\mathbf{v}$ to the heliocentric velocity of the comet at the orbital position in question, one obtains a new orbital velocity and thus new values of the orbital elements. Figure 9.2 illustrates the geometry considered.

The CIA computes the perturbation for a time span extending to infinity before and after closest approach; some of the differences between the results of CIA and IEM may result from this. However, this contribution to the total difference should be small, just like the contribution to the perturbation experienced outside d_{lim}. In principle, (9.1) may be modified to account for a finite time interval (see [6, 27]), but the result would be a large increase of the computing time. Since the principal advantage of the CIA is its speed, the use of such a procedure would hence be self-defeating.

9.4.2 Dybczyński's Impulse Approximation

In this case, which we denote by DIA, the comet is held fixed with respect to the Sun, while the star describes the part of its heliocentric, hyperbolic orbit

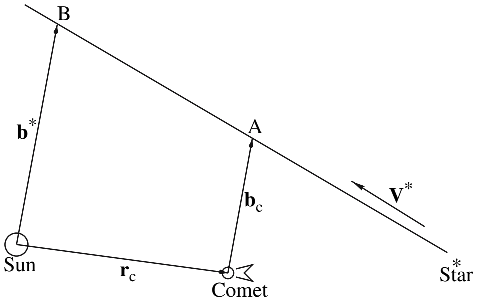

Fig. 9.2. Geometry of a stellar passage considered for the classical impulse approximation

that is contained within our limiting distance.[1] Just like the parameters of the straight line of the CIA, this hyperbola is uniquely defined by the parameters of the stellar encounter. Given the position and velocity vectors of the comet with respect to the Sun, the hyperbola characterizing the relative star–comet motion can also be uniquely defined.

As in the case of the CIA, we have to select a position of the comet along its orbit, and once again we pick the one that the unperturbed comet would have at the time of the stellar perihelion passage. Since we choose this time to be the same for the CIA and DIA, the positions of the comet are also the same.

As shown in [6], in a heliocentric frame of reference where the x-axis is anti-parallel to the stellar velocity vector, the y-axis is parallel to $\hat{\mathbf{b}}^*$ and the z-axis completes a right-handed system (this will be referred to as the 'impact frame'), the impulse vector of the comet relative to the Sun is given by

$$\begin{aligned}
\Delta v_x &= (a_\mathrm{c}\Delta v_{\mathrm{c}\xi} + b_\mathrm{c}\Delta v_{\mathrm{c}\eta})\frac{1}{c_\mathrm{c}} - (a_\mathrm{s}\Delta v_{\mathrm{s}\xi} + b_\mathrm{s}\Delta v_{\mathrm{s}\eta})\frac{1}{c_\mathrm{s}}\ , \\
\Delta v_y &= (a_\mathrm{c}\Delta v_{\mathrm{c}\eta} - b_\mathrm{c}\Delta v_{\mathrm{c}\xi})\frac{b_\mathrm{s} - y_\mathrm{c}}{c_\mathrm{c} b_\mathrm{c}} - (a_\mathrm{s}\Delta v_{\mathrm{s}\eta} - b_\mathrm{s}\Delta v_{\mathrm{s}\xi})\frac{1}{c_\mathrm{s}}\ , \\
\Delta v_z &= (a_\mathrm{c}\Delta v_{\mathrm{c}\eta} - b_\mathrm{c}\Delta v_{\mathrm{c}\xi})\frac{-z_\mathrm{c}}{c_\mathrm{c} b_\mathrm{c}}\ ,
\end{aligned} \tag{9.2}$$

where a_s, b_s and c_s are the semi-axes and focal distance of the heliocentric hyperbola ($c_\mathrm{s}^2 = a_\mathrm{s}^2 + b_\mathrm{s}^2$), and a_c, b_c and c_c are the same quantities for the cometocentric hyperbola. All the cometocentric quantities are computed taking into account the heliocentric velocity of the comet. This is an arbitrary choice that deviates from description given in [6], but the results are thereby slightly improved.

The cometary position is described by y_c and z_c, and the various Δv quantities are given by

$$\begin{aligned}
\Delta v_{\mathrm{s}\xi} &= \frac{-GM_*}{b_\mathrm{s} V_\infty}(\sin\vartheta_{\mathrm{s}2} - \sin\vartheta_{\mathrm{s}1})\ , \\
\Delta v_{\mathrm{s}\eta} &= \frac{-GM_*}{b_\mathrm{s} V_\infty}(\cos\vartheta_{\mathrm{s}1} - \cos\vartheta_{\mathrm{s}2})\ , \\
\Delta v_{\mathrm{c}\xi} &= \frac{-GM_*}{b_\mathrm{c} V_\infty}(\sin\vartheta_{\mathrm{c}2} - \sin\vartheta_{\mathrm{c}1})\ , \\
\Delta v_{\mathrm{c}\eta} &= \frac{-GM_*}{b_\mathrm{c} V_\infty}(\cos\vartheta_{\mathrm{c}1} - \cos\vartheta_{\mathrm{c}2})\ ,
\end{aligned} \tag{9.3}$$

where G is the gravitational constant and M_* is the stellar mass, $V_\infty = V^*$ is the stellar speed at infinity and ϑ is the true anomaly of the star with respect to the Sun or the comet, the indices '1' and '2' denoting the beginning and

---

[1] Dybczyński's method is more general, allowing any time interval to be considered, but this is our choice for comparing the results with the IEM.

end of the computation, respectively. All these quantities are easily computed, and thus the impulse vector is found from the above equations. A great simplification of (9.2) and (9.3) results from considering an infinite time interval like for the CIA, as explained in [6]. We have applied this procedure in some runs for comparison purposes, and we denote these runs by DIA*.

9.4.3 The Sequential Impulse Approximation

In this case, which we denote by SIA, the comet is allowed to move along its osculating orbit between the steps of a predefined sequence. At the beginning of the calculation, the star is placed at its proper position at distance d_{lim} from the Sun. For each step a preselected time interval is used to compute the corresponding change in the true anomaly ($\Delta\vartheta$) of the star's heliocentric or cometocentric orbit, depending on which object is closest to the star. Thus, during the whole calculation, a variable time step is used with the property that it always corresponds to $\Delta\vartheta$ for the orbit of the object that is closest to the star. As a result the time step varies roughly in proportion to the square of the minimum distance from the Sun or comet to the star.

We stress that – in principle – the SIA is capable of any level of precision, but both the precision and the CPU time are determined by the method and choice of parameters to choose the step length. As shown in Sect. 9.5, we have found the above procedure to be appropriate for practical needs.

In practice, the SIA is constructed as follows. After selecting an initial time step Δt_0, we first compute the initial star–comet distance d_{c0} and the true anomaly step size of the heliocentric orbit of the star:

$$\Delta\vartheta_{\mathrm{s}} = \frac{V^* b^*}{d_{\mathrm{lim}}^2} \Delta t_0 \ . \tag{9.4}$$

For each step, we start from the heliocentric position and velocity of the comet and the star in the above-described impact frame. The time is t. The following sequence is then stepped through:

- We compute the cometocentric orbital parameters of the star from the positions and velocities, and we find the values of the asterocentric true anomalies of the Sun (ϑ_{s1}) and the comet (ϑ_{c1}).
- We find which body, the Sun or the comet, is closer to the star. If it is the Sun, we compute the time step Δt from ϑ_{s1} and $\Delta\vartheta_{\mathrm{s}}$ given by (9.4). If it is the comet, we compute the cometary true anomaly step from

  $$\Delta\vartheta_{\mathrm{c}} = \frac{V^* b_{\mathrm{c}}}{d_{\mathrm{c0}}^2} \Delta t_0 \tag{9.5}$$

  and compute the time step Δt from ϑ_{c1} and $\Delta\vartheta_{\mathrm{c}}$ given by (9.5).
- In the former case, if the Sun is closer to the star, we compute the true anomalies at the end of the step from $\vartheta_{\mathrm{s2}} = \vartheta_{\mathrm{s1}} + \Delta\vartheta_{\mathrm{s}}$, and $\vartheta_{\mathrm{c2}} = \vartheta_{\mathrm{c}}(t+\Delta t)$. In the latter case, if the comet is closer to the star, these anomalies are found from $\vartheta_{\mathrm{s2}} = \vartheta_{\mathrm{s}}(t+\Delta t)$ and $\vartheta_{\mathrm{c2}} = \vartheta_{\mathrm{c1}} + \Delta\vartheta_{\mathrm{c}}$.

- We apply Dybczyński's formulae (9.2) and (9.3) to obtain the heliocentric impulse vector of the comet.
- We compute the heliocentric position and velocity vectors of the comet at the middle of the step and add the heliocentric impulse vector to the velocity.
- The heliocentric position and velocity vectors of the comet and the star are computed at the end of the step, thus preparing for the following step.

The calculation ends when the star reaches the heliocentric distance (d_{lim}) after closest approach.

Two important general remarks may be made on the above computation: (1) all the hyperbolic true anomalies are computed via the eccentric anomalies and (2) the inversions of the Kepler equations are made using (4) and (12) of [4] in the elliptic cases, and the hints given in [30] for the hyperbolic cases.

We have used several values for the initial time step Δt_0 in an attempt to compare them internally as well as with other methods and decide about the best choice.

9.5 Results

9.5.1 Computing Times

We consider the sample of 395,813 stellar encounters previously defined acting on 40 cometary orbits, having the same initial semi-major axis (a_0) and perihelion distance (q_0). Computations of the stellar perturbations have been performed using a particular method, for three different values of a_0 with always the same $q_0 = 100$ AU. Table 9.1 summarizes the total computing times spent on a 2.8 GHz XEON. The different SIA calculations are distinguished by the following initial time steps: 0.5×10^5 yr for SIA50, 2.5×10^5 yr for SIA250, 5×10^5 yr for SIA500 and 1×10^6 yr for SIA1000. Thus, the numbers used in the acronyms give the time step in thousands of years.

IEM calculations take more time for smaller values of the cometary semi-major axis, because this makes it more likely for the comet to be close to perihelion during the stellar passage. Since most stellar encounters are distant (see Fig. 9.1), it is in fact the cometary perihelion passages that dominate the use of CPU time. This effect is not seen for SIA, which works directly with the cometary orbital elements, and whose time step is independent of the Sun–comet distance—see (9.5) and (9.7).

Both CIA, DIA* and DIA are extremely quick estimators compared with IEM, and DIA* is just as fast as CIA. Both of these are $\sim$500 times faster than IEM, while DIA is only $\sim$200 times faster owing to the calculation of sines and cosines of true anomalies in (9.3). SIA is significantly slower, though this depends on the choice of the initial time step. SIA50 is practically useless, being only a little faster than IEM, but SIA500 and SIA1000 work at least 20–30 times faster than IEM for typical Oort cloud orbits. In fact, for a stellar encounter with a typical speed of 30 km/s, the time required to describe a rectilinear path of 2×10^6 AU is about 300,000 yr. This generally means only one step for SIA1000 and just a few for SIA500. Of course, the number of steps grows much larger for very slow and/or close stellar encounters.

9.5.2 Error Statistics of the Models

For each set of cometary elements a_0 and q_0, the set of $\sim 16 \times 10^6$ perturbations computed by IEM is divided into four quartiles (Q_1, Q_2, Q_3 and Q_4), each containing the same number of perturbations ($\sim 4 \times 10^6$) and such that the 25% smallest perturbations are in Q_1, etc. For each model under study and each perturbation in Q_i ($i = 1, 4$), an error EQ_i is computed as

$$\mathrm{EQ}_i = \frac{\Delta q_{\mathrm{IEM}} - \Delta q_{\mathrm{mod}}}{\langle |\Delta q_{\mathrm{IEM}}| \rangle_i} \tag{9.6}$$

for $i = 1, 2, 3$, and

$$\mathrm{EQ}_4 = \frac{\Delta q_{\mathrm{IEM}} - \Delta q_{\mathrm{mod}}}{\max(|\Delta q_{\mathrm{IEM}}|, \langle |\Delta q_{\mathrm{IEM}}| \rangle_i)} \ , \tag{9.7}$$

for $i = 4$. Here Δq_{IEM} and Δq_{mod} are the perturbations computed by IEM and the model under study, respectively, and $\langle |\Delta q_{\mathrm{IEM}}| \rangle_i$ is the arithmetic mean of the $|\Delta q_{\mathrm{IEM}}|$ included in Q_i.

In [29], it has been shown (see Table II of [29]) that the majority of the perturbations of Δq are very small, but the tail of the perturbation distribution extends to very large values. Moreover the models have also been compared against each other (see Table III of [29]). The main results are the following: (1) whatever the model, the average of EQ is always very small, which indicates that none of the models tend to introduce any systematic bias into Δq; (2) SIA1000 is not much better than DIA except for $a_0 = 10^5$ AU; (3) while the results obtained with DIA* are practically the same as the CIA results, the model DIA is distinctly better than CIA, implying that a large part of the CIA errors arise from the consideration of an infinite time interval.

9.5.3 Dependence of the Errors on the Encounter Parameters

To analyse how errors are distributed over the encounter parametric plane, we have divided this plane into cells and studied the error statistics in the cells individually. In Fig. 9.3 we present the results for the case of $a_0 = 3 \times 10^4$ AU with the CIA, DIA and SIA500 models. We divided the encounter sample into four equal parts corresponding to the quartiles of the $|\Delta q|$ distribution as computed by IEM. The left and right panels show the Q_1 and Q_4 quartiles, respectively, and from the population density level curves we see how the Q_4 sample preferentially populates the cells with smaller impact parameters and smaller approach velocities—as expected from (9.1).

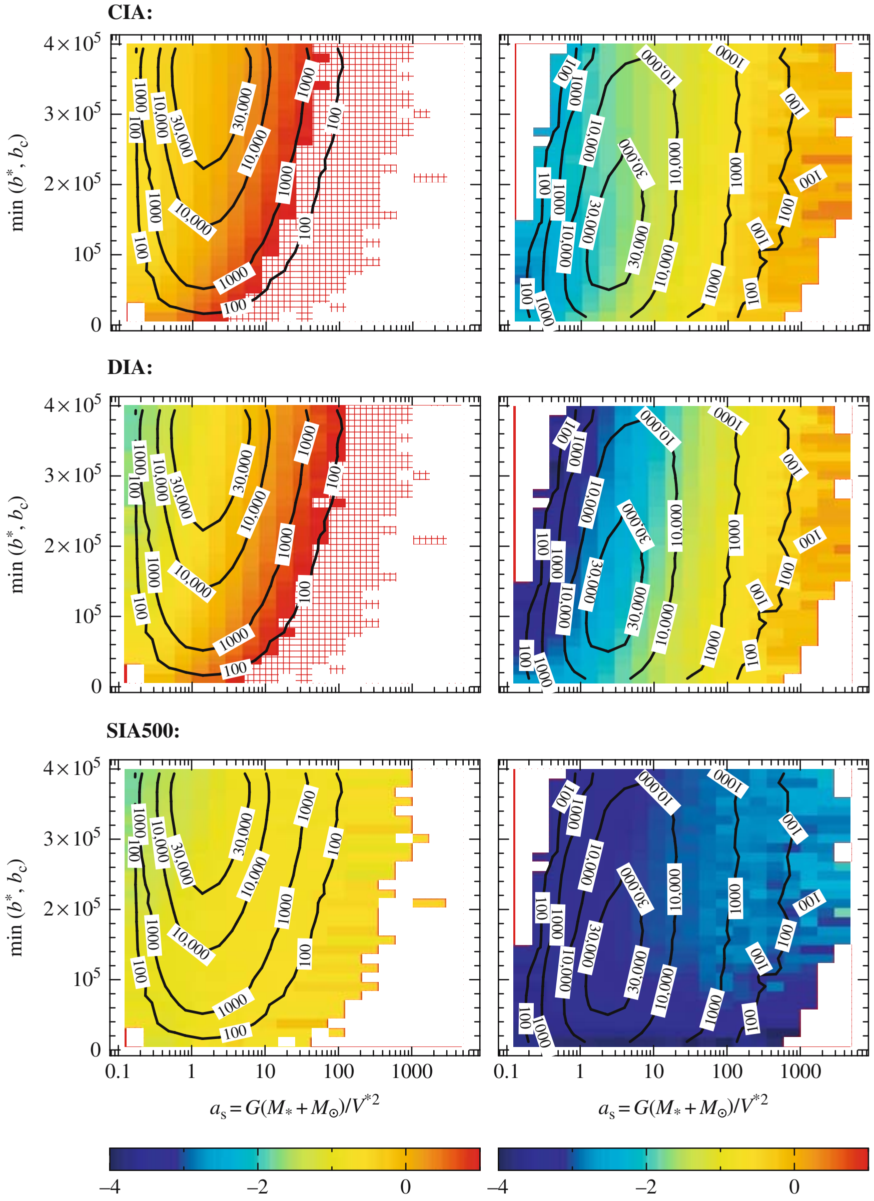

Fig. 9.3. Colour diagram of the model errors in the $a_\mathrm{s}, \min(b^*, b_\mathrm{c})$ plane. The plane is divided into 20×30 cells. Cells on the same line are gathered until a population of at least 20 stellar passages is reached. The *colour* indicates the value of $^{10}\log|\mathrm{EQ}_i|$ that is surpassed by 10% of all the errors $|\mathrm{EQ}_i|$ computed in each cell. For the *cross-hatched cells* this value is larger than 1. **Diagrams to the left** correspond to Q_1 and **diagrams to the right** correspond to Q_4. For each quartile, the isopopulation curves of the corresponding stellar encounters are also shown, indicating the numbers falling in each individual cell. The unit for both axes is AU

The colour coding is chosen to represent the 90th percentile, i.e. the value of |EQ| that is surpassed by 10% of the population in the cell. The orange–red colour range indicates errors larger than 100%.

Our first observation is that such conditions are commonplace for CIA and DIA in the first quartile, whenever the stellar approach velocity is relatively small, while they do not occur at all for the SIA500 model. Next we note that these very large relative errors are confined to Q_1 rather than Q_4, so that the actual errors in absolute terms are quite small. This is indicative of a component of the errors that is not proportional to the size of the perturbation, and thus becomes relatively important as the perturbations approach zero. Since mainly CIA and DIA are affected, we conclude that neglecting the cometary motion must be an important part of the problem.

For practical purposes it may be more interesting to study the errors of the largest perturbations as shown in the right-hand panels of Fig. 9.3. In this case the CIA and DIA errors occasionally reach the 100% level for the slowest encounters. By contrast, the SIA500 errors are always vanishingly small. It is noteworthy that the largest CIA and DIA errors in Q_4 do not occur for the closest encounters but for relatively distant ones with very low velocities—a detailed example will be discussed in Sect. 9.5.4.

A detailed study of the smallest impact parameters of our sample (see Fig. 9.4) shows that DIA yields much better results than CIA—especially for impact parameters less than a few thousand AU.

Neither CIA nor DIA competes in accuracy with SIA500 for these close encounters. However, for impact parameters <1000 AU the computing time is larger with SIA500 than using IEM. Hence, if a high accuracy of the stellar perturbations is desired, one should use IEM for such very rare and close encounters, while a lot of computing time may be saved by using SIA500 or SIA1000 in the rest of the encounter parameter plane.

Changing the value of a_0 to either 1×10^4 or 1×10^5 AU does not affect the above results very much. The use of CIA or DIA for the inner core of the Oort cloud, where $a_0 < 1 \times 10^4$ AU, especially for stars passing at low velocities, does not appear advisable.

9.5.4 Example of a Stellar Passage

In order to illustrate the differences between the models, one stellar passage will now be considered in detail. This example was chosen among those passages that CIA and DIA failed to reproduce. Figure 9.5a shows the geometry of the encounter in the plane of the stellar trajectory. The upper part of the figure lists the ecliptic elements of the stellar and cometary orbits. M_0 is the mean anomaly of the comet when the star is at its perihelion; b_c is the value of the cometary impact parameter at the time when the star passes perihelion and taking the heliocentric velocity of the comet into account, as computed for the DIA model; and $\min_{M_0}(b_\mathrm{c})$ is the minimum value of b_c on a sequence of encounters where M_0 varies between 0° and 360° (see below).

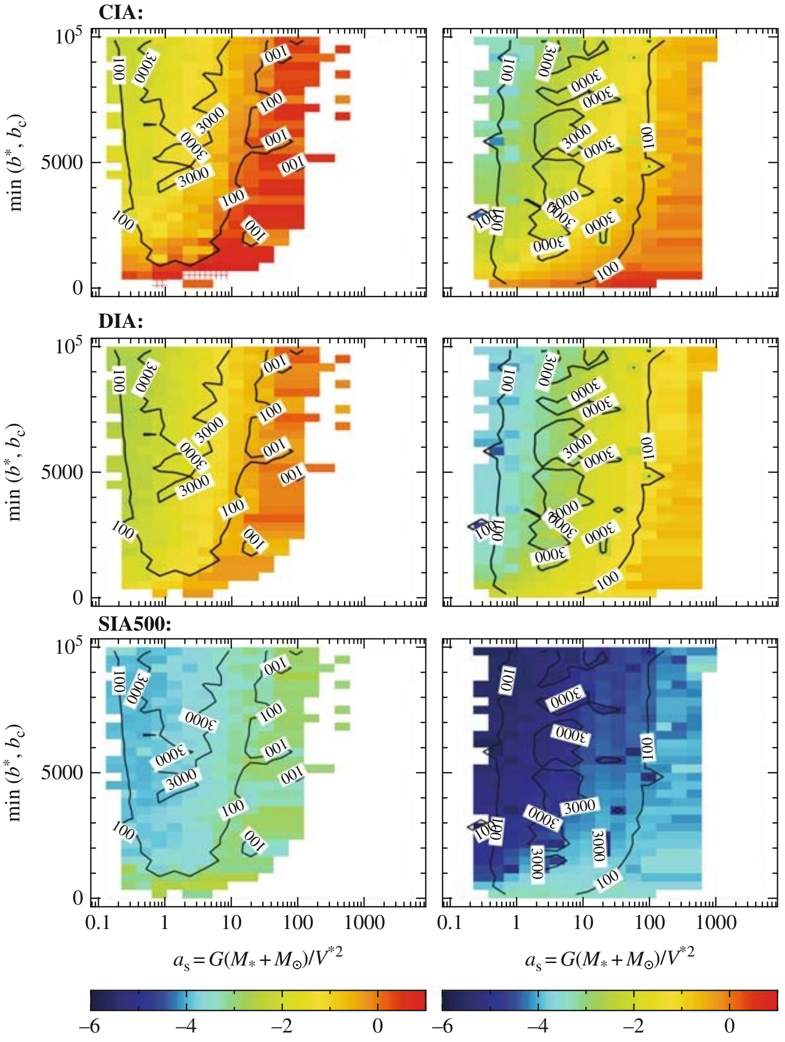
CIA:

DIA:

SIA500:

Fig. 9.4. Same as Fig. 9.3, but limited to minimum impact parameters less than 10^4 AU. All these data are contained within the lowest cells of Fig. 9.5

Also shown are the perihelion distance perturbations using the different models. Clearly, SIA500 and IEM are almost equivalent. In order to check if the discrepancy between DIA or CIA and IEM is due to the place where the comet is fixed during the stellar passage (which may yield a large difference when strong perturbations are involved), Fig. 9.5b gives the final perihelion distance of the comet, as M_0 varies between 0° and 360°.

Clearly, this encounter cannot be well reproduced by DIA or CIA. This is not due to a close encounter, since both b^* and b_c are always larger than

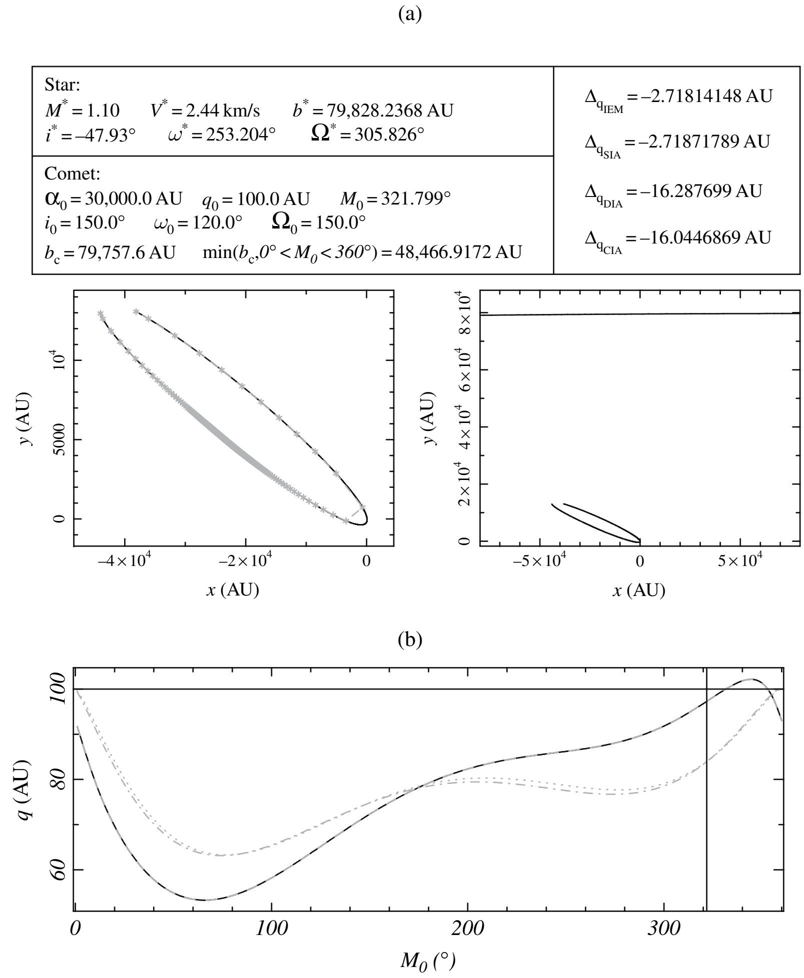

Fig. 9.5. (**a**) **Above**: Ecliptic orbital elements of the star and the comet; b_c is the comet–star impact parameter of the encounter shown, and $\min_{M_0}(b_c)$ is the minimum cometary impact parameter for the stellar passages used to plot part (**b**). To *the right*, perturbations of the perihelion distance computed with different models. ***Below***, **left panel**: Cometary orbit during the stellar passage using IEM (*full black line*), and cometary positions computed by SIA500 (*grey asterisks*) joined by a *grey dashed line*, in the plane of the stellar trajectory. **Right panel**: Stellar trajectory and cometary orbit computed by IEM in the same plane. (**b**) Final perihelion distance versus cometary mean anomaly M_0 at the time of the perihelion passage of the star using IEM (*full grey curve*), SIA500 (*dashed black curve*), DIA (*dot-dashed grey curve*) and CIA (*dotted grey curve*). *Horizontal line*: initial value of the cometary perihelion distance; *vertical line*: value of M_0 used in part (**a**)

48,000 AU, but rather to the small stellar velocity (2.44 km/s). Note from Fig. 9.5a that this causes the comet to perform almost a whole revolution around the Sun during the encounter. It is obvious that keeping the comet fixed at any point in its orbit cannot yield a good approximation to the integrated perturbation. Moreover, due to the large encounter distance, the hyperbolic deflection of the stellar trajectory is negligible, as is the variation of the stellar velocity—hence the CIA and DIA yield practically the same results.

There is an interesting difference between close and distant encounters in the time interval during which the main part of the perturbation builds up. For a close encounter, this is very short, and the motion of the comet is not of prime importance. But for a distant one, if it is very slow like in Fig. 9.5, the motion of the comet is indeed important and may destroy the accuracy of a one-step method. Thus we may explain why the CIA and especially DIA errors are the largest for slow, distant encounters, while for the close encounters in Fig. 9.4 they are not extremely large. Even if the point where one assumes the comet to reside in such a case may not be the best one, keeping the comet fixed is not a bad assumption.

9.6 Conclusions

In terms of computer time the CIA and the DIA are extremely quick estimators, since they are respectively $\simeq$500 and $\simeq$200 faster than IEM. The computing time of SIA depends on the initial time step as well as the accuracy. For a step choice of 5×10^5 or 1×10^6 yr the computations are 20–30 times faster than IEM at the expense of some little loss in accuracy, but the accuracy is significantly better than CIA and DIA. However, for small impact parameters (see Fig. 9.4) the CIA and DIA are not good estimators.

Moreover, for even a distant encounter, when the star velocity is very low the CIA and DIA give wrong results, since the comet is assumed to be fixed during the encounter. CIA (as found previously by Eggers and Woolfson) and DIA are not suitable for the inner core of the Oort cloud.

For simulations of the Oort cloud, CIA gives a reasonably good approximation for a very small computation time, but DIA works significantly better at almost the same amount of time.

The SIA should be used when modelling the inner core of the Oort cloud and the scattered disk. Our choice, according to the best compromise between accuracy and speed is the SIA500, taking into account that when the impact parameter of the star with the Sun or the comet is smaller than 1000 or 2000 AU the IEM is faster than the SIA500.

References

1. Bailey, M. E., 1983. *MNRAS* **204**, 603. 258
2. Bailey, M. E., 1986. *MNRAS* **218**, 1. 259

3. Breiter, S., Dybczyński, P. A., and Elipe, A., 1996. *A&A* **315**, 618. 258
4. Danby, J. M. A., 1987. *Celest. Mech.* **40**, 303. 265
5. Duncan, M., Quinn, T., and Tremaine, S., 1987. *AJ* **94**, 1330. 259
6. Dybczyński, P. A., 1994. *CeMDA* **58**, 139. 259, 262, 263, 264
7. Dybczyński, P. A., 2002. *A&A* **383**, 1049. 258, 261
8. Dybczyński, P. A., 2002. *A&A* **396**, 283. 258
9. Dybczyński, P. A. and Pretka, H., 1996. *EMP* **72**, 13. 258
10. Eggers, S. and Woolfson, M. M., 1996. *MNRAS* **282**, 13. 259
11. Everhart, E., 1985. In Carusi, A. and Valsecchi, G. B. (eds), *Dynamics of Comets: Their Origin and Evolution*, Reidel, Dordrecht, p. 185.
12. Fernández, J. A., 1980. *Icarus* **42**, 406. 259
13. Fernández, J. A., 1982. *AJ* **87**, 1318. 259
14. García-Sánchez, J., Weissman, P. R., Preston, R. A. et al., 2001. *AJ* **379**, 634. 260
15. Hills, J. G., 1981. *AJ* **86**, 1730. 258, 259
16. Heisler, J., 1990. *Icarus* **75**, 104. 258, 259
17. Heisler, J., Tremaine, S., and Alcock, C., 1986. *Icarus* **70**, 269. 259
18. Hut, P. and Tremaine, S., 1985. *AJ* **90**, 1548. 258
19. Levison, H., Dones, L., and Duncan, M. J., 2001. *AJ* **121**, 2253.
20. Maciejewski, A. J. and Pretka, H., 1998. *A&A* **336**, 1065. 258
21. Matese, J. J. and Lissauer, J. J., 2002. *Icarus* **157**, 228. 258, 259
22. Mazeeva, O. A., and Emel'yanenko, V. V., 2002. In *Asteroids, Comets, and Meteors*, ACM , pp. 445–448. 259
23. Morris, D. E. and O'Neill, T. E., 1988. *AJ* **96**, 1127. 259
24. Oort, J. H., 1950. *Bull. Astron. Inst. Neth.* **11**, 91. 258, 259
25. Öpik, E. J., 1932. *Proc. Am. Acad. Arts Sci.* **67**, 169. 259
26. Rémy, F. and Mignard, F., 1985. *Icarus* **63**, 1. 259
27. Rickman, H., 1976. *BAICz* **27**, 92. 259, 262
28. Rickman, H., Froeschlé, Cl., Froeschlé, Ch., and Valsecchi, G. B., 2004. *A&A* **428**, 673. 259, 260
29. Rickman, H., Fouchard, M., Valsecchi, G. B., and Froeschlé, Ch., 2005. *EMP* **97**, 411. 259, 261, 266
30. Serafin, R. A., 2002. *CeMDA* **82**, 363. 265
31. Weissman, P. R., 1979. In Duncombe, R. L. (ed.), *Dynamics of the Solar System*, IAU Symp. 81, Reidel, Dordrecht, p. 277. 259
32. Weissman, P. R., 1980. *Nature* **288**, 242. 259

2.3 Construction du modèle de perturbations planétaires

Lorsqu'on s'intéresse au flux de comètes nouvelles, c'est-à-dire les comètes qui arrivent pour la première fois dans la région planétaire du système solaire, il est fréquent de modéliser les perturbations planétaires par le concept de loss cone. Ce concept, déjà introduit par Oort (1950) stipule que l'effet des perturbations planétaires est tel qu'il existe une région définie par le moment angulaire des comètes, dans laquelle les comètes sont éjectées dès leur premier passage au périhélie, alors qu'en dehors de cette région les planètes n'ont pas d'effet.

Pour des comètes se trouvant sur des trajectoires presque paraboliques comme celles venant du nuage de Oort, ceci revient à définir un seuil q_c de la distance périhélique tel que si la distance périhélique d'une comète est telle que $q < q_c$ alors la comète est éjectée lors de son passage au périhélie, sinon sa trajectoire n'est pas affectée par les planètes.

Ceci est évidemment une simplification assez grossière. Afin de mieux tenir compte de l'effet des planètes tout en minimisant le temps de calcul pour déterminer ces perturbations planétaires, on a considéré les 4 planètes géantes sur des orbites circulaires (et donc les planètes ne se perturbent pas entres elles). Dès qu'une comète passe à une distance héliocentrique inférieure à r_C alors on considère qu'elle est affectée par les planètes. Comme pour les étoiles, cet effet est calculé sous la forme d'une impulsion appliquée à la trajectoire de la comète lorsqu'elle se trouve à son périhélie[1]. Le calcul de l'impulsion se fait alors sur la portion de trajectoire de la comète se trouvant à une distance héliocentrique inférieure à r_L.

Les tests effectués pour la mise en place de notre modèle nous ont conduit à choisir $r_C = 50$ AU et $r_L = 100$ AU. La mise en place de la méthode, ainsi qu'une preuve numérique de l'inexactitude du concept de loss cone sont présentés dans l'article Fouchard et al. (2013).

---

[1] En fait, tous les calculs se font dans un repère barycentrique mais pour faciliter la compréhension, on continue d'utiliser un vocabulaire se référant à un repère héliocentrique.

Icarus 222 (2013) 20–31

Contents lists available at SciVerse ScienceDirect

Icarus

journal homepage: www.elsevier.com/locate/icarus

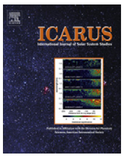

Planetary perturbations for Oort Cloud comets. I. Distributions and dynamics

M. Fouchard [a,*], H. Rickman [b,c], Ch. Froeschlé [d], G.B. Valsecchi [e]

[a] LAL-IMCCE, Université de Lille 1, 1 Impasse de l'Observatoire, F-59000 Lille, France
[b] PAS Space Research Center, Bartycka 18A, PL-00-716 Warszawa, Poland
[c] Dept. of Physics & Astronomy, Uppsala Univ., Box 516, SE-75120 Uppsala, Sweden
[d] Observatoire de la Côte d'Azur, UMR 6202, Bv. de l'Observatoire, B.P. 4229, F-06304 Nice cedex 4, France
[e] IAPS, INAF, via Fosso del Cavaliere 100, I-00133 Roma, Italy

ARTICLE INFO

Article history:
Received 5 July 2012
Revised 23 October 2012
Accepted 23 October 2012
Available online 1 November 2012

Keywords:
Comets, Dynamics
Comets, Origin
Celestial mechanics

ABSTRACT

This paper is the first in a series, where we aim to model the injection of comets from the Oort Cloud so well that the shape of the energy distribution of long-period comets (i.e., the distribution of reciprocal semi-major axis) together with the observed rate of perihelion passages can be used to make serious inferences about the population size and energy distribution of the cloud. Here we explore the energy perturbations caused by the giant planets on long-period comets with perihelia inside or near the planetary system. We use a simplified dynamical model to integrate such perturbations for large samples of fictitious comets and analyse the statistics of the outcomes. After demonstrating the sensitivity of derived parameters to the sample size, when close encounters are involved, we derive a map of the RMS energy perturbation as a function of perihelion distance (q) and the cosine of the inclination (i), which compares well with the results of previous papers. We perform a critical analysis of the *loss cone* concept by deriving the "opacity" (chance of leaving the Oort spike by planetary perturbations per perihelion passage) as a function of q and $\cos i$, concluding that the often made assumption of full opacity for $q < 15$ AU is seriously in error. While such a conclusion may also have been drawn from earlier studies, we provide the first full, quantitative picture. Moreover, we make a preliminary investigation of the long-term evolution of long-period comet orbits under the influence of planetary perturbations, neglecting the external effects of Galactic tides and stellar encounters. This allows us to make predictions about the production of decoupled objects like Halley-type comets and Centaurs from the injection of Oort Cloud comets, as well as of a related population of transneptunians deriving from the Oort Cloud with perihelia well detached from the planets.

1. Introduction

When plotting a histogram of original reciprocal semi-major axes $1/a_o$ of long-period comets (i.e., as found by integrating the near-perihelion osculating orbit backward until a time before the comet entered the planetary system), one finds a strikingly narrow peak near the parabolic limit (Oort, 1950). This so-called *Oort spike* is a signature of the distant comet reservoir known as the Oort Cloud and the dynamical processes which inject comets from this reservoir into observable orbits. For many years, the uncertainties of the calculated $1/a_o$ values along with the insufficient statistical sample have made it very difficult to draw detailed conclusions about this dynamics or the energy distribution of Oort Cloud comets from the shape of the Oort spike. One particular problem has been that comet orbit solutions have been known to be affected, in general, by non-gravitational effects. Those effects are much easier to recognise for short-period comets by linking several observed apparitions than for single-apparition, long-period comets. Purely gravitational solutions have been the rule, but there has been no proof of the absence of non-gravitational effects in the general case of real comet motions.

Among early work we note the one of Marsden and Sekanina (1973), who discovered that the distribution of $1/a_o$ gets more dominated by the Oort spike, the larger the perihelion distances one considers. This effect was also found by Marsden et al. (1978) for a total sample of 200 original orbits, which the authors divided into quality classes according to the mean error of the osculating $1/a$, the length of the observed arc, and the number of perturbing planets in the solution. These quality classes are still used, and their utility was proven by the fact that the Oort spike stands out for quality class I (the best) but not for class II (Marsden et al., 1978). It was also found that the mean $1/a_o$ varies linearly with the reciprocal perihelion distance $1/q$ and becomes negative

---

[*] Corresponding author.
E-mail addresses: fouchard@imcce.fr (M. Fouchard), Hans.Rickman@physics.uu.se (H. Rickman), froesch@obs-nice.fr (Ch. Froeschlé), giovanni@iaps.inaf.it (G.B. Valsecchi).

0019-1035/$ - see front matter © 2012 Elsevier Inc. All rights reserved.
http://dx.doi.org/10.1016/j.icarus.2012.10.027

for the largest values – something that the authors ascribed to the likely effect of unmodelled non-gravitational effects for comets with small perihelion distances. The smallest $1/q$ groups led to an average original semi-major axis of $a_o \simeq 25{,}000$ AU.

Following the discovery of the importance of Galactic tides for comet injection in the 1980s, it was established that the efficiency of this mechanism for reducing perihelion distances grows rapidly with semi-major axis (e.g., Heisler and Tremaine, 1985). Also, the concept of the loss cone or "loss cylinder" (Oort, 1950), corresponding to orbits within the Oort spike with perihelion distances small enough to be emptied by planetary perturbations during one perihelion passage, received new attention (Hills, 1981). On the basis of orbit integrations by Fernández (1981) (see also Duncan et al., 1987), the border of the loss cone has been taken as $q_{\max} = 10$–15 AU.

The very efficient removal of new comets from orbits crossing or approaching those of Jupiter or Saturn is known as the *Jupiter–Saturn barrier*. Within this picture, the injection of new comets by the Galactic tides requires semi-major axes larger than approximately 30,000 AU (Fernández, 2005). But, likely due to the realisation that comet injection also involves the effect of passing stars, the fact that this may be larger than the mean semi-major axis of new comets has not been generally considered a major problem.

Recent years have seen some important progress, however. While it was earlier found that non-gravitational orbit solutions very often led to indeterminate results or no improvement of the residuals, new methods and better data have led during the last decade to a new situation. Królikowska (2006) found that allowance for non-gravitational perturbations leads to improved fits in many cases, and that the resulting $1/a_o$ values are systematically shifted in the positive direction – thus leading to smaller semi-major axes. This conclusion was first drawn for comets with relatively small perihelion distances (Królikowska and Dybczyński, 2010), but Dybczyński and Królikowska (2011) showed that as many as one quarter of the comets with $q > 3$ AU also suffer significant non-gravitational effects. They also found by backward integrations that many comets have reached their current perihelia, not by injections across the Jupiter–Saturn barrier but by having left their preceding perihelia in the depth of the loss cone on orbits within the energy range of new comets, thus contributing to the Oort spike. This appears to indicate the need for a re-evaluation of the concept of new comets and the interpretation of the Oort spike.

There has been progress in dynamical simulations too. Kaib and Quinn (2009) discovered a previously unnoticed route from the inner core of the Oort Cloud into observable orbits in the Oort spike by a gradual, slow decrease of perihelion distance due to the Galactic tides until perturbations by Saturn or Jupiter kick the comet out into the energy range of new comets – a mechanism that Dybczyński and Królikowska found adequate to explain some of their results.

Finally, in our own work, we have drawn attention to the synergies that exist between Galactic tides and passing stars, when it comes to comet injection across the Jupiter–Saturn barrier. Much of this concerns the long term evolution of the cloud, but in (Rickman et al., 2008) we showed that the modelled Oort spike, resulting from a combination of tides and stars, extends to significantly larger $1/a_o$ than the one using tides only. There is also a difference in the modelled injection flux, which could affect the derivation of the number of comets in the Oort Cloud from the observed new comet flux. But it is clear from the above discussion that a realistic modelling of the Oort spike has to take the planetary perturbations into account rather than using the crude loss cone concept as in our previous work. At the same time, we see a real possibility to compare – for the first time in some detail – the predictions of simulations with the observed orbit distribution. This is the aim of the work to be presented in this paper and forthcoming ones.

This paper is devoted to an exploration of the planetary perturbations of $1/a$ experienced by long-period comets with perihelia inside or near the planetary system. In Section 2 we will describe our model and define its parameters. In Section 3, we will characterise and discuss the distributions of energy perturbations. In Section 4 we will present our results concerning the definition of the loss cone. In Section 5 we investigate the long term dynamical evolutions caused by planetary perturbations. Finally, Section 6 is devoted to a discussion of our results, and a summary of our conclusions.

2. Planetary perturbation model

As indicated above, our scope is to implement the present planetary perturbation model into a global model of Oort Cloud comet dynamics, where both the galactic tides and stellar effects are also represented. This model rests on the assumption that the effects of the planets, the tides and the stars are decorrelated, at least statistically. Consequently, we are allowed to apply the planetary perturbations as an impulse, i.e., only the orbital parameters of the comets are changed whereas the time is fixed. This impulse should naturally be applied when the comet is at its perihelion. Nevertheless, the computation of the impulse requires some numerical integration. This integration is performed as follows.

A restricted problem of six bodies is considered: the Sun, Jupiter, Saturn, Uranus, Neptune and the comet. The planets move on circular and coplanar heliocentric orbits with radii equal to the present semi-major axes and longitudes at $t = 0$ taken from a current epoch. It involves two technical parameters: r_C is the critical value of the barycentric distance that a comet has to pass in order for any planetary perturbation to be computed, and r_L is the limiting barycentric distance defining the orbital arc around perihelion that we use for integration of the planetary perturbations. Since $r_C < r_L$, the practical implementation into our Monte Carlo simulations is as follows. Each time a comet arrives at peribaryon at a barycentric distance less than r_C, it is shifted backward on its Keplerian barycentric orbit to a barycentric distance equal to r_L. The restricted 6-body problem is then integrated in the barycentric frame using RA15 (Everhart, 1985), until the comet reaches a barycentric distance equal to r_L in its outbound motion, reaches an apobaryon, or suffers an impact. Finally, in the first case, the comet is shifted backward on its new, Keplerian barycentric orbit to a point (normally, peribaryon), from where the further motion may be followed using external perturbers. From now on, in this paper, all orbital elements referred to are barycentric. But we will use the more intuitive terms aphelion and perihelion instead of apobaryon and peribaryon.

This model has the advantage of being very simple and fast, since during the integration only the comet will affect the step size of the integrator. It requires, however, two parameters (r_C and r_L), which should be chosen properly. To this purpose, we have built a synthetic sample of planetary perturbations, integrating comets on initial, parabolic orbits using the restricted 6-body problem. The initial inclination and argument of perihelion are taken equal to 0°, 45°, 90°, 135° or 180°. For each set of values, one experiment is made. The longitude of the ascending node is initially equal to zero, and the perihelion distance is distributed over a regular grid with 800 values between 0 and 80 AU. For each value of the perihelion distance, 10^4 different times of perihelion passage are randomly chosen between 0 and 10^4 years. The time of perihelion passage will thus essentially randomise the phases of the planets. Each comet is initially placed at a barycentric distance equal to 10^3 AU.

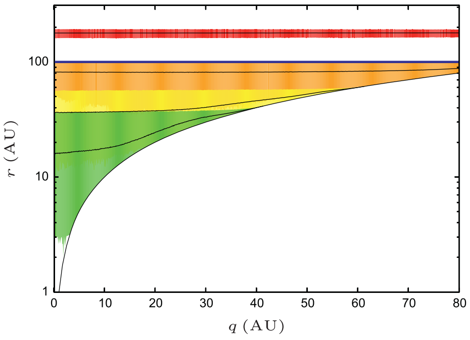

Fig. 1. Mean (black lines), minimum (lower bound of coloured areas) and maximum (upper bound of coloured areas) values of r_k ($k = 5$–8, see text for detail) versus initial perihelion distance for initial inclination equal to zero. The red, orange, yellow and green fields correspond to $k = 8, 7, 6, 5$, respectively. When fields of different colours overlap, we display the colour of the lower field, so that the upper bounds are always visible. The blue line corresponds to a barycentric distance of 100 AU.

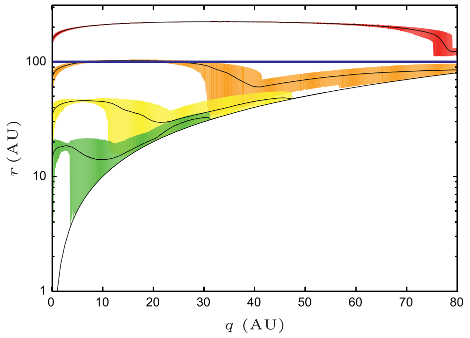

Fig. 2. Same as Fig. 1 for initial inclination $i = 90°$ and initial argument of perihelion $\omega = 45°$.

Keeping in mind that the initial orbital energy $z = -1/a$ (of the barycentric orbit) is zero for all the comets, while the integration is performed, the barycentric distances r_k at which the absolute value of the orbital energy becomes greater than 10^{-k} AU^{-1} are recorded individually, for $k = 5, \ldots, 8$. For each initial perihelion distance, we may compute the mean, minimum and maximum of the r_k values obtained from the 10^4 initial orbits with different times of perihelion passage.

In Fig. 1, those values of r_k are plotted versus the initial perihelion distance for initial inclination equal to zero. It can be seen that the cumulative variations of barycentric orbital energy suffered beyond $r = 100$ AU do not exceed 10^{-7} AU^{-1}. We have checked that this threshold is well obeyed for all the initial inclinations and arguments of perihelia under study (an example for initial inclination $i = 90°$ and initial argument of perihelion $\omega = 45°$ is given in Fig. 2). Consequently, we choose $r_L = 100$ AU as the limiting distance from which our restricted 6-body problem will be integrated.

In order to choose r_C, for each initial perihelion distance, inclination and argument of perihelion we consider the root mean square $\sigma(\Delta z)$, the maximum ($\max|\Delta z|$) and the 99th percentile ($|\Delta z|_{99}$) of the 10^4 perturbations of orbital energy computed for the respective values. Fig. 3 shows, for each initial inclination and for an initial argument of perihelion equal to zero, the variations of $\sigma(\Delta z)$ (black lines), $\max|\Delta z|$ (red[1] lines), and $|\Delta z|_{99}$ (orange lines) with the initial perihelion distance. In Fig. 4 we present the corresponding results for $\omega = 45°$.

Even though comets with $q > r_C$ also suffer planetary perturbations Δz, we aim to keep these below some practical minimum. To this end we prescribe that, for $q > r_C$, comets must be unlikely to be ejected by planetary perturbations from the Oort Cloud in a 5 Gyr time span, i.e., that the random walk in orbital energy stays within $|z|$ on the average. Comets with orbital energy z will suffer at most $N = 5 \times 10^9 \cdot |z|^{3/2}$ planetary kicks in the approximation of constant energy. Considering their perihelion distance to be fixed during this time span, at each perihelion passage the typical size of an energy change is equal to the value of $\sigma(\Delta z)$ relevant to the perihelion distance, and for N perihelion passages, we expect the total energy change to have a typical size of $\sqrt{N}\sigma(\Delta z)$. Consequently, our aim is to have $\sigma(\Delta z) < |z|/\sqrt{N}$. For $z = -10^{-3}$ AU^{-1} we get $|z|/\sqrt{N} \approx 2.5 \times 10^{-6}$ AU^{-1}, and for $z = -10^{-4}$ AU^{-1} we get $|z|/\sqrt{N} \approx 1.4 \times 10^{-6}$ AU^{-1}.

Alternatively, we may look at comets with semi-major axes in the Oort spike, i.e., within $a \sim 30{,}000$–$40{,}000$ AU. These comets have $|z| \sim 25$–30×10^{-6} AU^{-1}. But they will not stay with the same q for more than a few revolutions due to the effect of the tides and passing stars. Hence, our requirement for these comets is for the single-revolution sigma to be no larger than 10^{-6} AU^{-1}. This threshold is similar to the one found above for $z = -10^{-4}$ AU^{-1}, so we will use the latter to determine r_C.

The blue lines plotted in Figs. 3 and 4 correspond to this threshold value. The worst case is obviously the one for $i = 0°$, and we see that $\sigma(\Delta z) < 1.4 \times 10^{-6}$ AU^{-1} for $q > 50$ AU, approximately. Independent of the argument of perihelion, we verify that the same condition applies. Consequently, $r_C = 50$ AU is a threshold that fulfils our requirement. Hereafter, the values $r_L = 100$ AU and $r_C = 50$ AU will be used.

For comparison with previous work we note that Duncan et al. (1987) took $r_L = 150$ AU, and Kaib et al. (2011) used $r_L = 300$ AU as the map switching distance between RMVS (Levison and Duncan, 1994) and WH (Wisdom and Holman, 1991) in their new orbit integration package.

3. Perturbation distributions

Let us now discuss Figs. 3 and 4, which use the synthetic perturbation sample, in some more detail. For the smaller perihelion distances, where close encounters are possible, we see an interesting behaviour. For $q < 30$ AU, the maximum and root-mean square curves for coplanar orbits show an important amount of random noise, and the patterns of this noise are similar for both curves. Obviously, the root mean square value is dominated by the maximum perturbation in the corresponding interval. In fact, we see that the root mean square is generally close to the 99th percentile of the distribution for the sample size that we are using.

This behaviour reflects a situation, where nearly all the orbits receive tiny perturbations in the absence of very close encounters with the giant planets, while our samples tend to include one or few very close encounters as well. The latter dominate the root mean square by the sheer size of the perturbations, and since they are very few, we are under-sampling this dominant subset of the population.

A similar situation is seen in the non-coplanar cases, which exhibit high peaks at particular perihelion distances, where close encounters are possible. Also in these cases the height of the root

---

[1] For interpretation of colour in Figs. 1–8 and 10–13, the reader is referred to the web version of this article.

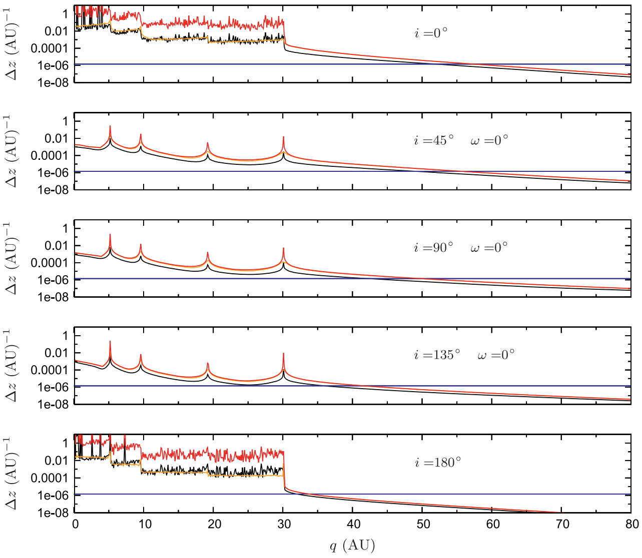

Fig. 3. For different initial inclinations and an argument of perihelion equal to zero, the variations of $\sigma(\Delta z)$ (black lines), $\max|\Delta z|$ (red lines) and $|\Delta z|_{99}$ (orange lines) with the initial perihelion distance are shown. The horizontal blue lines mark the value of 1.4×10^{-6} AU^{-1}.

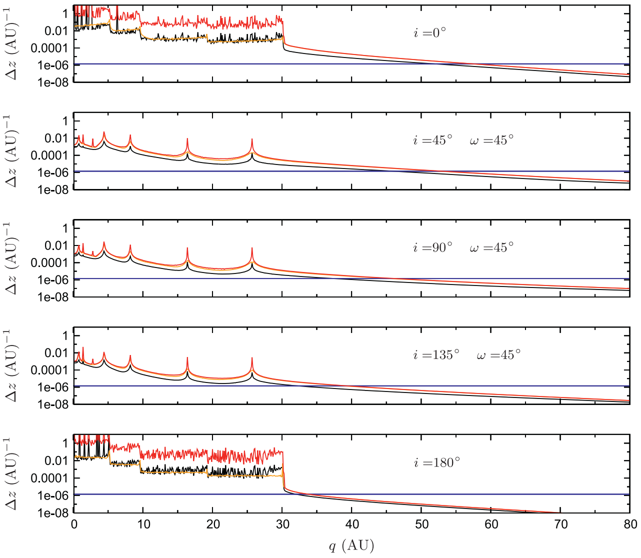

Fig. 4. Same as Fig. 3 for an argument of perihelion equal to 45°.

mean square peak follows that of the maximum peak and is close to the peak of the 99th percentile. We note in passing that, in Fig. 4, the high peaks are not located strictly along the planetary semi-major axes, but rather slightly below. This is because close encounters occur at the nodes of the cometary orbits. If $\omega \neq 0°$ or 180°, the perihelion is not located at a node, and consequently for such a comet, close encounters with a planet may occur if the perihelion is located somewhat inside the semi-major axis of the planet. This value of the perihelion distance is independent of the inclination, as can be seen on the figure. Moreover, a set of secondary peaks is seen inside Jupiter's orbit, and in these cases it is the distance of the outer node that coincides with a planetary semi-major axis.

The problem of accurately modelling perturbations when very close planetary encounters are possible is of course of crucial importance in the study of the dynamics of comets, and has been addressed in a number of papers. For example, in discussing the dynamics of Jupiter family comets, Fouchard et al. (2003) found that if the perturbation samples used to derive the statistical features of the perturbation distribution are not large enough, the results depend on the specific sample chosen – only beyond a certain sample size do the statistics become independent of the sample. This happens because, in the latter case, even the domain of initial conditions leading to extreme perturbations (which are the ones that determine the values of quantities like σ and the largest percentiles) is adequately represented in the sample.

Let us note here that the size of our synthetic sample, even though very large, is not enough to probe the extremely large perturbations properly for all the giant planets. Therefore, we caution the reader that the values of statistical parameters shown in the graphs are not the same as one would get with a quasi-infinite sample size. We will return to this point below, whenever a potential problem arises.

Some authors (e.g., Zhou et al., 2002) have suggested that the statistical evolution of the cometary energy follows a Lévy random walk; strictly speaking, this statement is not true, since it would imply that the maximum energy perturbation imparted by a planetary close encounter to a comet is unbounded, contrary to the findings of Everhart (1969) (see also Carusi et al., 1990; Valsecchi et al., 2000). As just said, it happens only for (practically) limited sample sizes that the distribution of energy perturbations behaves "as if" the process was a Lévy flight.

For coplanar orbits, prograde or retrograde, close encounters are possible at any perihelion distance smaller than the semi-major axis of the planet, and the statistics is dominated by these close encounters. On the other hand, for $q < 30$ AU, and non-coplanar orbits, close encounters with a giant planet are possible only for one perihelion distance determined by the argument of perihelion. This value is independent of the inclination, as shown by Figs. 3 and 4. Between the peaks seen in those close encounter regions, long range perturbations dominate the dynamics. We note that their effect decreases with perihelion distance and inclination. This is particularly evident for $q > 30$ AU, where no close encounters are possible at all.

In the rest of this paper we leave aside the synthetic sample discussed above. In particular, in Section 5 we will investigate, how planetary perturbations alone affect a population of Oort Cloud comets with perihelia inside the planetary region. For this purpose, an initial sample of 10^6 comets is integrated considering only planetary perturbations. The initial semi-major axis is 20,000 AU for all the comets, the perihelion distances are uniformly distributed on the interval [0, 50 AU], the cosines of the ecliptic inclination are uniformly distributed on $[-1, 1]$, and the other angles have a uniform distribution between 0° and 360°. The phases of the planets are obtained from those at the present epoch by shifting to each time of perihelion passage, when planetary perturbations should be applied.

All the comets suffer at least one energy kick, since their initial perihelion distances are smaller than r_C. Considering the first kick imparted to the comets, we thus have a sample of 10^6 planetary perturbations distributed uniformly in perihelion distance q and cosine of the inclination $\cos i$.

Let us first compare our set of perturbations with previous studies. Using a sub-sample of 135,000 perturbations and removing the case for which the comets enter the Hill sphere of any planet, we are able to compute the mean standard deviation $\sigma(\Delta z)$ of the orbital energy using the same perihelion distance and inclination boxes used by Fernández (1981). The results are shown in Fig. 5. The agreement with the historical Fig. 1 of Fernández (1981) and Fig. 1 of Duncan et al. (1987) is very satisfactory. One has to note that the selection made on the perturbations by removing the close encounters stabilises the behaviour of the standard deviation with respect to the sample of comets used. Indeed, with 135,000 perturbations, and even with 10^6 perturbations, the standard deviation would otherwise be driven by the rare but strongest perturbations coming from such encounters.

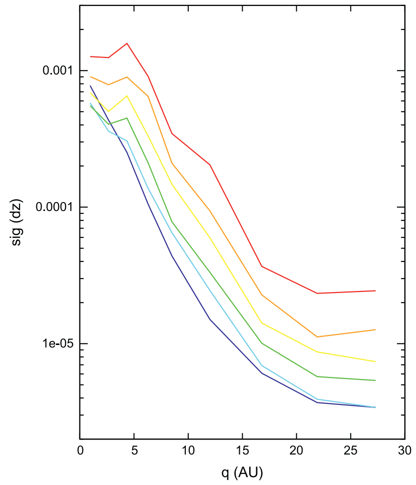

Fig. 5. Standard deviation of the perturbations of the orbital energy z, removing the comets that enter a planet's Hill sphere. Six different ranges of inclinations are used: [0°, 30°], ..., [150°, 180°] indicated by the colours red, orange, yellow, green, light blue and blue, respectively.

The second study one should compare with, is the distribution function fit given by Everhart (1968) (his Eq. (12)) for the orbital energy perturbations. In order to compare with this function, three sets of perturbations were selected, containing all the comets, i.e., whatever is the inclination, with original perihelion distance between 1.04 and 2.08 AU for the first set, between 2.08 and 3.12 AU for the second, and between 3.12 and 4.16 AU for the third set. The thresholds are used in order to use the parameters involved in the function fit listed by Everhart (1968). Each sample contains slightly more than 20,000 comets. Fig. 6 shows the distribution of the perturbation of the normalised orbital energy $Z = z \cdot a_J / M_J$, where a_J and M_J are the semi-major axis and the mass of Jupiter (in AU and solar masses) for the three sets and, for each set, the two distribution function fits obtained for the bounding values of the perihelion distance.

Our empirical distributions are well contained between the two fits computed with the parameters for the lower (red curves) and upper (blue curves) bounds for perturbations larger than 5×10^{-4} AU^{-1} in absolute value. For smaller perturbations, the agreement is not as good, since our distributions always peak around zero, whereas the function fits show a double-peaked feature symmetrical with respect to zero (except for perihelion distance $q = 1.04$ AU). The distributions obtained by Everhart (1968) also had such a feature. These dips at zero are likely an artifact of the procedure followed by Everhart, using in particular a shift from heliocentric to barycentric orbits, and vice versa, at only $r \simeq 20$–35 AU.

Let us now consider our entire set of 10^6 perturbations. We split the $(q, \cos i)$ plane into 50×20 cells of equal size. For each cell we compute the root mean square $\sigma(\Delta z)$ of the orbital energy perturbations, caused by the planets during the first perihelion passage of the comets. The results are shown in Fig. 7. We observe that, considering highly inclined orbits, there is an increase of the typical

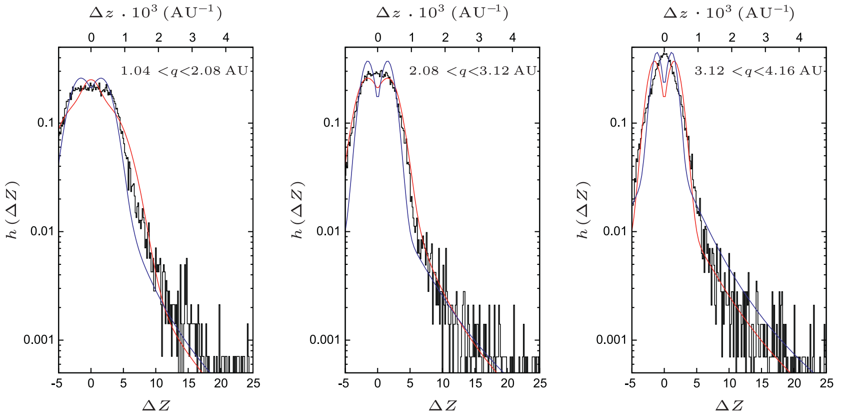

Fig. 6. Distributions of the perturbation of Z for three different sets of perturbations (see text for details). The red and blue curves correspond to the distribution functions given by Eq. (12) of Everhart (1968) using the lower (resp. higher) bound of the perihelion distance interval.

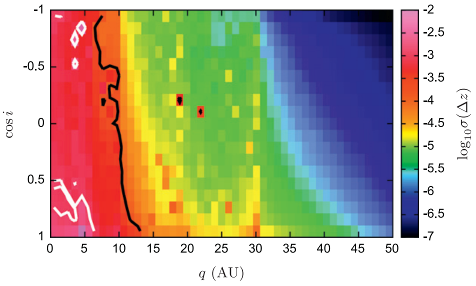

Fig. 7. RMS value of Δz, displayed by colour coding, versus the initial $(q, \cos i)$. The log-scale used for the colour coding is shown on the right. The level curves for $\sigma(\Delta z) = 10^{-4}$ and 10^{-3} AU^{-1} are also shown (black and white lines, respectively).

perturbation size for perihelion distances close to the semi-major axes of the giant planets. This appears to reflect the fact that, for such orbits, the range of the argument of perihelion that allows close encounters is broader than otherwise. Consequently, the figure appears to be more "noisy" around the semi-major axes of the planets, since $\sigma(\Delta z)$ is strongly affected by eventual close encounters with the planets. For perihelia outside Neptune's orbit, the perturbations range from 10^{-5} AU^{-1} to values smaller than 10^{-7} AU^{-1}, being stronger for smaller inclinations and perihelion distances.

The black level curve corresponding to 10^{-4} AU^{-1} (i.e., the width of the Oort spike) goes from $q \approx 13$ AU for $\cos i \approx 1$ to $q \approx 6$ AU for $\cos i \approx -1$. This is an indication that the inclination independent threshold of 15 AU, usually defining the border of the loss cone, may be overestimated. Finally, for perihelia inside and near Jupiter's orbit, we note that the planetary perturbations are able to inject a large fraction of the comets into orbits with semi-major axis smaller than 1000 AU (this corresponds to the region enclosed by the white 10^{-3} AU^{-1} level curve) in a single perihelion passage.

4. Opacity of the Solar System

Splitting the $(q, \cos i)$ domain into rectangular cells, we may compute the fraction of comets in each cell that is lost from the Oort Cloud after the first planetary kick. This leads to our definition of the opacity factor P (the same as was called 'transparency factor' by Dybczyński (2005)). A comet may be considered as lost from the Oort Cloud, if either its orbital energy becomes less than -10^{-4} AU^{-1} (an "inward" transfer, for which the probability is denoted $P_{\rm in}$), or if it grows larger than -10^{-6} AU^{-1} ("outward" transfer, which almost always means ejection from the Solar System, for which the probability is denoted $P_{\rm out}$). We thus have $P = P_{\rm in} + P_{\rm out}$. Note that the thresholds for the size of planetary perturbations contributing to $P_{\rm in}$ and $P_{\rm out}$ are both approximately equal to 5×10^{-5} AU^{-1}.

In Fig. 8, we show the dependence of P, $P_{\rm in}$ and $P_{\rm out}$ first on the perihelion distance, and then on the cosine of the inclination within different ranges of q. We first note the nearly equal contributions of $P_{\rm in}$ and $P_{\rm out}$ to P, which result from the fact that all our initial orbits are located in the middle of the Oort spike with $z = -5 \times 10^{-5}$ AU^{-1}. Concerning the variation with perihelion distance, P decreases smoothly from a maximum at about 95% near $q = 0$ toward zero near Uranus' orbit (there are two maxima at 1.5% and 1% – too slight to be seen in the figure – near the Uranus and Neptune semi-major axes, respectively).

P is smaller than 27% for perihelion distance greater than 10 AU. Recalling that the loss cone concept is applied using $P = 1$ (all the comets are removed from the Oort Cloud) for $q < 15$ AU (sometimes 10 AU is used instead) and $P = 0$ (no comets are removed) for $q > 15$ AU, the behaviour of P found here demonstrates how far this usage is from reality. As regards the dependence on the cosine of the inclination, clearly P is smaller for retrograde orbits than for prograde ones in any range of perihelion distance. For $q > 8$ AU, the asymmetry between prograde and retrograde orbits is very strong with P decreasing toward zero when $\cos i$ tends to -1.

A global picture of the behaviour of P in the $(q, \cos i)$ plane is shown in Fig. 9. Again, the smooth variation of P with respect to both q and i is evident.

Returning to the loss cone problem, this primarily arises from replacing a continuously decreasing function $P(q)$ by a step function. The assumption of $P = 0$ for $q > 15$ AU is well verified, but using $P = 1$ in the q interval from 10 to 15 AU is a poor approximation, since we find that it decreases from 27% to nearly zero, and moreover, it is strongly inclination dependent. Very large values of P are found only for $q < 5$ AU (commonly identified with observable comets).

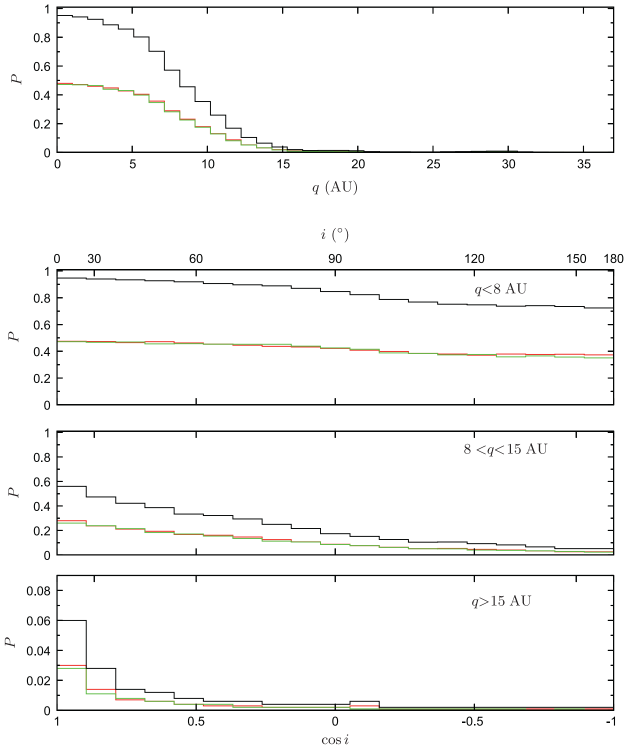

Fig. 8. Behaviour of P (black lines), P_{in} (green lines) and P_{out} (red lines) versus the initial perihelion distance (top), and below this, versus the cosine of the ecliptic inclination for three different ranges of perihelion distance: $q < 8$ AU, $8 < q < 15$ AU, and $q > 15$ AU (top to bottom). Note that the P scale of the lowest panel is different from the others.

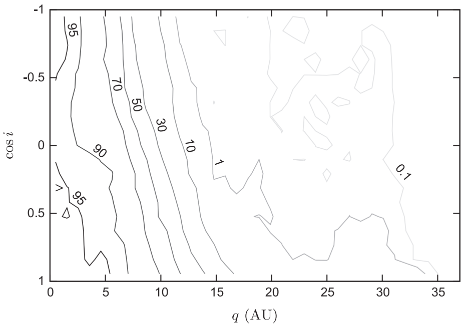

Fig. 9. The opacity factor P (in percent) versus the initial $(q, \cos i)$, displayed as a contour plot.

In Fig. 10 we show the distribution of original orbital energy for observed Oort spike comets according to the class 1 (A and B) comets listed by Marsden and Williams (2008), augmented by recent orbit determinations taken from IAU/MPC Minor Planet Electronic Circulars until 2011. All these orbits are determined without accounting for non-gravitational forces, and all perihelion distances are considered. The histogram is separated into three subgroups denoted by different colours: the comets perturbed into future orbits with positive energies (red area), those captured inside the spike (green area) and those remaining (white area). The latter represents about 11% of the total, thus corresponding to $\langle P \rangle = 0.89$ in good agreement with our above results.

Note that Dybczyński and Królikowska (2011) mentioned that their comet sample showed a remarkably small mean energy perturbation, but they argued that this could be due to a preference for large inclinations. In the case of (Królikowska and Dybczyński, 2010), 4–5 out of their 26 Oort spike comets were found to stay in the spike with their future orbits. While this would yield a smaller $\langle P \rangle$ than derived from Fig. 10, we caution that their numbers are small, and the inclinations might be non-randomly distributed.

5. Long term evolution

Let us now investigate how the sample of comets defined in Section 3 evolves dynamically under planetary perturbations only.[2] We use this sample for initial conditions, and we perform long-term integrations in a quasi-deterministic manner by computing each subsequent planetary perturbation using the time-dependent phasing of the planets, as mentioned in Section 3. For the display of results, we split the ranges of orbital energy, perihelion distance and cosine of inclination into equal intervals, thus creating, respectively, 40, 50 and 20 bins within the ranges $[-10^{-6}\ \mathrm{AU}^{-1}, -10^{-3}\ \mathrm{AU}^{-1}]$, $[0, 50\ \mathrm{AU}]$ and $[-1, 1]$. For each perihelion passage, we consider the comets according to the inbound

---

[2] In a previous paper (Rickman et al., 2001) we studied, using a somewhat different dynamical model, the first step of the inward evolution of Oort Cloud comets; both the purpose and the methods of that investigation are different from the present one.

values of their orbital parameters, i.e., analogous to the original orbital elements of observed long-period comets.

Let n_{pp} be the sequential number of a certain perihelion passage, regardless of which comet is considered. Our results will be displayed for nine different values of n_{pp}. First we will show the number of comets in each 2D cell, defined by the above-mentioned bins, by considering the bivariate distributions of $-1/a$ and $\cos i$ versus q. Since the individual comets of our integrations follow different random-walk patterns of orbital energy evolution, their orbital periods also evolve differently. Consequently, for different comets at the same n_{pp}, their elapsed times will differ. In order to keep track of this, we compute the average of the elapsed times $\langle t \rangle$ in each cell. In addition, for any given n_{pp}, we compute the critical semi-major axis $a_{\mathrm{lim}} = (5\ \mathrm{Gyr})/n_{\mathrm{pp}})^{2/3}$, for which $\langle t \rangle = 5$ Gyr on the assumption of constant semi-major axis. Obviously, comets remaining in the sample at this n_{pp} must have had on average smaller values of their semi-major axes.

We also investigate how the comets reach the end of their integrations. Three end states may occur: the "decoupled" end state,[3] for which z becomes smaller than $-10^{-3}\ \mathrm{AU}^{-1}$, the "ejected" end state, for which z becomes larger than $-10^{-6}\ \mathrm{AU}^{-1}$, and the "frozen" end state, for which the comet has experienced its last planetary perturbation during the 5 Gyr integration. At each n_{pp}, the cumulative numbers, N_d, N_e and N_f, respectively, of comets having reached each end state are counted. Comets with perihelion close to the upper limit $r_C = 50$ AU will not be considered for the frozen end state. Indeed, a tiny diffusion in perihelion distance may lead a comet beyond this limit with no chance of return since no planetary perturbations will be applied anymore. But this is an artifact of our model and concerns very few comets per perihelion passage.

The results are shown in Figs. 11–13, for $n_{\mathrm{pp}} = 2$, 10, 80 (Fig. 11), $n_{\mathrm{pp}} = 1000$, 2000, 6000 (Fig. 12) and $n_{\mathrm{pp}} = 15{,}000$, 30,000, 50,000 (Fig. 13). The graphs are arranged in columns, each corresponding to one value of n_{pp}. The two top panels show the number of survivors N_s in each cell of the $(q, -1/a)$ and $(q, \cos i)$ planes. The remaining ones show the distributions of N_f, N_e and N_d over the $(q, \cos i)$ plane.

5.1. Initial evolution

During the first interval shown in Fig. 11, the dynamics mainly features the direct injection or ejection of the comets due to relatively large energy kicks. In particular, for $n_{\mathrm{pp}} = 2$ the comets have suffered only one previous kick from the initial energy, which is $-5 \times 10^{-5}\ \mathrm{AU}^{-1}$ in all cases. For perihelia inside Saturn's orbit, the orbital energy already spreads all across the available range with a significant number of comets having reached the decoupled end state and a much larger one having reached the ejected end state. A considerable spread of orbital energy is also seen from the very beginning for perihelia in the range near Uranus' and Neptune's orbits. This feature gets more pronounced between $n_{\mathrm{pp}} = 2$ and 10. Remarkably enough, the region with perihelia inside Jupiter's orbit still contains many comets even at $n_{\mathrm{pp}} = 10$. Only the region with small inclination has then been almost completely emptied. The very few comets that initially reach the frozen end state have perihelion distances very close to 50 AU, where r_C is located. This is caused by slight planetary kicks that shift the perihelion distance just above r_C, such that the comets are no more affected by planetary perturbations until the end of the integration.

When $n_{\mathrm{pp}} = 80$, the region inside Jupiter's orbit is essentially emptied with just some tens of comets remaining with moderate semi-major axes (typically, less than 10,000 AU) and large inclinations. There are still thousands of comets with perihelia between Jupiter and Saturn with a clear preference for large inclinations. We also start to see a diffusion in orbital energy, caused by many small-step perturbations, taking place at perihelion distances larger than 30 AU.

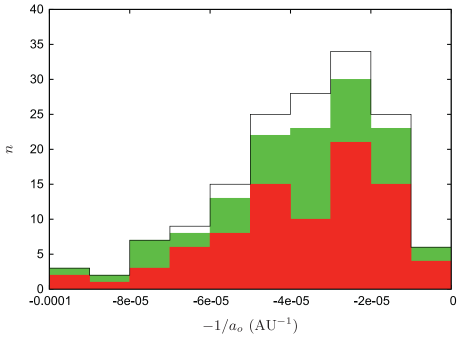

Fig. 10. Distribution of $-1/a_o$ for Oort spike comets (black line). The coloured areas indicate the number of comets with future orbital energy smaller than $-10^{-4}\ \mathrm{AU}^{-1}$ (green area) or larger than zero (red area). The white area shows the comets that remain in the Oort spike.

5.2. Intermediate evolution

For $n_{\mathrm{pp}} = 1000$, 2000 and 6000, as shown in Fig. 12, the region inside Saturn's orbit is essentially emptied (except for a few tens of comets at $n_{\mathrm{pp}} = 1000$ with inclinations around 110–130°). On this longer time scale, we mainly see a diffusion process operating in orbital energy rather than the strong kicks due to close encounters. The concentrations previously observed along the semi-major axes of Uranus and Neptune have now disappeared. For $n_{\mathrm{pp}} = 1000$, the diffusion reaches $a = 1000$ AU (decoupled end state) for perihelia inside Neptune's orbit. Moreover, we see from the distribution of decoupled end states that this preferentially concerns comets with small inclinations. For large perihelion distances, many comets have reached the frozen end state with a major contribution around $q = 40$ AU and inclinations around 120°.

Indeed, the 1, 2 and 3 Gyr level curves of $\langle t \rangle$ now start to be seen in the $N_s(q, \cos i)$ diagram (this was not the case before). We see that the surviving comets get dynamically older in terms of elapsed time with increasing perihelion distance and inclination. This is the general trend, although small local variations are also seen.

At $n_{\mathrm{pp}} = 2000$, $a_{\mathrm{lim}} = 18{,}400$ is smaller than the initial semi-major axis (we recall that initially the semi-major axes were all equal to 20,000 AU), and we observe that a large number of comets with $q > 40$ AU and large inclination have reached the frozen end state. At $n_{\mathrm{pp}} = 6000$ this region is getting fully depleted, with all the comets absorbed by the frozen end state. We also note an accumulation of comets reaching this end state with perihelia between Uranus and Neptune and large inclinations. This is consistent with the long time needed to have a significant diffusion in semi-major axis for such orbits. Thousands of comets still remain in the region between Saturn and Uranus. Finally, while there is very little change in N_e during this interval, we note that N_d increases significantly.

5.3. Terminal evolution

For the third period, i.e., for $n_{\mathrm{pp}} = 15{,}000$, 30,000 and 50,000 shown in Fig. 13, the distributions are shaped by a subtle balance

---

[3] The word *decoupled* refers to the fact that such comets would no longer feel the external perturbations caused by Galactic tides and stellar encounters, even if those had been included. We disregard the possibility for them to return into the considered energy range by further planetary perturbations.

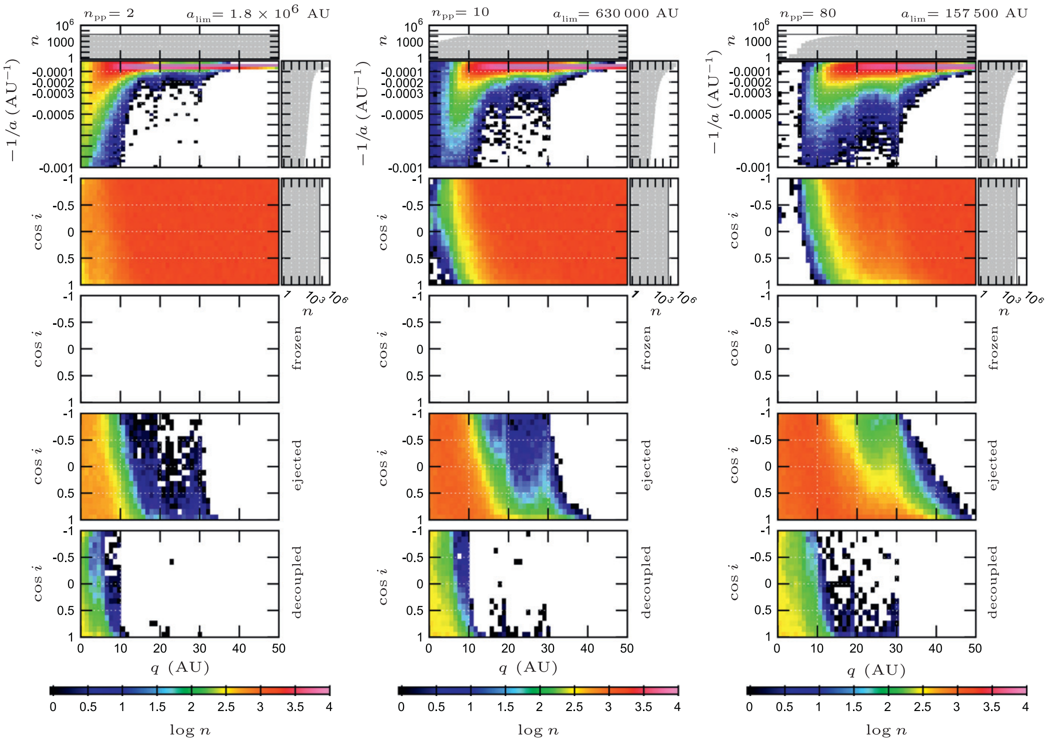

Fig. 11. The first row of colour diagrams gives the number of surviving comets N_s in each cell of the $(q, -1/a)$ plane, and the second row shows the same for the $(q, \cos i)$ plane. The grey side histograms give the marginal distributions of q (top) and $-1/a$ or $\cos i$ (right- hand-side plots). The black line on the top plot gives the initial cumulative number versus q. The black line to the right of the second plot gives the initial cumulative number versus $\cos i$. The three last rows of colour diagrams give the cumulative numbers, N_f, N_e and N_d, respectively, of comets in each end state. The colour log scale (common to all panels) is indicated at the bottom of each column. From left to right, the columns correspond to the 2nd, 10th and 80th perihelion passage (indicated at the upper left of each column). The critical semi-major axis $a_{\rm lim}$ is given at the upper right of each column.

between diffusion time, related to the strength of the perturbations, and the limited maximal time of integration.

For $n_{\rm pp}$ = 15,000, almost all the comets with perihelia inside Uranus' orbit have reached an end state (only a few hundred with high inclination still remain). The diffusion time is short enough in this region for the comets to avoid the frozen end state (except again at large inclination), thus having ended in the decoupled or ejected (preferred) state.

The main feature seen during this period is the loss of almost all the remaining survivors, leaving very few with perihelion distances generally larger than 40 AU. Since the majority of the initial comets had already been lost during earlier stages (essentially to the ejected or frozen end states, depending on the initial values of q and $\cos i$), we cannot note any large changes of N_f or N_e. But we do see an important increase in the number of decoupled comets with perihelia beyond Uranus' orbit.

A priori, it may seem curious that the decoupled end state has now gained in importance relative to the ejections. We noted the same feature also for the intermediate stage of evolution. The explanation is that all the comets are started with a = 20,000 AU in dangerous vicinity of the ejection limit but relatively far from that of decoupling in terms of energy. This is why most comets in planet-crossing orbits end relatively early by ejection, but the situation changes, when we consider the long-term survivors. In order to escape the frozen end state, these must evolve into orbits of relatively small semi-major axis, and hence they are at least as likely to be decoupled as to get ejected.

The last remarkable feature to comment upon is that not all comets with initial q > 40 AU reach the frozen end state. It is true that no close encounters occur for q > 40 AU, and the long-range energy perturbations are very small, as seen in Figs. 3 and 4, but they are different from zero. Thus, over Gyr time scales, by random walk, the energy may actually reach both the ejection and decoupling limits. For the reason discussed above, ejections occur first and decouplings come later for the non-frozen survivors.

6. Discussion and conclusions

We have applied a simple dynamical model of planetary perturbations, neglecting the orbital eccentricities and inclinations and the mutual perturbations among the giant planets as well as all contributions by the terrestrial planets. The justification for this is that, when simulating the effects on Oort Cloud or long-period comets, we are only interested in a statistical description that is correct to first order. Modelling detailed, individual outcomes is of no concern to us. On the other hand, capturing the main features of the probability distributions for planetary perturbations and

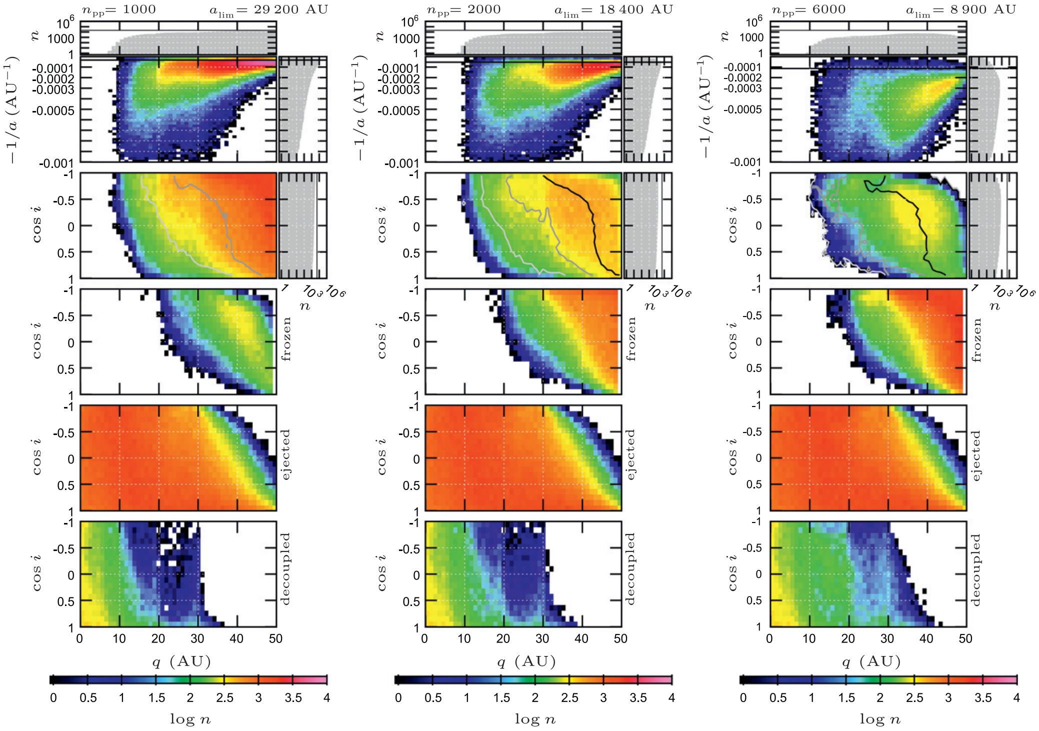

Fig. 12. Same as Fig. 11 for $n_{\rm pp}$ = 1000, 2000 and 6000. In the first row of colour diagrams, the horizontal black line marks the value of $a_{\rm lim}$. The averaged elapsed time level curves are shown in the second row for $\langle t \rangle$ equal to 1, 2 and 3 Gyr (light grey, dark grey and black lines, respectively).

their variation with orbital elements is of essence, and our model is good enough for this purpose. A related remark concerns the problem noted above regarding undersampling of the extreme tails of the perturbation distributions. In our long-term simulations this means that we treat only the close encounters with planets that our sample comets experience, but we treat them accurately. Since our sample is naturally much smaller than the Oort Cloud population of the real Solar System, it is a trivial consequence that our simulation does not capture the extremely large and extremely rare perturbations in a statistically accurate way. However, this is an unavoidable feature of all Monte Carlo simulations and does not pose a real problem.

We made a special study of what happens to new Oort Cloud comets as they make their first passage through the planetary system by giving them initial orbits in the middle of the Oort spike (a_o = 20,000 AU). Averaged over a uniform distribution of cos i, we found a chance for such comets to leave the energy range of the spike that decreases from 95% at $q \to 0$ to ~80% at q = 5 AU and ~30% at q = 10 AU. At q = 15 AU the chance has practically dropped to zero. There is hence little sense in modelling planetary energy perturbations by a loss cone that is completely opaque for q < 15 AU, as has often been done in the past. It has already been made clear, for instance by Kaib and Quinn (2009), that important aspects of comet injection are missed, if this kind of opacity is assumed, and our present results bring quantitative evidence that such must be the case. In our next paper we will discuss more deeply the role of planets in comet injection. For that purpose, our present results showing a general decrease of opacity with inclination are of special interest.

Concerning the results of long-term simulations that we presented in Section 5, special care is needed for a proper interpretation due to the limitations of the model used. First, while the ejected end state in fact marks the end of the existence of such comets in the Solar System, the situation is different for the decoupled end state. The comets that evolve into a < 1000 AU will continue to exist in orbits of shorter periods and may even return into the energy range covered by our simulation, but we do not retain any information about these events. We may say that the remaining dynamical lifetimes of decoupled comets with q < 10 AU are relatively short due to the large energy perturbations experienced by such comets, in agreement with the short time scale for getting decoupled in this range of perihelion distance. In reality this concerns objects that evolve into old long-period and Halley-type comets. We intend to study this evolution in future papers, including both the planetary perturbations and physical lifetime effects.

The (q, cos i) diagrams give the impression that such comets will have a preference for prograde orbits, as is in fact observed for the Halley types, but this impression is false. In fact, the steady state inclination distribution will have to include also the lifetimes, which we are here neglecting, and this gives more weight to the retrograde members. The situation is similar, although the time scale is much longer, for perihelia between the orbits of Saturn and Neptune. In this case, some of the objects may evolve into

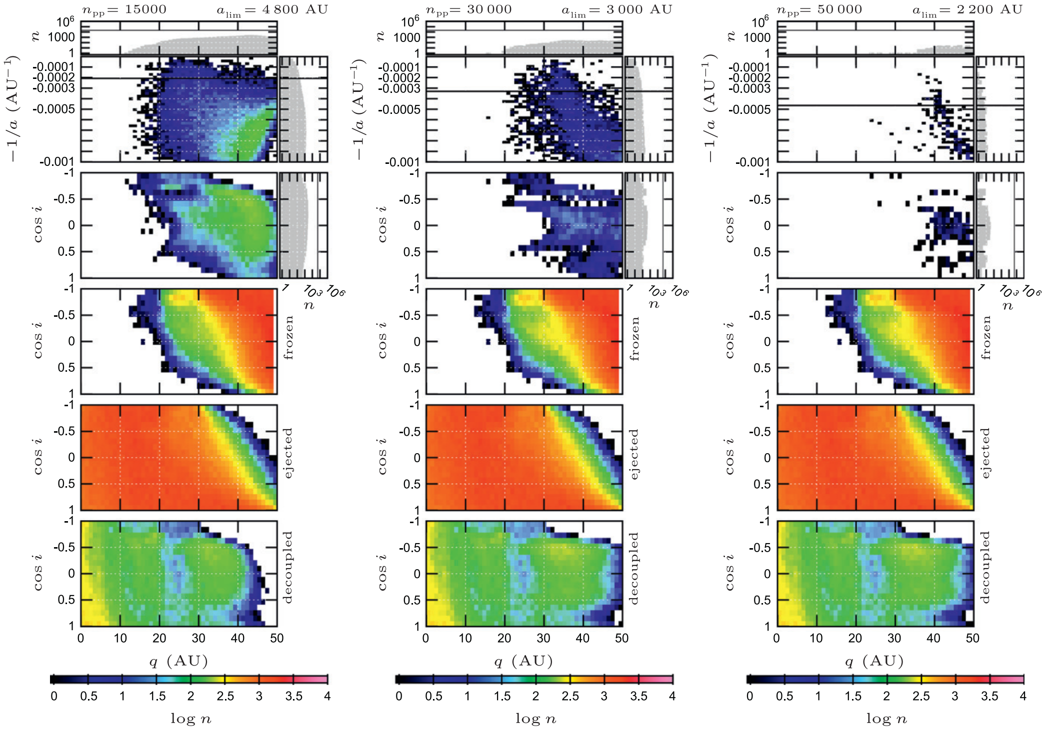

Fig. 13. Same as Fig. 12 for n_{pp} = 15,000, 30,000 and 50,000.

Centaur orbits, which according to our results would have a very broad inclination distribution. This agrees with the conclusions from numerical experiments by Brasser et al. (2012).

Another important point to note is that the simulations we are here presenting neglect the influence of external perturbers, i.e., Galactic tides and stellar encounters. These would add a significant spread in perihelion distance in the energy range of $z > -10^{-4}$ AU^{-1} and a slower migration at smaller values of z. We will model this in our next paper, but let us make some preliminary comments at this point. New comets with $q > 10$ AU are likely to stay within the Oort spike energy range for several revolutions at least, but contrary to our simulation, their perihelion distances will change significantly. Therefore, the slow energy diffusion at $q > 40$ AU will not occur in the way we simulated. On the other hand, we may expect an interplay between the slow diffusions in orbital energy and perihelion distance to occur for orbits with semi-major axes of a few thousand AU and perihelion distances larger than 20 AU.

This interplay may feed a population with perihelia beyond Neptune and semi-major axes much smaller than those of new comets. Over Gyr time scales, the evolution found in our present simulation may occur, leading to decoupled objects with large perihelion distances (40–50 AU). Given that the Oort Cloud is probably a very old structure, the present Solar System may thus contain such a population. It would appear somewhat like the detached scattered disc but be characterised by larger semi-major axes and a fairly isotropic distribution of orbital planes. It would not have any direct connection with the scattered disc but result from the long-term dynamics of usual Oort Cloud comets.

In conclusion, this paper has introduced a model of planetary perturbations on long-period comets with applications to long-term simulations of the dynamics of the Oort Cloud, which will be described in forthcoming papers. In addition, a major result concerns the transparency of the loss cone and leakiness of the Jupiter–Saturn barrier, which is here systematically demonstrated and quantified for the first time. From simulations of long-term orbital evolutions of injected comets without including external perturbations, we present evidence on how long such comets will linger in the vicinity of the Oort spike, when their perihelia are beyond Saturn's orbit, and we tentatively identify a mechanism to store Oort Cloud comets, arriving with perihelia beyond Neptune, into quasi-decoupled orbits with $a \sim 1000$ AU.

Acknowledgments

We are grateful for valuable advice provided by the referees, R. Brasser and J.A. Fernández. HR is indebted to Grant Nr. 74/10:2 of the Swedish National Space Board as well as Grant UMO-2011/01/B/ST9/05442 of the Polish National Science Agency.

References

Brasser, R., Schwamb, M.E., Lykawka, P.S., Gomes, R.S., 2012. An Oort Cloud origin for the high-inclination, high-perihelion Centaurs. Mon. Not. R. Astron. Soc. 420, 3396–3402.

Carusi, A., Valsecchi, G.B., Greenberg, R., 1990. Planetary close encounters – Geometry of approach and post-encounter orbital parameters. Celest. Mech. Dynam. Astron. 49, 111–131.

Duncan, M., Quinn, T., Tremaine, S., 1987. The formation and extent of the Solar System comet cloud. Astron. J. 94, 1330–1338.

Dybczyński, P.A., 2005. Simulating observable comets. II. Simultaneous stellar and galactic action. Astron. Astrophys. 441, 783–790.

Dybczyński, P.A., Królikowska, M., 2011. Where do long-period comets come from? Moving through the Jupiter–Saturn barrier. Mon. Not. R. Astron. Soc. 416, 51–69.

Everhart, E., 1968. Change in total energy of comets through the Solar System. Astron. J. 73, 1039–1052.

Everhart, E., 1969. Close encounters of comets and planets. Astron. J. 74, 735–750.

Everhart, E., 1985. An efficient integrator that uses Gauss–Radau spacings. In: Carusi, A., Valsecchi, G.B. (Eds.), ASSL, vol. 115. IAU Colloq. 83: Dynamics of Comets: Their Origin and Evolution, p. 185.

Fernández, J.A., 1981. New and evolved comets in the Solar System. Astron. Astrophys. 96, 26–35.

Fernández J.A. (Ed.), 2005. Comets – Nature, Dynamics, Origin and their Cosmological Relevance, Astrophysics and Space Science Library, vol. 328.

Fouchard, M., Froeschlé, Ch., Valsecchi, G.B., 2003. Is the dynamics of Jupiter family comets amenable to Monte Carlo modelling? Mon. Not. R. Astron. Soc. 344, 1283–1295.

Heisler, J., Tremaine, S., 1985. The influence of the galactic tidal field on the Oort comet cloud. In: Bulletin of the American Astronomical Society, vol. 17. p. 726.

Hills, J.G., 1981. Comet showers and the steady-state infall of comets from the Oort Cloud. Astron. J. 86, 1730–1740.

Kaib, N.A., Quinn, T., 2009. Reassessing the source of long-period comets. Science 325, 1234–1236.

Kaib, N.A., Quinn, T., Brasser, R., 2011. Decreasing computing time with symplectic correctors in adaptive time stepping routines. Astron. J. 141, 3.

Królikowska, M., 2006. Non-gravitational effects in long-period comets and the size of the Oort Cloud. Acta Astron. 56, 385–412.

Królikowska, M., Dybczyński, P.A., 2010. Where do long-period comets come from? 26 Comets from the non-gravitational Oort spike. Mon. Not. R. Astron. Soc. 404, 1886–1902.

Levison, H.F., Duncan, M.J., 1994. The long-term dynamical behavior of short-period comets. Icarus 108, 18–36.

Marsden, B.G., Sekanina, Z., 1973. On the distribution of "original" orbits of comets of large perihelion distance. Astron. J. 78, 1118–1124.

Marsden, B.G., Sekanina, Z., Everhart, E., 1978. New osculating orbits for 110 comets and analysis of original orbits for 200 comets. Astron. J. 83, 64–71.

Marsden, B.G., Williams, G.V., 2008. Catalogue of Cometary Orbits 17th Edition. Smithsonian Astrophys. Obser., IAU MPC/CBAT, Cambridge, MA.

Oort, J.H., 1950. The structure of the cloud of comets surrounding the Solar System and a hypothesis concerning its origin. Bull. Astron. Inst. Neth. 11, 91–110.

Rickman, H., Fouchard, M., Froeschlé, Ch., Valsecchi, G.B., 2008. Injection of Oort Cloud comets: The fundamental role of stellar perturbations. Celest. Mech. Dynam. Astron. 102, 111–132.

Rickman, H., Valsecchi, G.B., Froeschlé, Cl., 2001. From the Oort Cloud to observable short-period comets – I. The initial stage of cometary capture. Mon. Not. R. Astron. Soc. 325, 1303–1311.

Valsecchi, G.B., Milani, A., Gronchi, G.F., Chesley, S.R., 2000. The distribution of energy perturbations at planetary close encounters. Celest. Mech. Dynam. Astron. 78, 83–91.

Wisdom, J., Holman, M., 1991. Symplectic maps for the n-body problem. Astron. J. 102, 1528–1538.

Zhou, J.-L., Sun, Y.-S., Zhou, L.-Y., 2002. Evidence for Lévy Random walks in the evolution of comets from the Oort Cloud. Celest. Mech. Dynam. Astron. 84, 409–427.

Chapitre 3

Résultats

3.1 Synergie entre les perturbations stellaires et les marées galactiques

3.1.1 Synergie à long terme

Dans un premier temps le modèle dynamique a été utilisé uniquement avec les marées galactiques et les perturbations stellaires. On a ainsi pu mettre en évidence une synergie entre les perturbations stellaires et les effets des marées, de sorte que le flux de comètes observables avec un modèle incluant les deux effets est supérieur à la somme des flux obtenus avec deux modèles prenant en compte seulement un des deux effets.

Dans Rickman et al. (2008), inclus ci-après, cette synergie est clairement mise en évidence. Plus précisément deux types de synergie sont identifiés : (i) une synergie à long terme, c'est-à-dire agissant sur des échelles de temps de l'ordre de la période des oscillations de l'excentricité induites par les marées, (ii) et une synergie à court terme agissant pendant la dernière période orbitale de la comète avant de devenir observable. En outre, on a pu montrer qu'on ne peut pas se reposer sur la distribution des éléments orbitaux des comètes observées pour rejeter l'hypothèse qu'on subit actuellement une pluie cométaire modérée.

Une étude détaillée de la synergie à long terme est effectuée dans Fouchard et al. (2011a) (article inséré ci-après). Les marées galactiques sont un processus quasi-intégrable, donc les régions du nuage d'où les comètes peuvent devenir observables sous l'effet des marées galactiques (régions appelées TAZ, pour Tidal Active Zone) sont relativement bien cloisonnées. Ainsi, lorsque le temps s'écoule, les comètes de ces régions devenant observables en sont éjectées, de telle sorte que ces régions ont tendance à se vider et le flux de comètes observables à se tarir. La présence des perturbations stellaires change drastiquement cette image puisque les frontières de la TAZ deviennent perméables et de nouvelles comètes peuvent y être injectées grâce aux étoiles. On a pu mettre en évidence qu'une seule et unique étoile pouvait ainsi générer une augmentation du flux de comètes observables de 20 à 30% pendant plusieurs centaines de millions d'années. Ce qu'on a appelé "bruine cométaire".

Celest Mech Dyn Astr (2008) 102:111–132
DOI 10.1007/s10569-008-9140-y

ORIGINAL ARTICLE

Injection of Oort Cloud comets: the fundamental role of stellar perturbations

Hans Rickman · **Marc Fouchard** ·
Christiane Froeschlé · **Giovanni B. Valsecchi**

Received: 30 November 2007 / Revised: 5 March 2008 / Accepted: 11 April 2008 /

Abstract We present Monte Carlo simulations of the dynamical evolution of the Oort cloud over the age of the Solar System, using an initial sample of one million test comets without any cloning. Our model includes perturbations due to the Galactic tide (radial and vertical) and passing stars. We present the first detailed analysis of the injection mechanism into observable orbits by comparing the complete model with separate models for tidal and stellar perturbations alone. We find that a fundamental role for injecting comets from the region outside the loss cone (perihelion distance $q > 15\,\mathrm{AU}$) into observable orbits ($q < 5\,\mathrm{AU}$) is played by stellar perturbations. These act in synergy with the tide such that the total injection rate is significantly larger than the sum of the two separate rates. This synergy is as important during comet showers as during quiescent periods and concerns comets with both small and large semi-major axes. We propose different dynamical mechanisms to explain the synergies in the inner and outer parts of the Oort Cloud. We find that the filling of the observable part of the loss cone under normal conditions in the present-day Solar System rises from <1% for $a < 20\,000\,\mathrm{AU}$ to about 100% for $a \gtrsim 100\,000\,\mathrm{AU}$.

H. Rickman
PAN Space Research Center, Bartycka 18A, 00-716 Warszawa, Poland

H. Rickman
Uppsala Astronomical Observatory, Box 515, 75120 Uppsala, Sweden
e-mail: hans@astro.uu.se

M. Fouchard (✉)
LAL-IMCCE/USTL, 1 Impasse de l'observatoire, 59000 Lille, France
e-mail: fouchard@imcce.fr

C. Froeschlé
Observatoire de la Côte d'Azur, UMR 6202, Bv. de l'Observatoire,
B.P. 4229, 06304 Nice cedex 4, France
e-mail: froesch@obs-nice.fr

G. B. Valsecchi
INAF-IASF, via Fosso del Cavaliere 100, 00133 Roma, Italy
e-mail: giovanni@iasf-roma.inaf.it

Keywords Galactic tide perturbations · Monte Carlo simulation · Long period comets · Oort Cloud

1 Introduction

When analysing the distribution of original inverse semi-major axes of long-period comets, Oort (1950) concluded that the near-parabolic spike of this distribution reveals a distant reservoir of comets (the 'Oort Cloud'). His favoured mechanism of injection of comets from this reservoir into observable orbits (i.e., with small perihelion distances) was the passage of stars in the vicinity of the reservoir, whereby the long-term reshuffling of angular momenta would ensure a continuous infeed into the innermost part of the Solar System.

Until the 1980s stellar perturbation was the only mechanism considered when issues concerning the injection of comets from the Oort Cloud were discussed (e.g., Rickman 1976; Weissman 1979; Fernández 1980; Hills 1981; Remy and Mignard 1985). However, by that time it became clear that the tidal action of the Galaxy as a whole must also have an important influence—especially the part corresponding to the z-dependent disk potential (Heisler and Tremaine 1986). This was verified by noting that the Galactic latitudes of perihelia of new Oort Cloud comets have a double-peaked distribution that is characteristic of the disk tide (Delsemme 1987).

An important paper by Duncan et al. (1987) treated the formation of the Oort Cloud and showed that the characteristic time scale for changing the perihelion distances, independent of the semi-major axis, is shorter for the Galactic disk tide than for the stellar perturbations. This has been verified by later analytic work, e.g., by Fernández (2005), and further numerical simulations of Oort Cloud evolution (e.g., Heisler et al. 1987) have given support to the dominance of Galactic tides for comet injection.

Consequently, stellar perturbations have come to be practically neglected as a source of comet injection—except when discussing "comet showers" (Hills 1981) arising from rare stellar passages through the dense, inner parts of the Oort Cloud. The importance of stellar perturbations for randomizing the orbital distribution of the Oort Cloud and thus keeping the relevant infeed trajectories of the disk tide populated over long time scales has been realized (see Dybczyński 2002 and references therein), but the actual injection is often seen as due only to the tide. Hence it should be limited to semi-major axes large enough for the tidal perturbation to bring the cometary perihelion at once from outside the "Jupiter–Saturn barrier" (i.e., perihelion distance $q \gtrsim 15$ AU) into the observable region ($q < 5$ AU). The result is that one expects new comets to have $a_{ori} \gtrsim 3 \times 10^4$ AU (Bailey and Stagg 1988; Levison et al. 2001; Fernández 2005).

On the other hand, some recent papers indicate that this picture may have problems. The fractional population of the observable region—if fed only by Galactic tides—is small enough, and the orbital periods long enough, that the estimated total population of the Oort Cloud may be uncomfortably large (Charnoz and Morbidelli 2007). And in addition, when non-gravitational effects are included into orbit determinations for new Oort Cloud comets (Królikowska 2006), the resulting original orbits tend to be of shorter periods, having smaller semi-major axes—often much smaller than 3×10^4 AU.

Meanwhile, we have developed fast and accurate methods to treat both the Galactic tides (Breiter et al. 2007; Fouchard et al. 2007) and stellar perturbations (Rickman et al. 2005) in Monte Carlo simulations of Oort Cloud dynamics. This has allowed us to perform calculations, to be presented here, where the cloud is represented by as many as 10^6 sample comets and integrated over a time exceeding the age of the Solar System. This amounts to

5×10^{15} comet-years of individual evolutions (or only slightly smaller due to the loss of comets during the simulation), which is much more than in all previous long-term Oort Cloud simulations—e.g., 3×10^{13} comet-years for Duncan et al. (1987), 4×10^{14} comet-years for Mazeeva (2006), and $\sim 4 \times 10^{13}$ comet-years for Emel'yanenko et al. (2007) who used cloning. Heisler (1990) simulated $\simeq 7 \times 10^{15}$ comet-years but only thanks to extensive cloning during the course of the simulation. In fact her long-term simulations (4.5 Gyr) concerned only $\simeq 10^4$ "tokens", i.e., comets actually followed, while these were meant to represent $\simeq 150$ times as many comets by means of cloning.

Our work is the first to study the mechanism of injection of comets from the Oort Cloud over the age of the Solar System by simulating and comparing different dynamical models. The reason why models involving both the Galactic tide and stellar perturbations gave a much higher flux of injected comets than those involving only stars (Heisler et al. 1987; Heisler 1990) was never clarified, since comparisons with models involving only the tide were not made. In the present paper we concentrate on a comprehensive comparison of combined and separate models, thus describing and analysing for the first time the synergy effect of Galactic tide and stars.

We also take special care to define correctly the encounter velocities in our sample of passing stars, thereby arriving at somewhat larger values than those used previously. Finally, we study the relative filling of the observable part of the loss cone and the distribution of inverse semi-major axes of the injected comets. These studies are, however, only preliminary, since our current simulations do not include planetary perturbations, and thus we cannot account for those comets that arrive into the observable region after having "diffused" across the Jupiter–Saturn barrier in several revolutions.

Our calculations are presented in Sect. 2, and in Sects. 3–5 we describe our results in terms of the distribution of injection times into the inner planetary system, the flux of new, observable comets as a function of time, and the distributions of inverse semi-major axis and Galactic latitude of perihelion as well as loss cone filling at representative epochs. In Sect. 6 we discuss the results and summarize our conclusions.

2 Calculations

As a simplifying assumption, we consider the Oort Cloud to have been formed instantaneously at a given epoch, and that its orbital distribution was isotropic to begin with. Thus the initial conditions are chosen with flat distributions of $\cos i_o$, ω_o, Ω_o and M_o (we use common notations for the orbital elements, and the angles may be defined with respect to an arbitrary frame of reference). We consider a thermalized initial state of the cloud, where the semi-major axes (a_o) are chosen in the interval $3 \times 10^3 < a_o < 1 \times 10^5$ AU with a probability density $\propto a_o^{-1.5}$ (Duncan et al. 1987). The initial eccentricities (e_o) are chosen with a density function $\propto e_o$ in such a way that the perihelia are outside the planetary system ($q > 32$ AU). We thus initialise 1×10^6 comets.

The Galactic parameters used for calculating the tidal effects are the same as described in earlier papers (Fouchard et al. 2007). The most important one for comparison with other investigations is the mid-plane disk density, which we take as $0.1\,M_\odot \mathrm{pc}^{-3}$ (Holmberg and Flynn 2000). This is in agreement with Emel'yanenko et al. (2007), while Heisler (1990) used $0.18\,M_\odot \mathrm{pc}^{-3}$ (Bahcall 1984).

The simulation runs with a predefined set of 197,906 stellar encounters, occurring at random times during a lapse of $t_{max} = 5 \times 10^9$ years, with random solar impact parameters up to $d_{max} = 4 \times 10^5$ AU, and with random stellar masses and velocities. Our procedure for creating each of these encounters is as follows. Let ξ denote a stochastic, random number

Table 1 Stellar parameters

Type	Mass ($M_\odot$)	Enc. freq.	$v_\odot$ (km/s)	σ_* (km/s)	$\langle V\rangle$ (km/s)	σ_V (km/s)
B0	9	0.005	18.6	14.7	24.6	6.7
A0	3.2	0.03	17.1	19.7	27.5	9.3
A5	2.1	0.04	13.7	23.7	29.3	10.4
F0	1.7	0.15	17.1	29.1	36.5	12.6
F5	1.3	0.08	17.1	36.2	43.6	15.6
G0	1.1	0.22	26.4	37.4	49.8	17.1
G5	0.93	0.35	23.9	39.2	49.6	17.9
K0	0.78	0.34	19.8	34.1	42.6	15.0
K5	0.69	0.85	25.0	43.4	54.3	19.2
M0	0.47	1.29	17.3	42.7	50.0	18.0
M5	0.21	6.39	23.3	41.8	51.8	18.3
wd	0.9	0.72	38.3	63.4	80.2	28.2
gi	4	0.06	21.0	41.0	49.7	17.5

The types are mostly MK types for main sequence stars; ‘wd’ indicates white dwarfs, and ‘gi’ indicates giant stars. The encounter frequencies are given in number per Myr within 1 pc. The following two columns list the solar apex velocity with respect to the corresponding type, and the spherical Maxwellian velocity dispersion. The last two columns give the mean heliocentric encounter velocity and its standard deviation according to our results

with a uniform probability distribution on the interval [0, 1]. The solar impact parameter is chosen as $d = \xi_d^{1/2} \times d_{max}$, and the time of the encounter (specifically, the time of the star’s perihelion passage) is $t = \xi_t \times t_{max}$. The direction of stellar motion with respect to the Sun is defined in terms of Galactic latitude and longitude (b, ℓ) such that $\sin b = 2\xi_b - 1$ and $\ell = \xi_\ell \times 2\pi$, i.e., it has an isotropic distribution. The point at which the initial stellar velocity cuts the orthogonal impact plane is situated on a circle of radius d around the Sun, and its location is defined by an azimuthal angle (a) such that $a = \xi_a \times 2\pi$.

Next we choose the type of the star. We use 13 categories as in Rickman et al. (2004) with parameters listed in Table 1. To each category we associate one value of the stellar mass. These masses are generally taken as those of the archetypal spectral classes along the main sequence according to Allen (1985). However, in contrast to our earlier investigations, we replace the archetypal mass of 18 $M_\odot$ for B0 stars by a weighted average of 9 $M_\odot$, considering that the less massive, later types (B2, B5) are much more common than the earlier ones. The relative encounter frequencies f_i of Table 1 are taken from García-Sánchez et al. (2001), where they were derived from the respective products of number density and mean velocity, $n_i\langle v_i\rangle$. A random number ξ_i is used to pick a stellar category i with the probability $f_i/\sum f_i$.

Finally, we choose the speed of the stellar motion in the following way. The velocity dispersions (σ_{*i}) listed in Table 1 are taken from García-Sánchez et al. (2001), and they correspond to the semi-axes of the velocity ellipsoids $(\sigma_{ui}, \sigma_{vi}, \sigma_{wi})$ listed by Mihalas and Binney (1981) using: $\sigma_{*i}^2 = \sigma_{ui}^2 + \sigma_{vi}^2 + \sigma_{wi}^2$. For the peculiar velocity (v_*) of a star with respect to its LSR, we use a spherical Maxwellian by taking η_u, η_v and η_w as three random numbers, each with a Gaussian probability distribution with expectance 0 and variance 1, and computing $v_* = \sigma_{*i}\left\{(\eta_u^2 + \eta_v^2 + \eta_w^2)/3\right\}^{1/2}$. The star’s heliocentric velocity is found by combining the vector $\mathbf{v}_*$ with the Sun’s peculiar velocity with respect to the star’s LSR (“apex velocity”) $\mathbf{v}_\odot$, whose absolute value is listed in Table 1 for each stellar category. We assume a random relative orientation of the two vectors and thus compute:

$$V = \left\{v_{\odot i}^2 + v_*^2 - 2v_{\odot i}v_* \cdot C\right\}^{1/2} \tag{1}$$

where $C = \cos\theta$ is taken as $C = 2\xi_C - 1$, and θ is the angle between the two vectors.

Within each stellar category we have to account for the fact that the contribution to the encounter flux is proportional to V. Thus we define a constant, large velocity $V_{0i} = v_{\odot i} + 3\sigma_{*i}$ for each category, such that V is always smaller than V_{0i}, and we take a new random number ξ_V and keep the value just found for V, if $\xi_V < V/V_{0i}$. Otherwise we repeat the computation of V until the ξ_V condition is fulfilled. This procedure was not followed in our previous investigations, leading to underestimates of the average stellar velocities. Further underestimates were caused by programming errors, and we caution the reader that the stellar velocities in Rickman et al. (2004, 2005) were systematically too small. This is clearly seen by comparing Fig. 1 of Rickman et al. (2005) with the data in Table 1, which yield a mean velocity of 53 km/s with a dispersion of ≃20 km/s.

A few comments on the mean stellar encounter velocity are in order. The average peculiar velocity of stars in the solar neighbourhood is ≃40 km/s. This value was given by Hut and Tremaine (1985), and combining it in quadrature with a typical solar apex velocity of 23 km/s for the most common stellar categories (Table 1), one gets a mean heliocentric velocity of ≃46 km/s. Heisler et al. (1987) were the first to introduce the flux-weighting into the selection of random velocities, but they neglected the solar apex velocity. In fact, their flux-weighting was somewhat different from ours, because they considered only one of the three velocity components, namely, the radial heliocentric velocity. But the encounter flux is sensitive to the velocity with respect to the impact plane, i.e., the full speed of the star, instead of just the radial component. We have found that this difference has only a small effect on the resulting mean velocity, but we mention it for the sake of completeness. In both cases, we find that the weighting raises the mean velocity by 6–7 km/s. This explains our mean velocity of 53 km/s as resulting from including both the solar motion and the flux-weighting procedure. Finally, let us compare with the mean encounter velocity of ≃46 km/s in García-Sánchez et al. (2001). This resulted from a list of 92 stellar encounters within 5 pc and 1 Myr of the present, compiled with the aid of Hipparcos data, but the authors showed that there was a serious bias against faint absolute magnitudes in this sample, affecting all stars with $M_V > 4$. Thus, the stars with the highest velocities were essentially lacking, and the resulting mean velocity is that of the inherently brighter, slower moving stars.

Comparing with other investigators, we note that both Heisler (1990); Mazeeva (2006) and Emel'yanenko et al. (2007) based their stellar encounter frequencies on the analysis by Heisler et al. (1987), who ignored the solar motion—thereby underestimating the relative frequency of encounters with massive stars that have small velocity dispersions—and neglected the contribution of the massive giants. Our encounter sample contains as much as 3.5% of massive stars, i.e., the B0, A0, A5, F0, F5 and 'gi' categories in Table 1 with an average mass of 2.3 $M_\odot$, while counting the stars in the absolute magnitude range that corresponds to this average mass in Heisler et al. (1987), one arrives at <1% of the total encounter frequency. Since the massive stars have an average M/V ratio ∼10 times larger than the red dwarf stars that dominate the sample, each such star will affect ∼100 times as many comets. Hence one easily realizes that in our case a large fraction of the total stellar effect comes from the massive star category that is downplayed by the other investigators. This, to some extent, compensates for two other effects that make the stellar perturbations less efficient in our simulation. One is the larger encounter velocities, as already described, and the other is the total encounter frequency within 1 pc, which in our case is 10.5 per Myr, while for the others it is 13.1 per Myr.

Our calculations of the heliocentric impulse imparted to the comet (at time t) are done using the Sequential Impulse Approximation, which guarantees a good accuracy at a low cost of computing time (Rickman et al. 2005). During the simulation we keep track of all the perihelion passages with their q values. At each perihelion a decision is taken about which

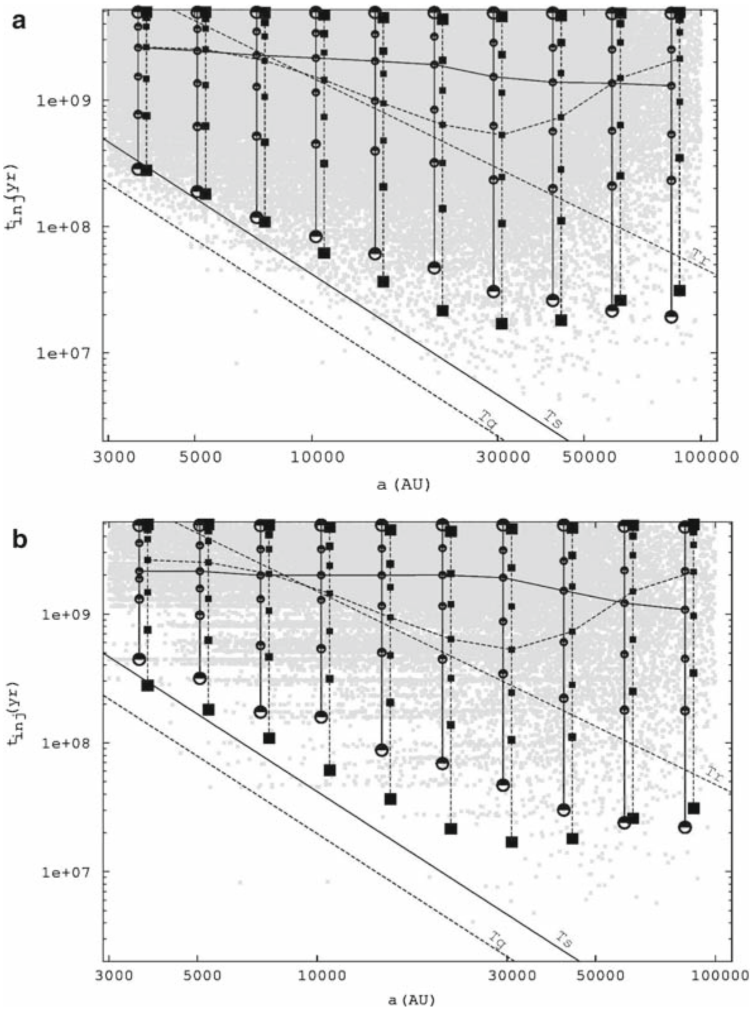

Fig. 1 Injection time versus initial semi-major axis. The semi-major axis range is split into 10 equal intervals of $\log a$. For each interval we plot different statistical parameters characterizing the distribution of injection times, as explained in the text. The dotted line labelled T_g corresponds to the tidal torquing time shown in Fig. 2 of Duncan et al. (1987), T_s to the corresponding stellar torquing time, and T_r to the period of (q, i_G) oscillation imposed by the vertical tide. The top panel (**a**) compares the model with only tides to the one with only stars, and the grey dots are individual stellar injections. In the bottom panel (**b**) the stars-only model is replaced by the combined model

method to use for the Galactic tide perturbation during the coming orbital period. The fastest method is a mapping (Breiter et al. 2007) that analytically computes the orbital elements at the subsequent perihelion, but this is used only for elliptic orbits with semi-major axis less than a critical value that depends on the eccentricity (Fouchard et al. 2007). Otherwise we use numerical integration with a symplectic integrator for KS-regularized equations of motion (Laskar and Robutel 2001) in case $1/a > 10^{-5}$ AU^{-1} and the 15th order RADAU integrator (Everhart 1985) for $1/a < 10^{-5}$ AU^{-1}.

During the orbital period in question, normally, several stellar passages occur. On those occasions the osculating cometary orbit is subject to an instantaneous impulse. In the numerical integration regime for the Galactic tide, one always comes back to perihelion. But in the mapping regime, when the starting orbital period has elapsed, the comet may not be at perihelion because of the intervening stellar perturbations, and we then resort to numerical integration until the next perihelion passage takes place.

The simulation proceeds for a maximum of 5 Gyr, unless an end state is reached. There are two such end states: either the comet reaches perihelion with $q < q_c = 15$ AU (it is lost due to planetary perturbations), or the comet reaches $r = 4 \times 10^5$ AU in outbound motion (it escapes directly into interstellar space).

What we have just described is the full simulation of the "combined" model including both the Galactic tide and stellar perturbations. In addition, we have run two simulations that include only one or the other of the two dynamical effects.

3 Injection time

We will first consider the time needed to shift any cometary starting perihelion distance $q_o > 32$ AU into a perihelion distance $q < 15$ AU. This is the time t_{inj} required to inject a comet into the target zone, and we call it the injection time. We have thus scrutinized all three simulations, and for each injected comet in every simulation we noted its value of t_{inj}. Let us now compare the statistics of injection times between all three dynamical models.

The range of initial semi-major axes $3\,000 < a_o < 100\,000$ AU is divided, according to $\log a_o$, into ten equal intervals. For each interval the following statistical parameters concerning the injection time are computed: its median value, its lower and upper quartiles (surpassed by 75%, respectively 25%, of the values), its lower and upper deciles (surpassed by 90%, respectively 10%, of the values), and finally its lower and upper percentiles (surpassed by 99%, respectively 1%, of the values).

Figure 1 presents the comparison of t_{inj} statistics by means of two plots. The top one (Fig. 1a) compares the model with only the Galactic tides to the combined model, while in the bottom one (Fig. 1b) the tides-only model is compared to the one with only stellar perturbations. In each case we plot the statistical quantities versus a_o. The tides-only model is represented by filled squares, and for the other models we use half-filled circles. At any particular value of a_o, the symbols for each model are joined by vertical bars. A slight horizontal shift between the symbols has been introduced for easy distinction of the models, but the real a_o intervals are identical. The median values have been joined by curves (dotted for the tides-only model, and solid for the other ones). The grey dots show individual injections for the stars-only model (Fig. 1b) and the combined model (Fig. 1a).

For comparison with Duncan et al. (1987), who plotted a similar diagram (their Fig. 2), we include three lines. The one labelled T_g shows their "tidal torquing time" and the one labelled T_s shows the corresponding "stellar torquing time", both as functions of a. These are meant to represent the typical time required to decrease the perihelion distance from 25 AU to 15 AU in the two cases. The third line labelled T_r refers to the period of (q, i_G) oscillation due to the tidal component normal to the Galactic plane (Duncan et al. 1987).

By inspecting Fig. 1, we can make the following observations. First, compare the tides-only median curve with the T_r line. The two agree fairly well in the range from $a \simeq 6\,000$ to 25 000 AU. This is natural, because T_r is twice the average time it takes for the vertical tide to bring any Oort Cloud comet into the target zone, as long as it is on a relevant trajectory with $q_{\mathrm{min}} < 15$ AU. For $a \lesssim 6\,000$ AU the median flattens out at about 2.5 Gyr, and this

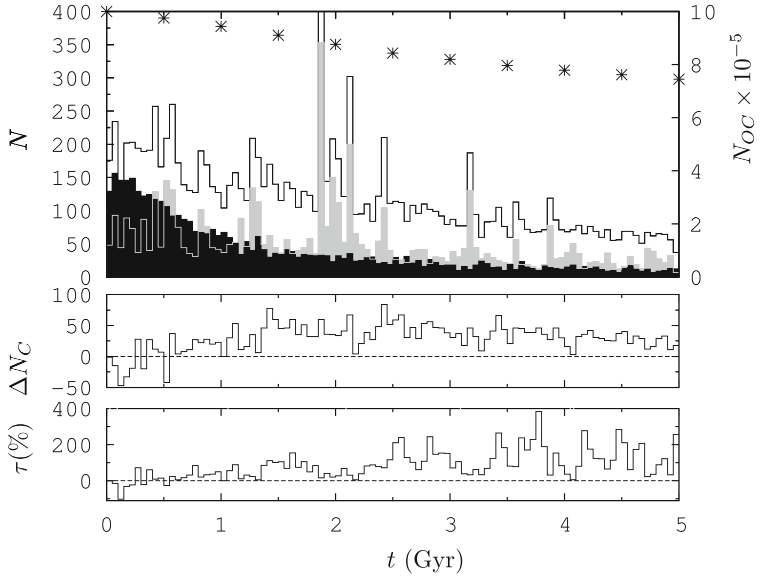

Fig. 2 The upper diagram shows the number of comets entering the observable zone per 50 Myr versus time. The white histogram corresponds to the combined model, the black histogram to the Galactic tide alone, and the grey histogram to the passing stars alone. The asterisks indicate the number of comets remaining in our simulation for the combined model at every 500 Myr with scale bars to the right. The middle diagram shows the excess number of injections into the observable region per 50 Myr in the combined model with respect to the sum of the stars-only and tides-only models. The lower diagram shows this excess expressed in percent of the mentioned sum

is due to the limit of our simulated interval at 5 Gyr. Had we let the simulation run for a much longer time, we would have seen the median curve follow the T_r line to even smaller a values. For $a \gtrsim 25\,000$ AU we see how the median curve turns upwards, while T_r continues to decrease. This can be explained as a result of a quick stripping of comets from all trajectories with $q_{\min} < 15$ AU, after which these have to be repopulated through the action of the non-integrable part of the tides. Since this works on a much longer time scale, it is obvious that the median of t_{inj} has to increase.

Already at this point we see evidence that the mean injection time—even in the tides-only model—does not follow the prediction of the $T_r(a)$ dependence at all semi-major axes. Studying the Oort Cloud over a long enough time allows other parts of the Galactic tide than the simple, vertical component to take control of comet injections, at least in the outer parts of the cloud. But consider now the median curves of the two models that involve stellar perturbations. They are mutually quite similar, but they differ strongly from the tides-only curve except at $a \lesssim 6\,000$ AU.

The mutual similarity—in spite of a much larger number of grey points (injections) in Fig. 1b—means that the same basic mechanism is at work. We identify this as the angular momentum reshuffling by stellar perturbations. In Fig. 1a (stars-only model) this in itself makes comets diffuse all over angular momentum space so that some reach the target zone. In Fig. 1b (combined model) the same angular momentum diffusion repopulates the "infeed trajectories" (with $q_{\min} < 15$ AU) of the vertical Galactic tide, whereupon the comets are injected at a rate given by $T_r(a)$. We interpret the flatness of the median curves at a level of roughly half the duration of our simulation as evidence that the time scale of angular momentum reshuffling is short enough to guarantee an injection rate that is at least as large during the first half (0–2.5 Gyr) as during the second half (2.5–5 Gyr). This is in agreement with the thermalization time scale reported by Duncan et al. (1987). The tendency for a slight decrease of the median t_{inj} at the largest semi-major axes is likely due to a progressive depletion of the outer parts of the cloud during the course of the simulation, while the reshuffling time scale is relatively short.

We thus realize that the behaviour of the median injection time, generally speaking, has very little to do with any of the theoretical time scales. Let us now instead consider the lowest percentiles, since these give information on the quickest injections that–in principle–might be governed by the T_g or T_s dependences. The lowest percentile of the tides-only model indeed decreases with a_o roughly parallel to the T_g line in the inner core of the cloud ($a < 10\,000$ AU), but we nonetheless see a somewhat smaller slope. This tendency gets stronger with increasing a_o and finally turns into an increase outside 30 000 AU. We interpret this as due to the same repopulation of infeed trajectories by the non-integrable part of the tide as we discussed in relation to the median curve.

The lowest percentile of the stars-only model shows a fall-off with a_o that is interestingly slow in comparison with the T_s line. This appears to be related to the horizontal bands of grey points, which are cometary showers. For each a_o interval in the inner core, the timing of the lowest percentile is that of the first shower reaching into that interval. The larger a_o, the sooner such a shower appears. But the showers also get weaker, being caused by more and more distant stellar encounters. Thus, in the outer parts of the cloud they are no longer of significance for defining the lowest percentile. Since this is instead controlled by a growing number of usual, inefficient stars passing through the outer regions, one has to wait longer.

When we look at the lowest percentile of the combined model, we see that it follows the same decrease as the tides-only model in the inner core. Indeed, with a much larger number of injections, the comet showers have lost their importance, and as we shall see in Sect. 4, during the first Gyr the injections are largely controlled by the Galactic tides. But outside the inner core the lowest percentile now behaves with respect to that of the tides-only model in a similar way as the median does, and the reason is the same. Going to larger semi-major axes, in both models we see an increasing number of late injections, although for different reasons, and these determine the behaviour of most statistical parameters, causing them to decrease less rapidly than the T_g line.

In summary we can state that we have found the theoretical time scales of Duncan et al. (1987) to give a rather poor representation of our statistics of injection times. On the other hand, we find evidence in the combined model for an important role being played by the repopulation of tidal infeed trajectories via stellar encounters—something that may be described as a synergy effect. This being said, one nonetheless realizes that T_r is one of the basic time scales that govern this synergetic injection, the other one being the angular momentum reshuffling time scale of stellar perturbations. Let us now move to a discussion of the rate of injections and how this depends on time.

4 Time dependent injection flux

The upper part of Fig. 2 shows a histogram plot of the number of comets injected into the observable region as a function of time from the beginning till the end of the simulation. Three histograms are shown together: the one in black corresponds to a model with only Galactic tides, and the grey one to a model including only stellar perturbations. Finally, the top, white histogram is for the combined model that includes both tides and stars.

The first thing to note is the gradual decline of the injection flux of the tides-only model over a few Gyr, after which it stays at a very low level. The reason is clear. In the beginning, the phase space trajectories that in the regular dynamics imposed by the vertical tide will periodically lead into the "loss cone" ($q < 15$ AU) are populated just as densely as any phase space domain and thus furnish an important flux of injections during the first period of (e, i_G) oscillations. This amounts to a typical time scale of < 1 Gyr for much of the initial cloud, but the population on these trajectories is depleted by each entry into the loss cone, and there is no efficient way to replenish them without including stellar passages. On the longer time scale, we see only the feeble flux coming from (1) the infeed into the tidal injection trajectories by the non-integrable part of the tide; (2) the inner parts of the cloud, where the period of oscillation is very long (Fouchard et al. 2006).

The other two histograms include the effects of stellar passages, and the stars are the same in both simulations. Therefore, we see the same comet showers appearing and the same quasi-quiescent periods in between. The white area at the top of each bin corresponds to the extra contribution of the combined model as compared with that of the stars only. If the numbers plotted in the white, grey and black histograms are called N_C, N_S and N_G, respectively, we can define $\Delta N_C = N_C - N_S - N_G$ as an absolute measure of this extra contribution.[1] Already at first glance, looking at the later part of the simulation, we see that this is very significant. In the two lower panels of the figure, we plot histograms of ΔN_C and $\tau = \Delta N_C/(N_S + N_G)$, i.e., the extra contribution expressed as a fraction of $N_S + N_G$.

The basic observations are as follows. The spiky nature of the grey histogram is due to comet showers caused by close stellar encounters (we will briefly treat these below). While during the first Gyr the level of N_G is generally higher than that of N_S, this situation gets reversed after more than 2 Gyr. Even outside the main showers, N_S is then at a somewhat higher level than N_G. The white histogram, showing N_C, shares the spikes of the strongest showers, but the contrast between the spikes and the background is less than in the grey histogram. Indeed, the ΔN_C histogram shows no spikes at all, and the general level does not seem to correlate with the stellar injection rate, as illustrated by Fig. 3. Therefore, during the later part of the simulation, the τ parameter shows fluctuations anticorrelated with those of N_S. It reaches a few hundred percent, when N_S drops to its lowest levels, but sometimes decreases to nearly zero during the peaks of N_S.

In order to smooth out those fluctuations we present in Table 2 time averages of τ over 1 Gyr periods along with the corresponding integrals of N_C, N_S and N_G. During the first Gyr the flux of the combined model is not much larger than the sum of the two fluxes with separate effects, and the difference is just a small fraction of the total flux. But toward the end the synergy effect of the combined model, as measured by ΔN_C, has grown—on the average—to nearly the same level as $N_S + N_G$. During the last Gyr we find that $\langle N_C \rangle$ is about 2.5 times larger than $\langle N_S \rangle$ in fair agreement with earlier estimates by Heisler et al. (1987) and Heisler (1990). After an initial, relatively fast decrease due to the emptying of the tidal infeed trajectories, $\langle N_C \rangle$ continues to decrease approximately in proportion to the total number of Oort Cloud comets (N_{OC}), and $\langle N_S \rangle$ and $\langle N_G \rangle$ show similar behaviours.

Looking in detail at the ΔN_C and τ histograms in Fig. 2 for the beginning of our simulation, we see that they start from negative values and turn into positive ones after ~0.5 Gyr. Thus, in the very beginning, the sum of the separate fluxes is larger than the combined flux. This phenomenon was found by Matese and Lissauer (2002), whose calculations were limited

---

[1] Towards the end of our simulation the number of Oort Cloud comets has decreased in all three models but most in the combined one. We then have about 930 000, 840 000 and 760 000 comets in the tides-only, stars-only and combined models, respectively. This means that ΔN_C actually underestimates the extra contribution of the combined model.

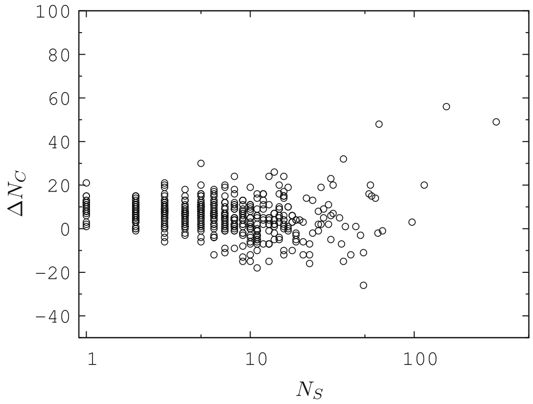

Fig. 3 ΔN_C versus N_S (plotted on a log scale), where the numbers refer to injections of comets into the observable region during intervals of 10 Myr

Table 2 Number of comets entering the observable region during periods of 1 Gyr

Model	[0–1] Gyr	[1–2] Gyr	[2–3] Gyr	[3–4] Gyr	[4–5] Gyr
G	2 128	797	481	307	248
S	1 425	1 555	1 030	717	511
C	3 618	3 141	2,412	1 733	1 274
$\langle\tau\rangle$	1.8%	33.6%	59.6%	69.2%	67.9%

Model G corresponds to the Galactic tide alone, S to passing stars alone, and C to Galactic tide and passing stars together. $\langle\tau\rangle$ is the increment from the sum of the two first rows (Galactic tide plus passing stars separately) to the third row (Galactic tide and passing stars together)

to only 5 Myr, and as they explained, it is typical of a situation where both tides and stars individually are able to fill the loss cone to a high degree. We will discuss this point again in Sect. 5.

The large amount of synergy ($\tau \sim 70\%$) seen in the later part of our simulation is remarkable and indicates that both the tides and the stars on their own are seriously inefficient in filling the loss cone. It is only by means of the synergy of both effects that we are able to explain an important degree of loss cone filling at the current epoch. We will look at this closer in Sect. 5 by separating the injection flux into different ranges of semi-major axis. For the moment we emphasize that *treating comet injections from the Oort Cloud in the contemporary Solar System simply as a result of the Galactic tide is not a viable idea*.

Already in Sect. 3 we identified a mechanism that offers a likely explanation of the synergy effect, i.e., the repopulation of tidal infeed trajectories via stellar encounters. But note in Fig. 2 that the initial flux of the model with tides only is not matched by the white areas in the later part of the simulation. Thus, even though there is an ongoing replenishment of the tidal infeed trajectories due to the randomizing effect of stellar encounters, this replenishment is not complete. *The critical trajectories remain largely depleted, and models that do not take this fact into account will overestimate the tidal contribution to the injection flux, as well as the efficiency of tides in filling the loss cone.*

The most important synergy mechanism of the Galactic tide and stellar perturbations is that the latter are able to repopulate the critical phase space trajectories that in the quasi-regular dynamics imposed by the tide lead into the loss cone (Dybczyński 2002; Fernández 2005). Our results appear to verify and quantify this picture. But in addition we see hints that a different effect is also at work. In Sect. 5 we will show that the distribution of $1/a$

of newly injected, observable comets—even during the typical, quiescent periods—has a significant extension inside the limit (at $a \simeq 3 \times 10^4$ AU), where the tide becomes able to feed comets from outside the loss cone into observable orbits. Our explanation for this effect is as follows.

In qualitative terms, when the Galactic tide is in the process of injecting a comet into the observable region from the region outside the loss cone, and stellar perturbations are added, the latter will sometimes aid in decreasing the perihelion distance of the comet ($\Delta q_* < 0$), and sometimes they will counteract the tide ($\Delta q_* > 0$). To first order, the two effects will cancel. But if we consider how much the critical value ($1/a_c$) of the inverse semi-major axis for tidal injection into the observable region ($a_c \simeq 3 \times 10^4$ AU) is decreased by a typical positive Δq_* or increased by the same typical value of Δq_* in the negative direction, we find that the latter effect dominates. Thus, a negative Δq_* causes a larger gain of comets with $a < a_c$ than the loss of comets with $a > a_c$ caused by a positive Δq_* of the same size. This holds for any nearly uniform distribution of $1/a$ in the Oort Cloud.

In mathematical terms, consider the expression for the maximum possible decrease of q in one revolution due to the Galactic tide:

$$\Delta q = -Sq^{1/2}z^{-7/2} \tag{2}$$

where $z = 1/a$ and $S = 2.8 \times 10^{-15}$ (Byl 1986), counting q and a in AU. This would hold for a Galactic latitude of perihelion of ±45°. We take this favourable orbital orientation as an example, but the following arguments apply for any other orientation as well.

Next, consider a particular value (q_p) of the perihelion distance preceding the injection into an observable orbit. Using Eq. 2, one can write down an approximate condition for the critical value $z = z_0$ in order to bring the comet into the observable region ($q < q_\ell = 5$ AU):

$$q_p = q_\ell + Sq_p^{1/2}z_0^{-7/2} \tag{3}$$

Equation 3 defines a unique relation between q_p and z_0, and by differentiating one easily finds that q_p decreases monotonously with z_0, while the second derivative is always positive.

Considering thus an arbitrary point (z_0, q_p) satisfying Eq. 3, we may introduce stellar perturbations by adding a term $-\Delta q_*$ to the right-hand member of Eq. 3, and we can write:

$$q_p = q_\ell + Sq_p^{1/2}z_1^{-7/2} - \Delta q_* \tag{4}$$

where z_1 is the new critical value of z. Hence, ($z_1, q_p + \Delta q_*$) also satisfies Eq. 3. Without the stellar perturbation all comets with $q = q_p$ and $z < z_0$ are injected into $q < q_\ell$, and including the stellar perturbation, the condition changes into $z < z_1$. From the negative slope of the $q_p(z_0)$ relation it is obvious that a negative value of Δq_* yields $z_{1+} > z_0$, and the same positive value yields $z_{1-} < z_0$. It is also obvious from the positive curvature of the graph that $z_{1+} - z_0 > z_0 - z_{1-}$. If $|\Delta q_*|$ is very small, this difference is negligible, but if it is large enough to compete with $|\Delta q_G|$, the effect will be important. The latter is indeed often the case, when we discuss injections from just outside the loss cone ($q_p \simeq 15$ AU), as has been shown, e.g., by Duncan et al. (1987) and Fernández (2005). Therefore, the gain of comets with $z > z_0$ occurs over a larger interval than the loss with $z < z_0$ for a symmetric distribution of stellar perturbations.

Another issue is the distribution function of z for the Oort Cloud. Our simulations start with a probability density $f(z) \propto z^{-1/2}$ as appropriate for an Oort Cloud formed according to the model of Duncan et al. (1987). In such a situation there would be more comets per unit interval of z at $z < z_0$ than at $z > z_0$, and the gain effect would be counteracted and possibly turned into a net loss of injected comets.

However, an interesting result of our simulations is that the gradual loss of comets from the Oort Cloud changes the distribution of $1/a$. In agreement with a recent study by Brasser et al. (2008), we find that the loss of comets from the outer parts of the cloud is not compensated by diffusion from the inner parts, so that after 4.5 Gyr, when the number of comets has decreased from 1×10^6 to 7.6×10^5, $f(z)$ has become roughly flat over the range from $a = 20\,000$ to 100 000 AU. This shows that we have to expect a net gain of newly injected, observable comets resulting from a synergy of Δq_G and Δq_*. Moreover, there should be a shift of comets from outside to inside the tidal injection limit—probably explaining why we see a significant flux of new comets all the way down to $a \simeq 20\,000$ AU.

Although we cannot provide exact numbers, it appears that the secondary synergy mechanism due to what we may call "constructive interference" of the two effects—even though it certainly exists—is not the dominating one. The tentative evidence comes from the relative smoothness of the ΔN_C histogram (Fig. 2) and the lack of correlation between ΔN_C and N_S (Fig. 3). These properties are expected of the repopulation of tidal infeed trajectories because of the long response time ($\sim$ several 10^8 years) for tidal infeed on the T_r time scale (Fig. 1). But if the constructive interference had been very important, we would have expected ΔN_C to increase immediately upon an increase of N_S—with the caveat that visible peaks of our N_S histogram might arise primarily from a temporary infeed of inner Oort Cloud comets with $z >> z_o$, which do not contribute to the interference. Further detailed studies are needed to clarify this issue.

The cometary showers, displayed in Fig. 4 by means of a histogram of the injection flux of the combined model with a bin width of only 10 Myr, are seen to be quite important for the injection of comets from the Oort Cloud, as expected and as found by other authors previously (e.g., Heisler et al. 1987). We are saving a detailed analysis of those for a later paper. At present, we can only remark that the results presented here are hard to compare with the treatments of cometary showers by Heisler et al. (1987) or Heisler (1990). The first of these papers treated only comets with $a = 10\,000$ or 20 000 AU with a full dynamical model and then only for a time interval of less than 200 Myr. The second gave only a brief account of a simulation for 4.5 Gyr and then only for injections from $q > 10$ to $q < 10$ AU instead of our requirement that the perihelion has to fall substantially from $q > 15$ to $q < 5$ AU.

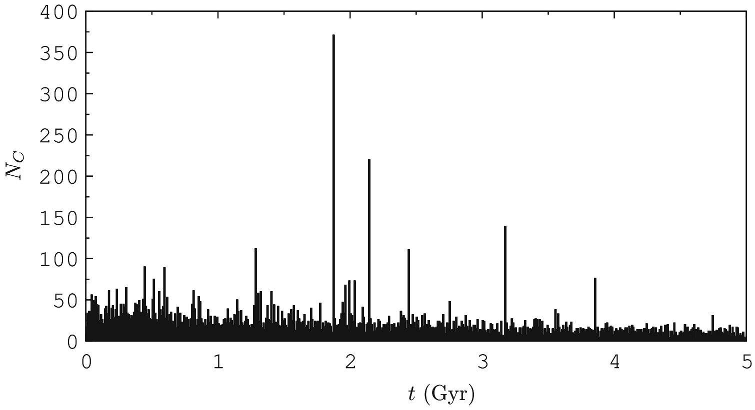

Fig. 4 Same as Fig. 2 (upper panel), but versus time per 10 Myr for the combined model only

5 Orbital element distributions of observable comets

Figure 5 shows the distributions of the opposite of the inverse semi-major axis ($-1/a$) and the sine of the Galactic latitude of perihelion (for clarity we use the absolute value $|\sin b|$) of the comets entering the observable region, i.e., heliocentric distance smaller than 5 AU, during a typical 170 Myr interval near the end of our simulation, where no strong comet showers are registered. We show an average of three such periods, i.e., 4.38–4.55 Gyr, 4.55–4.72 Gyr and 4.80–4.97 Gyr. In fact, comparing the three data sets, we find a rather good agreement, so that tentatively, the expected error of the mean is not very large. Three histograms are shown for each quantity: the one in black is for the model with Galactic tides only, the grey one is for the model with only stellar perturbations, and the white one shows the combined model.

After more than 4 Gyr the Galactic tides alone are practically only able to inject comets into the observable region if $a > 50\,000$ AU, so that the non-integrable part of the tides may provide new comets into the emptied infeed trajectories of the vertical component. Thus the feeble flux of new observable comets is strictly confined to the outermost parts of the Oort Cloud. If only the stellar perturbations are at work, the injected comets are almost as few as in the case of the Galactic tides. However, the distribution of $-1/a$ shows that the stellar perturbations are relatively efficient injectors of comets with semi-major axes in the whole range from 25 000 to more than 100 000 AU, and there is some marginal infeed all the way into the inner core. Note that this concerns a time interval without any strong comet showers.

When both the processes are at work, the number of comets entering the observable zone is 206, about 86% more than the sum of the two separate contributions (39 + 72). This estimate of τ is a bit higher than for the entire 1 Gyr interval, listed in Table 2, because the three intervals have been selected as particularly calm, avoiding even the smaller peaks of N_S that can be seen in Fig. 2. We have shown above that larger values of N_S lead to smaller values of τ. The distribution of $-1/a$ is as wide as for the stellar perturbations alone. However, the picture has changed, since the additional 86% of the comets are strongly concentrated to the

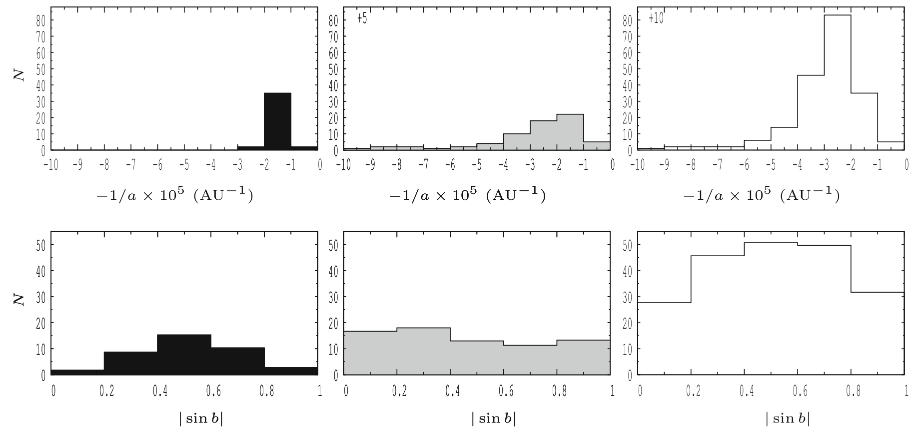

Fig. 5 Distributions of $-1/a$, where a is the semi-major axis (top panels) and $|\sin b|$, where b is the Galactic latitude of perihelion (bottom panels), for the comets entering the observable region during 170 Myr near the end of the simulation. When present, numbers in the top-left corners of $-1/a$ distribution panels correspond to comets with $-1/a < -1 \times 10^{-4}$ AU^{-1}. The left column corresponds to the model with Galactic tide alone, the middle column to passing stars alone, and the right column to the model with both effects

interval from -4×10^{-5} to -2×10^{-5} AU^{-1} ($25\,000 < a < 50\,000$ AU). The local values of ΔN_C for the five $1/a$ intervals (0–1), (1–2), (2–3), (3–4) and (4–5) $\times 10^{-5}$ AU^{-1} are -2, -22, $+63$, $+36$ and $+10$, respectively. We will comment on the negative values of the first entries in connection with Fig. 7.

We see that the mechanism of synergy that increases the flux of injections in the combined model prefers the range of semi-major axis ($a > 30\,000$ AU) where the vertical Galactic tide is able to provide the injections, once the relevant trajectories are populated. But there is an important extension of the synergy to smaller semi-major axes as well, extending at least to $a \simeq 20\,000$ AU. We conclude that both the above-described synergy mechanisms must be at work. The repopulation mechanism is obviously important, but the shift to smaller semi-major axes can only be explained by the ‘constructive interference’ mechanism.

Looking at the distributions of $|\sin b|$, indeed the signature of the Galactic tide is clearly present in the left diagram and absent in the middle one. However, it appears again to some extent in the right-hand diagram, where the combined model is presented. Thus we have evidence that the synergetic injection of comets in the combined model carries an imprint in the latitudes of perihelia similar to that of the Galactic tide, though the feature is strongly subdued. In fact, while the subdued tidal imprint is consistent with an important role being played by the ‘constructive interference’ synergy mechanism, our combined model does not appear to reproduce the observed $|\sin b|$ distribution of new Oort Cloud comets. An in-depth study of this problem and a consideration of ways out of this possible dilemma are deferred to future papers.

The shaping of the b distribution by the Galactic tide was first simulated numerically for a realistic Oort Cloud model by Matese and Whitman (1989). However, the left panels of Fig. 5 show a behaviour that is in stark contrast to their results. Practically all our tidal injections occur for $a > 50\,000$ AU, where Matese and Whitman (1989) found no tidal imprint in the b distribution because of complete loss cone filling independent of b. In the light of our results this can be seen as an artefact of their assumption of complete randomization of the Oort Cloud orbit distribution. Indeed, as we shall find below (Table 4), the tidal loss cone filling for $50\,000 < a < 100\,000$ AU towards the end of our simulation is far from complete, and therefore we see the imprint of the tide in our b distribution.

In Fig. 6 we show the corresponding distribution of $-1/a$ and $|\sin b|$ for the 10 Myr interval from 3.85 to 3.86 Gyr, where Fig. 4 shows that the number of observable comets has a high peak due to a moderately strong shower. Occurring near the middle of the period, this shower dominates the time-integrated injection rate. The trigger is a M5 star with an impact parameter $d \simeq 2\,000$ AU and a velocity $v_\star \simeq 18$ km/s.

The mid and right-hand $-1/a$ distributions show that, as soon as stars are involved, the injection of comets now extends over the whole cloud, including an important fraction from the inner core with $a < 10\,000$ AU. In fact, the synergy effect is now very strong in the range from 10 000 to 20 000 AU, amounting to $\tau > 150\%$. This is unexpected on the basis of both the above-mentioned mechanisms, since we are discussing orbits too far inside the tidal injection limit. We are instead led to hypothesize a different mechanism. In the present case we are comparing the number of comets injected by a particular, deeply penetrating star from the mentioned range of semi-major axes in the stars-only versus the combined model. In the absence of the Galactic tides it is likely that orbits with perihelia close to but outside the loss cone have been depleted by the preceding cometary showers, while in the combined model the disk tide provides a regular transfer of comets into this zone on a Gyr time scale, thus compensating for the losses. This means that the synergy works in the opposite sense compared to the normal situation outside the showers. *During a shower the tides are providing the material for injections by the stars, while in the normal situation the stars are*

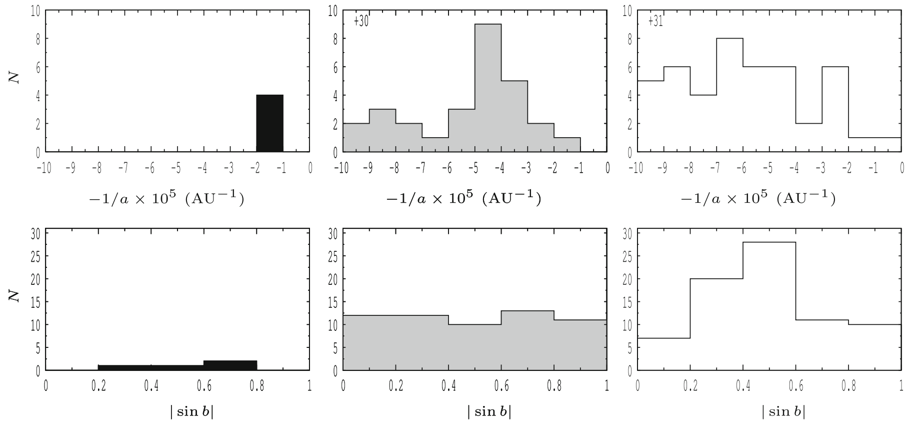

Fig. 6 Same as Fig. 5 but considering the comets that enter the observable region during a shower between 3.85 and 3.86 Gyr. The shower is due to a M5 star with impact parameter 2,055 AU, velocity 17.7 km/s and mass 0.21 $M_\odot$

providing the material for tidal injections. The absence of a synergy in the inner core may be explained by the very long time scale for tidal torquing, or by a smaller degree of depletion of the source region for stellar injections.

Naturally, in the stars-only model the shower does not carry any signature in the distribution of $|\sin b|$. The combined model does not exhibit any significant signature either, but there may nonetheless be a slight tendency. In case this is real, it might possibly reveal a somewhat more efficient synergy in the 10 000–20 000 AU range for the orbits experiencing a faster tidal decrease of q.

Let us now consider the situation at the beginning of the simulation, before the tides have had the time to completely empty the tidal infeed trajectories in the outer part of the cloud. The results are shown in Fig. 7 for a period between 0.63 and 0.80 Gyr, when no strong showers are noted. The number of comets entering into the observable region is 282, 128 and 463 for the tides, the stars, and the combined model, respectively. The action of the tides is still quite strong, since the infeed trajectories in the interval $20\,000 < a < 50\,000$ AU are not yet severely depleted (cf. Fig. 1). Therefore the net synergy effect amounts to only 13%.

The local ΔN_C values for the same five $1/a$ intervals as we discussed in connection with Fig. 5 are in this case −5, −66, +35, +61 and +19. We do not see any significant synergy effect for more tightly bound orbits. The distribution of positive synergy over the 2–5×10^{-5} AU^{-1} range is similar to that of Fig. 5, and our conclusions about the relevance of the two mechanisms are the same. Note that in both cases we see negative ΔN_C values in the two outermost $1/a$ ranges (0–2×10^{-5} AU^{-1}). The fundamental reason is the one discussed above in order to explain the negative τ values in the very beginning of the simulation, i.e., a saturation effect of the loss cone when both injection effects individually are able to cause a large degree of filling. The distributions of $|\sin b|$ exhibit the same features as in Fig. 5 and lead to the same conclusion: when both tides and stars act in synergy, the signature of the Galactic tide may be seen but appears quite marginal.

Since we noted in Sect. 4 that the replenishment of the tidal infeed trajectories by stellar perturbations is not complete during the later part of our simulation, an obvious consequence is that the filling of the loss cone for the relevant semi-major axes cannot be complete either. To quantify this statement, we consider the rate of perihelion passages $\dot{n}$ with $q < q_0$ as

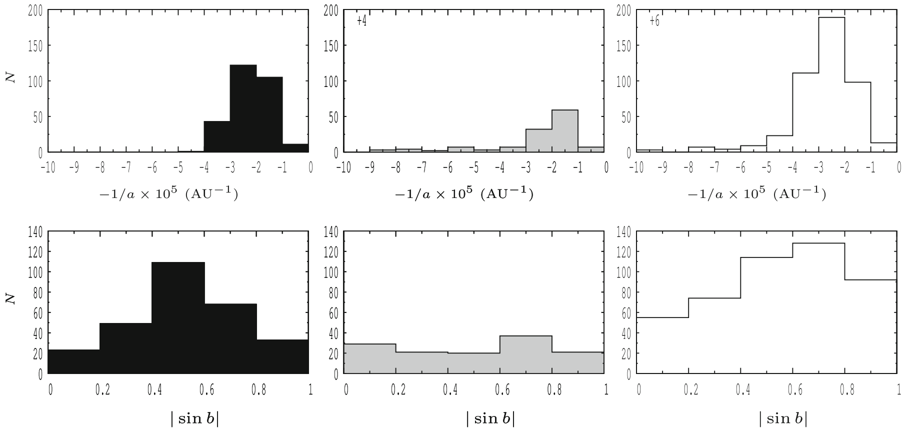

Fig. 7 Same as Fig. 5 but considering the comets entering the observable region during 170 Myr near the beginning of the simulation

a function of the semi-major axis, assuming complete loss cone filling and a completely thermalized Oort Cloud (Hills 1981; Bailey and Stagg 1988):

$$\dot{n}(a) = N_{\mathrm{OC}} \cdot f(a) \cdot \frac{2q_0}{a} \cdot a^{-3/2}. \tag{5}$$

Here, N_{OC} is the number of comets in the entire Oort Cloud (initially 10^6 in our model) and $f(a)$ the frequency function describing the distribution of semi-major axes: $f(a) \propto a^{-1.5}$ initially in our model.

We have computed injection rates in the combined model for the three time intervals of Figs. 5–7 using Eq. 5 and finding the integrals $\int N_{\mathrm{OC}} f(a) a^{-5/2} da$ over different ranges of $-1/a$ directly from the simulation output at neighbouring moments. The calculation of these integrals is done by simply adding the values of $a^{-5/2}$ of all the comets found in the relevant range. Multiplying by the length of each interval and putting $q_0 = 5$ AU, we find the numbers N_{comp} listed in Table 3.

The numbers of comet injections for each $1/a$ range and each time interval can be read off from the figures, and they are listed as N_{sim} in the table along with the ratios $N_{\mathrm{sim}}/N_{\mathrm{comp}}$, which give the filling factor of the observable part of the loss cone (f_{lc}). We find that this factor is close to 100% in the beginning of the simulation for $a > 50\,000$ AU and remains >80% for such semi-major axes even towards the end during quiescent periods. But the factor drops rapidly with decreasing a to values near 2% at $a \simeq 20\,000$ AU. These results may be compared with those of Heisler (1990), who used a similar procedure for deriving f_{lc}. She did not consider semi-major axes $a > 40\,000$ AU, and inside this limit we find somewhat smaller filling factors than she did, consistent with the fact that we use a lower value for the Galactic mid-plane density and somewhat higher stellar velocities.

Note that the filling factors have decreased somewhat, when we compare the final quiescent period with the initial one. Except in the outermost parts of the Oort Cloud, there is always a depletion of comets in the regions of phase space near the tidal infeed trajectories and in the vicinity of the loss cone, and this depletion grows slowly with time.

The numbers N_{sim} found for the shower period are too small to be statistically useful for the outer parts of the cloud, and the filling factors listed are very uncertain. However, we see an obvious effect in the inner parts, when comparing f_{lc} with the corresponding values of

Table 3 Numbers of comet injections during the time intervals of Figs. 5–7 for different ranges of inverse semi-major axis, as computed from Eq. 5 and found from our simulation of the combined model

$\Delta(1/a)$	Beginning			End, showers			End, quiescent		
$(10^{-5}\ \mathrm{AU}^{-1})$	N_{comp}	N_{sim}	f_{lc} (%)	N_{comp}	N_{sim}	f_{lc} (%)	N_{comp}	N_{sim}	f_{lc} (%)
(0–2)	106	111	~100	3.2	2	~60	48	40	83
(2–3)	303	189	62	10	6	~60	160	83	52
(3–4)	616	111	18	24	2	~8	367	46	13
(4–5)	1 044	23	2.2	44	6	14	692	14	2.0
(5–10)	15 600	23	0.15	740	29	3.9	12 100	13	0.11
>10	672 000	6	0.0009	37 200	31	0.08	626 000	10	0.0016

The ratio of simulated to computed number, expressed in percent, is also listed in each case

Table 4 Filling factors for the observable part of the loss cone, computed for different ranges of semi-major axis and separately for the three dynamical models (tides-only, stars-only, and combined)

$\Delta(1/a)$	f_{lc} (Beginning)			f_{lc} (End)		
$(10^{-5}\ \mathrm{AU}^{-1})$	Tidal (%)	Stellar (%)	Combined (%)	Tidal (%)	Stellar (%)	Combined (%)
(0–1)	~400	~100	~200	~100	~100	~100
(1–2)	86	60	~100	30	45	78
(2–3)	36	10	62	0.6	10	52
(3–4)	6.5	1.1	18	–	2.3	13
(4–5)	0.09	0.3	2.2	–	0.5	2.0
(5–10)	–	0.1	0.15	–	0.06	0.11
>10	–	0.0006	0.0009	–	0.0008	0.0016

quiescent periods. The shower increases f_{lc} by factors ~20–100, and thus the overall flux exhibits the peak seen in Fig. 4 due to comets with $a < 20\,000$ AU.

We have already made the remark that neither ΔN_C nor τ provides a fully satisfactory measure of the synergy effect, because they do not account for the difference of the number of Oort Cloud comets between different dynamical models—especially towards the end of the simulation. After 5 Gyr the total number of comets in the combined model is only ~80% of that in the tides-only model, and if we concentrate on comets with $50\,000 < a < 100\,000$ AU where the losses are the largest, the ratio of the two models is only 35%. In order to compensate for such effects we have computed the f_{lc} parameter separately for the three models and for all the ranges of $1/a$, and we present the results in Table 4. The time periods referred to are the quiescent periods of Figs. 5 and 7.

The outermost energy range is empty in all models, when the simulation starts, but it gets populated quickly—at least when stars are involved. We interpret the very large value of f_{lc} in the tides-only model at the beginning as evidence that the radial tide has not extracted comets into this energy range in a uniform manner, so that our assumption of thermalization when deriving N_{comp} is not justified. To a lesser extent this appears to be true also in the combined model, where stars have extracted many more comets. It is likely that this extraction too—at the early time in question—has not populated all the angular momenta in a thermalized fashion. However, the statistics is too poor to be confident about such conclusions. In any case, the loss cone filling is extremely efficient for all models, thus explaining the negative values of ΔN_C.

For the next energy range we see the saturation effect again, especially in the beginning. At the end, the value of f_{lc} in the combined model is close to the sum of those in the other two models. Hence there is no apparent synergy in this case, but probably a real synergy has been concealed by the saturation effect. In any case the large negative value of ΔN_C results entirely from the small number of comets in the combined model, as discussed above. In the next three energy ranges ($20\,000 < a < 50\,000$ AU) we see that f_{lc} in the combined model is much larger than the sum of the two other entries, and for $a < 20\,000$ AU the effect continues: adding the tides to the stars increases the loss cone filling by a factor 1.5–2.

6 Discussion and conclusions

We have simulated the evolution of the Oort Cloud over 5 Gyr, using for initial conditions a relaxed model with a distribution of semi-major axis $f(a) \propto a^{-1.5}$ within the interval 3 000–100 000 AU. This model is based on the results of simulation of Oort Cloud formation and evolution by Duncan et al. (1987). However, we do not find this to be a steady distribution. More comets are lost from the outer parts of the cloud than can be replaced from inside, so that our model cloud evolves into a distribution close to $f(a) \propto a^{-2}$—i.e., flat in $1/a$.

Our dynamical model has two main limitations. We do not treat encounters with very massive Galactic perturbers, such as star clusters or Giant Molecular Cloud complexes, the justification being that they occur so rarely that the current Solar System is unlikely to feel the direct reverberations of any such encounter, and that even if they modify the structure of the Oort Cloud, our interest is not primarily in its dynamical history but rather in the way stars and Galactic tides currently interact when injecting observable comets.

Moreover, we do not treat planetary perturbations in any direct manner. Like most previous investigators (e.g., Heisler 1990) we use a loss cone defined by a limiting perihelion distance (in our case, 15 AU) outside which no planetary effects are included and inside which all comets are considered lost from the cloud through perturbations by Jupiter and Saturn. In terms of "transparency" of the planetary system (Dybczyński and Prętka 1997; Dybczyński 2005), our model is completely opaque ($P = 1$). This means that we are limiting our attention to a subset of the observed population of "new" Oort Cloud comets, i.e., those that have jumped directly from $q > 15$ AU into their observed orbits with $q < 5$ AU. We are neglecting the rest of the population, which consists of comets that passed perihelia in the outer part of the loss cone without being perturbed away before arriving into observable orbits. We are also neglecting a possible contribution to the observed new comets by a "leakage" from the scattered disk (Levison et al. 2006). Therefore we prefer not to draw any conclusions in this paper regarding the total number of Oort Cloud comets or the exact values of the filling factors. Nor do we claim to make any prediction on the detailed shape of the $1/a$ distribution of new Oort Cloud comets, until we have included the planetary perturbations in a realistic manner.

We have shown that the concept of tidal and stellar torquing time scales (Duncan et al. 1987) gives a very incomplete picture of the speed of comet injection, whether it may concern Galactic tides or stellar encounters. The distribution of injection times is largely shaped by other effects—like comet showers or the repopulation of the emptied infeed trajectories of the disk tide due to the non-integrable part of the tides or stellar perturbations.

We have also shown how—for semi-major axes large enough for the tide to populate observable orbits—the regions of the phase space occupied by trajectories leading into the loss cone get depleted during the first Gyr of Oort Cloud evolution. This would leave little chance for the tide to produce a significant number of observable comets at the current time, were it not for the capability of stellar perturbations to replenish the tidal infeed trajectories.

We have indeed demonstrated that, during the later parts of our simulation, there is a very important synergy effect of the Galactic tide and stellar perturbations such that the combined injection rate is on the average ~70% larger than that of the stars alone plus that of the tide alone. This synergy is strongest for semi-major axes between ~20 000 and 50 000 AU but continues all the way into the inner core. During comet showers the synergy effect in the outer parts of the cloud practically disappears, but the one affecting the inner parts becomes very important.

We have identified two mechanisms for the synergy during quiescent periods in the outer parts of the Oort Cloud. One is that the stellar perturbations provide a supply of new comets that replenishes the depleted tidal infeed trajectories, and the other is that the gain of comet injections, when stellar perturbations decrease the perihelion distance, dominates over the loss caused by opposing perturbations. For the synergy of the inner cloud we hypothesize that the Galactic tides provide the material for stellar injections by slowly feeding the region of phase space in the vicinity of the loss cone. Thus, the general picture spawned by our results is that injection of comets from the Oort Cloud is essentially to be seen as a team work involving both tides and stars. It appears meaningless to rank the two effects in terms of strength or efficiency.

Indeed, for the smaller semi-major axes the Galactic tide does not dominate the injection of comets, contrary to the conclusions of Heisler et al. (1987) and Heisler (1990).[2] It only contributes to a synergy with stellar perturbations, and without the stars one would not have any injections of comets with $a \lesssim 20\,000$ AU.

The distribution of Galactic latitudes of perihelia of the observable comets exhibits a maximum for $|\sin b| \simeq 0.5$ as expected in the tides-only model, but in the combined model this feature can hardly be seen at all. The tides form part of the synergetic injection, but their imprint is largely washed out by the stellar contribution. But, likely due to the role of the tides in helping the stars to create comet showers, the pattern can be seen at least as clearly during a shower as during the quiescent periods. Therefore, it tentatively appears that the shape of the observed b distribution can not be used to indicate whether we are experiencing any shower at present. However, since none of our model distributions appears to agree with the observed one, we have to defer any conclusions to future papers. It may be interesting to see, for instance, if the leakage from the scattered disk into the Oort Cloud with an ensuing direct transfer into observable new comets may alleviate the problem.

We have measured the filling of the observable part of the loss cone by comparing our simulated injection rates for different intervals of semi-major axis with the rates of observable perihelion passages ($q < 5$ AU) computed for a completely thermalized distribution of cometary orbits involving a filled loss cone. The deficiency of our simulated rate likely reflects not only a lack of comets in the loss cone but a general depletion in a wider phase space region in its vicinity, as remarked by Heisler (1990). Our results can be compared with hers, and in contrast to her inference that f_{lc} may level out at ~60% for $a \gtrsim 30\,000$ AU, we find an average filling factor during quiescent periods in the current Solar System, which drops steadily from ~100% at $a > 100\,000$ AU to 1% or less at $a < 20\,000$ AU in the combined model. However, there are important differences between the two investigations, one being that she simulated a much shorter time period than we do, and in addition our parameters for the Galactic tides and stellar encounters also differ from hers.

---

[2] The main reason for this discrepancy is that the Heisler papers considered injections into the loss cone—mainly by slight perturbations of q across the limiting value $q_c = 10$ AU—while we consider large jumps from $q > 15$ AU into the observable region with $q < 5$ AU. Interestingly, Heisler et al. (1991) commented that the injection into orbits with $a \lesssim 20\,000$ AU and $q < 2$ AU is indeed dominated by stellar perturbations.

In agreement with Weissman and Hut (1986), we find that cometary showers do not significantly increase the loss cone filling at large semi-major axes. However, near 25 000 AU there is an abrupt change into the regime of the inner cloud, where the filling factor increases by orders of magnitude during moderate to strong events. The showers of course involve direct injections by the passing stars, but the synergy with the Galactic tide is as important as during quiescent periods.

Acknowledgements We are greatly indebted to the referees of this paper, Ramon Brasser and Julio A. Fernández, for having pointed out various weaknesses in a previous version, which inspired us to exert more care in all parts of our analysis. M.F. is grateful to GDRE 224 CNRS INdAM, GREFI-MEFI and Ch. F. to the plan National de Planétologie (PNP) for financial support. For H.R., this work was supported by Grants nr. 78/06 and 119/07:1 of the Swedish National Space Board. The work of G.B.V. was supported by the contract ASI/INAF I/015/07/0.

References

Allen, C.: Astrophysical Quantities, 3rd edn. Athlone Press, London (1985)

Bahcall, J.N.: Self-consistent determinations of the total amount of matter near the sun. Astrophys. J. **276**, 169–181 (1984)

Bailey, M.E., Stagg, C.R.: Cratering constraints on the inner Oort cloud—steady-state models. Mon. Not. R. Astron. Soc. **235**, 1–32 (1988)

Brasser, R., Duncan, M.J., Levison, H.F.: Embedded star clusters and the formation of the Oort Cloud III: the Galactic phase. Icarus (in press) (2008)

Breiter, S., Fouchard, M., Ratajczak, R., Borczyk, W.: Two fast integrators for the Galactic tide effects in the Oort cloud. MNRAS **377**, 1151–1162 (2007)

Byl, J.: The effect of the Galaxy on cometary orbits. Earth Moon Planets **36**, 263–273 (1986)

Charnoz, S., Morbidelli, A.: Coupling dynamical and collisional evolution of small bodies II. Forming the Kuiper belt, the scattered disk and the Oort cloud. Icarus **188**, 468–480 (2007)

Delsemme, A.H.: Galactic tides affect the Oort cloud—an observational confirmation. Astron. Astrophys. **187**, 913–918 (1987)

Duncan, M., Quinn, T., Tremaine, S.: The formation and extent of the solar system comet cloud. Astron. J. **94**, 1330–1338 (1987)

Dybczyński, P.A.: Simulating observable comets. I. The effects of a single stellar passage through or near the Oort cometary cloud. Astron. Astrophys. **396**, 283–292 (2002)

Dybczyński, P.A.: Simulating observable comets. II. Simultaneous stellar and galactic action. Astron. Astrophys. **441**, 783–790 (2005)

Dybczyński, P.A., Prętka, H.: The galactic disk tidal force: simulating the observed Oort cloud comets. In: Wytrzyszczak, I.M., Lieske, J.H., Feldman, R.A. (eds.) IAU Colloq. 165: Dynamics and Astrometry of Natural and Artificial Celestial Bodies, pp. 149–154. Kluwer, Dordrecht (1997)

Emel'yanenko, V.V., Asher, D.J., Bailey, M.E.: The fundamental role of the Oort cloud in determining the flux of comets through the planetary system. Mon. Not. R. Astron. Soc. **381**, 779–789 (2007)

Everhart, E.: An efficient integrator that uses Gauss-Radau spacings. In: Carusi, A., Valsecchi, G.B. (eds.) ASSL Vol. 115: IAU Colloq. 83: Dynamics of Comets: Their Origin and Evolution, pp. 185–202. Reidel, Dordrecht (1985)

Fernández, J.A.: Evolution of comet orbits under the perturbing influence of the giant planets and nearby stars. Icarus **42**, 406–421 (1980)

Fernández, J.A. (ed.): Comets—Nature, Dynamics, Origin and their Cosmological Relevance. Astrophysics and Space Science Library, vol. 328. Springer, Dordrecht (2005)

Fouchard, M., Froeschlé, Ch., Valsecchi, G., Rickman, H.: Long-term effects of the Galactic tide on cometary dynamics. Celest. Mech. Dyn. Astron. **95**, 299–326 (2006)

Fouchard, M., Froeschlé, Ch., Breiter, S., Ratajczak, R., Valsecchi, H., Rickman, G.: Methods to study the dynamics of the Oort cloud comets II: modelling the galactic tide. In: Benest, D., Froeschlé, C., Lega, E. (eds.) Topics in Gravitational Dynamics. Lecture Notes in Physics, vol. 729, pp. 273–296. Springer, Berlin (2007)

García-Sánchez, J., Weissman, P.R., Preston, R.A., Jones, D.L., Lestrade, J.-F., Latham, D.W., Stefanik, R.P., Paredes, J.M.: Stellar encounters with the solar system. Astron. Astrophys. **379**, 634–659 (2001)

Heisler, J.: Monte Carlo simulations of the Oort comet cloud. Icarus **88**, 104–121 (1990)

Heisler, J., Tremaine, S.: The influence of the galactic tidal field on the Oort comet cloud. Icarus **65**, 13–26 (1986)

Heisler, J., Tremaine, S., Alcock, C.: The frequency and intensity of comet showers from the Oort cloud. Icarus **70**, 269–288 (1987)

Heisler, J., Tremaine, S., Weissman, P., Greenberg, R: Sky distributions of Oort cloud comets during and outside of showers. Lunar and Planetary Institute Conference Abstracts, vol. 22, p. 553 (1991)

Hills, J.G.: Comet showers and the steady-state infall of comets from the Oort cloud. Astron. J. **86**, 1730–1740 (1981)

Holmberg, J., Flynn, C.: The local density of matter mapped by Hipparcos. Mon. Not. R. Astron. Soc. **313**, 209–216 (2000)

Hut, P., Tremaine, S.: Have interstellar clouds disrupted the Oort comet cloud?. Astron. J. **90**, 1548–1557 (1985)

Królikowska, M.: Non-gravitational effects in long-period comets and the size of the Oort cloud. Acta Astron. **56**, 385–412 (2006)

Laskar, J., Robutel, P.: High order symplectic integrators for perturbed Hamiltonian systems. Celest. Mech. Dyn. Astron. **80**, 39–62 (2001)

Levison, H.F., Dones, L., Duncan, M.J.: The origin of Halley-type comets: probing the inner Oort cloud. Astron. J. **121**, 2253–2267 (2001)

Levison, H.F., Duncan, M.J., Dones, L., Gladman, B.J.: The scattered disk as a source of Halley-type comets. Icarus **184**, 619–633 (2006)

Matese, J.J., Lissauer, J.J.: Characteristics and frequency of weak stellar impulses of the Oort cloud. Icarus **157**, 228–240 (2002)

Matese, J.J., Whitman, P.G.: The Galactic disk tidal field and the nonrandom distribution of observed Oort cloud comets. Icarus **82**, 389–401 (1989)

Mazeeva, O.A.: Dynamical evolution of Oort cloud comets to near-Earth space. In: Milani, A., Valsecchi, G., Vokrouhlický, D. (eds.) Near Earth Objects, our Celestial Neighbors: Opportunity and Risk. IAU Symposium, vol. 236, pp. 43–54 (2006)

Mihalas, D., Binney, J.: Galactic Astronomy: Structure and Kinematics. Freeman, San Francisco (1981)

Oort, J.H.: The structure of the cloud of comets surrounding the solar system and a hypothesis concerning its origin. Bull. Astron. Inst. Neth. **11**, 91–110 (1950)

Remy, F., Mignard, F.: Dynamical evolution of the Oort cloud. I—A Monte Carlo simulation. II—a theoretical approach. Icarus **63**, 1–30 (1985)

Rickman, H.: Stellar perturbations of orbits of long-period comets and their significance for cometary capture. Bull. Astron. Inst. Czech **27**, 92–105 (1976)

Rickman, H., Froeschlé, Ch., Froeschlé, Cl., Valsecchi, G.B.: Stellar perturbations on the scattered disk. Astron. Astrophys. **428**, 673–681 (2004)

Rickman, H., Fouchard, M., Valsecchi, G.B., Froeschlé, Ch.: Algorithms for stellar perturbation computations on Oort cloud comets. Earth Moon Planets **97**, 411–434 (2005)

Weissman, P.R.: Physical and dynamical evolution of long-period comets. In: Duncombe, R.L. (ed.) IAU Symp. 81 Dynamics of the Solar System, pp. 277–282. Reidel, Dordrecht (1979)

Weissman, P., Hut, P.: Dynamics of cometary showers. Lunar and Planetary Institute Conference Abstracts, vol. 17, pp. 935–936 (1986)

Icarus 214 (2011) 334–347

Contents lists available at ScienceDirect

Icarus

journal homepage: www.elsevier.com/locate/icarus

The key role of massive stars in Oort cloud comet dynamics

M. Fouchard [a,*], Ch. Froeschlé [b], H. Rickman [c,d], G.B. Valsecchi [e]

[a] LAL-IMCCE, Université de Lille 1, 1 Impasse de l'Observatoire, F-59000 Lille, France
[b] Observatoire de la Côte d'Azur, UMR 6202, Bv. de l'Observatoire, B.P. 4229, F-06304 Nice cedex 4, France
[c] PAS Space Research Center, Bartycka 18A, PL-00-716 Warszawa, Poland
[d] Dept. of Physics & Astronomy, Uppsala Univ., Box 516, SE-75120 Uppsala, Sweden
[e] IASF-Roma, INAF, via Fosso del Cavaliere 100, I-00133 Roma, Italy

ARTICLE INFO

Article history:
Received 15 January 2011
Revised 30 March 2011
Accepted 14 April 2011
Available online 23 April 2011

Keywords:
Comets, Dynamics
Comets, Origin

ABSTRACT

The effects of a sample of 1300 individual stellar encounters spanning a wide range of parameter values (mass, velocity and encounter distance) are investigated. Power law fits for the number of injected comets demonstrate the long range effect of massive stars, whereas light stars affect comets mainly along their tracks. Similarly, we show that the efficiency of a star to fill the phase space region of the Oort cloud where the Galactic tides are able to inject comets into the observable region – the so-called "tidally active zone" (TAZ) – is also strongly dependent on the stellar mass. Power laws similar to those for direct injection are obtained for the efficiency of stars to fill the TAZ. This filling of the tidally active zone is crucial for the long term flux of comets from the Oort cloud. Based on long-term Monte Carlo simulations using a constant Galactic tide and a constant flux of stellar encounters, but neglecting the detailed effects of planetary perturbations, we show that this flux essentially results from a two step mechanism: (i) the stellar injection of comets into the TAZ; and (ii) the tidal injection of TAZ comets into the loss cone. We find that single massive stars are able to induce "comet drizzles" – corresponding to an increase of the cometary flux of about 40% – which may last for more than 100 Myr by filling the TAZ to a higher degree than normal. It appears that the stars involved in this process are the same that cause comet showers.

1. Introduction

Long period comets are believed to come from a nearly spherical reservoir of comets – the so-called Oort cloud (Oort, 1950) – extending over roughly a hundred thousand astronomical units. According to Oort, due to perturbations by stars passing in the vicinity of the cloud, the perihelia of some comets in this distant region have been reduced enough for those comets to become observable. In fact, until the 1980s stellar perturbation was the unique mechanism considered to be able to inject comets from the Oort cloud into the inner Solar System (heliocentric distance $r < 5$ AU). At that time, the important role of the Galactic tides in making Oort cloud comets observable was established. Beginning with the work of Byl (1983), several studies (see Matese and Whitman, 1992; Wiegert and Tremaine, 1999, and references therein) have shown that the distribution of the observed Galactic latitudes of perihelia of new comets correlates with the action of the disc tide (*i.e.*, the tidal force caused by the variation of the Galactic gravitational potential with distance from the mid-plane). Based on this finding and the realization that, judged as a separate mechanism, the disc tide would be on average more efficient than stellar passages in providing new observable comets, stellar perturbations have later tended to be practically neglected as injection mechanism.

More recently, Matese and Lissauer (2002) studied the evolution of Oort cloud comets over a time scale of 5 Myr, suffering simultaneously the perturbations due to the Galactic tides and due to stellar impulses. They found that the sum of the separate injection rates of new comets is significantly larger than the combined rate, and they concluded that over this short time scale, both the Galactic tide and the stars are individually able to fill the loss cone efficiently.

In a previous paper (Rickman et al., 2008) – hereafter RFFV08 – we have also explored the dynamical evolution of Oort cloud comets, but over a time scale of 5 Gyr, including the action of both perturbers, *i.e.*, the stellar perturbations and the Galactic tides, simultaneously. Over the first 5 Myr we confirmed the result found by Matese and Lissauer. But over much longer time scales we found the situation to be reversed, the combined flux being larger than the sum of the separate fluxes. When both perturbers act together, a synergy is generated that significantly increases the flux of comets into the observable region (defined by $r < 5$ AU). According to RFFV08, one main reason for this synergy is that passing

---

[*] Corresponding author.

E-mail addresses: fouchard@imcce.fr (M. Fouchard), froesch@obs-nice.fr (Ch. Froeschlé), hans@fysast.uu.se (H. Rickman), giovanni@iasf-roma.inaf.it (G.B. Valsecchi).

0019-1035/$ - see front matter © 2011 Elsevier Inc. All rights reserved.
doi:10.1016/j.icarus.2011.04.012

stars cause a randomization of cometary orbital elements and consequently may send comets into orbits that are linked through the Galactic tides with the observable region.

An important finding was published by Kaib and Quinn (2009), dealing with the role of the giant planets in comet injection from the inner region of the Oort cloud (semi-major axis $a < 2 \times 10^4$ AU). They found that this region contributes to the flux of observable comets by means of the planets perturbing the semi-major axis into $a > 2 \times 10^4$ AU, while the perihelia stay at distances $q \sim 10$–15 AU, after which the Galactic tides may bring the perihelia below the limit of observability.

The main purpose of the present paper is to study the influence of stellar perturbations, according to their physical characteristics (stellar mass, velocity and impact parameter), on the efficiency of (i) direct injection of comets into the observable region, and (ii) filling of what we call the *tidally active zone* (see Section 3.3). In both cases special attention will be given to the role of stellar masses. In order to analyze the star-induced dynamics in a comprehensive way, our strategy is to proceed in steps. Therefore, in the present paper we limit ourselves to a simplified model (typical of all earlier works of ours), where the planets are assumed to perturb all comets with $q < 15$ AU away from the Oort cloud. A full description of the planetary perturbations, capturing the effects of the Kaib–Quinn mechanism, will be the subject of a forthcoming paper. We caution the reader that the results of the present paper are preliminary as far as the real Solar System is concerned, but they will form a necessary background in order to understand the outcome of the full model.

We begin by a brief description of our dynamical model in Section 2. The action of single stars is then studied in Section 3. The stellar samples and the initial conditions used for the Oort cloud are described in Section 3.1. The amount of direct injections of comets into the observable region, in dependence of the stellar encounter characteristics, is presented in Section 3.2. Using the definition of the tidally active zone (TAZ) as a function of the semi-major axis obtained in Section 3.3, the efficiency of single stars to fill the TAZ is evaluated in Section 3.4.

In Section 4 – like in RFFV08 – we perform three kinds of Monte Carlo simulations of Oort cloud evolution. Each simulation is named after the dynamical model used, *i.e.*, the perturbations considered. Model G is the simulation for which the Galactic tides provide the unique perturber. In Model S(all) the comets are perturbed only by passing stars whose masses span the whole range from 0.21 $M_\odot$ to 9 $M_\odot$, and in model C(all) the two perturbers (tides and stars) act together. In addition, two more sets of simulations are made. Here, rather than considering the whole range of stellar masses, we perform simulations like those of models S(all) and C(all), but considering two different subsamples of stars, one defined by masses $M_\star < 1.2\ M_\odot$ yielding models S(light) and C(light), and the other containing massive stars with $M_\star > 1.2\ M_\odot$ yielding models S(heavy) and C(heavy). Discussion and conclusions are given in Section 5.

2. Dynamical modelling

The Galactic tides and the stellar perturbations are modelled in the same way as in RFFV08. For the tides this means that we account for the full, non-averaged dynamics including both radial and vertical (disc) terms, using a local disc density of 0.1 $M_\odot$ pc^{-3} (Holmberg and Flynn, 2000) that characterizes the current solar neighbourhood. Our method of integration is a hybrid approach, described in Breiter et al. (2007), Fouchard et al. (2007). The stellar perturbations are treated by the sequential impulse approximation (Rickman et al., 2005), which builds on the improved impulse approximation by Dybczyński (1994). In the C models we use the tidal integrator, interrupting it at the predefined times of stellar encounters, when the computed heliocentric impulses are added to the cometary velocities. All the comets were integrated in parallel.

For a comparison of the model and parameters used in our simulations with those of earlier Oort cloud simulations, we refer to RFFV08.

3. Effects of individual stars

3.1. Stellar samples and initial conditions

As in RFFV08, we consider 13 types of stars (mostly represented by MK spectral classes), whose characteristics are listed in Table 1. The basic source for these data is García-Sánchez et al. (2001). For each type, we construct five sequences of 20 stellar encounters, occurring at intervals of 250 Myr during a 5 Gyr interval, the first encounter occurring 100 Myr after the beginning of the simulation.

The stellar velocities and encounter geometries are derived in the same way as in RFFV08. This means that – for any given type of star – we construct the encounter velocity from the data in Table 1 as the vector sum of the solar apex velocity and a randomly chosen, isotropically distributed stellar peculiar velocity. The absolute value of the latter is chosen using a Maxwellian distribution with the listed dispersion, and we use the resulting speed as a weight factor (see RFFV08), since stars contribute to the encounter flux in proportion to their velocities (Heisler et al., 1987). The direction of the encounter velocity is taken at random from an isotropic distribution.

The impact parameter $b_\odot$ with respect to the Sun is randomly chosen between 3×10^3 AU and 4×10^5 AU with a uniform distribution in $\log b_\odot$. This choice of distribution makes us sample the whole range of encounter distances more equally than in the case of real stellar encounters, where the closest ones are very rare compared to the distant ones.

These 65 stellar encounter sequences (corresponding to a total of 1300 individual encounters) perturb a cloud of 10^6 fictitious comets having the following statistical characteristics. The initial semi-major axes are taken in the interval: $3 \times 10^3 < a_0 < 1 \times 10^5$AU with a flat distribution of orbital energy (*i.e.*, inverse semi-major axis). Thus we sample the whole range of energies equally, whereas in simulations of the real Oort cloud – following (Duncan et al., 1987) – a probability density $\propto a^{-3/2}$ is often used, giving

Table 1
Stellar parameters. The types are mostly MK types for main sequence stars; 'wd' indicates white dwarfs, and 'gi' indicates giant stars. The encounter frequencies are given in number per Myr within 1 pc. The following two columns list the solar apex velocity with respect to the corresponding type, and the spherical Maxwellian dispersion of peculiar velocities. The last two columns give the mean heliocentric encounter velocity and its standard deviation.

Type	Mass ($M_\odot$)	Enc. freq.	$v_\odot$ (km/s)	σ_* (km/s)	$\langle V \rangle$ (km/s)	σ_V (km/s)
B0	9	0.005	18.6	14.7	24.6	6.7
A0	3.2	0.03	17.1	19.7	27.5	9.3
A5	2.1	0.04	13.7	23.7	29.3	10.4
F0	1.7	0.15	17.1	29.1	36.5	12.6
F5	1.3	0.08	17.1	36.2	43.6	15.6
G0	1.1	0.22	26.4	37.4	49.8	17.1
G5	0.93	0.35	23.9	39.2	49.6	17.9
K0	0.78	0.34	19.8	34.1	42.6	15.0
K5	0.69	0.85	25.0	43.4	54.3	19.2
M0	0.47	1.29	17.3	42.7	50.0	18.0
M5	0.21	6.39	23.3	41.8	51.8	18.3
wd	0.9	0.72	38.3	63.4	80.2	28.2
gi	4	0.06	21.0	41.0	49.7	17.5

more weight to the inner core. Like in the case of stellar impact parameters, since the present model is not intended to mimic the real Oort cloud, we prefer to use a uniform sampling.

The initial eccentricities e_0 are chosen with a density function $\propto e_0$ in such a way that the perihelia are outside the planetary system, *i.e.*, $q_0 > 32$ AU. The angular elements ω_0, Ω_0 and M_0 (we use common notations for the orbital elements, and the angles may be defined with respect to an arbitrary frame of reference), like $\cos i_0$, are randomly chosen with flat distributions.

The motion of comets is integrated for a maximum of 5 Gyr, and the integration stops if either a perihelion passage occurs with $q < 15$ AU, or the heliocentric distance increases beyond $r = 4 \times 10^5$ AU. The comet is then considered as lost from the Oort cloud – either by planetary perturbations (the first case) or by tide-induced escape into interstellar space (the second case). The term *injection* will be reserved for comets that reach the observable zone at perihelion ($q < 5$ AU).

3.2. Direct injections

In this Subsection we will present the results of S models, neglecting the action of Galactic tides.

Table 2 gives the fractions of stars in three groups, corresponding to different mass ranges, which yield numbers of injected comets in different intervals. We note that even with as many as 10^6 comets in our simulated Oort cloud, the statistical sampling of the number of injected comets is rather poor – especially for the lightest stars, where the number is zero in more than half the cases. More than 20 comets are injected by most of the B0 stars (the heaviest) and 46% of the other heavy stars but only 13% of the light stars.

Let us base our discussion on the classical impulse approximation (Rickman, 1976), which involves the following assumptions: (i) the star moves with constant velocity with respect to the Sun, and the motion follows a straight line, (ii) in accordance with the high stellar speed, the comet is considered at rest in the heliocentric frame during the stellar passage, and (iii) the stellar effect is computed for a star moving from infinity to infinity. This approximation is useful for discussing and interpreting statistical results, although it is not at all accurate in individual cases for the relatively fast-moving comets of the inner core.

With the above assumptions, the heliocentric impulse imparted to the comet is given by:

$$\Delta\mathbf{V} = \frac{2GM_\star}{V_\star}\left(\frac{\mathbf{b}_C}{b_C^2} - \frac{\mathbf{b}_\odot}{b_\odot^2}\right), \tag{1}$$

where $M_\star$ is the stellar mass, $V_\star$ is the stellar velocity, and $\mathbf{b}_\odot$ and $\mathbf{b}_C$ are the vectors from the Sun and the comet, respectively, to the closest points on the stellar trajectory.

For a close encounter with the comet only, we get approximately:

$$\Delta\mathbf{V} \propto \frac{M_\star}{V_\star b_C}, \tag{2}$$

while in the case of a distant encounter with both the Sun and the comet, as shown by Rickman (1976), we obtain:

$$\Delta\mathbf{V} \propto \frac{M_\star r}{V_\star b_\odot^2}, \tag{3}$$

where r is the heliocentric distance of the comet.

Table 2
Fraction of stars, given as per cent, in three different groups – namely, B0 stars (9 $M_\odot$), A0 to F5 and red giant stars (1.3–4 $M_\odot$), and all the other stars (0.2–1.1 $M_\odot$) – yielding numbers of injected comets in different ranges.

Mass ($M_\odot$)	9	[1.3,4]	[0.2,1.1]
$n_{\text{inj}} = 0$	6	23.6	52.9
$n_{\text{inj}} = 1$	9	8.2	9.9
$2 \leqslant n_{\text{inj}} \leqslant 5$	12	11.4	10.9
$6 \leqslant n_{\text{inj}} \leqslant 20$	20	10.8	13.4
$21 \leqslant n_{\text{inj}} \leqslant 200$	17	25.2	12.9
$201 \leqslant n_{\text{inj}}$	36	20.8	0.1

Now, consider the case of close encounters between the star and the injected comets. Our modelled Oort cloud has a flat distribution of $1/a$ and thus a distribution like a^{-2} in the semi-major axis. In terms of heliocentric distance, the distribution function is then proportional to r^{-2}, and the number density of comets in the cloud (n) varies as r^{-4}. We want to find the number of comets that may be injected due to close encounters along the track of the star through the Oort cloud. This will depend on the along-track integral of the number density of comets multiplied by the cross-sectional area perpendicular to the track, within which the comets may suffer large enough impulses to inject them.

The requirement is for $|\Delta q|$ to overcome a certain value – typically, the 10 AU needed in order to cross the Jupiter–Saturn barrier (this means the range of perihelion distances within the loss cylinder, where the comets are not observable). Let G be the angular momentum of the cometary orbit. Using the approximate relation $q \propto G^2$ for high-eccentricity orbits, we obtain:

$$|\Delta q| \propto G|\Delta G|. \tag{4}$$

If v_t is the size of the transverse velocity component, we have: $G = rv_t$. Hence, $|\Delta G| = r|\Delta v_t|$, and we may consider $|\Delta v_t|$ to be some standard fraction of $|\Delta\mathbf{V}|$ for a random orientation of the impulse vector. Taking $|\Delta\mathbf{V}|$ from Eq. (2), we find that in order to have $|\Delta q| > 10$ AU, we require $b_C < b_\ell$ with:

$$b_\ell \propto r \cdot \frac{M_\star}{V_\star}. \tag{5}$$

Here we consider G to be a constant, given by the pre-injection perihelion distance.

The above-mentioned cross-sectional area (A) is hence:

$$A \propto r^2 \frac{M_\star^2}{V_\star^2}, \tag{6}$$

and in order to estimate the number (N_S) of injected comets, we have to take the along-track integral through the cloud of $n \cdot A$. The latter product varies as r^{-2}, and for a spherical cloud with radius R_{cl} the result is:

$$N_S \propto \frac{M_\star^2}{V_\star^2} \cdot \frac{1}{b_\odot} \operatorname{arctg}\left(\frac{R_{\text{cl}}}{b_\odot}\right). \tag{7}$$

This is an approximation that holds for $b_\odot \ll R_{\text{cl}}$, which is the case of interest for us, and we may use the limiting value of $\operatorname{arctg}(R_{\text{cl}}/b_\odot) = \pi/2$ as a constant factor.

As a result, in case stars inject comets basically by close encounter perturbations, we expect the injected number to scale with the square of the parameter:

$$I_{\text{close}} = \frac{M_\star}{V_\star \sqrt{b_\odot}}. \tag{8}$$

We will look for a correlation between N_S and I_{close} as an indicator of the importance of close star-comet encounters as injection mechanism.

Next, consider the case of distant, tidal encounters described by Eq. (3). In this case the injected comets are not situated near the star track but in a region much closer to the Sun. Let us estimate the size of that region, since this will influence the number of injected comets. If we consider the mean transverse velocity change to be proportional to the change of total velocity (see above), we get: $|\Delta v_t| \propto M_\star r V_\star^{-1} b_\odot^{-2}$ from Eq. (3). Thus, according to Eq. (4), we obtain the expected change of perihelion distance as:

$$|\Delta q| \propto r^2 \cdot \frac{M_\star}{V_\star b_\odot^2}. \tag{9}$$

In order for $|\Delta q|$ to overcome the estimated value of 10 AU, we see that r must be larger than some $r_{\min}$, where $r_{\min}^2 \propto V_\star b_\odot^2 / M_\star$. This means that the injected comets must be outside a 'forbidden region' around the Sun, whose size decreases with increasing values of the parameter:

$$I_{\mathrm{dist}} = \frac{M_\star}{V_\star b_\odot^2} \tag{10}$$

Hence we expect N_S to correlate positively with I_{dist} and will look for such a correlation as an indicator of tidal interactions as injection mechanism.

We will refer to I_{close} and I_{dist} as "strength parameters" for close and tidal encounters, respectively, and the units to be used are solar masses ($M_\odot$) for $M_\star$, 40 km/s for $V_\star$, and 2×10^4 AU $\simeq 0.1$ pc for $b_\odot$. The common factor $S_\star = M_\star / V_\star$ may be regarded as a specifically stellar strength parameter independent of the encounter geometry (Dybczyński, 2002). Within each stellar type of Table 1 some scatter of $S_\star$ is caused by the spread in velocities as indicated by σ_V, but if we calculate mean values $\langle S_\star \rangle = M_\star / \langle V \rangle$ using the listed mean values $\langle V \rangle$, we find that these vary by a factor ~90 from B0 stars with $\langle S_\star \rangle \simeq 15$ to M5 stars with $\langle S_\star \rangle \simeq 0.16$ in the above units.

These differences are in reality compensated by the different encounter frequencies – also listed in Table 1. Encounters with M5 stars are more than 1000 times more frequent than those with B0 stars. When discussing our results for N_S versus I_{close} and I_{dist}, it is worth keeping in mind the actually expected minimum encounter distances of each stellar type over a 1 Gyr time scale (taken as representative for the long-term evolution of the Oort cloud). Using the listed encounter frequencies, we may calculate the area that yields 1/2 encounters during 1 Gyr for the type of star in question, and we may take the radius of the corresponding circle for the distance of the expected closest encounter. The result is ~60,000 AU for B0 stars and ~2000 AU for M5 stars.

In Fig. 1 we plot N_S as found in our simulations versus the strength parameter of the corresponding stellar encounter I_{close} (left panels) and I_{dist} (right panels). The upper panels display results for the stellar types with the smallest $\langle S_\star \rangle$. These are K0, K5, wd, M0 and M5 stars. The lower panels show gi, A5, A0 and B0 stars, which have the largest $\langle S_\star \rangle$ values. In both cases we use colours to identify the individual types. We also include the intermediate types (F0, F5, G0 and G5) in all diagrams, plotted with grey circles.

The most striking result appears for the high-mass stars. These are seen to show a very good correlation between N_S and I_{dist} over a major part of the plotted range, while no correlation whatsoever is observed for I_{close}. The top, rightmost part of the diagrams exhibit a saturation effect, to which we shall return below. In the lower part of the I_{dist} diagram, for $N_S < 10$, we also see an increasing effect of statistical noise. For the low-mass stars the picture is somewhat less clear – partly due to the small values of N_S in many cases. However, the correlation of N_S with I_{close} is clearly better than the one with I_{dist}.

If we look at any particular stellar type, the closest encounters with $b_\odot \sim 3000$–5000 AU (generally shown by the rightmost points in each diagram) cannot be expected to inject most comets by tidal perturbations. For the high-mass stars we might have seen this as an extra scatter, if there had not been the mentioned saturation effect. But it would not matter in practice, since even over the age of the Solar System not a single such encounter is statistically expected, given the rarity of such stars. For the low-mass stars the correlation with I_{close} is quite good all the way from the closest encounters to the region, where the statistical noise prevents safe judgements. This means encounter distances up to $b_\odot \sim 30{,}000$ AU if not more.

Hence we conclude that as regards stellar injections from the Oort cloud, the stars of highest mass are basically distant, tidal perturbers, while the common, low-mass stars act mostly via close

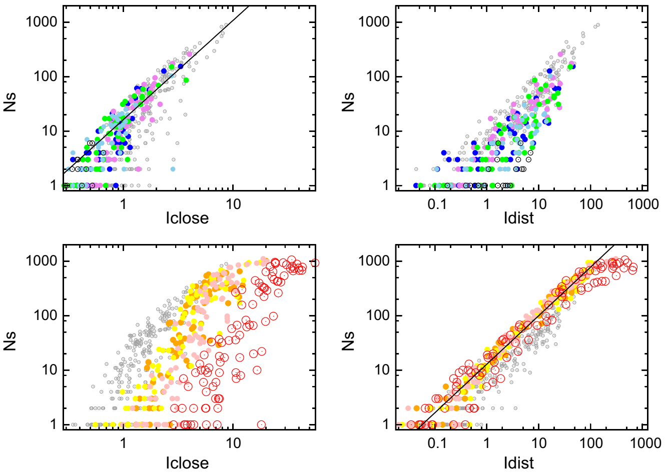

Fig. 1. Number of comets entering the observable region due to individual stellar encounters versus I_{close} (left panels) and I_{dist} (right panels). In the upper panels we plot low-mass stars ($M_\star \leqslant 0.9\, M_\odot$), using violet colour for K0 stars, blue for K5 stars, green for white dwarf stars, skyblue for M0 stars (in all cases filled circles), and open black circles for M5 stars. In the lower panels we plot high-mass stars ($M_\star > 2\, M_\odot$), using orange colour for giant stars, yellow for A5 stars, pink for A0 stars (in all cases filled circles), and open red circles for B0 stars. The grey circles indicate the stars of intermediate masses (F0, F5, G0 and G5 stars). We have plotted regression lines (linear fits in log scale) at the upper left for low-mass stars, and at the lower right for high-mass stars. (For interpretation of the references to colour in this figure legend, the reader is referred to the web version of this article.)

encounters with comets – at least when passing through the inner or central parts of the cloud. We interpret this as a trend with increasing stellar mass for comet injection to move from close encounters along the stellar track to distant ones affecting large parts of the Oort cloud at the same time. Since this trend should be continuous, the stars of intermediate masses (including the solar type stars) are likely to act in both ways, so the mechanism could be different for different, individual comets.

The lines drawn are regression lines, yielding power-law fits for N_S. In the case of low-mass stars we have excluded all the M5 stars and those other stars that yield $N_S < 5$ for lack of statistical significance. For the high-mass stars we excluded the saturated region with $I_{\mathrm{dist}} > 0.1$. The mathematical expressions for the power laws are:

$$N_S = I_{\mathrm{close}}^{1.82} \times 10^{1.21}, \tag{11}$$

(low-mass stars), and:

$$N_S = I_{\mathrm{dist}}^{0.89} \times 10^{1.11}, \tag{12}$$

(high-mass stars). The scaling factors play the role of referring N_S to an Oort cloud with 10^6 comets. The power law indices of the above formulae are defined with standard deviations of ±0.11 for I_{close} and ±0.01 for I_{dist}. The standard deviations of the exponents entering into the scaling factors are ±0.39 and ±0.13, respectively. Note the good agreement of our result for the I_{close} index with the theoretical value of 2 derived above.

Our results for injection probabilities due to stellar encounters should be compared with those of Dybczyński (2002). We find much larger values than he did, but this is essentially a result of different initial conditions. Instead of choosing the initial cometary orbits with perihelion distances $q > 50$ AU (Dybczyński, 2002), we start the simulations with $q > 32$ AU, and each new stellar encounter brings some comets closer to the loss cone so that the next star may act on comets with q closer to 15 AU. Apart from this difference, we note a general similarity of the results – *e.g.*, Dybczyński (2002) found a variation of injection efficiency for $b_{\odot} = 30{,}000$ AU that is slower for large stellar strength parameters than for small ones (cf. his Fig. 6), and this may be interpreted using our results as a shift from tidal injections in the first case to close encounters in the second.

Our results demonstrate quantitatively that heavy stars are long-range perturbers, typically injecting comets from large parts of the Oort cloud without having to pass very close to the Sun, while low-mass stars in general affect comets mainly near their tracks and need to pass very close to the Sun in order to induce large numbers of injections. In reality, of course, such close encounters are very rare, and even though high-mass stars have much lower encounter frequencies (see Table 1), the latter enjoy the advantage of not having to pass as close in order to cause large effects.

The last feature to be noted in Fig. 1 is an apparent saturation of the injected number at about 1000. While the low-mass stars never reach this level, the high-mass stars sometimes do. The reason for the saturation is the complete filling of the loss cone (cf. RFFV08). This orbital domain, defined by $q < 15$ AU, is normally almost empty in our model of the cloud, and it gets repopulated by each stellar encounter. However, these encounters can do no more than thermalize[1] the velocity distribution of the comets – there is no reason for them to aim in particular at the loss cone when perturbing the velocities or to overpopulate any part of it, like for instance, the observability zone. Therefore the number of injected comets has a maximum given by the number of comets in our modelled Oort cloud, which would have $q < 5$ AU in a thermalized distribution.

This number is easy to estimate, using the fraction $2q_o/a$ with $q_o = 5$ AU (Bailey and Stagg, 1988) and the probability density function $f(a)$. Integrating the product of these with respect to a over the extent of the cloud, and normalizing to a total population of 10^6 comets, we get a value between 1000 and 2000, in agreement with the ceiling observed in Fig. 1.

From these results, even though the distribution of encounter distances that we use is very different from reality, our results suggest high-mass stars to be at least as important as low-mass stars for direct injection of comets from the Oort cloud in the long run despite their much lower encounter frequency. This will be further discussed in Section 4.

3.3. The tidally active zone

The synergy observed in RFFV08 during periods outside comet showers may result largely from the fact that stellar encounters randomize the comet orbital elements and consequently repopulate the regions of phase space, from which the tides may inject the comets into the observable region.

Let us consider the case of integrable dynamics involving only the Galactic disc tide. In this framework, we have to assume that the semi-major axes of the comets are small enough to allow the averaging of the equations of motion with respect to the mean anomaly (see Heisler and Tremaine, 1986; Breiter et al., 1996; Fouchard et al., 2005), and we neglect the radial component of the tides as well as stellar encounters.

In this case it is well known (Breiter et al., 1996) that the evolution of the perihelion distance is strictly periodic. Hence, a comet can be injected into the observable region only, if the minimum value of the perihelion distance over one cycle is smaller than 5 AU. The phase space region of the Oort cloud which contains all such comets will be called the *tidally active zone* (TAZ).

According to the work of Matese and Whitman (1992) one can easily define the TAZ, using the integrability of the system. Indeed, the minimum value of the angular momentum G_{min} of a comet orbit is given by:

$$G_{\mathrm{min}}^2 = \frac{1}{8} 5L^2 + 5H^2 - G_0^2 - \sqrt{\left(5L^2 + 5H^2 - G_0^2\right)^2 - 80L^2H^2},$$

where

$$G_0^2 = H^2 + \left(1 - \frac{H^2}{G^2}\right)\left(G^2 + 5(L^2 - G^2)\sin^2\omega\right),$$

and we have $L = \sqrt{\mu a},\ G = \sqrt{\mu a(1 - e^2)}$ and $H = \sqrt{\mu a(1 - e^2)}\cos i$.

Consequently, under an integrable Galactic tide, the minimum value that the perihelion distance of a comet can reach is:

$$q_{\mathrm{min}} = a\left(1 - \sqrt{1 - \frac{G_{\mathrm{min}}^2}{\mu a}}\right). \tag{13}$$

The TAZ can then be obtained as the region of phase space in which, according to the equations above, L, G and H are such that $q_{\mathrm{min}} < 5$ AU. We may compare with the work of Maciejewski and Prętka (1998), who gave a criterion for an Oort cloud comet in order certainly not to become observable under the effects of a quasi-integrable tide. Specifically, considering only the normal component of the tide but without averaging, they computed a global minimum r_{min} of the heliocentric distance depending only on the total energy and the normal component of the angular momentum. Doing this for a comet on a given orbit, in case the result is $r_{\mathrm{min}} > 5$ AU, the comet would never become observable according to our criterion. However, because the minimum is

---

[1] The fact that we exclude comets with $q < 32$ AU makes very little difference and the effect may be neglected.

global, $r_{\min}$ is not the same as the minimum heliocentric distance reached by this comet with its specific values of initial eccentricity and argument of perihelion during an arbitrarily long time. The latter is instead approximated by our result for $q_{\min}$. This conclusion is independent of the fact that their system was not averaged.

Consequently, their criterion might be efficient for speeding up simulations, since one would integrate only the comets for which $r_{\min} < 5$ AU (as far as neither the radial component of the tide nor stars are taken into account). Because 5 AU $\geqslant q_{\min} \geqslant r_{\min}$ for our TAZ, all its comets would be integrated using the (Maciejewski and Prętka, 1998) criterion, but if we would define the TAZ using $r_{\min}$ instead of $q_{\min}$, we would have many comets inside that TAZ, which in fact cannot enter the observable region. Consequently, even though we have one additional hypothesis since we have averaged our equations of motion, we will use the above $q_{\min}$ to define the TAZ.

Let us now consider three regions: the inner region ($a < 20{,}000$ AU), the central one ($20{,}000 < a < 50{,}000$ AU), and the outer one ($50{,}000 < a < 100{,}000$ AU). The part of the cloud outside these regions is not considered, since it is empty at the beginning and remains almost empty during the integrations. Furthermore, we cannot consider an integrable tide for such comets. Strictly speaking, integrability only holds true for the inner region and part of the central region.

Fig. 2 shows the fraction of comets in the TAZ (in per cent) versus time, as found in the Model G simulation, for the three regions of the Oort cloud and for the entire Oort cloud (excluding any comets with $a > 100{,}000$ AU). Note that this tide model includes the radial component in addition to the obvious fact that we treat non-averaged equations of motion. We may thus expect important effects (see below) for the outer Oort cloud region, when applying the theoretical TAZ to the simulation results. The three regions are plotted using different colours, while the black curve shows the result for the entire cloud.

In the beginning of the integration, *i.e.*, at time $t = 0$, the filling of the TAZ is generally at its maximum. The outer region shows a special behaviour, as discussed below. Moreover, since our choice of initial orbital elements assumes that the Oort cloud is thermalized, we may consider that the initial fraction corresponds to a completely filled TAZ. The fractions of comets in the TAZ when it is completely filled are thus: $p_{\text{full}} = 5.85\%$, 2.63% and 1.80% for the inner, central and outer regions of the cloud, respectively. For the entire Oort cloud we have $p_{\text{full}} = 5.42\%$. We note that p_{full} is higher for the regions closer to the Sun. This can be realized from Eq. (13), since it is easily seen that $G^2_{\min} \propto \mu a$, and thus $q_{\min} \propto a$. Hence,

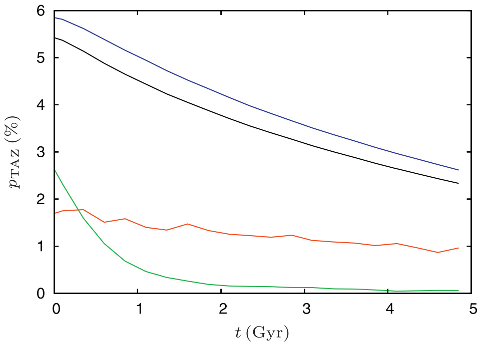

Fig. 2. Percentage of comets in the TAZ for different regions of the Oort cloud. The blue, green, red and black curves illustrate, respectively, the inner, central, outer, and entire Oort cloud. (For interpretation of the references to colour in this figure legend, the reader is referred to the web version of this article.)

everything else being fixed, $q_{\min}$ decreases for decreasing semi-major axis, and consequently, the relative measure of the TAZ increases.

As time goes on, the TAZ gets depleted, since the comets that enter the observable region on account of $q < 5$ AU get removed from the integration. Let us now consider this depletion of the TAZ in more detail for each region of the Oort cloud separately.

- In our dynamical model, no comets of the inner region are able to jump the Jupiter–Saturn barrier, since the tides are not strong enough to decrease the perihelion distance from $q \geqslant 15$ AU to below 5 AU in only one orbital period. Hence, even though the TAZ gets depleted as seen in the Figure, there are no comets injected into observable orbits. The relatively slow depletion of the TAZ is explained as follows. As specified in Section 3.1, the simulation is stopped and the comet is lost as soon as its heliocentric distance $r \leqslant r_c = 15$ AU.[2] As time goes on, the TAZ population is reduced in relative terms, since more comets located in the TAZ reach the limiting value $r_c = 15$ AU than comets that are outside the TAZ. The low speed of the depletion is due to the very long periods of the perihelion cycle for inner region comets. Indeed, this period is proportional to $1/P_{\text{orb}}$, where P_{orb} is the orbital period (see Matese and Whitman, 1992; Breiter et al., 1996).
- The depletion of the TAZ is particularly evident for the central region (see Fig. 2) and occurs mainly during the first billion years. This fast depletion is explained by the fact that the period of the perihelion cycle (P_q) is shorter than for the inner region. In fact, most comets in the inner region have $P_q > 5$ Gyr, so there is not enough time in our simulation for the TAZ to get fully depleted. But in the central region we can expect that most comets have $P_q < 5$ Gyr, so the TAZ should have time to get nearly fully depleted. However, we see that even at the end of the integration, the TAZ is not entirely empty. This fact is explained by two properties of the dynamics. First, we recall that the integration of a comet is stopped, when its heliocentric distance becomes less than 15 AU. Thus, a necessary condition for a TAZ comet to be excluded is that at the time when its perihelion distance is smaller than 15 AU, the comet should actually be close to its perihelion. For large semi-major axes, the probability of this event decreases as the inverse of the square of the orbital period (Fouchard et al., 2010). A comet may hence stay in the TAZ even if the period of its perihelion cycle is short (implying a large orbital period). Second, and probably the main point, the real dynamics is not integrable, since the assumption of an orbit-averaged Hamiltonian as implicit in our definition of the TAZ breaks down. In addition there is also the radial component of the tide, which is not considered in the TAZ definition. As a result, the TAZ border cannot be strictly hermetic. This permeability of the TAZ increases with the semi-major axis, since the influence of the non-integrable part of the dynamics (including the radial component) increases with increasing semi-major axis (Heisler and Tremaine, 1986; Fouchard et al., 2005).
- These two properties obviously apply to the outer region as well. The permeability of the TAZ is now very high. This is why the filling of the TAZ is almost constant with time for this region of the Oort cloud.

3.4. Filling of the tidally active zone by stars

What happens when the stars are at work? Each time a star passes through the Oort cloud, it perturbs the orbital elements of

---

[2] If the perihelion distance at this time is $q < 5$ AU, we record a case of comet injection.

many comets – notably those placed near its track – injecting some of them into the TAZ, and ejecting some of them from the TAZ. If the Galactic tides are not at work, from a statistical point of view, nothing happens. But, if the tidal effects are included, the density inside the TAZ will be lower than the density outside it. Then the action of the stars will be to fill the TAZ, thereby tending to balance these two densities. We will now study this phenomenon by simulating the evolution of an Oort cloud in the presence of both the Galactic tides and the stellar encounter sequences described in Section 3.1.

In order to quantify the effect of a star, we define a TAZ filling efficiency at time $t^\star$ (the time of perihelion passage of the star, when its perturbations on the comets are applied) by:

$$f = \frac{n_{\text{inj}}(t^\star)}{n_{\text{Oort}}} \cdot \frac{1}{p_{\text{full}}},$$

where n_{inj} is the number of comets passing from outside the TAZ at $t^\star - \epsilon$ to inside the TAZ at $t^\star + \epsilon$; ϵ is a short interval of time, n_{Oort} is the number of comets at $t^\star + \epsilon$ in the Oort cloud, and p_{full} is the full TAZ fraction of the Oort cloud as given in Section 3.3. Obviously, one may compute f for each sub-region of the Oort cloud (inner, central, or outer). The quantity ϵ should be taken sufficiently small in order that no, or at most very few, comets are removed from the integrations between $t^\star - \epsilon$ and $t^\star + \epsilon$. We have taken $\epsilon = 1000$ yr.

Fig. 3 shows the value of f in per cent versus the impact parameter with respect to the Sun ($b_\odot$) for each cloud region and for all the stars used in our simulations. The following observations may be made.

- All plots show a rather clear separation of the efficiency factor with respect to the stellar type, which shows that the stellar mass and velocity are key parameters for TAZ filling. A saturation effect is often seen, whereby – for obvious reasons – the f values are limited to $\simeq$100% or less.
- As regards the inner Oort cloud region, (1) for low-mass stars (wd stars and lighter), f is at most 24% for a white dwarf with a solar impact parameter $b_\odot \sim 3300$ AU. For $b_\odot > 12{,}000$ AU, f is always smaller than 3.5% and drops to values below 1% for $b_\odot > 25{,}000$ AU. (2) For the massive B0 stars, values of $f > 80\%$ are reached, when the impact parameters $b_\odot$ are less than 5000 AU, while for $b_\odot > 25{,}000$ AU, f decreases below 15%.
- For the central Oort cloud region, the picture changes drastically. High-mass stars (A5 stars and heavier) excluding the B0 type are now able to fill up 70% of the TAZ for impact parameters around 20,000 AU or less. For impact parameters around 50,000 AU, up to about 25% of the TAZ is refilled by these stars (and up to 50% for B0 stars). Regarding the low-mass stars, the best filling efficiencies are 60–70% for impact parameters less than 4000 AU. For impact parameters around 10,000 AU and 50,000 AU, f drops to values around 30% and 2.5%, respectively, *i.e.*, one order of magnitude smaller than the values obtained for high-mass stars.
- Concerning the outer Oort cloud region, despite the fact that the TAZ is not well defined as already pointed out in Section 3.3, we still observe that massive stars are 5–10 times more efficient than light stars in filling the TAZ. The filling efficiency can reach high values even for large impact parameters (it may be larger than 100% at $d_\odot > 60{,}000$ AU for B0 stars). However, one should note that even the tide alone is able to fill the TAZ in this case. Indeed, it appears that during the time span $\Delta t \simeq 250$ Myr separating the stellar encounters of our simulations, the tides fill the outer TAZ almost completely. This demonstrates the large permeability of the TAZ at such large semi-major axes.

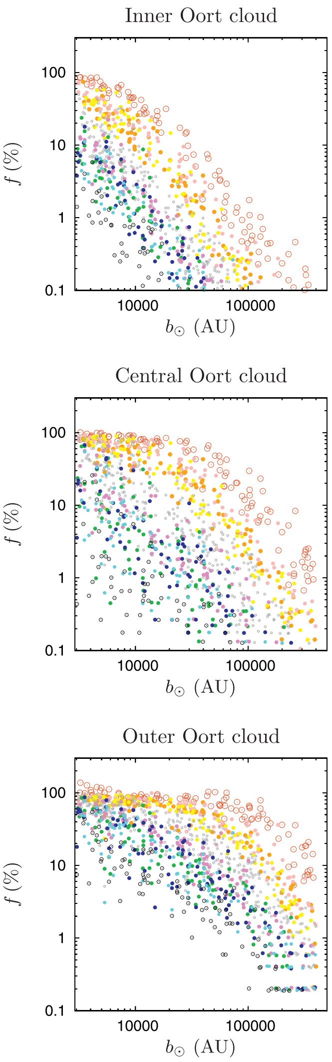

Fig. 3. Efficiency f of individual stars to fill the TAZ for the inner Oort cloud region (top diagram), central region (middle diagram) and outer region (bottom diagram) versus the solar impact parameter. The colour codings of stellar types are the same as in Fig. 1. (For interpretation of the references to colour in this figure legend, the reader is referred to the web version of this article.)

In Fig. 4 we plot the value of the TAZ filling efficiency f as computed *between* the stellar encounters versus the stellar mass of the preceding encounter, for the three regions of the Oort cloud. Specifically, we count n_{inj} from $t^\star + \epsilon$ for one stellar encounter to $t^\star - \epsilon$ for the next one, and we use n_{Oort} at the latter occasion. In this case the TAZ filling is only due to the tides. We see that for the three regions the values of f are gathered in different ranges: [0.15%, 0.88%], [0.74%, 21.2%] and [38%, >100%] for the inner, central and outer Oort cloud, respectively. This is a demonstration that the TAZ is indeed almost hermetic in the inner Oort cloud, moderately

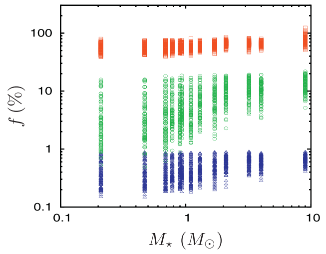

Fig. 4. For the inner (blue open triangles), central (green open circles) and outer Oort cloud (red open squares), we plot the efficiency *f* of the tides to fill the TAZ *between* stellar encounters, versus the stellar masses. (For interpretation of the references to colour in this figure legend, the reader is referred to the web version of this article.)

permeable for the central Oort cloud and completely permeable for the outer Oort cloud.

Interestingly, we observe a slight dependence on the stellar mass with higher values of *f* for higher stellar masses. A priori, the stellar perturbations should not affect the TAZ filling, since *f* is computed between these encounters. Our explanation is that just outside the frontier between the TAZ and the rest of the phase space there is a transition region in which the tide is inefficient (as anywhere outside the TAZ), but the perturbation needed to transfer the comet from this transition region into the TAZ is so small that it can be provided by the non-integrable component of the tide. When the TAZ gets depleted due to comets falling into the loss cone, this mobility acts to resupply comets into the TAZ, whereby the transition region also gets depleted. Since massive stars are more efficient to fill the TAZ, they are also more efficient to fill the transition region, and hence the tides are more efficient to fill the TAZ *after* such stellar encounters.

Because the inner Oort cloud does not contribute to the flux of observable comets without the direct help of a stellar perturbation,[3] and since the TAZ of the outer Oort cloud is easily refilled by the tides only, we will now concentrate on the central part of the Oort cloud.

For the central Oort cloud, Fig. 5 gives *f* (in per cent) versus $I_{\rm close}$ (upper panel) and versus $I_{\rm dist}$ (lower panel) for individual stars. Linear fits in log scale (shown by the straight lines) are given by:

$$f \propto I_{\rm close}^{2.74\pm0.08}, \qquad (14)$$

where the fit has been made for the ensemble of wd, K0, K5 and M0 stars (upper panel), and:

$$f \propto I_{\rm dist}^{1.00\pm0.02}, \qquad (15)$$

for gi, A5, A0 and B0 stars together (lower panel). Note that a cut-off has been made for $I_{\rm dist} > 0.002$ in this case in order to avoid the saturated region.

Comparing Eqs. (14) and (15) with Eqs. (11) and (12), we note that the power law indices are similar. This is an indication that the relative efficiencies of stars to inject comets into the TAZ are similar to those of injecting comets directly into observable orbits.

3.5. Long term dynamics

Let us now study the effect of the TAZ filling efficiency on the flux of observable comets over a long time scale. We will consider two sets of stars, one including 20 A5 stars ($M_\star = 2.1\ M_\odot$) and the other including 20 K0 stars ($M_\star = 0.78\ M_\odot$). The geometries of the encounters are different in the two cases except in the very beginning of the sequence.

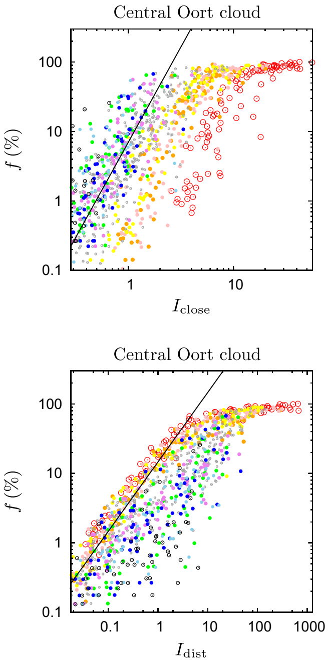

Fig. 5. Efficiency *f* of individual stars to fill the TAZ of the central Oort cloud versus $I_{\rm close}$ (upper panel) and $I_{\rm dist}$ (lower panel). The colour coding of the points is the same as in Fig. 3. The full-drawn lines indicate linear fits in log scale. (For interpretation of the references to colour in this figure legend, the reader is referred to the web version of this article.)

We perform three computations including: (i) the Galactic tides only, (ii) stars only, and (iii) both Galactic tides and stars, and we compare the results as in RFFV08. Our model parameters for the cloud are the same as described in Section 3.1, *i.e.*, all regions (inner, central and outer) are included. The results of the simulations in terms of numbers of injected comets during 20-Myr intervals over a total time scale of 5 Gyr are plotted in Fig. 6.

The direct injections (Section 3.2) are limited to the time bin of the respective encounter, as shown by the grey spikes. We notice that for similar solar impact parameters, the height of these spikes is always smaller for K0 stars than for the higher-mass A5 stars. This is in agreement with the results found in Section 3.2.

We also notice that the combined models (white histograms) show a continuous excess of injected comets with respect to the tide-only models (black histograms) of the kind seen in RFFV08. This reflects the synergy discussed in RFFV08 and is largely explained by the filling of the TAZ induced by stellar perturbations. The lower plots of Fig. 6 show the time evolution of the amount of TAZ filling given by

$$p_{\rm TAZ} = \frac{n_{\rm TAZ}}{n_{\rm CR}} \cdot \frac{1}{p_{\rm full}}, \qquad (16)$$

in the central Oort cloud region, for the combined model with A5 stars (lower plot of Fig. 6a), and for the combined model with K0 stars (lower plot of Fig. 6b).

Concentrating on times larger than 1 Gyr, and comparing the two kinds of stars, we clearly see a correlation between the filling

---

[3] Note that this may not be true in reality but is implied by our simplified treatment of planetary perturbations.

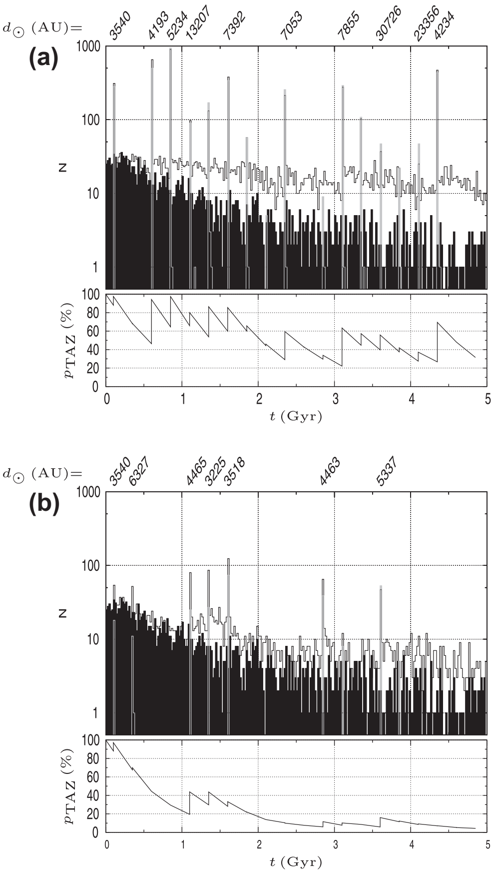

Fig. 6. The upper panels show the number of injected comets per 20 Myr versus time. The black histograms correspond to the tide-only model, the grey ones to the star-only model, and the white histograms to the combined model. The impact parameters of the closest encounters are written above each plot. Lower panels: amount of the TAZ filling versus time for the central cloud region. Figure (a) is for A5 stars (2.1 $M_\odot$) and (b) for K0 stars (0.78 $M_\odot$).

of the TAZ and the excess of injected comets of the combined models. We may also recognize that the excess jumps to higher levels in connection with the closest, most effective stellar encounters. These results prove that the filling of the TAZ by passing stars is the fundamental mechanism behind the synergy between the Galactic tides and stellar perturbations. As seen from the diagrams, this synergy is able to trigger "comet drizzles" due to single encounters filling the TAZ, inducing a significant increase of the flux of observable comets lasting up to a few hundred Myr.

4. Cumulative stellar effects in long term simulations

4.1. Initial conditions and simulations

We now consider the same thermalized initial Oort cloud as in RFFV08. Specifically, the cloud is constructed in the same way as in Section 3.1, but the semi-major axes are chosen with a probability density $\propto a_0^{-1.5}$ (Duncan et al., 1987).

Table 3
Number of comets entering the observable region during periods of 1 Gyr. Model G corresponds to the Galactic tide alone, S to passing stars alone, and C to Galactic tide and passing stars together (all, heavy and light mean that all, only the heavy or only the light stars are taken into account in the simulations). $\langle\tau\rangle$ is the increment from the sum of the two first rows (Galactic tide plus passing stars separately) to the third row (Galactic tide and passing stars together).

Model	[0–1] Gyr	[1–2] Gyr	[2–3] Gyr	[3–4] Gyr	[4–5] Gyr
G	2117	801	473	307	252
S(all)	1367	1620	1101	688	480
C(all)	3703	3244	2450	1782	1276
$\langle\tau\rangle$	6.29%	33.99%	55.65%	79.1%	74.32%
S(heavy)	855	985	352	306	205
C(heavy)	3075	2391	1583	1259	934
$\langle\tau\rangle$	3.47%	33.87%	91.88%	105.38%	104.38%
S(light)	810	901	915	622	482
C(light)	3174	2617	2292	1831	1487
$\langle\tau\rangle$	8.44%	53.76%	65.13%	97.1%	102.59%

We also use the same sample of passing stars as in RFFV08, defined as follows: we build a predefined set of 197,906 stellar encounters, occurring at random times during an interval of time from $t = 0$ to 5 Gyr, with random solar impact parameters up to $d_{\max} = 4 \times 10^5$ AU, and with random stellar masses and velocities (see Table 1) (Rickman et al., 2004, 2008).

As seen from Table 1, the encounter frequency is much smaller for heavy stars than for light ones, and consequently the number of encounters is much larger for light stars than for heavy stars. In fact, out of a total number of 197,906 stellar encounters, 191,036 are due to light stars and only 6870 are due to heavy stars.

We recall that for models S(light) and C(light) only the light stars ($M_\star < 1.2\ M_\odot$) are taken into account, and for models S(heavy) and C(heavy) only the heavy stars ($M_\star > 1.2\ M_\odot$) are at work.

4.2. Synergy induced according to the star samples

In Table 3 we list the number of comets entering the observable region during intervals of 1 Gyr, for the different sets of models described at the end of the Introduction.

Moreover, as in RFFV08, in order to quantify the synergy we have computed the quantities: $\Delta N_C = N_C - N_G - N_S$ and $\tau = \Delta N_C/(N_S + N_G)$.[4]

Looking at Table 3, we notice that we always have $N_S(\text{all}) < N_S(\text{heavy}) + N_S(\text{light})$. This means that the intersection between the sets of comets injected by heavy stars and by light stars is not empty. Specifically, we observe from Table 3 that the sum of the injected numbers in the S(heavy) and S(light) models exceeds N_S(all) by about 20%.

Now, consider the total number of comets injected during the whole time span of 5 Gyr in the S(light) or S(heavy) model, and let us define an efficiency factor of a star sample to inject comets by: η_S = (number of comets injected)/(number of stellar encounters). We get, respectively: $\eta_{\rm light} \simeq 1.9 \times 10^{-2}$ and $\eta_{\rm heavy} = 39 \times 10^{-2}$.

However, due to the high encounter frequency of light stars (one every 26,000 yr), we have to expect that the stars of the S(light) model will as a rule interfere with each other, as comets are being injected. The number of injected comets may be affected by these interferences, and thus it is not directly comparable to the injected number in the S(heavy) model, where the amount of interference is much smaller (one star every 730,000 yr). Thus, in order to compute $\eta_{\rm heavy}$ for an encounter frequency similar to the one of light stars, we rather consider the difference between the number

---

[4] For the all-stars models, a small discrepancy with the results of RFFV08 may be noticed. This is due to a correction of our code in the check of perihelion passages. However, the discrepancy does not change in any sense the results of RFFV08.

of comets injected by all the stars in model S(all) and those injected by the light stars only in model S(light), *i.e.*, 5256–3730 = 1526. We consider the injection of this number of comets to be due to the heavy star encounters. Finally, we compute $\eta_{\text{heavy}} = 1526/6870$, obtaining: $\eta_{\text{heavy}} \simeq 22 \times 10^{-2}$.

Consequently, even in a full simulation where several stars almost always act simultaneously, heavy stars are *at least* 10 times more efficient than light stars in order to directly inject comets into the observable region.

As regards the synergy, we note that the values of $\langle\tau\rangle$ after more than 2 Gyr are higher for those combined models where only one subset of stars is included. The main circumstance contributing to this feature is the lower number of injected comets for the star-only models when only one subset of stars is considered. The corresponding number in the combined models is smaller too but by far not to the same extent.

In view of the small number of heavy stars, the high values of $\langle\tau\rangle$ for the heavy-star combined model are striking. As already noted in RFFV08, and as shown in Section 3.3, this synergy is mainly explained by the injection of comets by stars into the TAZ.

In Fig. 7 we plot the results of three sets of simulations: those obtained with all (heavy + light) stars (Fig. 7a), with only heavy stars (Fig. 7b), and with light stars only (Fig. 7c). The upper panel of each figure shows the number of comets injected into the observable region (perihelion passages with $q < 5$ AU) per period of 20 Myr versus time for three models. The black histograms correspond to the tide-only model (model G), the grey histograms correspond to the star-only models, *i.e.*, models S(all), S(heavy) and S(light), and the white histograms correspond to the combined models: C(all), C(heavy) and C(light). Let N_G, N_S and N_C be the numbers of comets plotted in the black, grey and white histograms, respectively. Then the lower panels show the quantity: $\Delta N_C = N_C - N_G - N_S$, which measures the synergy arising, when both the Galactic tide and the stars act simultaneously. Fig. 7a shows the same results as Fig. 2 of RFFV08.

In RFFV08, we found over the first ∼500 Myr that the synergy was negative, *i.e.*, the sum of the separate fluxes was larger than the combined flux. As explained by Matese and Lissauer (2002), this result is a typical outcome, when both tides and stars are individually able to fill the loss cone. The same phenomenon is observed in the present results for all three sets of simulations. But, in addition, in the lower panels of Fig. 7 – showing the values of ΔN_C computed every 20 Myr – we see that over the entire 5 Gyr of simulation, the synergy parameter ΔN_C becomes negative several times later on, namely, when showers occur. During those periods both the tides and the stars are indeed able to fill the loss cone individually. This phenomenon was not observed in RFFV08, since ΔN_C was then computed over periods of 50 Myr, which smoothed out the effect of the showers.

As may be noticed in Fig. 7b, the flux of comets generated by the heavy-star model shows large fluctuations and drops to zero several times. This indicates that the flux is characterized by comet showers completely filling the loss cone, which are separated by quiescent periods, during which the loss cone may become empty. On the contrary, the flux induced by the light stars is rather characterized by a permanently non-empty loss cone. Because strong comet showers occur during the two first billion years for the heavy-star model, the two fluxes (heavy stars and light stars) are overall comparable. Note that the relative difference between these two fluxes is much less than the corresponding difference in the number of stars (about a factor 28).

4.3. TAZ filling and flux of observable comets

In order to highlight the fundamental role of the TAZ filling to explain the flux of injected comets, we have devised the following experiment. We perform three different Oort cloud simulations (using a probability density $\propto a^{-1.5}$ in semi-major axis, as explained above) including both Galactic tides and stars: these differ only in terms of the set of initial conditions and the sequence of passing stars. The same three simulations have also been used as the basis of a different investigation of comet injection, which we are publishing separately in a paper submitted to Astronomy and Astrophysics.

The TAZ filling only relates to the flux of injected comets during quiescent periods, *i.e.*, outside comet showers. Thus, for the present purpose we need to identify the latter. We consider that a star induces a shower, when its encounter parameters $d_{\odot}$, $V_{\star}$ and $M_{\star}$ give an estimated number of injected comets $N_S > 25$, as computed from Eqs. (11) or (12) (depending on the stellar mass). The number 25 corresponds more or less to the background flux observed at the end of the simulations (see Fig. 8). In the case of such an encounter, we consider the shower to start at the perihelion passage of the star and to last for 10 Myr.

The full time span of each simulation is split into intervals of 100 Myr, starting 50 Myr after the beginning. Now consider specifically the central region of the Oort cloud. For each time interval we consider the number n_{TAZ} of comets in the TAZ of the central region computed at the middle of the interval, and the number n_{obs} of injected, observable comets coming from the central region during the quiescent part of the interval. We denote the length of this quiescent part, which is obtained by subtracting all the 10 Myr shower periods, by T_q. We then compute the quiescent flux τ_{obs} of observable comets per Myr by:

$$\tau_{\text{obs}} = \frac{n_{\text{obs}}}{T_q}. \tag{17}$$

Let us now assume that the quiescent flux of new, observable comets per Myr is strictly proportional to the number of comets in the central TAZ, *i.e.*,

$$\tau_{\text{est}} = n_{\text{TAZ}} \cdot C, \tag{18}$$

where C is a constant. We will use a value of C defined by the quiescent, injected comets between 300 and 500 Myr (this period is chosen because a transient effect is still at work in our simulations during the first 200 Myr[5]) (see Fouchard et al., 2005). The reason we do not choose this period of normalization even later is that we want the TAZ to be almost full, allowing more confidence in the results. We have:

$$C = \frac{\tau^{\star}_{obs}}{n^{\star}_{\text{TAZ}}}. \tag{19}$$

where the asterisks denote the specific use of the above-mentioned time interval.

Each simulation yields a different value of C – namely, $C = 0.644$, 0.569 and 0.652 in units of 10^{-3} Myr^{-1} – the differences being due to the specificity of each period. Because we want to treat C as a constant, applicable to any simulation, we will use the mean value $C = 0.622 \times 10^{-3}$ Myr^{-1}.

Note that, knowing the number n_{CR} in the central region of the Oort cloud (this is ∼200,000), n_{TAZ} may be replaced by $p_{\text{TAZ}} p_{\text{full}} n_{\text{CR}}$, according to Eq. (16). Consequently, we can also compute a maximum estimated flux corresponding to a completely filled TAZ ($p_{\text{TAZ}} = 100\%$) by:

$$\tau_{\max} = n_{\text{CR}} p_{\text{full}} C, \tag{20}$$

For the three present sets of initial conditions, $p_{\text{full}} = 2.542\%$ for the central Oort cloud. This is slightly different from the previous value

---

[5] This transient effect is due to the flat initial distribution of arguments of perihelia, which is not stable under the action of the Galactic tides. The tides modify this distribution, resulting in an increase of the flux at the beginning of the integrations.

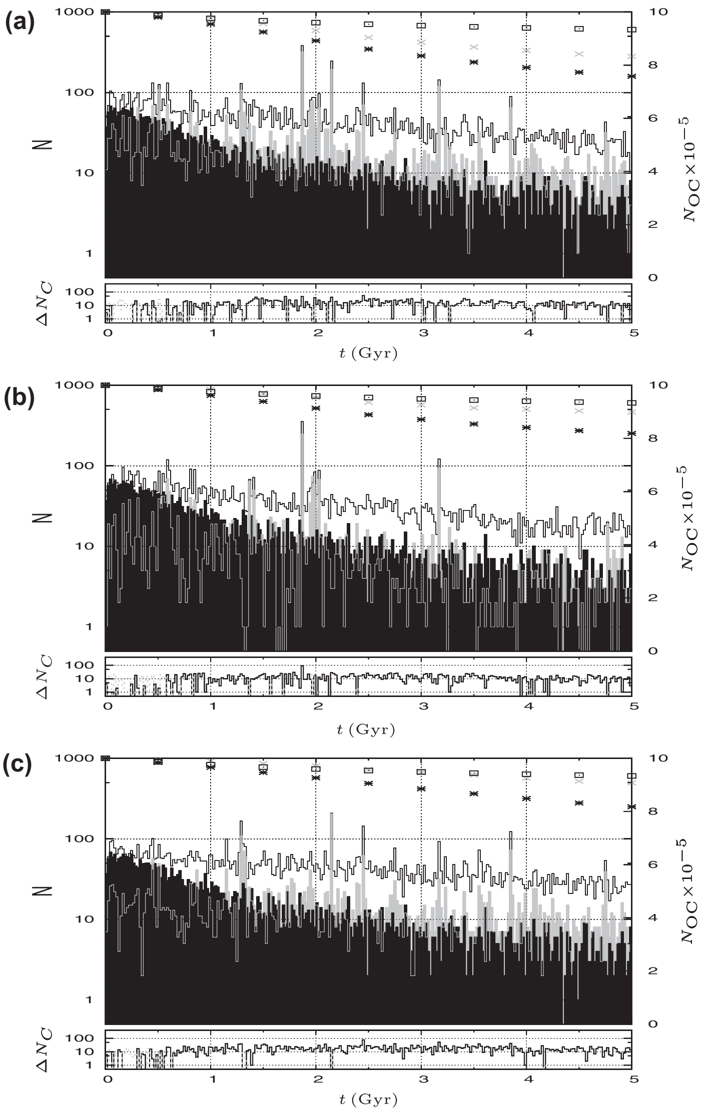

Fig. 7. The upper diagrams show the number of injected comets per 20 Myr versus time (in Gyr). The black histograms correspond to the tide-only model (N_G), the grey ones to the star-only model (N_S), and the white ones to the combined model (N_C). The lower graphs exhibit the values of $\Delta N_C = N_C - N_G - N_S$ in each 20 Myr time bin. When positive, ΔN_C is plotted by a full black line; otherwise we use a dotted grey line. Figure (a) is for the all-stars models, (b) for heavy-stars models and (c) for light-stars models. The black asterisks, grey asterisks and black rectangles in the upper panels indicate the number of comets remaining in the Oort cloud at intervals of 0.5 Gyr scale on the right axis for the combined models, the only stars models and only tides models respectively.

$p_{\rm full} = 2.63\%$, since the probability density of the semi-major axes is now chosen as $\propto a_\circ^{-1.5}$ instead of $a_\circ^{-1}$. Thus, the present Oort cloud is less concentrated toward the Sun, resulting in a lower value of $p_{\rm full}$.

Fig. 8a–c shows in the top panels the number of injected, observable comets per interval of 20 Myr and the number of comets in the Oort cloud at 500 Myr intervals versus time. The largest values of $I_{\rm dist}$ for passing stars are plotted in the middle panels, and at the bottom the values of $\tau_{\rm obs}$ for the central and entire Oort cloud are plotted along with $\tau_{\rm est}$ and $\tau_{\rm max}$. Each figure shows the output of one of the three simulations (Fig. 8a corresponds to the model C(all) already used in Section 4.2).

The agreement between $\tau_{\rm est}$ and $\tau_{\rm obs}$ for the central Oort cloud is rather good and improves with time along the span of the simulations. Thus the assumption behind the calculation of $\tau_{\rm est}$ appears warranted. This highlights the importance of the Galactic tides for comet injection from the central Oort cloud. The

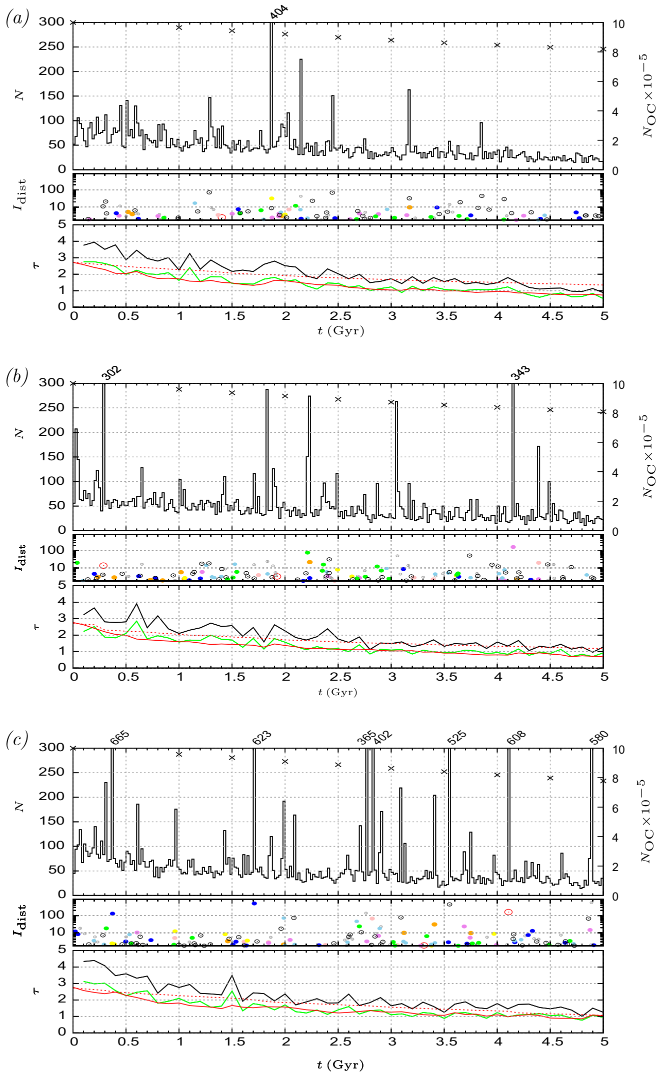

Fig. 8. In each diagram (a–c) the top panel gives the number of injected comets per 20 Myr (histogram) and the number of comets in the Oort cloud every 500 Myr (crosses). The middle panel shows the largest values of I_{dist} for passing stars (the colours denote different stellar types as in previous figures). The bottom panel shows the flux of injected, observable comets per Myr outside showers during each 100 Myr interval (τ_{obs}) for the central Oort cloud (green line) and the entire Oort cloud (black line), the estimated flux (τ_{est}) for the central Oort cloud (full red line) and the flux (τ_{max}) considering a filled TAZ (dashed red line). The figures represent three simulations using different sets of initial conditions and sequences of passing stars. (For interpretation of the references to colour in this figure legend, the reader is referred to the web version of this article.)

fluctuations shown by τ_{obs} are partly due to small number statistics, since T_q is sometimes rather small, and partly to inherent fluctuations in the efficiency of non-shower making stars between different intervals. The relatively small difference between τ_{obs} computed for the central and entire Oort cloud during the later part of the simulations shows that the central Oort cloud gives the major contribution to the quiescent flux of observable comets.

In addition, considering τ_{max} as an indicator of the number of comets in the central Oort cloud, we observe that the overall depletion of the Oort cloud comes mainly from its central part, whose population is depleted by almost a factor two in each simulation.

It is difficult to disentangle the role of individual stars in these simulations. For each sufficiently large increase of τ_{est} as judged by visual inspection of Fig. 8, Table 4 gives: the period during which the increase occurs (column 1), the TAZ filling expressed by the percentages $p^{(i)}_{\mathrm{TAZ}}$ and $p^{(f)}_{\mathrm{TAZ}}$ at, respectively, the beginning *(i)* and the end *(f)* of the 100 Myr periods (column 2), and the mass(es) of the star(s) with the largest value(s) of I_{dist} (if a single star is

Table 4
The periods during which clear increases of $\tau_{\rm est}$ are observed in Fig. 8, the values of the TAZ filling at the beginning $\left(p^{(i)}_{\rm TAZ}\right)$ and at the end $\left(p^{(f)}_{\rm TAZ}\right)$, and the masses of the stars with the largest values of $I_{\rm dist}$ that passed during the respective periods.

Period (Gyr)	$p^{(i)}_{\rm TAZ}$–$p^{(f)}_{\rm TAZ}$ (%)	$M_\star$ ($M_\odot$)
Simulation # 1		
0.5–0.6	83–89	**4**, **0.21**, **4**
1.8–1.9	71–83	2.1
3.1–3.2	62–69	**4**, **0.21**
Simulation # 2		
1.8–1.9	70–82	1.3
4.1–4.2	59–70	0.78
Simulation # 3		
1.4–1.5	68–78	2.1
2.7–2.8	78–83	1.3
3.5–3.6	74–86	0.21
4.1–4.2	75–88	9
4.8–4.9	76–101	1.1

clearly identified, only one mass is given, while otherwise several masses are listed) (column 3). This Table summarizes the most significant cases of instant TAZ filling, leading to "comet drizzles" as discussed in Section 3.5.

Most of the guilty stars are high-mass stars ($M_\star > 1.2\ M_\odot$). Among the ten comet drizzles listed, five involve stars of lower masses, but one of these is a marginal case ($M_\star = 1.1\ M_\odot$), and two others involve high-mass stars as well. A striking feature in Fig. 8 is the frequent occurrence of large $I_{\rm dist}$ values for the lightest M5 stars. This is due to the large overall frequency of these encounters, but note that Fig. 5 showed that even large $I_{\rm dist}$ values mostly lead to poor TAZ filling for those stars.

As seen in Fig. 8, the comet drizzles are generally associated to one comet shower (except for the one starting between 0.5 and 0.6 Gyr in the first simulation, where three showers seem to contribute to the TAZ filling). On the other hand, showers do not always give rise to visible drizzles, since it is harder to detect a TAZ filling than a loss cone filling. This is mainly due to the fact that the TAZ is never empty, whereas the loss cone is generally empty – at least for moderate semi-major axes.

The influence of these few stellar encounters on the long term flux is evident. Indeed, from a statistical point of view, the three sets of stellar encounters should lead to an identical background flux, whereas the comet showers and the comet drizzles may differ. In Fig. 8 we see that this is verified.

We observe in the top plots of Fig. 8a–c that during the last Gyr the first simulation has no strong stellar encounters, whereas the third one is affected by two such encounters yielding two comet drizzles (Table 4). The final observed fluxes from the central Oort cloud are 0.52 Myr^{-1} for the first simulation, and 0.97 Myr^{-1} for the third one. Thus the third simulation produces 1.87 times more comets from the central cloud at the end than the first one does.

This, again, is directly related to the TAZ filling, since at the end the central TAZ is filled only to 55% in the first simulation, whereas for the third simulation it is almost completely filled (97%). Considering the whole Oort cloud, the third simulation produces 1.39 times more observable comets at the end than the first one does. This ratio is lower, since in our dynamical model the contribution from the inner cloud outside showers is negligible, and the contribution from the outer cloud is not affected by the comet drizzles – its TAZ being always full.

Consequently, it appears that the flux of comets toward the observable region is closely related to the population of comets inside the TAZ. At the end of the simulations, we note that a TAZ filled at the level of 50–60% is guaranteed by the "background" passing stars. However, a single passing star – preferably massive – is able to fill the TAZ completely, resulting in an almost 100% increase of the flux of observable comets from the central cloud and of 40% from the entire cloud. Such increases may last for more than 100 Myr.

5. Conclusions

We have investigated the effect of stellar perturbations on the flux of comets coming from the Oort cloud into the observable region. We considered 13 different spectral types including 11 main sequence types, white dwarfs and giant stars.

As a first result it has been demonstrated and verified quantitatively (to our knowledge the first time) that high-mass stars ($M_\star > 2\ M_\odot$) – and in particular the most massive ones like the B0 stars – inject comets from large parts of the cloud during each encounter, whereas light stars ($M_\star < 1\ M_\odot$) mainly affect comets in their close vicinity. The number of injected comets is generally much larger for high-mass than for low-mass stars, thus partly compensating for the relative rarity of their encounters. Moreover, the efficiency of the stars to fill the *Tidally Active Zone* (the region from which the Galactic tides are able to decrease the perihelion distance of a comet below 5 AU) is also strongly dependent on the stellar mass.

Let us compare our study with that of Heisler et al. (1987). They simulated the cloud for only about 300 Myr and were thus not able to see the effects of very massive stars in creating comet showers. Their conclusion was that such stars are too rare to be efficient, but ours is quite different, since we follow the cloud for the full age of the Solar System. We may add that even more massive perturbers, like the GMCs, have so far been neglected in all Oort cloud simulations of the present type. Only analytic studies have been devoted to their effect on the Oort cloud (Hut and Tremaine, 1985) or wide binaries (Weinberg et al., 1987).

We have shown that the TAZ filling due to stellar encounters is a fundamental condition for injection of comets into the observable region. Indeed, as was already asserted in RFFV08, we have shown that the filling of the TAZ is directly related both to the synergy between the Galactic tides and stellar perturbations and to the flux of injected, observable comets.

The massive stars not only induce stronger comet showers than light stars do, but they are also able to trigger a synergy with the Galactic tides that may last for a few hundred Myr. Because of this synergy, a single star – preferably massive – is able to almost double the flux of comets from the central cloud for more than 100 Myr. If one considers the entire Oort cloud, the flux of comets is thus multiplied by about 1.4. We have called such events *comet drizzles*. It is important to keep in mind that the current flux of new Oort cloud comets may be influenced by an encounter with a massive star that occurred more than 100 Myr ago.

In conclusion, one may consider the flux of observable comets as a two steps mechanism: (i) First the comet is injected into the TAZ under the effects of stellar perturbations. This zone acts like a "waiting room" before entering the loss cone. (ii) Then the comet is sent from the TAZ into the depth of the loss cone under the action of the tides. Consequently, the long term synergy between tides and passing stars is crucial in order to maintain a flux of observable comets on a long time span. This is yet another new feature as compared with Heisler et al. (1987). Their ~300 Myr simulations started with a thermalized cloud, *i.e.*, a filled TAZ, and there was no time to empty it. Thus they found that comet injection is dominated by the Galactic tide. We too find that this is the case at the present time, but we emphasize that the reason is the long-term refilling of the TAZ by stellar encounters, especially those of high-mass stars.

As a final remark, note that on a time scale of ~100 Myr, the Sun is orbiting the Galactic centre and oscillating "vertically" through the Galactic mid-plane. Thus, the frequency of stellar encounters – and in particular that of high-mass stars – may show important variations, and it will eventually be important to include those variations (Gardner et al., 2011) when studying the likely origin of the currently observed new comets. While there is currently no way to verify observationally, whether we are living in a comet drizzle, the results of Gardner et al. (2011) show that the current location of the Sun near the Galactic mid-plane and near its peri-Galacticon causes the present, tidally induced flux of new comets to be higher (likely by $\sim$35%) than the long-term average. As far as we can tell, the amplitudes of both variations are similar.

Acknowledgments

We thank Ramon Brasser and Nathan Kaib, who as referees made numerous suggestions that greatly helped to improve the quality of the paper. This work was made possible due to a research Grant from the Polish Government (NN 203 392 734). In addition, HR was supported by a Swedish National Space Board Grant (119/07), and the work of GBV was supported by the Italian Space Agency, under contract ASI/INAF I/015/07/0.

References

Bailey, M.E., Stagg, C.R., 1988. Cratering constraints on the inner Oort cloud – Steady-state models. Mon. Not. R. Astron. Soc. 235, 1–32.

Breiter, S., Dybczyński, P., Elipe, A., 1996. The action of the Galactic disk on the Oort cloud comets. Astron. Astrophys. 315, 618–624.

Breiter, S., Fouchard, M., Ratajczak, R., Borczyk, W., 2007. Two fast integrators for the Galactic tide effects in the Oort cloud. Mon. Not. R. Astron. Soc. 377, 1151–1162.

Byl, J., 1983. Galactic perturbations on nearly-parabolic cometary orbits. Moon Planets 29, 121–137.

Duncan, M., Quinn, T., Tremaine, S., 1987. The formation and extent of the Solar System comet cloud. Astron. J. 94, 1330–1338.

Dybczyński, P.A., 1994. Impulse approximation improved. Celest. Mech. Dynam. Astron. 58, 139–150.

Dybczyński, P.A., 2002. Simulating observable comets. I. The effects of a single stellar passage through or near the Oort cometary cloud. Astron. Astrophys. 396, 283–292.

Fouchard, M., Froeschlé, Ch., Matese, J.J., Valsecchi, G.B., 2005. Comparison between different models of Galactic tidal effects on cometary orbits. Celest. Mech. Dynam. Astron. 93, 229–262.

Fouchard, M., Froeschlé, Ch., Breiter, S., Ratajczak, R., Valsecchi, G.B., Rickman, H., 2007. Methods to study the dynamics of the Oort cloud comets II: Modelling the Galactic tide. In: Benest, D., Froeschlé, Cl., Lega, E. (Eds.), Topics in Gravitational Dynamics, Lecture Notes in Physics, vol. 729. Springer Verlag, Berlin, pp. 271–293.

Fouchard, M., Froeschlé, Ch., Rickman, H., Valsecchi, G.B., 2010. Dynamical features of the Oort cloud comets. In: Souchay, J., Dvorak, R. (Eds.), Lecture Notes in Physics, vol. 790. Springer Verlag, Berlin.

García-Sánchez, J., Weissman, P.R., Preston, R.A., Jones, D.L., Lestrade, J.-F., Latham, D.W., Stefanik, R.P., Paredes, J.M., 2001. Stellar encounters with the Solar System. Astron. Astrophys. 379, 634–659.

Gardner, E., Nurmi, P., Flynn, C., Mikkola, S., 2011. The effect of the Solar motion on the flux of long-period comets. Mon. Not. R. Astron. Soc. 411, 947–954.

Heisler, J., Tremaine, S., 1986. The influence of the galactic tidal field on the Oort comet cloud. Icarus 65, 13–26.

Heisler, J., Tremaine, S., Alcock, C., 1987. The frequency and intensity of comets showers from the Oort cloud. Icarus 70, 269–288.

Holmberg, J., Flynn, C., 2000. The local density of matter mapped by Hipparcos. Mon. Not. R. Astron. Soc. 313, 209–216.

Hut, P., Tremaine, S., 1985. Have interstellar clouds disrupted the Oort comet cloud? Astron. J 90, 1548–1557.

Kaib, N.A., Quinn, T., 2009. Reassessing the source of long-period comets. Science 325, 1234.

Maciejewski, A.J., Prętka, H., 1998. Galactic disc tidal action and observability of the Oort cloud comets. Astron. Astrophys. 336, 1065–1071.

Matese, J.J., Lissauer, J.J., 2002. Characteristics and frequency of weak stellar impulses of the Oort cloud. Icarus 157, 228–240.

Matese, J.J., Whitman, P.G., 1992. A model of the galactic tidal interaction with the Oort comet cloud. Celest. Mech. Dynam. Astron. 54, 13–35.

Oort, J.H., 1950. The structure of the cloud of comets surrounding the Solar System and a hypothesis concerning its origin. Bull. Astron. Inst. Neth. 11, 91–110.

Rickman, H., 1976. Stellar perturbations of orbits of long-period comets and their significance for cometary capture. Bull. Astron. Inst. Czech. 27, 92–105.

Rickman, H., Froeschlé, Ch., Froeschlé, Cl., Valsecchi, G.B., 2004. Stellar perturbations on the scattered disk. Astron. Astrophys. 428, 673–681.

Rickman, H., Fouchard, M., Valsecchi, G.B., Froeschlé, Ch., 2005. Algorithms for stellar perturbation computations on Oort cloud comets. Earth Moon Planets 97, 411–434.

Rickman, H., Fouchard, M., Froeschlé, Ch., Valsecchi, G.B., 2008. Injection of Oort cloud comets: The fundamental role of stellar perturbations. Celest. Mech. Dynam. Astron. 102, 111–132.

Weinberg, M.D., Shapiro, S.L., Wasserman, I., 1987. The dynamical fate of wide binaries in the solar neighborhood. Astrophys. J. 312, 367–389.

Wiegert, P., Tremaine, S., 1999. The evolution of long-period comets. Icarus 137, 84–121.

3.1.2 Synergie à court terme

La synergie à court terme n'agit que pendant la dernière période orbitale de la comète avant d'être observable. On peut résumer ses effets en trois points essentiels (résultats publiés dans Fouchard et al., 2011b, inséré ci-après) :

- l'introduction des perturbations planétaires déplace le pic de Oort vers de plus petites valeurs du demi-grand axe ;
- alors que les marées seules sont incapables de rendre observable une comète ayant un demi-grand axe de l'ordre de 24 000 UA, l'aide des étoiles permet de rendre observables des comètes ayant un demi-grand axe de l'ordre de 20 000 UA (les étoiles seules pouvant injecter des comètes avec des demi-grands axes bien plus petits, mais le flux est très faible en dehors des douches cométaires) ;
- il existe une interférence constructive entre les perturbations stellaires et les effets des marées galactiques engendrant une augmentation du flux de l'ordre de 20%.

Cette synergie a donc des effets déterminants sur la localisation et la forme du pic de Oort. Or ce pic est pour le moment le seul indice observable que l'on ait sur le nuage de Oort lui-même, et donc sur sa formation. Il est donc important de bien pouvoir modéliser cette synergie à court terme sur les comètes observées. Pour cela on a besoin de connaître l'historique récent des rencontres stellaires de notre système solaire. On a montré que les données provenant de la mission HIPPARCOS sont insuffisantes pour bien modéliser cette synergie alors que celles que nous fournira la mission GAIA le seront. Rickman et al. (2012) est plus spécifiquement consacré à cet apport de la mission GAIA sur la possibilité de bien modéliser cette synergie.

A&A 535, A86 (2011)
DOI: 10.1051/0004-6361/201116514

Astronomy & Astrophysics

The last revolution of new comets: the role of stars and their detectability

M. Fouchard[1,2,⋆], H. Rickman[3,4], Ch. Froeschlé[5], and G. B. Valsecchi[6]

[1] University Lille 1, LAL, 59000 Lille, France
e-mail: `marc.fouchard@univ-lille1.fr`
[2] Institute de Mécanique Céleste et Calcul d'Éphémérides, 77 Av. Denfert-Rochereau, 75014 Paris, France
[3] P.A.S. Space Research Center, Bartycka 18A, 00-716 Warszawa, Poland
[4] Dept. of Physics and Astronomy, Uppsala University, Box 516, 75120 Uppsala, Sweden
[5] UNSA CNRS UMR 6202, Observatoire de la Côte d'Azur, Bd de l'Observatoire, BP 4229, 06304 Nice Cedex 4, France
[6] IASF-Roma, INAF, via Fosso del Cavaliere 100, 00133 Roma, Italy

Received 14 January 2011 / Accepted 30 August 2011

ABSTRACT

Context. This work is a follow-up of a previous study, where we simulated the dynamical evolution of the Oort Cloud over 5 Gyr with special attention to the injection of comets into observable orbits.
Aims. We wish to clarify how comet injection operates with two types of perturbers: Galactic tides and passing stars. We illustrate why attempts to identify the stars that might have played an important role in injecting the observed new Oort Cloud comets are as yet unlikely to succeed, and investigate how large an improvement can be expected from the *Gaia* mission.
Methods. We simulate a 5 Gyr time span, concentrating on the injections found during the last 3 Gyr by extracting detailed information about the last revolution of the injected comets. We analyse the contributions of both the Galactic tides and the stars separately, and assess their importance as a function of the semi-major axis of the comets. We also compute the distances and motions of the perturbing stars at the time the comets reach their perihelia and thus estimate their observability.
Results. By studying more than 20 000 injected comets, we determine how the likelihood of tidal and stellar injections varies with the semi-major axis. We establish the range of semi-major axis for which a real-time synergy between stellar and tidal perturbations is important. We find how many perturbing stars could be identified using H and *Gaia* data, and how the dynamics of injections would change, if only the observable stars were acting.
Conclusions. The number of injected comets peaks at a semi-major axis (a) of about 33 000 AU but the comets spread over a wide range around this value. The tides are unable to inject any comets at $a < 23\,000$ AU but would be able to inject almost all of them at $a > 50\,000$ AU. The real-time synergy is found to extend between $a \sim 15\,000$ AU and $a \sim 45\,000$ AU and to be the main contributor at $a \sim 25\,000$ AU. Stellar perturbations make important contributions at all semi-major axes. On the basis of H data, only a minority of the stars that may contribute to comet injections are detectable, since most stars have escaped to distances beyond the H detection limit. For *Gaia*, on the other hand, a large majority of the perturbing stars will be both identifiable and measurable.

Key words. celestial mechanics – comets: general – Oort Cloud

1. Introduction

When Oort (1950) introduced the concept of a very distant source region for long-period comets (the "Oort Cloud"), he was aware of the need for an efficient mechanism to bring the perihelia of comets from the region well beyond the orbits of Jupiter and Saturn (typically, perihelion distance $q > 15$ AU) into the observable range (nowadays, $q < 5$ AU). If this does not happen during just one orbit, it is likely that the comet is lost from the process because of a planetary perturbation that either ejects it from the Solar System or captures it into a much more tightly bound orbit.

Oort (1950) identified the impulses imparted to comets by passing stars as a likely mechanism for comet injection. Under usual conditions, it would work exclusively for the orbital range of the "new comets", i.e., for semi-major axes $a > 10\,000$ AU. Comets orbiting at closer distances would not have the time to experience a relevant perturbation during one orbital revolution. However, Hills (1981) pointed out that an Oort Cloud extending inward of the above limit will from time to time be perturbed by close stellar encounters – possibly leading to large, episodic increases in the flux of new comets including smaller than usual semi-major axes. These events have been termed "comet showers".

In the mid-1980's, it was realized that the Galactic tidal force also has an important influence on comet injection, and may in fact represent the predominant effect (Duncan et al. 1987; Delsemme 1987). In particular, Heisler & Tremaine (1986) showed that the "vertical" disk tide is an efficient perturber, causing regular q oscillations in the range of a of about 30 000–40 000 AU. On the basis of H results (Perryman et al. 1997), the local density of the Galactic disk has been found to be lower than previously thought (Holmberg & Flynn 2000) thus reducing the influence of the disk tide, but its significance remains indisputable.

In a previous paper (Rickman et al. 2008), we simulated the evolution of the Oort Cloud assuming that it is perturbed by both Galactic tides and passing stars over a time interval of up to 5 Gyr. We found that the injection of new comets at present – as well as during the past few Gyr – is dominated by a synergy

---

[⋆] *Present address*: Observatoire de Lille, 1 impasse de l'Observatoire, 59000 Lille, France.

between the two perturbers. While it may be that this synergy is largely due to the stars filling the "tidally active zone", from where the disk tide may bring the comets into observable orbits (Fouchard et al. 2011, to be referred to as FFRV11), there also appears to be a more direct involvement of the stars that is quite significant at $a < 30\,000$ AU (Rickman et al. 2008).

Another way to analyse the process of comet injection was followed by Dybczyński (2001, 2006), who took a sample of high-quality original orbits of observed long-period comets, integrating them backward to the previous perihelion passage. In his first paper, he considered only the Galactic tides and found that, while comets with original semi-major axes of $a_\mathrm{o} > 25\,000$ AU tend to have moved from orbits with $q > 15$ AU, those with smaller values of a_o have not. By performing additional integrations including the perturbing action of the Algol system during its slow encounter about 7 Myr ago, he was able to show that a few additional comets made the jump from $q > 15$ AU. He thus proposed that the inclusion of the stellar perturbations in the dynamical model would be very important in revealing which comets are indeed "new" rather than simply fulfilling a criterion based on a_o.

The second paper (Dybczyński 2006) presented an improvement to the search for H stars experiencing close encounters with the Sun in the recent past or near future, which had earlier been made by García-Sánchez et al. (1999, 2001). This may be said to represent the state of the art of the matter, and the result was a list of 23 stars identified to have passed within 2.5 pc of the Sun during the previous 3 Myr. Only 11 of these actually penetrated to within 2 pc, which is ~10% of the statistically expected total of ~120 based on an expected flux of about 10 encounters within 1 pc per Myr (García-Sánchez et al. 2001). None of the passages was found to have triggered the injection of any observed comet, and Dybczyński's conclusion was that the current comet injections are dominated by the Galactic tides.

Królikowska & Dybczyński (2010) selected a sample of 26 comets for which high-quality original orbits could be derived while accounting for non-gravitational (NG) effects (Królikowska 2006). All these comets have original values of $1/a_\mathrm{o}$ less than 10^{-4} AU^{-1}, so they are "new" in Oort's sense. For swarms of clones compatible with the observations, these authors integrated the orbits backward and forward until the subsequent perihelion passage or the ejection of the comet from the Solar System. In accordance with Dybczyński (2006), only the Galactic tides were considered as a perturbing force in these integrations. Thus, taking account of observational uncertainties as well as NG effects, they concluded that fewer than 30% of the comets are actually new in the sense of having passed from $q > 15$ AU during the last revolution. This result is largely caused by non-gravitationally determined original orbits tending to have smaller semi-major axes than one obtains when neglecting the NG effects.

Dybczyński & Królikowska (2011) performed a similar study, focusing on relatively recent comets with perihelia beyond 3 AU. They again found a large fraction of "dynamically old" comets, which apparently had their previous perihelion passage well within the "loss cylinder". Thus, the Jupiter-Saturn barrier does not appear to be as efficient an obstacle as has been thought. While the actual role of this barrier was recently investigated by Kaib & Quinn (2009) and shown to allow the passage of comets via previously unexpected routes, it is also of interest to re-evaluate the conclusions about the insufficiency of stars to act in the current comet injections. In this paper, we investigate the roles of passing stars and the Galactic tides during the last revolution before an observable comet appears, based on our dynamical simulations.

In Sect. 2, we introduce three different hypothetical Oort Clouds containing 10^6 comets perturbed simultaneously by the Galactic tides and three different sequences of stellar encounters, each sequence acting on one Oort Cloud. Section 3 is devoted to our results, paying special attention to the role of the stars in connection with that of the tides. In Sect. 4, we investigate, based on our simulations, the observability by the H or *Gaia* missions of the stars that have passed during the last revolution of the currently discovered new Oort Cloud comets, and whether only those that are observable would be able to inject a sufficiently large amount of comets. Our conclusions are summarized in Sect. 5.

2. Models and calculations

2.1. Models

As in Rickman et al. (2008), we build a thermalized initial Oort Cloud of 10^6 fictitious comets with orbital elements chosen at random, and we study their dynamical evolution over 5 Gyr. Each comet is subject to both tidal and stellar perturbations. The initial conditions of these fictitious comets are as follows: the semi-major axes a_0 are chosen such that $3 \times 10^3 < a_0 < 1 \times 10^5$ AU with a probability density $\propto a_0^{-1.5}$ (Duncan et al. 1987), and the eccentricities e_0 are chosen with a density function $\propto e_0$ with the constraint that the perihelia are outside the planetary system, i.e., $q_0 > 32$ AU. The initial angular elements, ω_0, Ω_0 and M_0, which may be defined with respect to an arbitrary frame of reference, are randomly chosen with a flat distribution, and the same holds for $\cos i_0$.

We choose three different sets of initial conditions, i.e., we consider three different initial Oort Clouds. They form three realizations of the distributions described above. We also consider three different samples of passing stars. Each sample corresponds to a sequence of 197 906 stellar encounters, occurring at random times during an interval from zero to $t_\mathrm{max} = 5 \times 10^9$ yr, with random solar impact parameters up to $d_\mathrm{max} = 4 \times 10^5$ AU, and with random stellar masses and velocities according to the procedure described by Rickman et al. (2004, 2008). Each cloud defined previously is perturbed by one of the three stellar samples.

For the computation of the stellar perturbations acting on the heliocentric orbit of a comet, we use the "sequential impulse approximation" (Rickman et al. 2005), which employs hyperbolic deflections to compute the impulses (Dybczyński 1994) while accounting for the motion of the comet by integrating the instantaneous acceleration over time using finite steps. This method has been shown to be quite accurate even for comets moving in the inner core.

Our simulation proceeds for each comet by integrating the Galactic tidal effects as described in Breiter et al. (2007) and Fouchard et al. (2007) between successive moments of closest approach to the Sun by stars. At these moments, the tidal integration is stopped, and the orbital elements of the comet are updated using the stellar impulses.

The motions of the fictitious comets are integrated at most over 5 Gyr. However, the integration is stopped when the heliocentric distance of a comet becomes either $r > 4 \times 10^5$ AU or $r < 15$ AU. The threshold of 15 AU is a crude way to model planetary perturbations. A comet with $q < 15$ AU is assumed to either be ejected into interstellar space, which means that the current perihelion passage is the last one, or be sent into a much more tightly bound orbit, in which case the influence of external perturbers (Galactic tides or passing stars) is effectively cut off. Each time we stop an integration on account of $r < 15$ AU, we take note of the actual perihelion distance and record a case of injection into an observable orbit, if $q < 5$ AU. We refer to this as a post-injection orbit. For every comet that is thus injected, its orbital elements at the previous perihelion passage are saved. These refer to what we shall call the pre-injection orbit.

The number of injected comets per interval of 20 Myr versus time is shown in Fig. 1. The sequences of stellar encounters are seen to be quite different, the third simulation having more frequent strong stellar encounters than the other two. This is shown by the large number of high peaks, corresponding to comet showers. However, the background fluxes are similar with a global decrease in each case. In this regard, we emphasize that all the stellar encounter sequences are constructed in the same way and are consistent with the observed number densities and velocities of stars in the current solar neighbourhood. Obviously, these data do not provide strong constraints on the history of the Oort Cloud in terms of major stellar perturbations, but we can see that the quiescent flux of comet injections is not very strongly affected by this uncertainty.

The decrease in the flux is explained by the depletion of the tidally active zone (TAZ) – i.e., the region of phase space from which the Galactic tides are able to decrease the perihelion distance below 5 AU – with time. We describe this phenomenon in detail in FFRV11. The strong stellar perturbations that induce comet showers are efficient in re-injecting comets into the TAZ, thereby influencing the flux of injected comets during several hundred Myr hence, but they also accelerate the loss of comets from the "central part" of the cloud (intermediate range of semi-major axes), where most of the injections occur. That the background flux behaves similarly in the three simulations in spite of the different numbers of shower-inducing events can thus be understood by considering that the flux of injections is proportional to both the number of comets in the central Oort Cloud and the relative amount of TAZ filling in this zone. With a larger number of shower-inducing stellar encounters, the first factor decreases while the second one increases.

At the beginning of the integrations, the TAZ is full. Because this situation is rather exceptional the first 2 Gyr of each integration will not be taken into account (see FFRV11). This 2 Gyr time span is more or less the time needed for the central Oort Cloud to settle into a normal state of TAZ filling.

2.2. The comet enhancements

The high peaks seen in Fig. 1 are indicative of comet showers caused by specific stellar encounters. The comets injected during a shower have different characteristics in terms of their number and distribution of orbital elements than the comets injected during a quiescent period. For instance, the high rate of injections that characterizes comet showers is often due to the rarely seen passage of a star through the inner core of the Oort Cloud. This causes lots of injections from this inner core (small values of the semi-major axis), which is more or less immune to injections under normal circumstances. Consequently, we need to take care to separate the injected comets into those that experienced quiescent conditions and those that might have suffered an abnormally large stellar perturbation. In particular, we aim to use the set of quiescent comets as a proxy for the current conditions in order to draw conclusions about the injection of the observed "new comets".

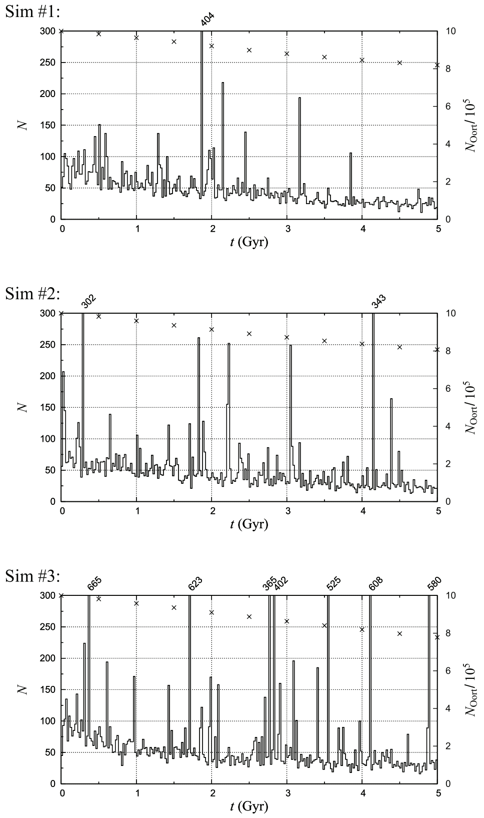

Fig. 1. Number of observable comets per interval of 20 Myr versus time for the three simulations. When the number exceeds 300, it is written above the respective graph. The crosses give the number of comets in the Oort Cloud as counted every 500 Myr (scale to the right).

The problem is how can we define a comet shower? Such an event is due by definition to a single star. Hence, the best approach is to assess, for each star, whether the star is capable of inducing a large enhancement of the rate of comet injections or not. To this aim, we use the results of the simulations described in FFRV11, which tell us that, using $\simeq 10^6$ sample comets, the number $N_\star$ of injected comets, following a single stellar encounter, is statistically approximated by[1]

$$N_\star = \left(\frac{M_\star}{V_\star \sqrt{d_\odot}}\right)^{1.82} \times 16.23 \tag{1}$$

for low-mass stars, and

$$N_\star = \left(\frac{M_\star}{V_\star d_\odot^2}\right)^{0.89} \times 12.83, \tag{2}$$

for high-mass stars. The units for $M_\star$ (stellar mass), $V_\star$ (stellar speed at infinity), and $d_\odot$ (impact parameter with respect

---

[1] These two power laws were obtained from a different initial Oort Cloud, i.e., with a flat distribution of orbital energy. It is, however, quite close to our simulated initial Oort Cloud, also because the distribution of orbital energy evolves with time, as we see later. Consequently, we apply these power laws to our simulated Oort Cloud.

to the Sun) are, respectively, the solar mass, 40 km s^{-1}, and 20 000 AU. High-mass stars were found to be those with $M_\star > 2$ and low-mass stars those with $M_\star \leq 0.9$. The two formulae are relevant for close encounter perturbations and distant, tidal perturbations, respectively (FFRV11). Stars of intermediate masses would likely act in either way, depending on the detailed circumstances.

In this investigation, we use the term *comet enhancement* for cases when a star passes with $N_\star > 5$. For each star of our simulations, we know $M_\star/V_\star$, and using Eqs. (1) and (2) one can derive two values of $d_\odot^{(c)}$ (one per equation) such that $N_\star > 5$ for $d_\odot < d_\odot^{(c)}$. If $M_\star/V_\star = 0.60077$, both values of $d_\odot^{(c)}$ are equal, amounting to 1.316 (i.e., 26 320 AU). In general, when selecting the value of $d_\odot^{(c)}$ to use, we always take the smallest one, i.e., the most restrictive definition of enhancement-producing stars.

In terms of the 13 stellar types that we consider, the most common ones (red and white dwarfs) predominantly have $M_\star/V_\star < 0.60077$, which means that we identify the enhancement makers among such stars using Eq. (1) – as indeed we should (FFRV11). For all the other types (giants and main-sequence stars down to K0), we mostly use Eq. (2). Judging from Fig. 1 of FFRV11, this choice is actually relevant – not only for the high-mass stars defined above but also for the lower mass types.

We subdivide the injected comets into two categories according to whether or not there was any passage by an enhancement-producing star during the last revolution of the comet. We use the term *quiescent comets* strictly for those comets that did not experience any such stellar passage, and all the others will be described as *non-quiescent comets*. Only the first category will be used as a proxy for the observed new comets.

We note that in our simulations, two comets injected into simultaneous perihelion passages may actually belong to different categories, because their last revolutions may have taken different amounts of time. Thus, the comet with the shorter period may fulfil the requirement of being quiescent, while the other one does not. Hence, we do not consider comet enhancements in terms of specific time intervals. We use instead “quiescent” and “non-quiescent” as flags of injected comets indicating whether their last orbit may or may not have been influenced by a star with a high injection efficiency[2].

With the above criteria, we have a total of 1227 enhancement-producing stars out of a total of 593 718 passing stars during the full length of all three simulations. During the last 3 Gyr, the number of enhancement-producing stars is 755 out of a total of 355 821 passing stars. While this fraction is very small, the number of enhancement makers is much larger than the number of high peaks in Fig. 1. Thus, we can expect all high peaks (major showers) to be caused by enhancement makers, and conversely, the stars that do not cause enhancements also not to cause any significant peaks.

From Fig. 1 of FFRV11, one can see that the number of injections caused by non-enhancement-producing stars is never much larger than 10 for an Oort Cloud of the same size as the current ones. This confirms the above expectation. Moreover, some enhancement-producing stars actually produce no comet injections at all, even though the statistical expectation is at least 5. We conclude that our definition of enhancement-producing stars is rather liberal, and many comets that we consider as non-quiescent actually behave in the same way as the quiescent ones.

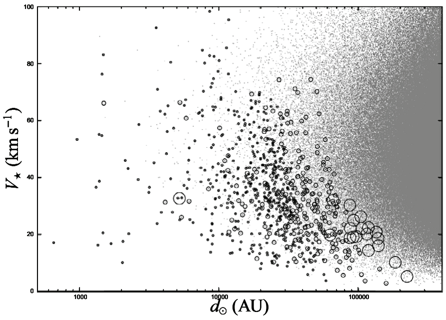

Fig. 2. Velocity at infinity versus solar impact parameter for all the stars passing during the last 3 Gyr of the simulations. Tiny, grey dots correspond to stars that do not cause enhancements, black dots to enhancement-procucing stars with $M_\star < 1.2$, small black circles to enhancement-producing stars with $1.2 < M_\star \leq 4$, and large black circles to enhancement-producing stars with $M_\star = 9$ (B0 stars).

If the number of injections by a certain star in our simulations were 5–10, the corresponding number for the real Oort Cloud in case this contains 10^{12} comets would be ~(5–10)× 10^6. Over an interval of several million years, the flux of new comets with $q < 5$ AU would only be a few per year, which would be barely noticeable as an increment upon the estimated flux of 0.8 comets per year per AU of perihelion distance after correction for discovery bias (Francis 2005). Thus, what we call enhancements are not comparable to the comet showers discussed in previous literature. They are much less significant, so our criterion for defining quiescent comets is indeed conservative.

Such conservatism is of relevance, since the Solar System is statistically unlikely to be experiencing a major comet shower at the moment (Dones et al. 2004), and the orbital distribution of long-period comets does not show the expected features of a shower (Dybczyński 2002). Hence, the observed new comets are most likely quiescent ones, and in order for our model to be applicable to these, our quiescent comets should indeed be quiescent, i.e., unaffected by any significant enhancement.

Figure 2 plots the velocity at infinity $V_\star$ versus the solar impact parameter $d_\odot$ for stars passing during the last 3 Gyr of all three simulations. The masses of the enhancement-producing stars are indicated by different black symbols, while all other stars are shown by tiny, grey dots. As expected, the enhancement-producing stars are stars with small impact parameter and/or low velocity as a general feature. However, the higher the mass of the star, the larger the impact parameter is allowed to be. In particular, the highest-mass stars may produce enhancements at almost any impact parameter, if their velocity is low enough.

We have a total of 20 446 injected comets during the last 3 Gyr, among which 29.9% are of the quiescent type and 70.1% are non-quiescent. During the first 2 Gyr, we had 21 385 injected comets, out of which 36.7% were quiescent. The higher proportion of quiescent comets initially is due to the TAZ being more populated, which facilitates the role of the tides in injecting comets. As mentioned above, this is the reason why we study only the comets injected during the last 3 Gyr.

---

[2] Note that a non-quiescent comet does not have to be strongly perturbed by the enhancement-producing star. Its injection may well have been caused by the Galactic tides or by another star.

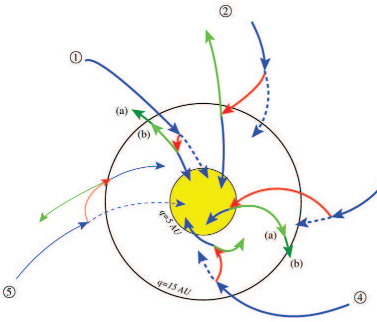

Fig. 3. Schematic representation of the variation in the angular momentum for different injection scenarii. The distance to the centre in this diagram represents the angular momentum of the comets, i.e., the perihelion distance in the present case of quasi-parabolic orbits. The full black circle corresponds to a perihelion distance of 15 AU, and the yellow disk corresponds to perihelion distances smaller than 5 AU. The meaning of the arrows is explained in the text. For each trajectory, the comet starts at perihelion before its last revolution.

2.3. Injection scenarii

Before explaining our results we need to describe the different main scenarii for the last orbital period of injected comets. To begin with, we note that stellar perturbations are rarely negligible – thus the pre- and post-injection orbits are rarely connected by a single tidal trajectory. As illustrated in Fig. 3, there are not very many cases to distinguish. The figure shows the main features of dynamical evolutions leading to comet injection during the last orbit before the observable perihelion passage. We note that it does not cover all possible scenarii but has been simplified for clarity.

We represent the generally decreasing trend of perihelion distance associated with injections by arrows directed toward the centre. The yellow region denotes the observable orbits, and the white, surrounding one represents the Jupiter-Saturn barrier. The red and blue arrows show the evolution – forwards in time – caused by stellar impulses and the Galactic tides, respectively. By dashed blue arrows, we indicate how the tidal perturbation would have continued to act in the absence of the stellar impulse. The green arrows show the backward evolution starting from the time of the stellar perturbation, if only the tides are allowed to act. We assume for simplicity that there is only one significant stellar impulse during the last revolution of the comet.

The cases numbered 1−4 represent the vast majority of all injections. Case 1 refers to tidal injections, where stars play a relatively insignificant role. They may perturb the comets, thus affecting somewhat the post-injection orbits, but even in their absence the initial trajectory would lead to an injection because of the tides. We distinguish two subclasses called *a* and *b*, depending on the outcome of a backward integration with only tides. In case 1*a*, the comets cross the barrier into orbits with $q > 15$ AU, while in case 1*b* they do not. Case 2 is different, since the injection would have failed in the absence of the stellar impulse. However, the star does not inject the comet by itself – it is only a helper to the tides.

Case 3 is again different, because now the star actually performs the injection, and the tidal action is generally rather insignificant. We may again distinguish two subclasses in the same way as in case 1. Thus, case 3*b* refers to comets that get injected by a stellar impulse but would appear to have been tidally injected as judged from a purely tidal backward integration. As previously mentioned, this is a relatively rare phenomenon. Case 3*a* is the more common one, where the injected comets bear no traces of tidal injection. Finally, in case 4 an injection is achieved, but it is impossible to ascribe it to either stars or tides.

Case 4 may also be considered as a real-time synergy between the stars and tides, since these two mechanisms interact in a constructive way to ensure that the comets are injected. In reality, however, it must also happen that an injection, which the tides alone would have achieved, fails because of a stellar impulse. This is indicated as case 5 by thinner arrows, since our normal simulation does not register such outcomes. Nonetheless, we did investigate these outcomes, as described in the next section.

We now define three sets of injected comets:

- set $\mathbb{G}$ consists of those for which a backwards integration using only the Galactic tides yields a previous perihelion distance larger than 15 AU. In other words, these are comets whose post-injection orbits would have been reached by tidal injections in the absence of stars. This set involves cases 1*a*, 2, and 3*b* of Fig. 3;
- set $\mathbb{G}'$ contains those for which the forward integration yields a perihelion distance smaller than 5 AU even when turning off the stellar perturbations during the last revolution. In other words, the pre-injection orbits would lead to tidal injections in the absence of stars. This set involves case 1 of Fig. 3;
- set $\mathbb{S}$ contains the injected comets for which there is one passing star during the last revolution that induces a crossing of the Jupiter-Saturn barrier. This set is represented by case 3 of Fig. 3.

These three sets intersect to some extent. For instance, comets that follow trajectory 1*a* belong to both $\mathbb{G}$ and $\mathbb{G}'$, whereas case 1*b* comets belong only to $\mathbb{G}'$ and case 2 comets belong only to $\mathbb{G}$. Moreover, there are injections that do not belong to any of the sets, as illustrated by case 4 of Fig. 3.

3. General results

3.1. The injected comets

Among the total of 20 446 comets injected during the last 3 Gyr of our simulations, 9642 comets belong to the $\mathbb{G}$ set, out of which 5107 (52.9%) are non-quiescent, and 8915 comets belong to the $\mathbb{S}$ set, out of which 8257 (92.6%) are non-quiescent. We note that 739 comets belong to both $\mathbb{G}$ and $\mathbb{S}$ sets, and out of these 624 (84.4%) are non-quiescent. Finally, 2628 injected comets belong to neither $\mathbb{G}$ nor $\mathbb{S}$. Out of these, about 60% are non-quiescent.

It is well-known that both tidal and stellar perturbations depend strongly on the semi-major axis of the comets, and in Fig. 4 we show the effect of these dependences on the injection statistics in terms of our $\mathbb{G}$ and $\mathbb{S}$ sets. For this purpose, we divided the range of the semi-major axis (i.e., [3000, 100 000] AU) into 150 bins such that the comets are initially equi-partitioned among the bins. For each interval, we show the number of injected comets (n_{inj}), as well as the fractions $p_{\mathbb{G}}$ and $p_{\mathbb{S}}$ of comets belonging to sets $\mathbb{G}$ and $\mathbb{S}$, respectively, among the injected comets. This is done separately for quiescent and non-quiescent comets.

From top to bottom, the first four panels of Fig. 4 show the behaviour of n_{inj}, $p_{\mathbb{G}}$, $p_{\mathbb{S}}$ and $p_{\mathbb{S}} + p_{\mathbb{G}}$ versus the semi-major axis

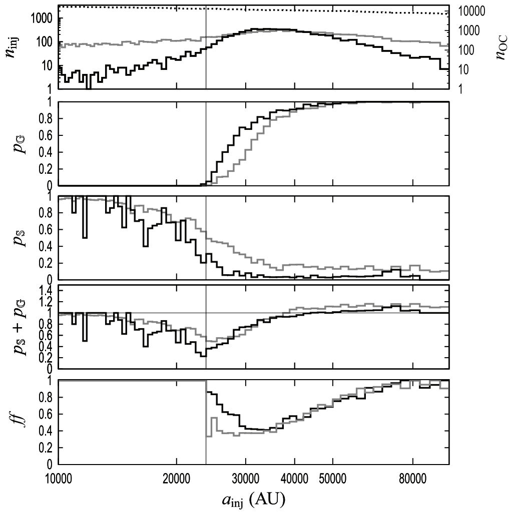

Fig. 4. The first four panels show, from top to bottom: the number of injected comets, the fraction of injected comets in set $\mathbb{G}$, the fraction in set $\mathbb{S}$, and the sum of these two fractions, all plotted versus the semi-major axis at injection (a_{inj}). In these plots, the full black lines correspond to quiescent comets and the full grey lines to the non-quiescent comets. The dotted black line in the uppermost plot shows the number of comets (given on the right axis) in the Oort Cloud at 3 Gyr. The horizontal grey line in the bottom plot indicates the value of unity for the sum of the two fractions. The fifth panel shows the fraction of injected comets that are not injected any more, if one removes the stellar perturbations during the last revolution (black line), and the fraction of comets injected in a tides-only model that are not injected any more, when one adds the stellar perturbations (grey line). In all the plots, the vertical dashed line indicates the threshold a_{crit}, below which no comets belong to the $\mathbb{G}$ set.

at injection (a_{inj}). The fifth panel is different, as we describe it later.

Because we consider only the last three gigayears, the distribution of comets in the Oort Cloud has changed from the initial state. Some comets have left the cloud, and some have migrated between different ranges of semi-major axis. To illustrate the effect of the population of the Oort Cloud at injection, the distribution of the semi-major axis at 3 Gyr is plotted in the upper panel. Initially, the number of comets in each bin was close to 20 000, which is situated at the top of the plot. We see that some depletion has occurred and that this depletion gets stronger for more distant parts of the cloud. The outermost parts have been depleted by more than a factor of two, while the innermost parts are left practically unchanged. At times later than 3 Gyr, which we consider, these depletions will have grown further.

Our results on the number of injected, quiescent comets are in general agreement with the location of synthetic Oort spikes found by others using similar experiments (e.g., Wiegert & Tremaine 1999; Emel'yanenko et al. 2007). Our maximum of the injection efficiency occurs around 33 000 AU. The decrease in n_{inj} toward smaller semi-major axes is due to the well-known decrease in the average size of both tidal and stellar perturbations. For larger semi-major axes, the decrease is partially explained by the strong depletion of the outer parts of the Oort Cloud that we commented on above. However, the main reason is that the Galactic tides change the perihelia of outer Oort Cloud comets very rapidly. The timescale is shorter than the orbital period. Thus, under the action of the tides alone, the probability for a comet to reach its perihelion when the perihelion distance is below 5 AU, i.e., the ratio of the time spent with $q < 5$ AU to the orbital period P, behaves as P^{-2} (Fouchard et al. 2010). For stellar injections, the same problem arises, i.e., the tides are likely to remove the comet from the observable zone, if there is sufficent time. Consequently, even though the number of potential comets to be injected increases with a because of the growing size of the perturbations, this effect is more than offset by the aforementioned a^{-3} dependence.

We note that for non-quiescent comets, the injection efficiency is almost flat with respect to the semi-major axis. This is consistent with previous results (Rickman et al. 2008) because during a comet shower the loss cone is filled at almost any semi-major axis. We conclude that, even though this category has been very liberally defined, it terms of numbers it is dominated by shower comets.

The smallest semi-major axis of the $\mathbb{G}$ set at injection is 23 774 AU. We interpret this to mean that below $a_{\mathrm{crit}} \simeq$ 23 000 AU the tides are unable to inject comets on their own. However, for larger a_{inj} the $\mathbb{G}$ set fraction of injected comets rises rapidly, especially for quiescent comets, so that for $a_{\mathrm{inj}} >$ 50 000 AU it is almost unity for both categories. This illustrates the rapidly growing efficiency of tidal perturbations, which eventually even acts to quench the injection rate, as discussed above.

In the range where the rate of quiescent comet injections is at its maximum, we have $p_{\mathbb{G}} = 0.812$, implying that for almost 20% of the injected comets stars must have played important roles. In some cases, these may have been as in case 1*b* of Fig. 3, and in other cases as in cases 3*a* or 4. This fraction increases for smaller semi-major axes, reaching 33% for $a_{\mathrm{inj}} = 30\,000$ AU and almost 85% for $a_{\mathrm{inj}} = 25\,000$ AU. We thus observe that comet injections in the inner part of the Oort peak are generally governed by stellar perturbations.

The fraction of $\mathbb{S}$ set comets decreases continuously from unity for $a_{\mathrm{inj}} \sim 10\,000$ AU to very small values for $a_{\mathrm{inj}} >$ 40 000 AU. For quiescent comets in the latter range, $p_{\mathbb{S}}$ is always below 5%, and even for non-quiescent comets it remains below 20%, owing to the very efficient tidal perturbations in the outer part of the Oort Cloud. As we see in the next subsection, large stellar perturbations of q are common for these comets, but most stellar injections are sabotaged by subsequent tidal increases in q, as mentioned above. On the other hand, for comets that are indeed injected – regardless of the mechanism – a backwards integration with the Galactic tides is almost sure to bring the perihelion beyond 15 AU, so that the comets will be counted with the $\mathbb{G}$ set. Thus, the tides appear to dominate the injections at large semi-major axes because of our definitions of the $\mathbb{S}$ and $\mathbb{G}$ sets. Stellar perturbations may play important roles in the game, but they are unlikely to get credit.

For quiescent comets at the other end of the a-range, we note that for $a_{\mathrm{inj}} \simeq a_{\mathrm{crit}}$, we have $p_{\mathbb{S}} = 30\%$, and for $a_{\mathrm{inj}} = 15\,000$ AU, $p_{\mathbb{S}} \simeq 85\%$. Hence, for this range of semi-major axes, the sum of the $\mathbb{S}$ and $\mathbb{G}$ fractions is less than unity, as shown in the fourth panel of Fig. 4, so the injections are often due to neither the tides nor any single star alone. We are dealing instead with a synergy between the tides and stellar perturbations, which acts "in real time", i.e., the tides and stars collaborate in making comets cross the Jupiter-Saturn barrier. The plot shows that this synergy reaches a maximum for $a_{\mathrm{inj}} \simeq a_{\mathrm{crit}}$, where the sum of the two fractions barely reaches 30%, and the synergy is at work over the whole range $a_{\mathrm{inj}} \in [15\,000, 45\,000]$ AU. What happens is illustrated by case 4 of Fig. 3.

Finally, for $a_{\rm inj} > 45\,000$ AU, we observe the opposite behaviour, namely, a "duplication of effort" of tides and stars with $p_{\mathbb{S}} + p_{\mathbb{G}} > 1$. A star injects a comet into an orbit that could also have been reached by a tidal injection. This relatively rare phenomenon is illustrated by case 3b of Fig. 3. As already mentioned, it is almost impossible for an injected comet of the outer Oort Cloud not to belong to the $\mathbb{G}$ set, so the stellar injections that do not get sabotaged will generally be assigned double membership.

To summarize the peculiarities of comet injection from the outer part of the Oort Cloud, we have seen that the very rapid tidal changes in the perihelion distance (timescale shorter than the orbital period) is an obstacle to injection owing to the difficulty in timing the perihelion passage. Another problem is that the concept of a tidally active zone (FFRV11) is no longer valid in the sense of a phase space region permanently linked to the observable orbits by tidal trajectories. We are dealing with a loosely defined set that in the presence of stars is neither filled nor empty, but whose occupation is continuously changing, involving different comets at different times. Moreover, in the case of stellar injections, we later demonstrate that the largest ones occurring per orbital period are much larger than the "target", i.e., the interval $0 < q < 5$ AU. Thus, the target is difficult to reach, and overshoots will be the rule.

We now attempt to determine the difference between the injection rates from the Oort Cloud, if we include or exclude the stellar perturbations during the last revolution of the comets. We have seen that these perturbations may both cause and prohibit injections, and we now wish to compare these two effects. For the triggering effect, we can use the sample of injected, quiescent comets during the last 3 Gyr of our simulations and calculate the fraction that are no longer injected, if we remove the stellar perturbations during the last revolution. For the prohibiting effect, we consider the injected comets during the first 2 Gyr in a different simulation using only the Galactic tides, and we calculate the fraction that are no longer injected after stellar perturbations are added during the last revolution.

The bottom panel of Fig. 4 plots these two fractions versus the semi-major axis at injection. Since the tides are unable to inject comets for $a < a_{\rm crit}$, the stellar triggering effect is obviously at work in this range, while the prohibiting effect is not defined. Between $a_{\rm crit}$ and 36 000 AU, the triggering effect is clearly larger than the prohibiting one. The largest difference is obtained for $a_{\rm inj} \sim 25\,700$ AU, where the star-triggered fraction amounts to nearly 71%, while the prohibited one is only 40%.

Above $a \simeq 36\,000$ AU, the two effects balance and grow to unity in the outer Oort Cloud. In this region, we have seen that the injections appear to be mainly tidal. However, as noted above comet injection is actually a delicate balance, and stellar perturbations are so important that injections with and without stars are completely different matters. If injection happens when stars are included, it likely vanishes when the stars are excluded, and conversely, if it happens without the stars, it likely disappears when the stars are added.

The upper panel of Fig. 5 shows the appearance of our simulated Oort peak for quiescent comets as a histogram of the $1/a$ distribution. Different colours are used to denote the contributions of the $\mathbb{G}$ and $\mathbb{S}$ sets as explained in the figure caption. In white, we see the extent of the synergistic contribution with a maximum around 30 000 AU. The $\mathbb{S}$ set injections are predominant at small semi-major axes, but overall they contribute only a small fraction and disappear completely beyond 60 000 AU. The $\mathbb{G}$ set dominates the peak at $a > 30\,000$ AU, but we have to point out two features. The first is that this is due to the phenomenon of TAZ filling, for which massive stars are largely responsible (see FFRV11). The second is what we drew attention to above, namely, that the injections in the outer Oort Cloud are caused by an intricate interplay between the tides and the stars such that we cannot ascribe the main cause to either one alone.

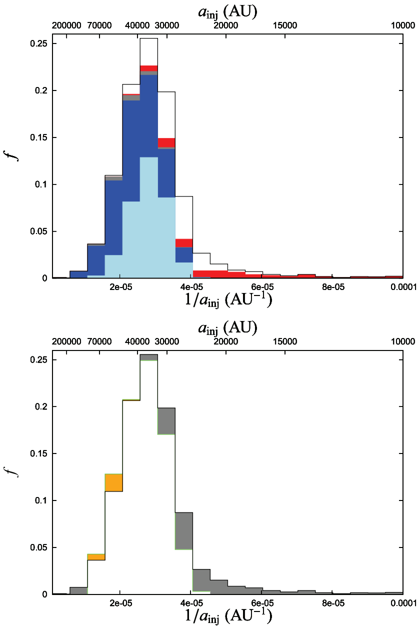

Fig. 5. Fraction f of quiescent injected comets with respect to the total number (6119) plotted as a histogram versus the inverse of the semi-major axis at injection (the upper horizontal scale gives the corresponding semi-major axis). Two percent of the injected comets have $a_{\rm inj} < 10\,000$ AU and fall to the right of the diagram. In the upper panel, the dark-blue area corresponds to comets belonging exclusively to set $\mathbb{G}$, the sky-blue area corresponds to comets belonging to sets $\mathbb{G}$ and $\mathbb{G}'$ but not to set $\mathbb{S}$, the grey area corresponds to comets belonging to sets $\mathbb{G}$ and $\mathbb{S}$, the red area corresponds to comets belonging to only set $\mathbb{S}$, and the white area to comets belonging to neither set. In the lower panel, the green line gives the estimated fraction of injections when the stellar perturbations are turned off during the last revolution. The orange and grey areas correspond to the excess and shortage, respectively, of the number of injections in this case.

In the lower panel, we attempt to compare the triggering and prohibiting effects of stars during the last revolution. The black histogram is the same as in the upper panel. We can correct the fraction of comets in the $\mathbb{G}'$ set by increasing it using the percentages of tidal injections prohibited by stars as plotted in the bottom panel of Fig. 4. This enables us to get an estimate of the number of injections, shown by the green histogram, for the case in which the stellar perturbations were turned off for the last revolution. The orange area corresponds to the stellar prohibiting effect and the grey one to the stellar triggering effect. We see that in the outer part of the Oort peak there is a range where the stellar prohibiting effect slightly dominates but this is more than compensated for by the predominance of the triggering effect in the inner part of the peak and the region inside it.

We emphasize that only the sky-blue area in the upper panel of Fig. 5 corresponds to comets that are essentially injected by

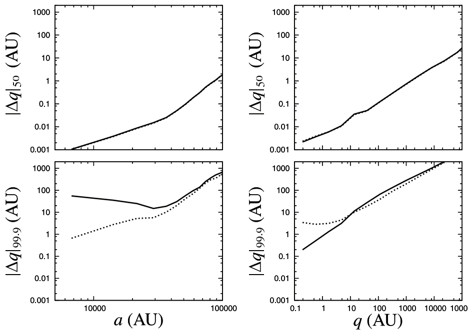

Fig. 6. Medians and 99.9th percentiles of the absolute value of the perturbation of perihelion distance. Solid curves correspond to negative perturbations and dotted curves to positive perturbations. The upper plots show the median versus the semi-major axis (*left*) and versus the perihelion distance (*right*). The lower plots show the same for the 99.9th percentile.

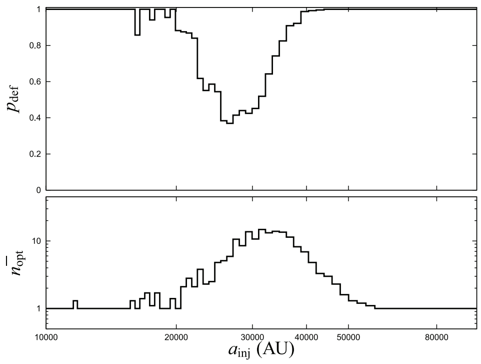

Fig. 7. *Upper plot*: fraction (p_{def}) of quiescent comets for which n_{opt} is defined versus a_{inj}. *Lower plot*: mean $\overline{n_{\mathrm{opt}}}$ versus a_{inj} for the same set of comets.

the tides so that stellar perturbations are of no consequence. Since this area amounts to a total of only ~1/3 of the injections and never exceeds 1/2 of the injections in any bin of the histogram, we conclude that the action of stars during the last revolution is critically important for most new comets injected from the Oort Cloud.

We note that the distribution shown in Fig. 5 is a long-term time average, and it is worth asking, whether one can expect a nearly continuous flux of comets across the whole range of $1/a$ that we have plotted. Taking $a = 10\,000$ AU as an example, and requiring a rather close stellar encounter to accomplish the injection of such a comet, we find that a solar encounter distance of $d_{\odot} \sim 20\,000$ AU is needed. Such encounters are expected at the rate of one per 10 Myr approximately, so even though it may be that a star injects comets that arrive at perihelion over an extended period of time, we cannot expect a truly continuous flux. Moreover, according to Fig. 2, most stars that pass at such a close distance are enhancement-producing stars, which we do not consider in Fig. 5. We conclude that the whole far tail extending to the right of the Oort peak is of sporadic occurrence and should not necessarily be represented in the sample of observed new comets.

3.2. The role of stars

In Fig. 6, we show the behaviour of the median and the 99.9th percentile (1 perturbation out of 1000 is larger than this) of $|\Delta q|$ for positive and negative stellar perturbations versus a and q. The sample in question is the 20 446 injected comets that we discussed above – both quiescent and non-quiescent ones. The number of individual perturbations during the last revolutions is about 5×10^6.

The medians of the negative and positive perturbations behave identically versus a. The curve shows a break in the slope for $a \sim 40\,000$ AU, which we relate to, based on previous results, stellar perturbations for smaller semi-major axes being important to comet injection, while for larger semi-major axes the Galactic tides would be perfectly capable of injecting comets on their own.

Similarly, we see a strong asymmetry of the 99.9th percentiles building up and increasing with decreasing a for $a < 40\,000$ AU. The values are much larger for negative perturbations, because these are the ones that inject the comets. The positive perturbations obviously have nothing to do with the injections and thus are not biased toward large values by this selection. The increase in the negative values toward smaller a flattens out at $a \sim 15\,000$ AU, where the injections start to be completely dominated by stellar perturbations.

That this asymmetry is more or less absent for $a > 40\,000$ AU tells us that the injected comets in this range are typical of comets in general and do not require exceptionally large stellar perturbations. The number of stellar encounters during the last revolution is indeed generally larger than 300, so the 99.9th percentile should be a rough estimate of the largest individual perturbation experienced by an injected comet. We thus see that those comets tend to have experienced very significant stellar perturbations of q, amounting to tens or hundreds of AU.

The larger values of the 99.9th percentile for positive perturbations found at the smallest perihelion distances demonstrate the effect already noted by Öpik (1932), namely that stellar perturbations preferentially lead to an increase in the perihelion distance, when the initial orbit – in a similar way to those of meteors and observed comets – has a small perihelion distance. The reason is obvious, i.e., a large negative change in the angular momentum along the vector itself, when the absolute value is small to begin with, will increase this absolute value (and thus the perihelion distance) while reversing the sense of motion. We indeed see that the largest negative perturbations (as approximated by the 99.9th percentile) are exactly equal to the initial perihelion distance, while the largest positive ones are much larger.

We now consider whether the stellar influence on comet injections is generally due to only one star or to several stars. We investigate this by considering for each quiescent injected comet all the stars that perturbed its motion during the last revolution and counting the minimum number of stars needed to build up a total decrease in q larger than 10 AU (corresponding to a jump across the Jupiter-Saturn barrier). We call this number n_{opt}, where "opt" stands for optimistic, because there is no guarantee that the perturbations in question actually led to a crossing of the barrier.

Figure 7 plots, versus a_{inj}, the fraction p_{def} of quiescent comets for which n_{opt} is defined (i.e., for which it is possible to reach a decrease in q by more than 10 AU by adding individual perturbations) and, for those comets, the mean $\overline{n_{\mathrm{opt}}}$.

The fraction for which $n_{\rm opt}$ is defined is less than unity only for $a_{\rm inj}$ between 16 000 and 44 000 AU – the same interval where the direct synergy in comet injection was noted. This fraction indeed follows almost exactly the behaviour of $p_{\mathbb{S}} + p_{\mathbb{G}}$ as shown in Fig. 4. From 16 000 AU to $a_{\rm crit}$, there are many comets for which neither the tides nor the stars are able to perform the injections on their own, so that the synergy is strictly necessary. In addition, while it appears that a single star may be responsible for injections below $a \sim 20\,000$ AU, for larger semi-major axes several stars usually contribute.

Below $a = 16\,000$ AU and above 58 000 AU, we have strictly $\overline{n_{\rm opt}} = 1$, so that the injections might be due to a single star. While this is certainly the case below 16 000 AU, since Fig. 4 shows that $p_{\mathbb{S}} \simeq 1$, we know that above 58 000 AU the situation is quite different. Figure 6 provides an indication that stellar perturbations are systematically strong for such large semi-major axes, and if there had been no Galactic tides, they would certainly have injected comets on their own. However, we saw in connection with Fig. 4 that the same can be said of the Galactic tides. As discussed above, each comet injection is indeed likely caused by the interplay of both perturbers and would disappear if either of them were removed.

4. Star detection by HIPPARCOS and *Gaia*

In the previous section, we saw that stellar perturbations play an important and direct role in comet injections from all parts of the Oort Cloud, and that this role is crucial for semi-major axes smaller than about 25 000 AU. Figure 6 (lower left panel) shows that stellar perturbations leading to a significant decrease in q occur in general for injected comets. However, in the Introduction, we referred to the work of Dybczyński (2006), which concluded that none of the observed stars that passed near the Sun in the recent past caused any significant perturbation of the new Oort Cloud comets. To investigate the origin of this apparent conflict, we have to see whether the responsible stars behind the currently observed comets may be hiding from discovery along with most other stars that recently encountered the Sun.

4.1. Observational data

The identification of previous close encounters between other stars and the Sun has been discussed by, for example García-Sánchez et al. (2001); Dybczyński & Kwiatkowski (2003); Dybczyński (2006). The following discussion repeats some points made in these papers.

As a simplified approach, we judge the observability of stars and the access to relevant data on their positions and velocities by considering two space missions – one past and one future. The ESA H mission (1989−1993) represented a milestone in the mapping of the solar Galactic neighbourhood. It led to much improved parallaxes and proper motions of good quality for about 120 000 stars (Perryman et al. 1997) and revolutionized searches for recent close encounters of stars with the Solar System (García-Sánchez et al. 2001). However, its limited magnitude coverage makes it reasonably complete only within a minute volume around the Sun relative to the extent of the Galaxy. A new revolution is expected from the ESA *Gaia* mission, to be launched in 2012. This will survey significant volumes with respect to all stellar types considered as Oort Cloud perturbers in this paper, including both accurate proper motion measurements and – with the aid of ground-based follow-up programmes – good-quality radial velocities.

H observed all the stars with visual magnitude $V < 7.5$−9 (depending on direction), and had a limiting magnitude $V = 13$ (García-Sánchez et al. 2001). In our experiments, we assume that H observed all stars with $V < 8$ (independent of direction) and use a linearly decreasing detection probability between $V = 8$ and $V = 13$. We also consider that H was able to measure proper motions larger than the limit accuracy, i.e., 1 mas/yr. Radial velocities were not observed by H but could often be found from the literature for the relatively bright stars in question (Dybczyński 2006).

For *Gaia*, the magnitude criterion is $V < 20$, and we can assume that detection is practically complete everywhere on the sky for stars brighter than this limit. The parallax accuracies, as currently specified, are such that all stars within 500 pc will have their parallaxes accurately measured, including almost all recent Oort Cloud perturbers. Moreover, although somewhat dependent on stellar spectral type, these accuracies can be used to deduce the limits of detectability for proper motions of 4 μas/yr for $V < 12$, 10 μas/yr for $12 < V < 17$, and 160 μas/yr for $17 < V < 20$.

The radial velocities measured by *Gaia* or later merit special attention. A relative error of ∼10% is a reasonable goal in order to identify whether a given star has passed near the Oort Cloud or not, and this translates into a few km/s for most stars. Even though *Gaia* is expected to measure radial velocities, this goal will not be easy for early-type stars (B or A), whose spectra have only few and broad spectral lines. Hence, we may only be able to study stars with magnitudes as bright as $V < 8$, and early-type stars more distant than 100 pc may not be able to have *Gaia*-measurable radial velocities. The later types on the other hand can be both relatively close and relatively faint at the same time. It appears that *Gaia* can then reach the required radial-velocity accuracy only down to $V \sim 14$, thus again excluding most of the detected stars.

We now consider the problem of identifying the possible Oort Cloud perturbers that have affected the currently observed new comets. We assume that all stars in our simulations are of this category ($d_{\rm min} < 4 \times 10^5$ AU $\approx$ 2 pc). In a forthcoming paper, we will examine in more detail the possibility of using more restrictive criteria. The stars of interest must have passed during the last revolution of the new comets with the longest periods. Since our quiescent Oort peak is mostly contained within $a < 60\,000$ AU, we use a time interval extending 15 Myr into the past. On the basis of the estimated stellar encounter frequency, we expect there to be ∼600 such stars. Assume that a star is found at distance d, which is measured with good accuracy. If $d < 2$ pc, the star must obviously be identified independently of its motion, but this is a very unlikely outcome – in practically all cases the observed stars are much farther away. In these situations, the radial velocity $v_{\rm r}$ carries important information. If $v_{\rm r} < 0$, the star is approaching and may thus be discarded. For $v_{\rm r} > 0$, we may compute a good estimate of the time since closest approach ($t_{\rm min}$) from

$$t_{\rm min} \approx \frac{d}{v_{\rm r}}, \tag{3}$$

and if $t_{\rm min} > 15$ Myr, the star can be discarded. Otherwise the proper motion μ may be used to estimate $d_{\rm min}$ from

$$d_{\rm min} \approx \frac{\mu d^2}{v_{\rm r}}, \tag{4}$$

using $v_{\rm t} = \mu d$ for the transverse velocity.

If both $v_{\rm r}$ and μ are known, it is thus a trivial decision about whether to earmark the star. However, since these stars are only

Table 1. Absolute visual magnitudes for the 13 different spectral types used in our simulations.

B0	A0	A5	F0	F5	G0	G5	K0	K5	M0	M5	gi	wd
−2.95	0.55	1.85	3	3.8	4.35	5.1	5.95	7.25	9	13.95	1	12

Table 2. Statistics on the stars perturbing injected comets during their last orbital period.

Stars	All	10 best	5 best	2 best	Best
Gaia	70%; 96%	85%; 90%	85%; 88%	86%; 85%	87%; 84%
Hipp	9%; 74%	22%; 38%	25%; 33%	26%; 26%	26%; 20%
$\langle V_\star \rangle$ (km s^{-1})	52.8	44.2	43.3	42.3	42.0
$\langle M_\star \rangle$ ($M_\odot$)	0.46	0.90	1.00	1.07	1.09

Notes. "All" refers to all the stars, "10 best" to the stars responsible for the ten largest negative perturbations of the perihelion distances, etc. Line "*Gaia*" gives the mean percent of stars detected by *Gaia* (first number) and, among the detected stars, the proportion for which the proper motion is above the corresponding limit accuracy of *Gaia* (second number). Line "Hipp" gives the same values for H . The two last lines give the mean of the stellar encounter velocity and stellar mass.

a minority, we have to consider the case where either or both are unknown. If only v_r is unknown, one may use a likely upper limit such as, e.g., 100 km s^{-1} (see Dybczyński 2006) and thus obtain a minimum value of $d_{\min}$. Stars that are found to have certainly passed beyond 2 pc may then be discarded, while the remaining ones will be considered as suitable targets for radial velocity observations.

The procedure just described is the motivation behind using proper motion information in the identification process. The proper motion serves to discard stars for which no radial velocity observations have to be carried out. If on the other hand neither v_r nor μ is known, μ must be smaller than the above-mentioned limits and there is no way to exclude the possibility of a very close encounter.

To characterize this case, we estimate $\mu_{\max}$ by inserting $(v_r)_{\max} = 100$ km s^{-1} into Eq. (4). For $d = 100$ pc, we then obtain $\mu_{\max} \approx 4$ mas/yr. Since the majority of H -detected stars are closer than this, an undetected proper motion almost necessarily means that the star is a possible Oort Cloud perturber. For *Gaia*, the proper motion detection limits are smaller, and out to about 500 pc an undetectable proper motion will always mean that the star is an interesting candidate for a radial velocity measurement, but we note that this will only yield a maximum value for the closest approach distance.

4.2. Simulations

For each injected comet in our simulations, we study all the stars that encountered the Oort Cloud during the last revolution of the comet, and for each star we compute its visual magnitude V, its proper motion, and its radial velocity at the time when the comet reaches its observable perihelion. In performing these calculations, we use the straight-line approximation rather than tracing the actual Galactic orbits. This is justified for time intervals of just a few Myr but may lead to significant errors in cases of >10 Myr. For the absolute magnitudes, we use the values given in Table 1 for the different spectral types. Every star considered here is regarded as an Oort Cloud perturber, although the actual perturbations affecting the injected comets are mostly very small.

From the calculated V magnitude, we determine whether the star would have been detected by H assuming that the comet is passing its perihelion at the present time, and whether it will be detected by *Gaia*. We also calculate the proper motion and determine whether this would have been measurable by H and will be measurable by *Gaia*. Finally, for the radial velocity we consider two scenarios for *Gaia*. According to the "optimistic" case, the radial velocities will be measurable for all stars that could possibly be Oort Cloud perturbers, while in the "pessimistic" scenario no velocities will be attainable from the ground, and the magnitude limits for *Gaia*-observed radial velocities will apply, as given above.

Table 2 presents some statistics on the stars perturbing the quiescent injected comets during their last orbital period. We list the fraction of stars detected by *Gaia* and H and, for the detected stars, the fraction for which the proper motion is accessible. The mean velocity and mass of the perturbing stars is also given. Each quantity is listed first for all the perturbing stars, and then for only the stars with the ten, five, two, and one largest negative perturbations of the perihelion distance.

Looking at the entries for all the stars in Table 2, we note that H detects only 9% of the perturbing stars, whereas *Gaia* should detect 71% of these stars. Since the current stellar observations rely mainly on the H catalogue, most close-encounter stars are thus being missed. If we instead focus on the stars that provide the most important contributions to the decrease in the perihelion distance, these detection percentages increase for both *Gaia* and H . For the latter, detection rises from 22% (for the ten most effective stars) to 26% (for the single most effective star), and *Gaia* detection similarly rises from 85% to 87%. These increases in the detection probability are caused by the stars that have the greatest effect on the perihelion distances being those of both low velocity and high mass. They will have bright apparent magnitudes, because they are close by (owing to the small velocity) and luminous (owing to the large mass). We indeed note in Table 2 that the mean velocity decreases and the mean stellar mass increases, when going from all stars to the 10 best, 5 best, 2 best, and the very best among the stars (in terms of their contributions to the decrease in perihelion distance).

We also note that, because of its very high astrometric accuracy, *Gaia* will be able to measure the proper motions of the vast majority of Oort Cloud encountering stars, while the performance of H was not as good in spite of the detected stars being on the average closer[3]. Counting all the stars, the fraction with proper motion measurements is 96% for *Gaia* and 74% for H . Focussing on the most effective perturbing

---

[3] The most accurate proper motions currently available do not use only H data but also ground-based astrometry obtained far earlier.

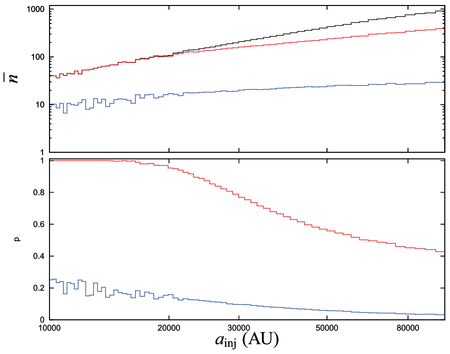

Fig. 8. *Top*: mean number of perturbing stars during the last orbital period of injected comets versus the semi-major axis at injection (black line) and number of perturbing stars detected by *Gaia* (red line) and H (blue line). Only quiescent comets are considered. *Bottom*: fraction of perturbing stars observed by *Gaia* (red line) and H (blue line) versus the semi-major axis at injection.

stars, i.e., the closest and slowest encounters, the fraction decreases for both *Gaia* and H, but while it falls all the way to ~20% in the H case when zooming in on the best star, for *Gaia* it remains above 80%. Regarding radial velocities, these velocities were often available in the literature for H stars, and for *Gaia* stars even in the pessimistic case, the fraction of detected stars for which the radial velocity is measured is 35% according to our simulations.

4.3. Detection efficiencies

The probability of the detection by each satellite strongly depends on the semi-major axis at injection ($a_{\rm inj}$). This is because with increasing orbital period, the time from stellar encounter to cometary perihelion statistically increases, so that the stars will tend to be more distant and thus fainter at the time of comet injection. Figure 8 shows, versus $a_{\rm inj}$, the mean number of stars perturbing the quiescent injected comets during their last orbital period (this varies more or less as $a_{\rm inj}^{3/2}$), the mean numbers of these stars detected by *Gaia* and H, and the corresponding fractions of detected stars in the *Gaia* and H cases. We see how the probability of detection decreases with increasing semi-major axis. We note that *Gaia* detects all the perturbing stars for comets with $a < 15\,000$ AU and 78% of the perturbing stars for $a \sim 30\,000$ AU. The detections by H are never complete with only 20% of stars detected for $a \sim 15\,000$ AU and 10% for $a \sim 30\,000$ AU.

Figure 9 is another clear indication of the improvements to be expected from *Gaia*. The diagrams show, for four different instants chosen at random during the last 3 Gyr of our simulations, the stars that passed within 400 000 AU at times no later than 3 Myr before that instant. This time interval corresponds to the orbital period of comets with $a \sim 20\,000$ AU. For larger semi-major axes, the relevant stars for injection could have passed further back in time. The four random instances are interpreted as the perihelion times of injected comets.

For each star, the closest encounter distance is plotted versus the time of closest encounter measured from the cometary perihelion time ($t = 0$). When we find the star to be detectable by H, we indicate it with a sky-blue dot (left panels), and detectability by *Gaia* is marked by red dots (right panels). In each diagram, we have also plotted these data for the real stars found by Dybczyński (2006) as a representation of the best that could be done with the H data. We have also indicated at which distance a comet on a parabolic or elliptic orbit would have been as a function of time, if it reaches perihelion at time zero. The "elliptic" curve corresponds to aphelion passage at the times in question.

The number of stars detected by H is clearly very small, and we see that the work of Dybczyński (2006) corresponds well to the criteria used in our simulation. Recent encounters are strongly preferred, and thus the most effective stars are generally missed. For encounters further back in time, the stars tend to have moved to distances beyond the detectability limit of H. On the other hand, the diagrams for *Gaia* illustrate the hope that one can place in this mission, when it comes to clarifying the origin of the observed, new Oort Cloud comets.

Finally, we performed the integration of the last orbital period of injected comets once more, taking into account only the stars detectable by either H or *Gaia*. Figure 10 shows the number of quiescent comets that become injected versus the semi-major axis $a_{\rm inj}$, taking into account all the stars, only the H stars, and only the *Gaia* stars. We have also plotted the fraction of injected comets using each sub-sample of stars with respect to the case where all the stars are taken into account.

Using only the stars detectable by H, we obtained a flux of injections that is less than half of the total flux, except near the maximum at $a_{\rm inj} \sim 33\,000$ AU, where the H stars and the tides are able to inject a little more than 65% of the total. We note, however, that most of these injections are essentially tidal as in case 1*a* of Fig. 3.

The calculations taking into account only the *Gaia*-detectable stars show that we have more than 80% of the total quiescent flux for $a_{\rm inj} < 40\,000$ AU. Then, however, the flux decreases to less than 10% of the total for $a_{\rm inj} \sim 100\,000$ AU. Nevertheless, since the observed Oort spike is certainly situated mainly at $a < 40\,000$ AU, one can hope that, when the *Gaia* mission is over, it will be possible to simulate the last period of the observed comets far more reliably than one can do with the current data.

The fall-off in both H and *Gaia* relative fluxes toward very large semi-major axes illustrates an important feature of comet injection dynamics. In Fig. 4, we saw that practically all the injected comets with $a_{\rm inj} > 50\,000$ AU belong to the $\mathbb{G}$ set, and this means that they *might* have been injected by the Galactic tides alone. However, as noted above, this result carries no information on the relative roles of stars and tides in the real injections. What we can now see in Fig. 10 is that the stars play a decisive role in comet injection at large semi-major axes, because even the removal of a small fraction of them mostly inhibits the injections that were found using the entire sample.

5. Summary and conclusions

We have performed three simulations of the evolution of the Oort Cloud, using one million test comets in each case. Perturbations due to the Galactic tides and passing stars have been incorporated. The three simulations differ in the selection of initial orbits and the sequence of stellar encounters. Each simulation extends over 5 Gyr, and during the last 3 Gyr we register over 20 000 comet injections, i.e., comets passing from perihelia $q > 15$ AU to $q < 5$ AU in one revolution. We have analysed in detail which events took place during these final revolutions

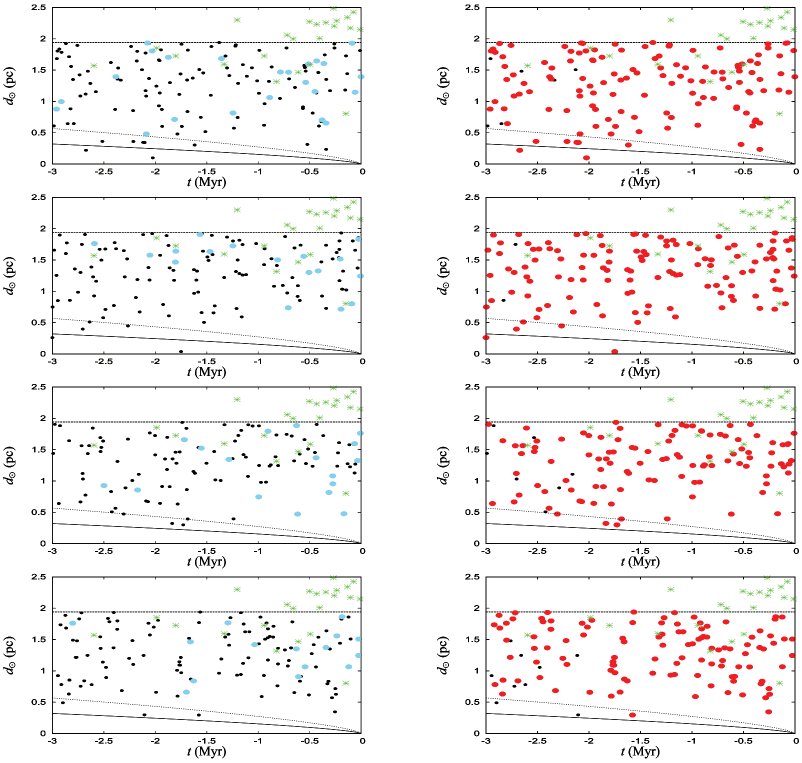

Fig. 9. For four different instants (one per line), we plot the encounter distance of stars versus the time of encounter counted from the perihelion passage of an injected comet ($t = 0$). The two curves indicate at which distance the comet would have been on a parabolic (dotted) or elliptic orbit (solid; the comet being at aphelion in this case). The black dots correspond to all the simulated stars passing during the 3 Myr time span. In the left column, the sky-blue dots show the stars detected by H . The same is done using red dots in the right column for the stars detected by *Gaia*. The green asterisks indicate the real stars identified by Dybczyński (2006). His sample extends to larger encounter distances than those of our simulation.

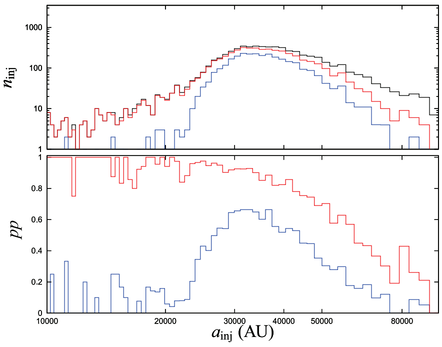

Fig. 10. *Top*: number of injected quiescent comets versus the semi-major axis at injection taking into account all the stars (black line), only the H stars (blue line), and only the *Gaia* stars (red line). *Bottom*: fraction of injected comets using each sub-sample with respect to the all stars sample.

and assessed the roles played by the Galactic tides and by the passing stars.

One new feature of our analysis is the way in which we distinguish between cometary showers and the intervening, quiescent periods. We do not divide the time axis into shower and quiescent periods but instead classify each injected comet according to whether its last revolution could have been affected by an efficient, enhancement-producing stellar encounter or not. Our criterion has been chosen to be conservative in the sense that quiescent comets have to be injected only under the influence of stars with unremarkable injection efficiencies.

For quiescent comets, our simulated Oort peak agrees with the shapes found in other simulations with a maximum at a semi-major axis of about 33 000 AU. We have found that the sharp decline in the injected flux with increasing semi-major axis beyond the maximum is consistent with the increasing difficulty in sending a comet to perihelion when the perihelion distance is shorter than the observable limit. The distribution for non-quiescent comets is quite flat, as expected for a situation where the loss cone is filled at practically any semi-major axis.

We have defined two sets of injected comets according to whether the post-injection orbit could have been reached by a purely tidal injection ($\mathbb{G}$ set) or whether an actual jump from $q > 15$ AU to $q < 5$ AU was caused by a stellar encounter ($\mathbb{S}$ set). The smallest semi-major axis found in the $\mathbb{G}$ set is about 23 000 AU, which is the limit below which it is impossible for the Galactic tides to inject comets on their own. On the other hand, for semi-major axes larger than 50 000 AU almost all the injected comets belong to the $\mathbb{G}$ set, which is unsurprising, because for these semi-major axes the tides will always have time to remove the perihelion from the observable zone during one orbital revolution of the comet. We conclude that the tides, in principle, could have injected the comets, but that it is impossible to state whether they actually did so. We argue that owing to the short timescales and large perturbations involved, comet injection from the outer part of the Oort Cloud is quite a precarious operation, involving a fine tuning of stellar and tidal perturbations.

The $\mathbb{S}$ set comprises essentially all the injections at semi-major axes of about 10 000 AU, which shows the predominance of stellar injections in this range, but drops to smaller fractions around 15 000 AU. We have identified a range of semi-major axis, extending from ∼15 000 AU to ∼45 000 AU, where the union of the $\mathbb{S}$ and $\mathbb{G}$ sets fails to cover the ensemble of all injected comets – indicating that a synergy is at work between the two perturbers. This synergy is found to reach its maximum close to the critical limit of tidal injections, where as much as 70% of the actual injections can be ascribed to the synergy, and extends across most of the Oort peak.

We also investigated whether the inclusion of stellar perturbations during the last revolution has either a positive or negative effect on the number of injected comets. The result is that the overall effect is positive because of an increase in the injection efficiency inside and at the inner part of the Oort peak, while at the outer part the differences are very small.

After demonstrating that passing stars should have had a large influence on most of the injections responsible for the observed new Oort Cloud comets, we checked the observability of those stars using our simulations by computing the magnitude, proper motion, and radial velocity of each perturbing star at the moment the injected comet reaches perihelion. We then compared these results with the detectability limits of both H and *Gaia*. One result that we found is that H is mostly unable to detect the perturbing stars, even when we concentrated on the stars causing the largest decrease in perihelion distance, while *Gaia* is likely to detect nearly all the most efficient perturbers and most of the perturbers at large. We have thus shown why Dybczyński (2006) was unable to identify the stellar perturbations that affected the new comets, while confirming that his search for stars using H data was about as good as one can reasonably expect. We also note that using only the stars that H could have detected and the tides, our simulated flux of quiescent injected comets is much reduced.

The proper motions of the perturbing stars have been generally difficult to obtain using H data but will become accessible in the vast majority of cases using *Gaia*. Regarding the radial velocities, *Gaia* will provide them in many cases, and we argue that in the remaining cases, these velocities will likely be attainable using ground-based follow-up observations. Therefore, the prospects for clarifying the origin of the new comets after *Gaia* look rather good.

Finally, we comment on what is lacking in our model. We note that we have only studied the present situation, using the Galactic tides and stellar perturbations typical of the Sun's present position in its Galactic orbit, while owing to radial and vertical orbital oscillations of the Sun, large changes may be expected with time (Gardner et al. 2011). Since our study has not been concerned with comet injection at other times in the history of the Solar System, this may not be a large problem, but obviously the past motion of the Sun – including possible encounters with GMCs as well – may have left its imprints on the structure of the Oort Cloud in ways that our model does not account for.

A potentially more serious problem is that our model of comet injection does not incorporate a realistic treatment of planetary perturbations. For instance, it may not be in reality impossible for comets to enter into orbits with perihelion distances shorter than 5 AU via a preceding passage with $q \sim 10$ AU. Kaib & Quinn (2009) started to investigate this problem, but their model did not include the stellar perturbations during the analysed time interval except as a check, and we propose that a careful study of the complete dynamics of comet injection will be needed to reach safe conclusions. We intend to perform such a study in the near future, and the present one will then serve as a useful comparison case.

Acknowledgements. We gratefully acknowledge the remarks made by Ramon Brasser and an anonymous referee, which greatly helped to improve the quality of the paper. This work was possible thanks to research grants from the Polish Government (NN 203 392 734) and the Swedish National Space Board (119/07). The work of G.B.V. has also been supported by the Italian Space Agency, under contract ASI/INAF I/015/07/0.

References

Breiter, S., Fouchard, M., Ratajczak, R., & Borczyk, W. 2007, MNRAS, 377, 1151
Delsemme, A. H. 1987, A&A, 187, 913
Dones, L., Weissman, P. R., Levison, H. F., & Duncan, M. J. 2004, Comets II, 153
Duncan, M., Quinn, T., & Tremaine, S. 1987, AJ, 94, 1330
Dybczyński, P. A. 1994, Celest. Mec. Dyn. Astron., 58, 139
Dybczyński, P. A. 2001, A&A, 375, 643
Dybczyński, P. A. 2002, A&A, 396, 283
Dybczyński, P. A. 2006, A&A, 449, 1233
Dybczyński, P. A., & Kwiatkowski, T. 2003 [`arXiv:astro-ph/0307019v3`]
Dybczyński, P., & Królikowska, M. 2011, MNRAS, 416, 51
Emel'yanenko, V. V., Asher, D. J., & Bailey, M. E. 2007, MNRAS, 381, 779
Fouchard, M., Froeschlé, Ch., Breiter, S., et al. 2007, Lect. Not. Phys., 729, 271
Fouchard, M., Froeschlé, Ch., Rickman, H., & Valsecchi, G. B. 2010, Lect. Not. Phys., 790, 401
Fouchard, M., Froeschlé, Ch., Rickman, H., & Valsecchi, G. B. 2011, Icarus, 214, 334
Francis, P. J. 2005, ApJ, 635, 1348
García-Sánchez, J., Preston, R. A., Jones, D. L., et al. 1999, AJ, 117, 1042
García-Sánchez, J., Weissman, P. R., Preston, R. A., et al. 2001, A&A, 379, 634
Gardner, E., Nurmi, P., Flynn, C., & Mikkola, S. 2011, MNRAS, 411, 947
Heisler, J., & Tremaine, S. 1986, Icarus, 65, 13
Hills, J. G. 1981, AJ, 86, 1730
Holmberg, J., & Flynn, C. 2000, MNRAS, 313, 209
Kaib, N. A., & Quinn, T. 2009, Science, 325, 1234
Królikowska, M. 2006, Acta Astron., 56, 385
Królikowska, M., & Dybczyński, P. 2010, MNRAS, 404, 1886
Oort, J. H. 1950, Bull. Astron. Inst. Neth., 11, 91
Öpik, E. 1932, Proc. American Academy of Arts and Science, 67, 139
Perryman, M. A. C., Lindegren, L., Kovalevsky, J., et al. 1997, A&A, 323, L49
Rickman, H., Froeschlé, Ch., Froeschlé, Cl., & Valsecchi, G. B. 2004, A&A, 428, 673
Rickman, H., Fouchard, M., Valsecchi, G. B., & Froeschlé, Ch. 2005, Earth Moon and Planets, 97, 411
Rickman, H., Fouchard, M., Froeschlé, Ch., & Valsecchi, G. B. 2008, Cel. Mech. Dyn. Astron., 102, 111
Wiegert, P., & Tremaine, S. 1999, Icarus, 137, 84

3.2 Interaction entre les perturbateurs galactiques et les perturbations planétaires

3.2.1 Implications sur le flux de comètes observables

On a vu, dans Fouchard et al. (2013) qu'une modélisation réaliste des perturbations planétaires conduit à un système solaire bien plus transparent que ce qui est considéré lorsqu'on utilise le concept de loss cone. Ainsi une comète peut passer à de nombreuses reprises à l'intérieur de la barrière de Jupiter et de Saturne, *i.e.* à moins de 15 UA du Soleil, tout en restant dans le nuage de Oort, même si les perturbations planétaires vont modifier le demi-grand axe de ces comètes. Or une modification du demi-grand axe change de manière significative l'efficacité des marées galactiques et des étoiles à modifier la distance périhélique des comètes et donc à les rendre observables.

Cette interaction entre perturbations planétaires et perturbations galactiques nous a permis de mettre en valeur les propriétés suivantes du flux de comètes observables (ces résultats correspondent à ceux de l'article (Fouchard et al., 2014a) inséré ci-après) :

- près de la moitié des comètes sont observables grâce à une perturbation planétaire reçue lors du passage au périhélie précédent. Sous l'effet de cette perturbation, le demi-grand axe a considérablement augmenté permettant ainsi aux marées galactiques, avec éventuellement l'aide des étoiles, de rendre ces comètes observables ;
- entre 15% (lorsqu'on tient compte des étoiles) et 25% (sans les étoiles) des comètes observables ayant franchi la barrière de Jupiter-Saturne sont passées à moins de 15 UA du Soleil au cours de leur histoire ;
- au total plus de la moitié des comètes observables se trouvait à une distance inférieure à 15 UA du Soleil lors du passage au périhélie précédant l'observabilité ;
- le pic de Oort est réduit à une distance de l'ordre de 30 000 UA avec 2/3 des comètes se trouvant vers la partie interne du nuage ;
- enfin, les comètes observables faisant des passages répétés à une distance inférieure à 15 UA du Soleil sont très largement sur des orbites rétrogrades, conduisant à une proportion totale de comètes observables sur des orbites rétrogrades de l'ordre de 60%.

Icarus 231 (2014) 110–121

Contents lists available at ScienceDirect

Icarus

journal homepage: www.elsevier.com/locate/icarus

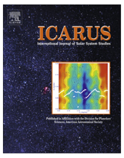

Planetary perturbations for Oort cloud comets: II. Implications for the origin of observable comets

M. Fouchard [a,*], H. Rickman [b,c], Ch. Froeschlé [d], G.B. Valsecchi [e,f]

[a] LAL-IMCCE, Université de Lille 1, 1 Impasse de l'Observatoire, F-59000 Lille, France
[b] PAS Space Research Center, Bartycka 18A, PL-00-716 Warszawa, Poland
[c] Dept. of Physics & Astronomy, Uppsala Univ., Box 516, SE-75120 Uppsala, Sweden
[d] Observatoire de la Côte d'Azur, UMR Lagrange 7293, Bv. de l'Observatoire, B.P. 4229, F-06304 Nice cedex 4, France
[e] IAPS, INAF, via Fosso del Cavaliere 100, I-00133 Roma, Italy
[f] IFAC-CNR, Via Madonna del Piano 10, I-50019 Sesto Fiorentino (FI), Italy

ARTICLE INFO

Article history:
Received 6 May 2013
Revised 27 November 2013
Accepted 27 November 2013
Available online 9 December 2013

Keywords:
Comets, dynamics
Comets, origin
Celestial mechanics

ABSTRACT

We present Monte Carlo simulations of the dynamical history of the Oort cloud, where in addition to the main external perturbers (Galactic tides and stellar encounters) we include, as done in a companion paper (Fouchard, M., Rickman, H., Froeschlé, Ch., Valsecchi, G.B. [2013b]. Icarus, in press), the planetary perturbations experienced each time the comets penetrate to within 50 AU of the Sun. Each simulation involves an initial sample of four million comets and extends over a maximum of 5 Gyr. For better understanding of the outcomes, we supplement the full dynamical model by others, where one or more of the effects are left out. We concentrate on the production of observable comets, reaching for the first time a perihelion within 5 AU of the Sun. We distinguish between four categories, depending on whether the comet jumps across, or creeps through, the Jupiter–Saturn barrier (perihelion distances between 5 and 15 AU), and whether the orbit leading to the observable perihelion is preceded by a major planetary perturbation or not. For reasons explained in the paper, we call the strongly perturbed comets "Kaib–Quinn comets".

We thus derive a synthetic picture of the Oort spike, from which we draw two main conclusions regarding the full dynamical model. One is that 2/3 of the observable comets are injected with the aid of a planetary perturbation at the previous perihelion passage, and about half of the observable comets are of the Kaib–Quinn type. The other is that the creepers dominate over the jumpers. Due to this fact, the spike peaks at only 31 000 AU, and the majority of new comets have semi-major axes less than this value. The creepers show a clear preference for retrograde orbits as a consequence of the need to avoid untimely, planetary ejection before becoming observable. Thus, the new comets should have a 60/40 preference for retrograde against prograde orbits in apparent conflict with observations. However, both these and other results depend on our model assumptions regarding the initial structure of the Oort cloud, which is isotropic in shape and has a relatively steep energy distribution. We also find that they depend on the details of the past history of external perturbations including GMC encounters, and we provide special discussions of those issues.

1. Introduction

In a previous paper (Fouchard et al., 2013a), we have developed a model to simulate the planetary perturbations on Oort cloud comets. That paper, in the following referred to as Paper I, was devoted to an analysis of these perturbations in order to evaluate precisely the dynamical opacity of the planetary system and the long term evolution of an Oort cloud of comets under their effect only. It was shown that the opacity of the Solar System is far from the step function of perihelion distance assumed in the definition of the loss cone, and rather decreases continuously from almost one (all the comets are lost) inside Jupiter's orbit to almost zero close to 15 AU. As regards the long term dynamics, it was shown that different regimes prevail from inside 15 AU, where the orbital energy of the comets evolves rapidly, to outside the orbit of Neptune, where a smooth diffusion is at work.

The aim of the present paper, i.e., Paper II, and the following one (Fouchard et al., 2013b) which we will call Paper III, is to examine what happens, when Galactic tides and stellar perturbations

---

[*] Corresponding author.

E-mail addresses: fouchard@imcce.fr (M. Fouchard), Hans.Rickman@physics.uu.se (H. Rickman), froesch@oca.eu (Ch. Froeschlé), giovanni@iaps.inaf.it (G.B. Valsecchi).

0019-1035/$ - see front matter © 2013 Elsevier Inc. All rights reserved.
http://dx.doi.org/10.1016/j.icarus.2013.11.032

operate together with the planetary perturbations. The output of long term simulations using different models including different perturbers will be compared in order to highlight the way in which these perturbers interact and to reach a deeper understanding of the effects displayed by the complete model. The present paper is devoted to the flux of observable comets, i.e., comets that reach heliocentric distances smaller than 5 AU for the first time, while Paper III will deal with the long term evolution of the cloud and the production of decoupled comets, entering into semi-major axes less than 1000 AU.

Our initial conditions and models used are presented in Section 2. The fluxes of observable comets obtained with each model are compared in Section 3. Section 4 is devoted to an analysis of the obtained Oort spikes. We discuss our main results and draw conclusions in Section 5.

2. Initial conditions and different models

We consider an initial, thermalized Oort cloud containing 4×10^6 comets. The shape of the initial distribution of orbital energy is as given by Duncan et al. (1987), and we take the initial semi-major axis between 3000 and 100000 AU. All comets have perihelion distances $q > 32$ AU, so that the loss cones are initially cleaned out. The Galactic tides and stellar encounter effects are modeled as in our previous papers (Rickman et al., 2008; Breiter et al., 2007; Fouchard et al., 2007). The planetary perturbations are applied as described in Paper I, and we simulate the dynamics of the Oort cloud over a time span of 5 Gyr, using different models. The reason for sticking to one model of the initial Oort cloud, which may not even be realistic, is that we want to focus attention on the dynamics rather than on interpreting the observed orbits. The latter will be the goal of forthcoming papers, where the choice of initial conditions will indeed be crucial. Here we will limit ourselves to a preliminary discussion in Section 5.

Four models are considered: tides only (T), tides and passing stars (TS), tides and planets (TP), and tides, passing stars and planets (TSP). For the TS and TSP models, four different random sequences of passing stars are used, leading to different evolutions of the Oort cloud. These are just different realizations of the same underlying model, using different random number seeds. The subscript $i = 1, \ldots, 4$ after the letter S will indicate the stellar sequence used. As we shall see, there are significant differences between the four sequences – nrs. 3 and 4 contain more encounters at close range with dramatic consequences than nrs. 1 and 2.

During the simulation, the orbital elements of the comets are always given in a fixed Galactic frame centered at the barycenter of the Solar System. Each time a comet enters into distances from the barycenter[1] less than $r_C = 50$ AU, a planetary kick is applied to the comet. The osculating, barycentric ecliptic elements are computed at peribaryon, and based on these, an integration of planetary perturbations only is carried out within a limiting distance $r_L = 100$ AU. After this, the new barycentric elements are applied at peribaryon, and we compute new elements in the fixed Galactic frame. Then the integration goes on with Galactic tides and passing stars until the next perihelion passage. See Paper I for details.

As regards the passage between ecliptic and Galactic coordinates, we use the present ecliptic coordinates of the Galactic pole throughout the integrations, thus assuming that the two fundamental planes do not precess with respect to each other (e.g., Levison et al., 2006). This is in line with neglecting the non-circularity and secular changes of the Sun's Galactic orbit, which are additional approximations of our long term model.

The T and TS models do not consider planetary perturbations explicitly, but the masses of the four giant planets are added to the Sun. Moreover, it is not a question of neglecting the planetary perturbations but of treating them by the classical *loss cone*[2] recipe. Each comet is integrated for a maximum time span of 5 Gyr, unless it reaches an end state. It may escape from the Solar System, i.e., reach a heliocentric distance larger than 4×10^5 AU, suffer a collision with the Sun or a giant planet (when planets are explicitly modeled) or penetrate within 15 AU of the Sun (when the loss cone model is used), or evolve into orbits with semi-major axis less than 1000 AU. The last end state corresponds to the decoupled comets.

In the present paper, our analysis will focus on the *observable comets*, i.e., comets reaching for the first time a heliocentric distance less than 5 AU. Since we are now mainly interested in the effect of planetary perturbations, all the results are expressed using barycentric and ecliptic elements of the comets. The focus will be placed on the TP and TSP models, while the T and TS models will serve mainly as material for comparison.

3. Production of observable comets

3.1. Time dependence of the flux

The numbers of observable comets produced by our models per period of 50 Myr are plotted versus time in Fig. 1. The fluxes of models without stellar perturbations are the same in each panel, while the panels differ with respect to the specific stellar sequences used in the TS and TSP models. For these models the background fluxes are seen to be similar in all panels whereas the high peaks are related to comet showers, caused by close stellar encounters that obviously differ between the four sequences.

The long term synergy between the tides and the stellar effects is visible in the difference between the T and TS models. This is caused by the filling of the so-called Tidally Active Zone (TAZ), where an integrable tide is able to make comets observable, via stellar perturbations. The effect was discussed in previous papers (Rickman et al., 2008; Fouchard et al., 2011a).

In the TP model we also observe a large increase of the flux of observable comets over the T model. However, in contrast to the difference between the T and TS models, where the synergy needs about 2 Gyr to reach its maximal effect, the difference between the T and TP models is seen from the very beginning. This is because the planetary perturbations help to inject observable comets through an almost real time interference with the tides, allowing a new path from the Oort cloud to the observable region (Kaib and Quinn, 2009). From Fig. 1 we can see that, toward the end of our simulations, the TS and TP models yield roughly similar increases of the new comet flux with respect to the T model. We regard this similarity as coincidental, since no obvious reason can be identified.

Could there also be a long term synergy in the TP model, like in the TS model, due to TAZ filling? The chances for such a synergy are reduced by two effects: (i) the comets affected by the planets are already close to, if not inside, the TAZ; (ii) the planets mainly affect the orbital energy, while the amplitude of the eccentricity cycle caused by the tides is almost unaffected, and consequently the planets have to reduce the semi-major axis in order to reduce the minimal perihelion distance and send a comet into the TAZ (Matese and Whitman, 1992; Fouchard et al., 2011a). This in turn makes the tides work more slowly in making the comet observable.

---

[1] From now on, all the orbital parameters will refer to the barycenter, but the terms perihelion, aphelion, etc. will mostly be used for simplicity.

[2] This means that below a threshold in angular momentum, represented by a perihelion distance below 15 AU, comets are modeled as lost from the Oort cloud; otherwise their orbits remain unchanged.

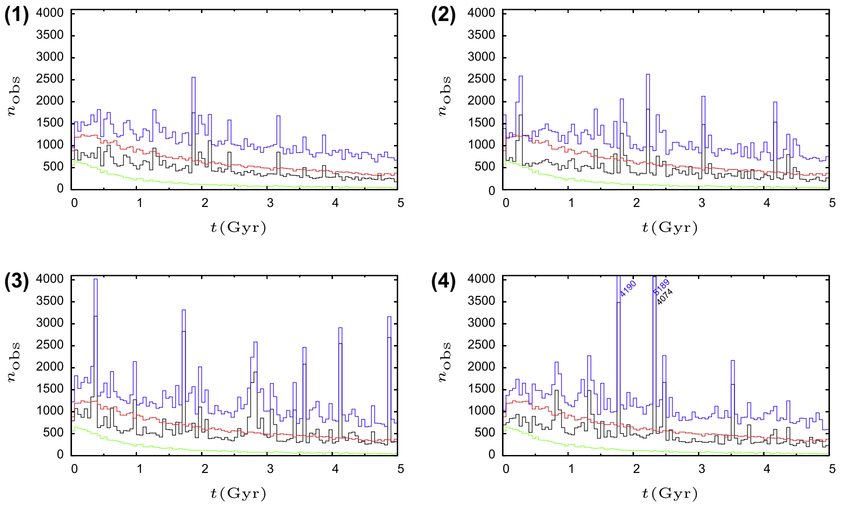

Fig. 1. Number of observable comets per period of 50 Myr versus time for the four different models: T (green line), TS_i (black line), TP (red line) and TS_iP (blue line). The number to the left above each plot indicates the index of the stellar sequence used. For the 4th sequence, the numbers on the right side of the highest peaks give the ordinate of the top, when the flux exceeds the plotted range. (For interpretation of the references to color in this figure legend, the reader is referred to the web version of this article.)

However, as shown by Kaib and Quinn (2009), planetary perturbations may shift a comet from the inner TAZ, i.e., semi-major axis $a < 20\,000$ AU, into the central TAZ, i.e., semi-major axis $20\,000 < a < 50\,000$ AU – thereby drastically speeding up their injection. Using the loss cone concept, we have seen (Fouchard et al., 2011a) that the tides are unable to directly inject observable comets from the inner TAZ, whereas they are very efficient from the central TAZ.

When adding the stellar perturbations in the TSP models, comparing with the TP model, we again see a large increase of the flux of observable comets. We interpret this to show that the TAZ filling that was not performed by planetary perturbations is now at work. In conclusion, the role of stars, at least in the long term, is still relevant for the flux of observable comets, since these are the only perturbers among the three kinds considered, which are able to efficiently inject comets into the TAZ.

Finally, we note that the increase of the TSP new comet flux over that of the T model is roughly equal to the sum of the increases exhibited separately by the TS and TP models. This means that there is no extra synergy introduced by combining the stellar and planetary perturbations.

3.2. Definition of observable classes

In our previous papers, where planetary perturbations were replaced by the loss cone concept, a comet could become observable only if its perihelion distance decreased sharply from above 15 AU to below 5 AU during one orbital period. On the other hand, when the planetary perturbations are modeled more realistically as described in Paper I, the perihelion is allowed to diffuse through the Jupiter–Saturn barrier before reaching the observable region. In a complete model, both mechanisms of comet injection must coexist, and in the following we will separate the observable comets into two classes, which we call *jumpers* and *creepers*. Specifically, creepers are comets that become observable without performing the above-described jump, and thus their preceding perihelion passage took place within the Jupiter–Saturn barrier.

There is another very important aspect of planetary perturbations concerning comet injection, related to their effects on the orbital energy. Levison et al. (2001) argued that the inner part of the Oort cloud could be a source of Halley-type comets and thus provide an explanation for the observed preference for prograde orbits among such comets. The dynamical route to follow should involve planetary perturbations of orbital energy in order to expose these inner Oort cloud comets to the Galactic tides and make them observable. In a similar vein, Levison et al. (2006) proposed that scattered disk objects would reach into the realm of Galactic tides and contribute to the flux of long-period comets via planetary perturbations due to the outer giants.

Following these ideas, Kaib and Quinn (2009) highlighted a previously unexplored route into observability in the Oort cloud, which may in fact dominate the new comet flux. It concerns Oort cloud comets with semi-major axis smaller than 20 000 AU – i.e., the inner part of the cloud. In this region, while passing stars are able to inject comets on their own across the Jupiter–Saturn barrier, the Galactic tides are too weak, even with the help of background stellar perturbations, and the perihelion distance normally evolves slowly under the influence of tides and stars (Fouchard et al., 2011b). On the other hand, in the course of this diffusion a planetary perturbation may push the semi-major axis of a comet to a value larger than 20 000 AU, at which the tides are able to make the comet observable in a single orbital period.

Due to the similarity between the explicit results of Kaib and Quinn (2009) and some of our results to be presented below, we will refer to comets injected by such a mechanism as *Kaib–Quinn comets*. This group involves both jumpers and creepers. Its inherent feature is that the comets are kicked by the planets strongly enough at the perihelion preceding observability that, by increasing the semi-major axis, the effect of the Galactic tide may be effectively turned on. Specifically, we require an increase from the last unobservable to the first observable perihelion passage of the original[3] orbital energy $z = -1/a$ by more than 1×10^{-5} AU^{-1}.

---

[3] This means the value of the corresponding quantity on the ingoing orbital branch, before the planetary perturbations are applied.

This number is arbitrary, but we have found it convenient in order to catch the above-described concept. For instance, the threshold may correspond to a jump in semi-major axis from 20 000 to 25 000 AU, i.e., from the inner Oort cloud into the part where the tides are efficient injectors of observable comets. Such an increase is consistent with the results of Kaib and Quinn (2009) and also with those of Fouchard et al. (2011b) and Rickman et al. (2012). In the latter papers we showed that the tides, even when helped by stars, are unable to make comets jump across the Jupiter–Saturn barrier if the semi-major axis is smaller than 20 000 AU, while the tides are able to make comets observable on their own for semi-major axis $a > 23\,000$ AU.

In summary, four classes of injected comets will be treated following the above definitions: "jumpers", "creepers", "Kaib–Quinn jumpers" and "Kaib–Quinn creepers". Fig. 2 provides a schematic illustration of the respective injection types.

3.3. Injection types and dynamical models

When stars operate, comet showers may occur. Since we want the results of such models to be reasonably representative of the current Solar System, and because it appears unlikely that an important shower would be directly responsible for the current flux of new comets (Dybczyński, 2002), we have decided to filter out all comets sent in by shower-producing stars. In addition, we want the long term synergy between the stars and the tides to be fully operational. Consequently, for the TS and TSP models, only the quiescent observable comets during the last 3 Gyr are taken into consideration. A quiescent comet as defined by Fouchard et al. (2011b) is a comet for which no enhancement-making star has passed close to the Sun during the last orbital period of the comet, and an enhancement-making star is a star that would inject more than five comets in the simulations by Fouchard et al. (2011a). As shown by Fouchard et al. (2011b), only stars injecting several times more than this limit would be able to contribute a majority of the new Oort cloud comets presently observed.

For the T and TP models, obviously all comets are quiescent. However, we want the tidal injection efficiency in these models to be at its maximum, i.e., we want the TAZ to be nearly full. Therefore, only the comets observable during the first 2 Gyr are considered. These differences between the models prevent quantitative comparisons between them, but nonetheless we are able to reveal and study the conditions for comet injection that characterize the respective models by comparing the relative distributions of injections of various kinds.

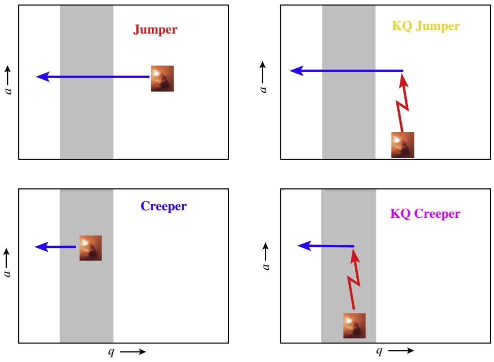

Fig. 2. Schematic view of the observable classes. The horizontal blue arrows correspond to the effect of the tides and passing stars on the comet during the last orbital period before it becomes observable, and the red vertical arrows to the effect of the planets at the perihelion preceding the observability. The gray zones mark the Jupiter–Saturn barrier. (For interpretation of the references to color in this figure legend, the reader is referred to the web version of this article.)

Table 1 gives the total number of observable comets during the corresponding interval, as mentioned above, for each model. The fractions of comets belonging to the jumper, creeper, Kaib–Quinn jumper and Kaib–Quinn creeper classes (p_j, p_c, p_{kqj} and p_{kqc}, respectively), and the fractions of prograde orbits in each class are also given.

Clearly, in the T model all the observable comets are jumpers. Using the loss cone concept, both the creeper categories are ruled out, and since the tides do not change the orbital energy of a comet much, the Kaib–Quinn jumpers are also lacking. Regarding the ecliptic inclination, the T model produces almost the same numbers of prograde and retrograde comets.

Very similar conclusions can be drawn for the TS model. There are important differences in the total numbers of observable comets between the four realizations, which are due to the differences in the stellar sequences that we already commented upon. Indeed, even though the comets counted are all quiescent, "comet drizzles" arise, resulting in an increase of the flux of quiescent observable comets for hundreds of Myr after major showers (Fouchard et al., 2011a).

The TS model is actually able to produce a few Kaib–Quinn jumpers, since stars may occasionally cause dramatic injections of single comets by very close encounters, even if they are not of the enhancement-making type. Such injections may produce Kaib–Quinn jumpers, since the large decrease of perihelion distance would generally be accompanied by a large perturbation of the orbital energy. As seen in Table 1, these cases are very rare. Note that they are different from the normal Kaib–Quinn jumpers, since their energy jump is produced by a star, not a planet.

When the planetary perturbations operate, the situation changes drastically. In the TP model, the fraction of jumpers is only about 44%, and the remaining 56% of the observable comets have followed routes involving planetary perturbations. Most of these comets are Kaib–Quinn creepers (about 38% of the total), while almost 13% are creepers and the remaining 5% are Kaib–Quinn jumpers.

The total number of jumpers, i.e., $n_{\rm obs}$ times p_j, increases by 38% from the T to the TP model. Consequently, even considering only the jumpers, we see a synergy between the tides and the planetary perturbations. As already noted, this synergy is due to a diffusion in orbital energy, which drives the comets from the inner part of the Oort cloud that is initially more populated into the central and outer parts, where the tides are able to decrease the perihelion distance of the comets in the way appropriate for the jumpers. This synergy does not affect the fraction of prograde orbits.

In the TSP model, the fraction of jumpers has decreased from 44% to about 34%, while the fractions of creepers and Kaib–Quinn creepers have increased by about 5% each. The number of jumpers has dropped, since the interval during which the observable comets are counted is now the last 3 Gyr instead of the first 2 Gyr for the TP model. Hence the TAZ has been depleted, especially in comets that are quickly injectable. This in turn reduces the rate of production of jumpers though not necessarily that of creepers or Kaib–Quinn creepers.

Comparing the TS and TSP models in terms of numbers, we note that the latter is about 3–4 times more efficient than the former in providing observable comets. Looking at the details, the number of jumpers shows only a moderate increase, and the main change is the appearance of the creeper groups. In fact, this is one of our most significant results. *The full dynamical model produces more creepers than jumpers, and most of the creepers are of the Kaib–Quinn type.* The latter feature is common to the TP and TSP models and is likely caused by the difficulty of avoiding large planetary kicks, when the perihelion diffuses inside Saturn's orbit.

Table 1
For each model type, described in the first column, the following columns give the total number of observable comets and the fraction in percent of prograde comets, and thereafter the fractions in percent of jumpers, creepers, Kaib–Quinn jumpers and Kaib–Quinn creepers followed by the corresponding fractions of prograde orbits. For the TS and TSP models, the data are averaged over the four TS_i (resp. TS_iP) realizations.

Model	n_{obs}	% prog	p_j (%)	% prog	p_c (%)	% prog	p_{kqj} (%)	% prog	p_{kqc} (%)	% prog
T	11884	50.0	100.00	50.0	0.00		0.00		0.00	
TS	8504	50.1	99.84	50.1	0.00		0.16		0.00	
TP	36828	44.5	44.40	49.3	12.56	31.5	4.58	65.7	38.46	40.2
TSP	30172	41.9	33.84	48.9	17.24	28.8	4.96	65.3	43.96	39.1

The predominance of retrograde orbits among both the creeper groups is a striking feature, which results from a risk for the creeping process of being discontinued by planetary perturbations – a risk that is obviously larger for comets on prograde orbits. This predominance increases somewhat from the TP to the TSP models.

3.4. Descriptions and illustrations

Let us now illustrate the different groups of observable comets and the underlying mechanisms by plots similar to Fig. 1 of (Kaib and Quinn, 2009), showing the orbital evolutions of comets until their injections. We choose examples from the TP model, which is the simplest one that exhibits all the relevant features. Each plot shows the evolution of a comet in the (q, a) plane. At each perihelion passage, two positions are plotted: the original one (before planetary perturbation) and the future one (after planetary perturbation) – except for the last perihelion at observability, for which only the original position is plotted. The dot color indicates the ecliptic inclination according to the scale on the right hand side of the plot. Consecutive positions are joined by a black line. The horizontal black lines are at $a = 20000$ and 25000 AU, and the gray area covers perihelion distances between 5 and 15 AU (the "Jupiter–Saturn barrier").

The comet shown in Fig. 3 enters the region where planetary perturbations are applied ($q < 50$ AU) with an inclination of 104° and $a \simeq 18000$ AU. The perihelion distance decreases under tidal effects, while the semi-major axis diffuses outward under planetary perturbations. When the latter reaches $a \simeq 26000$ AU, the tides are strong enough to directly inject the comet. In this case the last energy kick before the comet becomes observable is below the threshold chosen for the Kaib–Quinn comets, and thus the comet is a jumper. But, specifically, the kick amounts to 0.88×10^{-5} AU^{-1}, so the comet does not fail by much to be a Kaib–Quinn jumper. In fact, the classification of individual comets is a matter of chance in cases like the one shown. The dividing line is a borderline – not a gap that easily separates groups with entirely different properties.

The case in question shows how the TP model allows to obtain jumpers by a synergy between the tides and the planets. The Kaib–Quinn jumpers are in fact a special case of this synergy, where the diffusion of the orbital energy is ended by a strong planetary kick at the perihelion preceding the observability. Almost 2/3 of the comets in this group are prograde, since such orbits are more affected by planetary perturbations.

A typical Kaib–Quinn jumper is shown in Fig. 4. When this comet first arrives at $q < 50$ AU, its inclination equals 28° and its semi-major axis is $a = 4010$ AU. As long as $q > 30$ AU, a slow diffusion of the semi-major axis, lasting for 123 Myr, brings the comet to $a \simeq 7000$ AU. Then a first planetary kick by Neptune leads to $a = 16000$ AU, and a second one several revolutions later by Uranus, when $q = 19$ AU, leads to $a = 35000$ AU, from where the comet is directly injected into the observable region by the tides.

The Kaib–Quinn creepers follow paths similar to those of the Kaib–Quinn jumpers, except that their perihelion distance at the perihelion preceding the injection is less than 15 AU. This implies two important differences with respect to the Kaib–Quinn jumpers: (i) since the pre-injection perihelion may be close to the orbits of Jupiter or Saturn, the chance to have a large enough energy perturbation to qualify for Kaib–Quinn status is much larger, explaining the much higher fraction of Kaib–Quinn creepers than Kaib–Quinn jumpers (38% against 5% in the TP model); (ii) since the perihelion distance of Kaib–Quinn creepers must diffuse through the Jupiter–Saturn barrier, and because the planetary perturbations are stronger for prograde orbits, the risk of interrupting the process by ejection into interstellar space is more easily avoided for retrograde orbits (about 60% of this group are retrograde), contrary to the Kaib–Quinn jumpers. In fact, for the latter the prograde orbits are strongly preferred because of the need to undergo a large energy kick due to Uranus or Neptune, which are weak perturbers and almost unable to produce such perturbations unless the inclination is low.

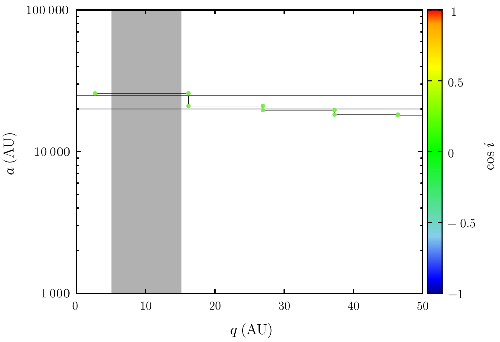

Fig. 3. Evolution in the (q, a) plane (see text for details) for a jumper comet, using the TP model.

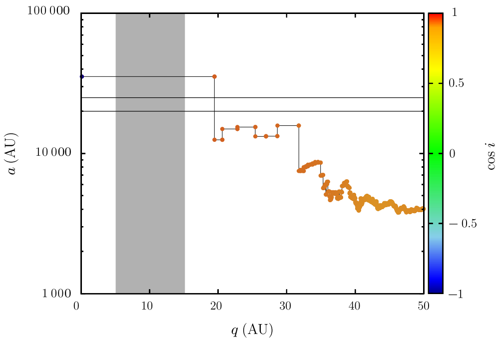

Fig. 4. Same as Fig. 3 for a Kaib–Quinn jumper, using the TP model. The critical energy kick preceding its injection amounts to 5.17×10^{-5} AU^{-1}.

Fig. 5 shows an example of a Kaib–Quinn creeper. It enters into $q < 50$ AU with a semi-major axis $a = 3200$ AU and an inclination equal to 138°. The perihelion distance slowly diffuses inward until $q \simeq 15$ AU. At this point the semi-major axis starts to diffuse more rapidly by first decreasing almost to 1000 AU, and then increasing again. A few moderate planetary kicks finally drive the semi-major axis slightly above 10 000 AU. When the perihelion distance reaches 8 AU, a kick by Saturn sends the comet into the central Oort cloud with $a = 25\,400$ AU. At this point, the tides may easily make the comet observable.

The comet shown in Fig. 5 is untypical of the Kaib–Quinn creepers only in one sense – the large number of perihelion passages inside the Jupiter–Saturn barrier. This is to be expected for comets originating in the inner core of the Oort cloud and moving on high-inclination, retrograde orbits, for which strong planetary perturbations are rare. However, it clearly demonstrates why creepers in general tend to be of the Kaib–Quinn type. Sooner or later, it is likely that a large planetary kick arises, like in the case shown, leading to observability via the Kaib–Quinn mechanism.

For the creepers, there cannot be a final planetary perturbation large enough to qualify for the Kaib–Quinn scenario, and the perihelion has to diffuse through the Jupiter–Saturn barrier. Consequently, the fraction of retrograde orbits is even higher than for the Kaib–Quinn creepers (almost 70%).

An example of a creeper is shown in Fig. 6, where the comet enters into $q < 50$ AU with a semi-major axis $a = 13\,800$ AU and an inclination equal to 70°. After a sequence of small or moderate planetary kicks, the comet is finally injected into the observable region with $a = 19\,700$ AU and an inclination of 80°. Like the previous comets, it remains within the TAZ with a steadily decreasing perihelion distance due to the tides. The step size of this continuous decrease is clearly related to the semi-major axis.

A remark has to be made regarding the past history of the injected, observable comets. We have observed that 25% of the jumpers in the TP model have passed at least once inside $q < 15$ AU – and, obviously, not just one revolution before their observability. How can such a large fraction be explained? Consider a comet that is sent by a planetary kick into the range of semi-major axis beyond 50 000 AU, i.e., the outer part of the cloud. This is an extreme case, but it serves well for illustration. As discussed by Fouchard et al. (2011b), the likelihood for such a comet to become observable is then limited by what we may call a timing problem. By the time the comet comes back to its next perihelion, the tidal eccentricity cycle will likely have made the perihelion distance pass its minimum and return to larger values. However, the comet being in the TAZ (with no possibility to get out from it since the stars are not present in this model), it can become observable many orbital periods later, when the timing condition is met for the first time and the comet can actually pass perihelion within 5 AU of the Sun.

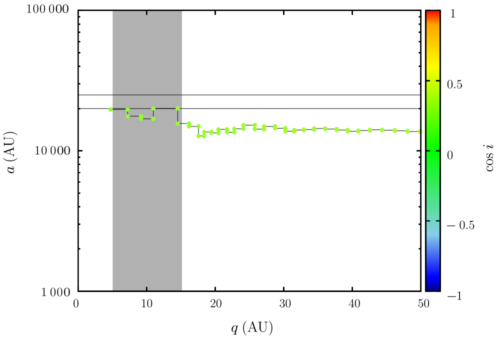

Fig. 6. Same as Fig. 3 for a creeper, using the TP model. The critical energy kick preceding its injection amounts to 0.59×10^{-5} AU^{-1}.

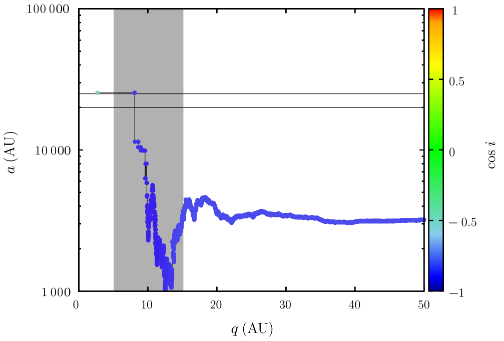

Fig. 5. Same as Fig. 3 for a Kaib–Quinn creeper, using the TP model. The critical energy kick preceding its injection amounts to 4.83×10^{-5} AU^{-1}.

Such an injection is shown in Fig. 7. The triggering planetary kick is given at $t = 110$ Myr with a perihelion distance equal to 13 AU. The resulting semi-major axis is $a \simeq 67\,000$ AU. Then the comet escapes the planetary region of the Solar System for many orbits and comes back at $t = 1990$ Myr with an almost unchanged semi-major axis.

The type of evolution in question is most clearly exemplified by the outer Oort cloud comets but is not strictly limited to them. The perihelion timing problem also concerns comets with $a \sim 40\,000$ AU, belonging to the central part of the cloud, though to a lesser extent. Concerning the TSP models, because of the presence of the stars, which can eject comets from the TAZ, the fraction of jumpers that have visited the Jupiter–Saturn region before their injection is lower, amounting to 15–20%.

4. The Oort spike

4.1. General shape and jumper class

Let us now discuss the orbital distribution of observable comets in more detail. An important remark has to be made at the outset, namely, that the energy distribution within the cloud reflects the assumed, initial energy distribution, and thus the quantitative results to be presented are to some extent model dependent. With

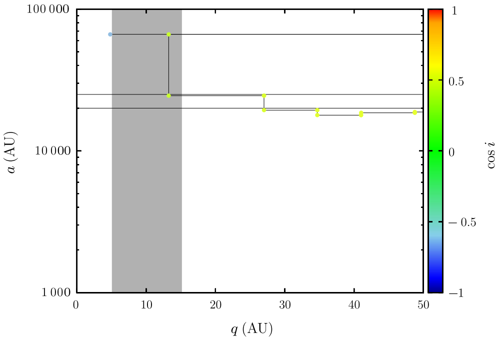

Fig. 7. Same as Fig. 3 for a jumper that has visited the Jupiter–Saturn region during its past history, using the TP model.

other assumptions, the results would likely be different. The extent of these differences is not known and remains to be explored.

Fig. 8 shows histogram distributions, normalized with respect to the total number of observable comets, of the original orbital energy $z_o = -1/a_o$ for the observable samples of the four models (black lines). We recall that this quantity refers to the first time these comets pass perihelia with $q < 5$ AU. The bell-shaped curves thus displayed will be referred to as *Oort spikes*. In addition, the distributions of initial orbital energy $z_i = -1/a_i$ at the start of the simulations ($t = 0$) for the same observable comets are also shown (green lines). For the TS and TSP models, these distributions are averaged over the four simulations with different sequences of stellar encounters. In order to evaluate the separate contributions of different injection scenarios, within each orbital energy bin, the red area is proportional to the number of jumpers, the blue area to the number of creepers, the orange area to the number of Kaib–Quinn jumpers and the violet area to the number of Kaib–Quinn creepers.

The distributions in the T and TS models were already described at length by Fouchard et al. (2011b) and Rickman et al. (2012). The main difference between them is that the TS Oort spike peaks at a smaller semi-major axis, i.e., 34 000 versus 48 000 AU. A feature not previously emphasized is that for the TS model, the distribution of a_i for the observable comets is very different from their a_o distribution. Specifically, a diffusion from the inner part of the Oort cloud into the central and outer parts is seen to have occurred from $t = 0$ to the time of observability.

On average, we find that 43% of the observable comets in the TS model come from the inner Oort cloud, i.e., $a_i < 20\,000$ AU and almost 10% even from $a_i < 10\,000$ AU. But the process that we vaguely described as diffusion may in fact have a significant component caused by a few dramatic events. In Paper III we will show that a large-scale migration occurs inside the Oort cloud, caused by the closest and strongest stellar encounters. At this point, let us note that the four different TS models with different stellar encounter sequences yield quite different results regarding the above-mentioned percentages. In model TS$_1$, which is the most quiescent, we find that 30% of the observable comets have migrated from the inner Oort cloud and 5% from $a_i < 10\,000$ AU, while in the relatively dramatic TS$_3$ model, we find 52% and 15%, respectively. Finally, note that, as expected, no migration is observed for the T model, since the tides are not able to significantly change the orbital energy, even on long time scales.

In the TP model, the Oort spike peaks at about 31 000 AU. This decrease from the T model is mainly due to the existence of creepers and Kaib–Quinn creepers, whose distributions peak at smaller a_o. However, even considering only the jumpers, their distribution peaks at 38 000 AU versus 48 000 AU for the T model. This difference is caused by the already mentioned synergy in observable comet injection between planetary perturbations and Galactic tides. Specifically, comets from the inner part of the cloud, where the tides are unable to inject them, migrate outward under planetary perturbations. During this process, the tides inject them as soon as possible, which favors the smaller semi-major axes of the injectable range.

Measuring the amount of synergy by the relative increase of the number of jumpers from the T to TP models, it reaches its maximum (about 53% in contrast to the overall 38% increase) for

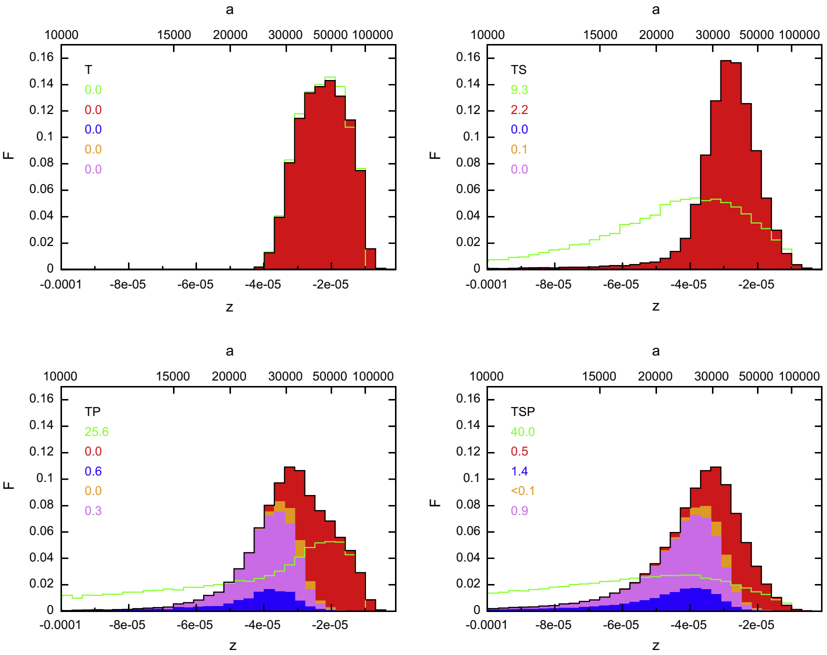

Fig. 8. Oort spikes (black lines) formed by four samples of observable comets along with the distributions of initial orbital energy (green lines). The histograms are normalized so that their integral is unity. The colors display the fractional contributions by the four groups of observable comets: red for jumpers, blue for creepers, orange for Kaib–Quinn jumpers, and violet for Kaib–Quinn creepers. The upper left panel shows the T model, and then, clockwise, the TS, TSP and TP models are shown. Note that some jumpers with $a_o < 20\,000$ AU in the TSP plot cannot be seen, because they are too few, and their colored area is covered by the black line. The colored numbers to the left in each panel indicate the cumulative fractions at $a < 10\,000$ AU, corresponding to the different histograms. (For interpretation of the references to color in this figure legend, the reader is referred to the web version of this article.)

$a_o \simeq 38\,000$ AU, coinciding with the maximum of the number of TP jumpers. On the other hand, below $a_o \simeq 24\,000$ AU, neither TP jumpers nor T jumpers exist, since the planets are unable to contribute directly to the decrease of the perihelion distance.

A clear sign of the semi-major axis diffusion caused by the planets is that 51% of the observable comets in the TP model have $a_i < 20\,000$ AU. This is higher than we obtained in the TS models, even though the observability is reached in the TP model already during the first 2 Gyr. This reflects the fact that planetary perturbations are much more efficient than the usual stellar perturbations in changing the orbital energy of Oort cloud comets.

Note that the Oort spike in the TP model differs from the TS model by an important number of very large semi-major axes ($a_o > 50\,000$ AU) even though it peaks at a lower value. This is almost exclusively caused by jumpers. Since the a_o and a_i distributions are identical, we conclude that the comets have not suffered any change in semi-major axis before their injection. Hence, they cannot have visited the Jupiter–Saturn region and most likely have not entered into the planetary system. In the absence of stars and a well-defined TAZ, they may have orbited many times since the start of the simulation with perihelia beyond 50 AU. They might indeed be victims of the "timing problem", such that the tides repeatedly brought their perihelion distances below 5 AU but never at the time of a perihelion passage.

In the TSP model, the peak of the Oort spike is located at the same place as in the TP model, i.e., at 31 000 AU. However, 67% of the observable comets have $a_o < 31\,000$ AU in the TSP model, compared to only 47% in the TP model. Several factors may contribute to this difference. During the preceding 2 Gyr of the TSP model, the stars have depleted the outer part of the Oort cloud, and this depletion continues throughout the time interval under consideration, thus favoring the inner and central parts. Moreover, stars play a role in comet injection via the real time synergy with the Galactic tides, and whether we consider jumpers or creepers, this help is mainly of importance for semi-major axes small enough for the tides to be inefficient. Another important role is that they may clean comets away from the TAZ and thereby reduce the number of the above-described "delayed entries" at $a_o > 50\,000$ AU, which was found important in the TP model.

The TSP jumpers have a maximum at 38 000 AU. This is slightly higher than in the TS model but equal to that of the TP jumpers. The synergy between the planets and the Galactic tides is still active with an overall increase of about 20% in the number of jumpers from the TS to the TSP models. The amount of this synergy, as defined above, is rather low (5%) for $a_o < 20\,000$ AU, and reaches a maximum (30%) at about 42 000 AU. This global shift to higher semi-major axes of the jumpers is caused by the diffusion toward larger semi-major axis due to the planets. The price to pay is that the stars may now eject the comets from the Oort cloud, thus reducing somewhat the synergy between the planets and the tides.

Another consequence of this diffusion is that the number of jumpers with small semi-major axis coming from stellar injections, in particular those with $a_o < 10\,000$ AU, is reduced from the TS to the TSP models. This region of the Oort cloud has suffered some depletion due to planetary perturbations in the latter models – especially comets with perihelion distances in the range from 15 to 50 AU, which tend to reach the decoupled end state in the course of more than 2 Gyr.

4.2. Effects of long-term evolution

The diffusion in orbital energy due to the planets also causes the percentage of observable comets with $a_i < 20\,000$ AU in the TSP model to be higher than in the TS model. In Table 2 we present those fractions for all models except T, where the percentage is always zero. We give the results for the simulated intervals before and after 2 Gyr in order for the TP model to be comparable to the others. We see that the TP and TSP models yield nearly the same results, while the TS model has a lower fraction of comets originating in the inner Oort cloud, especially in the beginning. It thus seems that, when planetary perturbations are at work, they largely conceal the star-induced migration and diffusion effects on orbital energies. However, a detailed analysis of the percentages resulting from the different versions of the TS model with different stellar encounter sequences reveals a clear correlation between these percentages and the strength of the strongest encounters, indicating an important role of star-induced migration. This correlation also exists for the TSP models but is weakened by the planetary effects.

A salient feature of Table 2 is the important increase of the fraction of observable comets originating in the inner part of the cloud from the first two to the last 3 Gyr of the simulations. This amounts to about 40% for the TP and TSP models and a full factor four for the TS model. Two phenomena that play important roles in controlling the feature are TAZ filling and the Kaib–Quinn mechanism, and comparing the TS and TP models, we realize that the TS model has only TAZ filling, while the TP model has only the Kaib–Quinn mechanism.

Actually, the results are then somewhat counter-intuitive, because TAZ filling is what keeps the injection rate of observable comets at a higher level toward the end of the simulation in the TS than in the TP model (cf. Fig. 1), and this means a continued production of observable comets mainly from the outer part of the cloud. Hence, the very large increase of the inner cloud fraction in the TS model needs yet another explanation, and the obvious candidate is the star-induced outward migration of comets.

Such migration must be present in the TSP model too, but the effect is much smaller in this case. Moreover, even though the star-induced migration is absent in the TP model, the results are very similar in the TP and TSP models. As far as we can judge, the Kaib–Quinn mechanism is the main reason why observable comets come from the inner cloud in both cases, and the increase of the fraction toward the end of the simulation is due to the decreasing contribution by the outer cloud due to the depletion of the TAZ.

4.3. Creepers and Kaib–Quinn comets

Let us now discuss the creepers and the two Kaib–Quinn groups. These kinds of observable comets are absent in the T and TS models, whereas, as already mentioned, they represent the majority of the injections when planetary perturbations are included (TP and TSP models).

In particular, we shall consider the number of passages within the Jupiter–Saturn barrier, i.e., perihelion passages with $5 < q < 15$ AU, before the comet becomes observable (by definition, this number is at least 1 for creepers and Kaib–Quinn creepers). We denote the number by n_{jsb}. For each model, we split the sample of four million comets into four equal samples of one million each. Then, for each such sample, we compute the median of n_{jsb} in each bin of a_o. The arithmetic mean of the four median values, denoted $\overline{n_{jsb}}$, is considered for analysis along with the arithmetic means of the related 10th and 90th percentiles.

Table 2
Fraction (in percent) of observable comets during the period given in the first row (in Gyr) initially in the inner Oort cloud ($a_i < 20\,000$ AU).

Model	$[0, 2]$	$[2, 5]$
TS	11	43
TP	51	72
TSP	53	73

Fig. 9 shows for each group (creepers, Kaib–Quinn creepers, and Kaib–Quinn jumpers), and from top to bottom, the value of $\overline{n_{jsb}}$, the fraction of prograde orbits, and the number of comets in the respective group, all versus $z_o = -1/a_o$, and finally the number of comets versus the original orbital energy at the last perihelion preceding the observable one (z_p). The left panel is for the TP model, and the right one shows the average of the TSP models.

As a general result, our analysis of the 10th and 90th percentiles shows that n_{jsb} is a quantity with a broad distribution. However, both the upper and lower fractions of the population behave similarly to the median concerning the variation with z_o. We note that the values presented for $\overline{n_{jsb}}$ are consistent with our findings in Paper I, where it was shown in Fig. 8 that only the comets with $q < 5$ AU had been strongly depleted by planetary perturbations after 10 revolutions, while those with somewhat larger perihelion distances were largely remaining.

4.3.1. TP model results

We first discuss the TP model. Here, for the creepers, the original semi-major axis at observability (a_o) has its maximum near 26 000 AU, and for the Kaib–Quinn creepers the maximum is at about 28 000 AU. But while the maximum of $a_p = -1/z_p$ is at the same position as that of a_o for the creepers, it is close to 17 000 AU for the Kaib–Quinn creepers. Indeed, for the latter group the distribution of z_p extends to very small semi-major axes, even including 317 comets with $a_p < 3000$ AU. More than 90% of the Kaib–Quinn creepers were in the inner Oort cloud ($a_p < 20 000$ AU) one orbital period before their observability, whereas this fraction is less than 20% for the creepers.

These are obvious consequences of the strong planetary kicks imparted to the Kaib–Quinn comets at their perihelia preceding the injection. This also explains why $\overline{n_{jsb}}$ is generally one order of magnitude larger for the Kaib–Quinn creepers than for creepers. Since their orbital energy before the injection was much smaller, the decrease of the perihelion distance caused by the tide was much slower. By contrast, the majority of the creepers are *fast creepers*, i.e., comets that made only a single passage within the Jupiter–Saturn barrier before their injection.

The large values of $\overline{n_{jsb}}$ that are seen at $a_o > 50 000$ AU for creepers and Kaib–Quinn creepers result from the contributions of a few comets that made many passages within the Jupiter–Saturn barrier with small semi-major axes before receiving one or two planetary kicks that sent them into a semi-major axis larger than 50 000 AU. At that point they could become observable as creepers or Kaib–Quinn creepers on the condition of avoiding the above-mentioned timing problem. However, since only single or very few comets contribute in this range of a_o, the results have no statistical significance.

The variations of $\overline{n_{jsb}}$ and the prograde fraction are broadly correlated, i.e., the fewer the previous entries within the Jupiter–Saturn barrier, the higher the fraction of prograde orbits. Both these properties correlate positively with the value of a_o. Beyond $a_o = 20 000$ AU, we note a steeper increase with a_o of the prograde fraction for Kaib–Quinn creepers than for creepers. This is explained by the fact that most of the Kaib–Quinn creepers (more than 90%) had $a_p < 20 000$ AU, so that for increasing a_o the strength of the last planetary kick should typically be larger, which calls for a larger prograde fraction.

Below $a_o = 20 000$ AU, the prograde fraction is small for both creepers and Kaib–Quinn creepers, showing relatively little variation with a_o. We mentioned the reason for the retrograde predominance above, namely, the risk of ejection by planetary perturbations before the creeping is over.

The behavior of the Kaib–Quinn jumpers is naturally quite different. Due to the constraint of a large tidal decrease of q leading to observability, their distribution of a_o peaks around 34 000 AU, and no Kaib–Quinn jumpers are found below 24 000 AU, as for the other jumpers. Similar to the Kaib–Quinn creepers, the distribution of a_p peaks at around 20 000 AU, i.e., much less than for the a_o distribution. Again, for this group, a majority of the comets (about 63%) were in the inner Oort cloud one orbital period before becoming observable. Obviously, as expected for Kaib–Quinn jumpers, in general n_{jsb} is always zero.

The prograde fraction of Kaib–Quinn jumpers is naturally high, since they have to receive a strong planetary kick. The trend for this fraction to decrease with a_o is at first glance surprising. However, if we had counted the inclination at the perihelion preceding

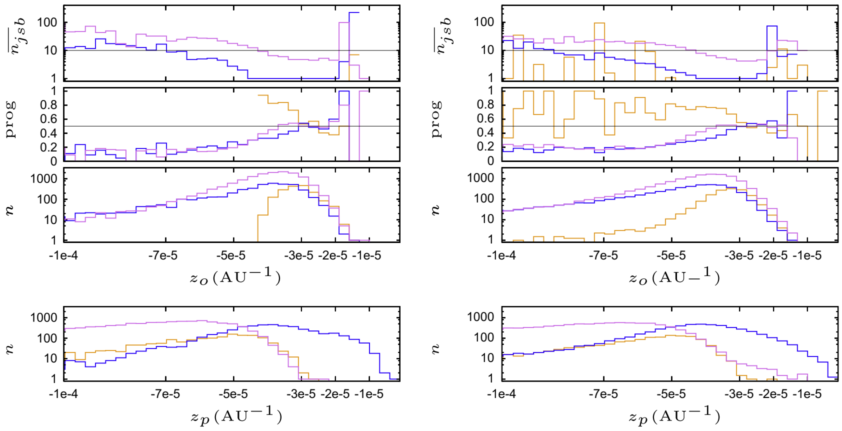

Fig. 9. For each group, i.e., creepers (blue lines), Kaib–Quinn creepers (violet lines), and Kaib–Quinn jumpers (orange lines), the value of $\overline{n_{jsb}}$ (top plot), the fraction of prograde orbits (middle top plot) and the number of comets (middle bottom plot) are shown versus z_o, and the number of comets in each group also versus z_p (bottom plot). The left and right panels show results of the TP and TSP models, respectively. Note that the absolute numbers shown in the lower plots cannot be straightforwardly compared between TP and TSP, since the respective time periods are different. (For interpretation of the references to color in this figure legend, the reader is referred to the web version of this article.)

the injection instead of at observability, then a flat fraction of prograde orbits around 70–80% would have been obtained. This is explained by the effect of the Galactic tides during the last orbital period. Indeed, the third component of the angular momentum with respect to the Galactic plane is a quasi-constant of motion, and consequently, if the perihelion distance undergoes a drastic change, so does the Galactic inclination. And obviously, the larger is the semi-major axis, the larger is the jump experienced in one orbital period. The inclination of the Galactic plane with the ecliptic finishes the job, introducing a loss of memory of the ecliptic inclination from the perihelion preceding the injection (Levison et al., 2006; Dones et al., 2005).

4.3.2. TSP model results

We now turn to the TSP model, illustrated in the right-hand panel of Fig. 9. Let us first consider the creepers and Kaib–Quinn creepers. As we remarked when discussing Table 1, their total numbers do not change much between the TP and TSP models, and we can now see that the plotted a_o distributions are also very similar (to within about a factor 2).

One difference between the models is that the TSP model has two agents (stars and tides) causing changes of the perihelion distance, which is of particular importance in the inner part, where the tides are very inefficient. This tends to increase the speed of creeping and hence also the number of both kinds of observable creepers.

A clear indication of the help offered by the stars to creepers is the decrease of $\overline{n_{jsb}}$ from TP to TSP models, generally for $a_o < 23\,000$ AU. In accordance with the lower value of $\overline{n_{jsb}}$, the prograde fraction is somewhat higher in the TSP than in the TP model for this inner part of the cloud. However, for $a_o > 23\,000$ AU, things work in the opposite sense. Here, in the TP model, all the creepers are fast, having $\overline{n_{jsb}} = 1$, which means that the tides are working quite efficiently, so the "help" of the stars is no longer appreciated. In fact, it turns into an obstacle, since stars are also able to slow down the decrease of the perihelion distance caused by the tides.

A typical example of a creeper, for which the injection is facilitated by stellar perturbations, is shown in Fig. 10. We note that, contrary to the TP model, the steps in perihelion distance are not related to the value of the semi-major axis. Large decreases may occur even for moderate semi-major axes. This example also shows that an enhancement-making star (the ones that we exclude from the statistics of observable comets; see above) may have had some importance in the past evolution of the real comets, helping to reduce their perihelion distances. Such an encounter may produce a reservoir of future creepers and Kaib–Quinn creepers. Clearly, then, close stellar encounters with the Sun will not only produce comet showers in the form of jumpers, but for some time after such an event they also produce an increase in the numbers of both kinds of creepers.

The stars have a small but noticeable effect on the distribution of a_p. For the TSP model, the maxima of a_p are at 24 000 AU for the creepers and 15 000 AU for the Kaib–Quinn creepers – in both cases about 2000 AU less than for the TP model. The fractions of comets with $a_p < 20\,000$ AU are almost 95% for the Kaib–Quinn creepers and 32% for the creepers.

Finally, as regards the Kaib–Quinn jumpers, a similar effect of stars as for the creepers and Kaib–Quinn creepers is observed, i.e., an increase of the injections toward small semi-major axis (that is extremely clear here, since the TP model was not able to produce Kaib–Quinn jumpers at all below 24 000 AU) and a decrease of the injections at large semi-major axis. About 70% of this group were in the inner Oort cloud at the perihelion passage preceding the injection. The stellar effects below 24 000 AU may be separated into two categories: between 20 000 and 24 000 AU the injections are mainly tidal but the real time synergy with stars is needed, while below 20 000 AU we essentially deal with stellar injections at rare, close encounters.

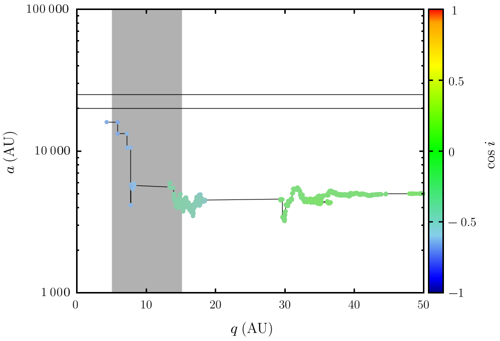

Fig. 10. Same as Fig. 3 for a creeper using the TSP model. The three major downward jumps in q are caused by dwarf stars penetrating to less than 10 000 AU from the Sun, which also cause moderate changes in the inclination.

4.4. Comparison with Kaib and Quinn

Since our TP model is very similar to the one used by Kaib and Quinn (2009), we need to compare our results with theirs. For instance, we find that 53% of the observable comets had their initial orbits in the inner Oort cloud ($a_i < 20\,000$ AU), while they found 56% with an initial inner to outer population ratio of 1.5 and 72% with a ratio of 3.5. In our case this ratio is 2.8, so we should find something in between. The reason that we find a somewhat smaller percentage likely stems from the fact that we count observable comets from time $t = 0$ to 2 Gyr, while they focused on injections after at least 1 Gyr. Since most of ours occur before 1 Gyr (see Fig. 1), the comets have had less time to migrate to larger semi-major axes than in their case. Indeed, our percentage of observable comets that started in the inner Oort cloud increases to 72%, if we instead consider the time from 2 to 5 Gyr.

The statistics of injection scenarii are not easy to compare, since Kaib and Quinn (2009) count comets that move outward across the $a = 20\,000$ AU limit at the perihelion preceding the final revolution, while we define Kaib–Quinn comets based on the size of the last planetary kick. If we make the reasonable assumption that all our Kaib–Quinn comets were initially in the inner Oort cloud, we find that 81% of all initially inner Oort cloud comets that become observable belong to the Kaib–Quinn category (mostly Kaib–Quinn creepers) – quite close to the value of 85% found by Kaib and Quinn (2009).

5. Summary and conclusions

We have produced several models of the dynamics of a large sample of Oort cloud comets affected by the Galactic tides, passing stars and giant planets over the age of the Solar System. The models differ in the kind of perturbers taken into account, or the sequence of passing stars used. Attention was paid to the observable comets, which enter within 5 AU of the Sun for the first time.

We classified the observable comets into the jumper group, for which the perihelion jumped across the Jupiter–Saturn barrier in a single orbital period, and the creeper group, for which at least one perihelion passage occurred inside this barrier. In addition, if the original orbital energy had undergone an increase larger than 10^{-5} AU^{-1} between the perihelion preceding the injection and the one at observability, then the comets were also flagged as Kaib–Quinn comets.

Generally, led by previous experience, we may characterize our results in terms of synergies, and the main one explored in this paper is that between the planets and the tides. It is driven by the diffusion of the orbital energy under planetary perturbations, which may push the semi-major axis of the comets to large values, helping the tides to directly inject them. We verify the results by Kaib and Quinn (2009), and we find this synergy to be responsible for all the Kaib–Quinn comets (43% of the observable comets in the model with tides and planets) as well as an increase of about 38% in the number of jumpers. One feature of the synergy is that $15-20\%$ of the jumpers (corresponding to about 6% of all the observable comets) in the TSP model have made a previous passage inside the Jupiter–Saturn barrier long before they get observable. During those passages, the orbital energy is strongly increased due to the planets. The tides being very efficient, the perihelion moves away from the planetary region during the following orbital revolution. Hence, the comets have to wait at least one tidal perihelion cycle (often several) before becoming observable.

The other key feature is the non-complete dynamical opacity – or ‘‘leakiness’’ – of the Jupiter–Saturn barrier, which was studied in Paper I. This implies the existence of creepers, and most of the Kaib–Quinn comets indeed belong to the creeper category. In addition to the above-mentioned 43% of the observable comets being of the Kaib–Quinn type in the TP model, another 13% are creepers lacking the large energy jumps of the Kaib–Quinn comets. All in all, mainly due to the introduction of the Kaib–Quinn and creeper categories, the injection rate of observable comets shows a dramatic increase, when planets are added to the tides.

The same happens, when we add planets to the model of tides and stars. We note that the flux of observable comets is 3–4 times larger in the average TSP model than in the average TS model. Since this may concern the present time, it is worth emphasizing that the number of comets in the Oort cloud derived from the observed flux of new comets passing perihelion will be roughly 3–4 times less using our current results for TSP models than it would have been based on our previous papers, e.g., (Rickman et al., 2008). Another interesting feature is that, considering Kaib–Quinn comets and others together, creepers dominate over jumpers. This means that we have found a likely explanation to the phenomenon noted by Królikowska and Dybczyński (2010) – namely, that many comets traditionally called new seem to have passed their previous perihelia deep within the planetary system. These may in fact be creepers like we predict for the majority of new comets. Further discussion of this is given by Rickman (2013).

The large abundance of creepers prompts a somewhat speculative remark as follows. If indeed the Oort cloud was formed as a by-product of scattered disk formation within the Nice Model scenario (Brasser and Morbidelli, 2013), the lack of a clear chemical distinction between Oort cloud and ecliptic comets (A’Hearn et al., 2012) has a natural explanation, since all comets were formed in the same trans-planetary disk. However, one can imagine that the jumper categories of new comets might show some special characteristics, because they did not approach the Sun to less than 15 AU before becoming observable. If so, one should expect that less than half the new comets would have those properties, and when looking for the fingerprints of chemical pristinity, it would be a mistake to lump all new comets together.

We will now consider the interpretation of the observed new comet flux in terms of the Oort cloud population, but we have to caution that using the numbers presented in this paper for such an estimate is subject to uncertainties, because we count only the ‘‘quiescent’’ observable comets applying a very strict definition. Thus, in case the current conditions are less quiescent than we require, we would be underestimating the injection efficiency.

According to Table 1, the TSP model yields on the average 3×10^4 comets with $q<5$ AU in 3×10^9 yr for an initial Oort cloud population of 4×10^6. The observed new comet flux with $q<5$ AU can be taken as 4 yr^{-1} with total absolute magnitude $H_T<11$ (Francis, 2005), and this yields an initial Oort cloud population of 1.6×10^{12}. Noting that the average TSP model has 5.3×10^5 survivors in the classical (i.e., central and outer parts) Oort cloud[4] after 5 Gyr, we estimate 6×10^5 at the present time, assuming the Oort cloud to have formed in the early Solar System. This means that the classical Oort cloud should currently have 2.4×10^{11} members with $H_T<11$. But the entire Oort cloud should have about 1×10^{12} – significantly more than estimated by Kaib and Quinn (2009) using the same estimate by Francis (2005).

Even though the magnitude limit $H_T<11$ is useful for comparison with other investigations like the one just made, it is worth mentioning that, according to Fernández and Sosa (2012), this will on the average correspond to comet nuclei as small as 0.6 km in diameter, for which there are serious issues regarding both physical lifetime and discovery completeness. Using $H_T<6.5$ as a proxy for nuclei with radii exceeding 1 km, the distribution function yields a cumulative number of about 40% of that for $H_T<11$, so our estimate can be expressed as 4×10^{11} km-sized comet nuclei in the entire Oort cloud. We finally note that this is model dependent, being coupled to our assumption for the initial energy distribution of the cloud. Also, the ratio between the populations of the total and classical Oort cloud is subject to a similar modeling uncertainty. Therefore, the issue of the total number of Oort cloud comets needs further study.

A case in point is the recent study of the origin of the Oort cloud by Brasser and Morbidelli (2013) in the framework of the Nice Model. This indicates that the mechanism explored is viable, though a problem still exists with the large number of comets in the present cloud, as indicated by previous papers and, tentatively, by this paper too. A resolution of this issue would be a major step forward, and we conjecture that a serious study of the population size of the Oort cloud by our present model, based on a realistic picture of the initial conditions for the newly formed cloud at the proper time (about 4 Gyr ago according to the Nice Model) will be an essential part of such a project.

The synthetic Oort spike produced by our TSP model is dominated by the creeper category (mostly of the Kaib–Quinn type). It peaks around 30000 AU, but 2/3 of the comets are on the inside of the peak, and this is caused by the creeper predominance. This feature of our results, like the creeper predominance itself that we commented upon above, is in agreement with what Królikowska and Dybczyński (2010) found from their non-gravitational orbit determinations, i.e., that real comets seem to prefer smaller a_o values than earlier believed.

An interesting result is found concerning the inclination distribution of Oort spike comets. Jumpers are equally prograde and retrograde, but Kaib–Quinn jumpers are mostly prograde and creepers are mostly retrograde. Considering the relative contributions, we find that nearly 60% of the comets are retrograde. This varies to some extent across the spike, because in the largest semi-major axis range, the efficiency of the Galactic tides to change the ecliptic inclination, even on a single orbital period, is so large that the fractions of prograde and retrograde orbits tend to be equalized. On the other hand, the creeper predominance on the inside of the peak causes an even larger excess of retrograde orbits there.

There is an obvious discrepancy between our expected retrograde predominance in most parts of the Oort spike and the apparent nearly uniform distribution of $\cos i$ for new Oort cloud comets.

---

[4] This result is discussed in Paper III.

In their Supporting On-line Material, Kaib and Quinn (2009) presented inclination distributions for the observable comets produced in their simulations, and they found a retrograde excess of 55% versus 45% even for a model, where the inner core of the cloud was taken to be predominantly prograde. Thus, the even stronger retrograde excess that we find cannot be canceled out by assuming such a flattened inner core. Our preferred explanation for the discrepancy is that the Oort cloud underwent a major external perturbation less than 1 Gyr ago, which caused a massive TAZ refilling. This may have been a GMC encounter (Hut and Tremaine, 1985), but an extremely strong stellar encounter is another possibility. As a result, the current new comets would have a larger jumper contribution (with an equal mix of prograde and retrograde comets) than we have found, thus largely offsetting the creeper predominance. This would in turn mean a larger comet injection efficiency than we have estimated and thus a lower estimate for the Oort cloud population.

As a final remark, our results have a clear bearing on the discussion of the real structure of the Oort cloud and scattered disk based on the inclination distributions of new, long-period and Halley type comets. The issues just mentioned concerning the inclination distribution of new comets, along with the one raised by Levison et al. (2006) concerning the contribution of the scattered disk to the flux of new comets and Halley types, need further study – in particular, incorporating realistic estimates for the initial energy distribution of the cloud, its age, its initial degree of flattening, and the effects of so far unmodeled perturbing agents such as GMC encounters.

Acknowledgments

We are grateful to an anonymous referee and Ramon Brasser for very helpful remarks on our submitted manuscript as well as on a previously submitted one that joined this paper and its companion paper. H.R. is indebted to Grant No. 74/10:2 of the Swedish National Space Board and Grant No. 2011/01/B/ST9/05442 of the Polish National Science Center.

References

A'Hearn, M.F. et al., 2012. Cometary volatiles and the origin of comets. Astrophys. J. 758, 29.

Brasser, R., Morbidelli, A., 2013. Oort cloud and scattered disc formation during a late dynamical instability in the Solar System. Icarus 225, 40–49.

Breiter, S., Fouchard, M., Ratajczak, R., Borczyk, W., 2007. Two fast integrators for the Galactic tide effects in the Oort Cloud. Mon. Not. R. Astron. Soc. 377, 1151–1162.

Dones, L., Weissman, P.R., Levison, H.F., Duncan, M.J., 2005. Oort cloud formation and dynamics. In: Festou, M., Keller, H.U., Weaver, H.A. (Eds.), Comets II. Univ. Arizona, Tucson, pp. 153–174.

Duncan, M., Quinn, T., Tremaine, S., 1987. The formation and extent of the Solar System comet cloud. Astron. J. 94, 1330–1338.

Dybczyński, P.A., 2002. Simulating observable comets. I. The effects of a single stellar passage through or near the Oort cometary cloud. Astron. Astrophys. 396, 283–292.

Fernández, J.A., Sosa, A., 2012. Magnitude and size distribution of long-period comets in Earth-crossing or approaching orbits. Mon. Not. R. Astron. Soc. 423, 1674–1690.

Fouchard, M., Froeschlé, Ch., Breiter, S., Ratajczak, R., Valsecchi, H., Rickman, G.B., 2007. Methods to study the dynamics of the Oort cloud comets II: Modelling the galactic tide. In: Benest, D., Froeschlé, C., Lega, E. (Eds.), Topics in Gravitational Dynamics, Lecture Notes in Physics, vol. 729. Springer Verlag, Berlin, pp. 271–293.

Fouchard, M., Froeschlé, Ch., Rickman, H., Valsecchi, G.B., 2011a. The key role of massive stars in Oort cloud comet dynamics. Icarus 214, 334–347.

Fouchard, M., Rickman, H., Froeschlé, Ch., Valsecchi, G.B., 2011b. The last revolution of new comets: The role of stars and their detectability. Astron. Astrophys. 535, A86.

Fouchard, M., Rickman, H., Froeschlé, Ch., Valsecchi, G.B., 2013a. Planetary perturbations for Oort Cloud comets. I. Distributions and dynamics. Icarus 222, 20–31.

Fouchard, M., Rickman, H., Froeschlé, Ch., Valsecchi, G.B., 2013b. Planetary perturbations for Oort Cloud comets. III. Evolution of the cloud and production of centaurs and Halley type comets, Icarus, in press.

Francis, P.J., 2005. The demographics of long-period comets. Astrophys. J. 635, 1348–1361.

Hut, P., Tremaine, S., 1985. Have interstellar clouds disrupted the Oort comet cloud? Astron. J. 90, 1548–1557.

Kaib, N.A., Quinn, T., 2009. Reassessing the source of long-period comets. Science 325, 1234–1236.

Królikowska, M., Dybczyński, P.A., 2010. Where do long-period comets come from? 26 comets from the non-gravitational Oort spike. Mon. Not. R. Astron. Soc. 404, 1886–1902.

Levison, H.F., Dones, L., Duncan, M.J., 2001. The origin of Halley-type comets: Probing the inner Oort cloud. Astron. J. 121, 2253–2267.

Levison, H.F., Duncan, M.J., Dones, L., Gladman, B.J., 2006. The scattered disk as a source of Halley-type comets. Icarus 184, 619–633.

Matese, J.J., Whitman, P.G., 1992. A model of the galactic tidal interaction with the Oort comet cloud. Celest. Mech. Dynam. Astron. 54, 13–35.

Rickman, H., 2013. The Oort Cloud and long-period comets. Meteor. Planet. Sci. 302R.

Rickman, H., Fouchard, M., Froeschlé, Ch., Valsecchi, G.B., 2008. Injection of Oort Cloud comets: The fundamental role of stellar perturbations. Celest. Mech. Dynam. Astron. 102, 111–132.

Rickman, H., Fouchard, M., Froeschlé, Ch., Valsecchi, G.B., 2012. Gaia and the new comets from the Oort cloud. Planet. Space Sci. 73, 124–129.

3.2.2 Implications sur la production à long terme d'objets du disque étendu

Comme on vient de le voir, les perturbations planétaires provoquent des fluctuations sur le demi-grand axe des comètes du nuage de Oort. Lorsque le demi-grand axe devient inférieur à 1 000 UA alors on considère que la comète n'est plus dans le nuage de Oort et qu'elle fait partie des objets du disque étendu (ou éventuellement des centaures ou des comètes à courte période suivant la valeur du demi-grand axe et de la distance périhélique). Ces comètes ne sont soumises aux effets des marées galactiques et des étoiles passantes que de manière marginale. Ainsi on peut considérer ces comètes comme *découplées* des perturbateurs galactiques.

Le modèle dynamique que j'ai conçu n'est pas encore habilité à poursuivre l'évolution dynamique des comètes découplées (les effets des résonances ne seraient pas pris en compte). Cependant, on s'est intéressé à la production de tels objets pendant les 5 milliards d'années d'intégrations des simulations effectuées pour l'article Fouchard et al. (2014a). Les résultats obtenus sont présentés dans l'article Fouchard et al. (2014b) inséré ci-après.

Les résultats principaux sont les suivants :

- pendant 5 milliards d'années, l'évolution du nuage de Oort est telle que sa partie interne est très érodée par les perturbations planétaires et les perturbations d'étoiles passant très proche du Soleil. Cette érosion se fait principalement au bénéfice de la partie centrale du nuage et d'un flux de comètes découplées. Pour ce qui est des comètes de la partie externe, prêt de 40% d'entre elles sont éjectées dans le milieu interstellaire sous l'effet des perturbations stellaires ;
- alors que le découplage d'une comète est essentiellement dû aux planètes, il existe une importante synergie entre les étoiles et les planètes générant des pluies de comètes découplées similaires aux pluies de comètes observables. Le découplage d'une comète pendant une pluie se fait en deux temps, une perturbation stellaire commence par placer la distance périhélique de la comète dans la région de Jupiter et Saturne, puis la perturbation d'une de ces planètes va découpler la comète lors d'un passage à son périhélie (plusieurs passages peuvent être nécessaires avant que le découplage se fasse).
- 30% des comètes découplées ont une distance périhélique inférieure à 5 UA, formant une source potentielle de comètes de type Halley, les 70% restant formant une source potentielle de centaures.
- Les comètes découplées ayant une distance périhélique inférieure à 5 UA viennent *(i)* d'un flux continu de comètes observables dont le demi-grand axe est fortement modifié par une perturbation planétaire lors

de leur passage au périhélie, et *(ii)* d'un flux sporadique lors de pluies cométaires. Les orbites de ces comètes ne montrent pas de préférence entre les mouvements progrades et rétrogrades, mais ce résultat est évidemment dépendant du choix fait sur notre nuage de Oort initial qui est isotropique.

- Les comètes découplées ayant une distance périhélique supérieure à 5 UA viennent préférablement de la partie interne du nuage de Oort suite à une diffusion très lente *(i)* de leur demi-grand axe sous l'effet d'Uranus et Neptune, *(ii)* et de leur distance périhélique sous l'effet des marées galactiques. Les pluies provoquées par les passages d'étoiles restent importantes puisqu'elles injectent de nombreuses comètes dans la région d'Uranus et Neptune qui pourront alors les découplées sur de grandes échelles de temps. Les orbites de ces comètes découplées ont une préférence pour les orbites prograde, mais ici aussi ce résultat dépend du choix de notre nuage de Oort initial.

Icarus 231 (2014) 99–109

Contents lists available at ScienceDirect

Icarus

journal homepage: www.elsevier.com/locate/icarus

Planetary perturbations for Oort cloud comets: III. Evolution of the cloud and production of centaurs and Halley type comets

M. Fouchard [a,*], H. Rickman [b,c], Ch. Froeschlé [d], G.B. Valsecchi [e,f]

[a] *LAL-IMCCE, Université de Lille 1, 1 Impasse de l'Observatoire, F-59000 Lille, France*
[b] *PAS Space Research Center, Bartycka 18A, PL-00-716 Warszawa, Poland*
[c] *Dept. of Physics & Astronomy, Uppsala Univ., Box 516, SE-75120 Uppsala, Sweden*
[d] *Observatoire de la Côte d'Azur, UMR Lagrange 7293, Bv. de l'Observatoire, B.P. 4229, F-06304 Nice cedex 4, France*
[e] *IAPS, INAF, via Fosso del Cavaliere 100, I-00133 Roma, Italy*
[f] *IFAC-CNR, Via Madonna del Piano 10, I-50019 Sesto Fiorentino (FI), Italy*

ARTICLE INFO

Article history:
Received 12 September 2013
Revised 27 November 2013
Accepted 27 November 2013
Available online 9 December 2013

Keywords:
Comets, dynamics
Comets, origin
Centaurs

ABSTRACT

We present Monte Carlo simulations of the dynamical history of the Oort cloud, where in addition to the main external perturbers (Galactic tides and stellar encounters) we include, as done in a companion paper (Fouchard, M., Rickman, H., Froeschlé, Ch., Valsecchi, G.B. [2013b]. Icarus, in press), the planetary perturbations experienced each time the comets penetrate to within 50 AU of the Sun. Each simulation involves an initial sample of four million comets and extends over a maximum of 5 Gyr. For better understanding of the outcomes, we supplement the full dynamical model by others, where one or more of the effects are left out. In the companion paper we studied in detail how observable comets are injected from the Oort cloud, when account is taken of the planetary perturbations. In the present paper we concentrate on how the cloud may evolve in the long term and also on the production of decoupled comets, which evolve into semi-major axes less than 1000 AU. Concerning the long-term evolution, we find that the largest stellar perturbations that may statistically be expected during the age of the Solar System induce a large scale migration of comets within the cloud. Thus, comets leave the inner parts, but the losses from the outer parts are even larger, so at the end of our simulations the Oort cloud is more centrally condensed than at the beginning. The decoupled comets, which form a source of centaurs and Halley type comets (roughly in the proportions of 70% and 30%, respectively), are mainly produced by planetary perturbations, Jupiter and Saturn being the most efficient. This effect is dependent on synergies with the Galactic tide and stellar encounters, bringing the perihelia of Oort cloud comets into the planetary region. The star-planet synergy has a large contribution due to the strong encounters that produce major comet showers. However, outside these showers a large majority of decouplings may be attributed to the tide-planet synergy.

1. Introduction

In a recent paper (Fouchard et al., 2013a), we have developed a model to simulate the planetary perturbations on Oort cloud comets. This has been used to implement planetary perturbations into a more general model able to account also for the effects of the Galactic tides and stellar encounters. The flux of observable comets, i.e., comets that reach a heliocentric distance smaller than 5 AU for the first time, when planetary perturbations interact with the Galactic tides and stellar effects was studied in a companion paper of the present one (Fouchard et al., 2013b). In the following, we will refer to the two mentioned papers as Paper I and Paper II.

The present paper (Paper III) will focus on two aspects. One is how the Oort cloud evolves on Gyr time scales from the initial conditions that we imposed. The other is the production of *decoupled comets* (see Paper I), i.e., comets reaching a semi-major axis $a < 1000$ AU. The dynamics of this sample may be considered as protected from the effects of Galactic tides and stellar passages (except for the rare, shower-producing encounters). The objects form a potential source of both centaurs and Halley type comets by means of further evolution under planetary perturbations.

Among previous papers dealing with similar subjects we note in particular (Wiegert and Tremaine, 1999), where the dynamical model was similar to one of those that we employ here (the TP model). However, we regard this model as useful only as a tool to understand the workings of the full dynamics (TSP model),

---

* Corresponding author.
E-mail addresses: fouchard@imcce.fr (M. Fouchard), Hans.Rickman@physics.uu.se (H. Rickman), froesch@oca.eu (Ch. Froeschlé), giovanni@iaps.inaf.it (G.B. Valsecchi).

0019-1035/$ - see front matter © 2013 Elsevier Inc. All rights reserved.
http://dx.doi.org/10.1016/j.icarus.2013.11.034

and comparisons are limited by the different choices made for the initial cloud structure, the observability criterion, and the organization of the output. In future papers, where we study the production of the above-mentioned short-period objects quantitatively, we will make an attempt to compare our findings with both the mentioned paper and others, like for instance, (Levison et al., 2001, 2006).

Our initial conditions and models used are briefly presented in Section 2. Section 3 is devoted to the time dependence of the production of decoupled comets. The long term evolution of the Oort cloud is studied in Section 4. Section 5 deals with the characteristics of the population of decoupled objects. We summarize our main results and draw conclusions in Section 6.

2. Initial conditions and dynamical models

We refer to the description given in Paper II, since the results to be presented here come from exactly the same calculations. However, for convenience, we will briefly repeat the most important aspects.

The initial state of the cloud is modeled as isotropic and thermalized, as concerns the distributions of inclination and eccentricity, and the energy distribution is taken from Duncan et al. (1987) with semi-major axis between 3000 and 100 000 AU. All initial orbits have perihelion distances $q > 32$ AU so as to avoid any initial planet crossers. We emphasize that our choices are somewhat arbitrary and are not intended to be the most realistic. Thus, care has to be exerted when interpreting our results to the extent that these may be specific to the chosen model of the initial cloud. We will come back to this point whenever needed.

Our four dynamical models involve: tides only (T), tides and passing stars (TS), tides and planets (TP), and tides, passing stars and planets (TSP). The TS and TSP models use the same four random sequences of passing stars, which are different realizations of the same underlying, statistical model (Rickman et al., 2008). The subscript $i = 1, \ldots, 4$ after the letter S will indicate the stellar sequence used.

In the T and TS models the masses of the four giant planets are added to the Sun, and the planetary perturbations are treated by the loss cone[1] recipe. In the TP and TSP models on the other hand, planetary perturbations are applied as described in Paper I.

3. Time dependent production of decoupled comets

The numbers of observable and decoupled comets produced by our models per period of 50 Myr are plotted versus time in Fig. 1. The upper panels represent observable comets and are the same as in Fig. 1 of Paper II, while decoupled comets are shown in the lower panels. In both cases, the fluxes of models without stellar perturbations are the same in each panel, while in the TS and TSP models the panels differ with respect to the specific stellar sequences used. For these models the background fluxes are seen to be similar in all panels, whereas the high peaks are related to comet showers, caused by close stellar encounters that obviously differ between the four sequences. Note that there are significant differences between those sequences – nrs. 3 and 4 contain more encounters with dramatic consequences than nrs. 1 and 2.

The flux of observable comets was discussed in Paper II, so we now focus on the decoupled comets. Clearly, this flux is always equal to zero for the T model (Galactic tides are unable to significantly change the semi-major axis of a comet). For the TS models, very few comets get decoupled, and this happens only during comet showers. However, the situation changes drastically, when the planetary perturbations are included. Planets act very efficiently in decreasing the semi-major axis of Oort cloud comets, whereas a star needs to have an impact parameter comparable to the final aphelion distance of the comet in order to be able to decouple it.

In the TP model we obtain a maximum flux after about 700 Myr, and then the flux decreases slowly. This decrease is partly due to the absence of a TAZ refilling mechanism, which causes a drop in the tidal injection rate of comets into planet-crossing orbits. By TAZ we mean the set of Oort cloud orbits, which are connected with observable orbits by the dynamics of the Galactic disk tide, and the refilling is performed by stellar perturbations, in case these are modeled. The delay of the maximum may be explained by the fact that the production of decoupled comets requires, first, a diffusion of the perihelion into the planetary region, and second, a diffusion of the orbital energy that may be very slow (see Paper I).

When stars are included along with the planets (TSP models), the background flux of decoupled comets is close to but somewhat larger than that obtained with the TP model. The slow decrease after the maximum is now likely coupled to the gradual depletion of the Oort cloud. In addition, many peaks stand out above the background, and each one is related to a shower seen in the flux of observable comets.

An important difference has to be noted between the observable and decoupled comets. For the observable comets of the TS and TP models, there are two categories: some result from the Galactic tide as found in the T model, and the rest are due to synergies with the stars or the planets (see Paper II). If we add the TS and TP fluxes of observable comets and subtract the T flux, we may expect to see what a simple addition of stellar and planetary synergies with the Galactic tide would yield. Now, note that the TSP observable flux is close to this prediction, showing that the observable comets are essentially due either to the tide alone or to either of the two independent synergies. But for the decoupled comets the situation is different. Here the T and TS fluxes are essentially zero, and we have to compare the TP and TSP fluxes. As already noted, the latter is clearly larger than the former.

We tentatively conclude that, while the injection of observable comets is largely a matter for the tide, assisted independently by stars and planets, the decoupling of comets is primarily a matter for the planets, assisted independently by synergies with the tide and stars. An easy way to view the star-planet synergy is to consider stellar perturbations as an important way to bring comets into the influence of planetary perturbations by reducing the perihelion distances (see Section 5).

Observing in detail what happens during a shower[2] (Fig. 2), we note that the production of decoupled orbits with perihelia outside the region where planetary perturbations are applied, i.e., beyond 50 AU, is identical for the TS and TSP models (above $q = 50$ AU, blue circles overlap red triangles), while it is zero for the TP model. This shows that the tides contribute nothing, and all these decouplings are due to the stellar perturbation causing the shower. They form a “spike” near the time $t = t_*$ of the star’s perihelion (indicated as $t = 0$ in Fig. 2), which can be discerned for perihelion distances down to about 20–30 AU, and the rest of the decouplings are due to planetary perturbations.

The latter are found in the TP and TSP models for $q < 50$ AU. In the TP model the rate of decouplings cannot change at $t = t_*$, but in the TSP model there may be a large increase caused by the comet shower. For the range $15 < q < 50$ AU, the increase in the rate of

---

[1] This means that below a threshold in angular momentum, represented by a perihelion distance below 15 AU, comets are modeled as lost from the Oort cloud; otherwise their orbits remain unchanged.

[2] The one selected is one of the strongest that we have modeled and is seen in panel (4) of Fig. 1 at $t = 1.774$ Gyr.

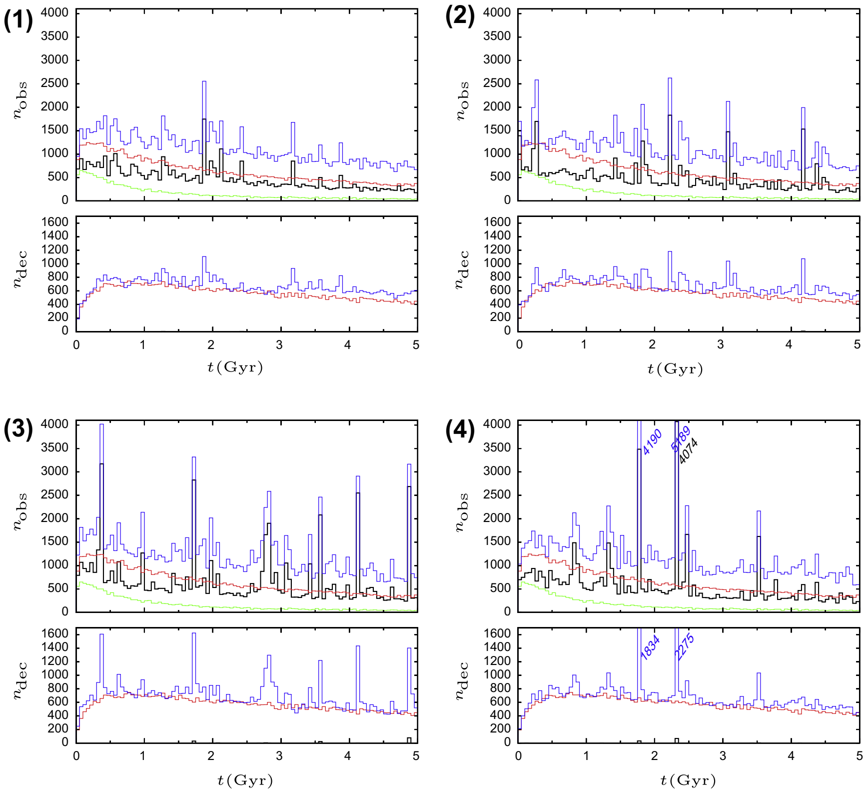

Fig. 1. Number of observable (upper diagram) and decoupled (lower diagram) comets per period of 50 Myr versus time for the four different models: T (green line), TS_i (black line), TP (red line) and TS_iP (blue line). The number to the left above each plot indicates the index of the stellar sequence used. For the 4th sequence, the numbers on the right side of the highest peaks give the ordinate of the top, when the flux exceeds the plotted range. (For interpretation of the references to color in this figure legend, the reader is referred to the web version of this article.)

decouplings is weak at best, in agreement with the fact that Uranus and Neptune are known to take 0.1–1 Gyr to scatter comets (Fernández and Ip, 1981), but the situation is drastically different for $q < 15$ AU. Here, the number of decoupled comets is very large in the TSP model, and their production occurs mostly during the first million years after the stellar encounter but continues for several Myr afterwards.

The sudden appearance of the decoupled comets at $t = t_*$ proves that the phenomenon is due to comet injections caused by the star. We have found that the vast majority of these decoupled objects come from the inner core of the Oort cloud with orbital periods less than 1 Myr. In fact, most of the periods are less than 0.1 Myr (roughly, $a < 2000$ AU). Thus, we conclude that first, the star sends the perihelia of the comets into the Jupiter–Saturn region, and then the comets receive the planetary kick that decouples their orbits after some extra time has passed. The delay may be seen as a waiting time in order for a large enough perturbation to arise.

We also note that the decoupled comet flux drops much faster for Jupiter-crossing orbits than for those that only may approach Saturn. Hence, the decoupling waiting time is longer for Saturn than for Jupiter, which is of course to be expected. Considering the typical orbital periods of the injected comets (see above), we find that the decoupling typically requires from tens to hundreds of orbital revolutions to occur.

At least for Jupiter crossers, we can clearly speak of a shower of decoupled comets analogous to the shower of observable comets, and since the time between stellar encounters of this strength is typically larger than 100 Myr, Saturn crossers can also be included into the shower. On the other hand, Uranus and Neptune crossers have such a long scattering time scale that they respond only vaguely to the stellar injection episode, so their decouplings do not show the shower features.

The shower duration is not easy to evaluate for decoupled objects. Most of the production occurs within 4 My after the stellar encounter, but as mentioned, this is strongly dependent on the perihelion distance. At the end of the plotted interval in Fig. 2 (t = 10 Myr), there is nothing left of the shower for Jupiter-crossing orbits, while the shower is still ongoing though subsiding for perihelia near Saturn's orbit.

4. Long term evolution of the Oort cloud

Let us now analyze the way the Oort cloud evolves and loses comets, and compare the efficiency of the loss mechanisms

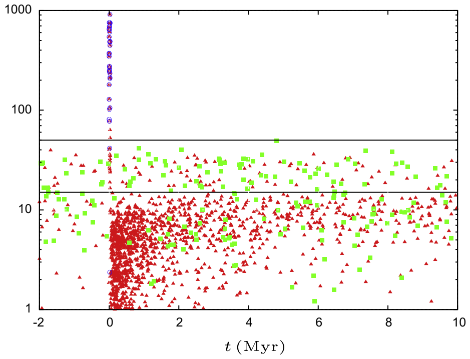

Fig. 2. Perihelion distance versus time for comet decouplings around a very close stellar encounter ($t = 0$ corresponds to the perihelion time of the star). Red triangles correspond to comets decoupled in the $\mathrm{TS_4P}$ model, green squares to decouplings in the TP model and open blue circles to decouplings in the $\mathrm{TS_4}$ model. The horizontal black lines correspond to the thresholds at 15 AU (the outer limit of the loss cone) and 50 AU (below which planetary perturbations are applied). (For interpretation of the references to color in this figure legend, the reader is referred to the web version of this article.)

between the different models. We divide the cloud into three parts: *inner*, *central* and *outer*, containing comets with $a < 20\,000$ AU, $20\,000 < a < 50\,000$ AU, and $a > 50\,000$ AU, respectively. The initial population and the final populations for each model are shown in Table 1. The fractions of comets in each part of the cloud are also given along with the corresponding losses from the initial population (in percent). The negative sign means an increase of the corresponding number. Note that the final population is the one at the end of the simulation after 5 Gyr, but we do not present information on the lifetimes of the lost objects or the distribution of their exit times.

For the total population, the fractions of comets that are lost from the cloud in the different models are given along with some information on the end states reached. For this purpose, we divide the exits into two parts. Independent of the model, comets that leave the cloud by reaching a distance larger than 4×10^5 AU are counted in the *out* category. The remaining exits depend to some extent on the model used. All decouplings belong to this category independent of the model, but in the T and TS models we count all comets that reach the end state of $q < 15$ AU, some of which will actually be ejected while the rest become decoupled. We denote this category by *qd*. The total loss (in percent) for any given model is the sum of the 'out' and 'qd' losses.

For the T model, comets are lost from the cloud practically only[3] because they pass at heliocentric distance less than 15 AU. Each part of the cloud contributes rather evenly to the total loss.

In the TS models, the Oort cloud loses between 25% and 40% of its total initial population. The worst case is the $\mathrm{TS_3}$ model, which is also the model with the largest number of comet showers according to Fig. 1. The differences between individual models reflect mainly the numbers of comets in the 'out' category (from 14% to 30%) and of comets originating in the inner Oort cloud, suggesting that they arise from showers ejecting comets into interstellar space. We will return to this point below. The central and outer parts are depleted in a more similar way for different stellar sequences, probably because they both lose and gain comets – the former due to interstellar ejection, and the latter due to replenishment from the inner part of the cloud. The fraction of comets lost by $q < 15$ AU (the decoupled ones are negligible) is about 12% for each model. This is twice the loss fraction in the T model, again illustrating the synergy between the tides and the stars for comet injection from the Oort cloud (Rickman et al., 2008).

The tides and planets model (TP) is remarkably similar to the T model as regards the total population. The fact is that comets that are now not lost by $q < 15$ AU will likely be removed from the cloud by planetary perturbations anyway, given enough time, either by decoupling or by ejection into interstellar space. This is easily seen by comparing the 'qd' and 'out' fractions between the T and TP models. The non-complete opacity of the planetary system below 15 AU (Paper I) gives only temporary relief and does not save the comets from being lost in the long run.

The losses from individual parts of the Oort cloud in the TP model are quite different from those in the T model. The loss now arises mainly from the inner Oort cloud, whereas the outer Oort cloud gets even more populated than at the beginning. The last feature is caused by the diffusion of the orbital energy that is now allowed by the planetary perturbations.

The TSP models gather the characteristics of the TS and TP models, where the loss from the inner part is mainly caused by close stellar encounters, whereas the outer parts become both depleted and replenished, as noted above. Comparing TSP to TS models, we note the same thing as when we compared TP to T models, namely, a shift of the majority of lost comets from the 'qd' to the 'out' category. This shift is now even more important.

In both TSP and TS models, the total losses are large and variable due to the statistical fluctuations in the number and strength of the most important stellar encounters. Moreover, even though the majority of lost comets come from the inner Oort cloud, in relative terms the losses are more important for the central and outer parts, so at the end of the simulations the cloud is even more dominated by its inner part than at the beginning.

The data presented in Table 1 allow us to roughly estimate the relative importance of the few, most dramatic stellar encounters for the total loss of comets from the Oort cloud. We concentrate on the TP and TSP models, but the T and TS models would give the same result. The total loss in the TP model amounts to about 6% due to the tidal injection of comets into unstable, planet crossing orbits, and we may estimate that the corresponding fraction in the TSP models is somewhat higher – perhaps ~10% – due to the TAZ filling performed by the stars. The rest of the TSP losses are due to the stars, either by injection into planet crossing orbits or by the energy transfer performed by the stellar impulses. If we assume that the only reason for the difference in loss percentage between the four models is the effect of the strongest encounters, we see that about half the losses in the $\mathrm{TS_3P}$ model are due to a few encounters exceeding all encounters of the $\mathrm{TS_1P}$ model. We may then conclude that the losses are largely due to the strongest encounters.

Let us now offer some comments in support of this conclusion. Consider the very strongest encounters among all the four sequences. One of these is the one considered in Fig. 2, caused by a G0 star with impact parameter 690 AU relative to the Sun. For common stellar encounters, penetrating only the outer parts of the Oort cloud, it is well known that the perturbations of heliocentric orbital energy are very small, and any ejections from the Solar System will be due to a slow diffusion in energy. But the situation is very different for an encounter like the one of Fig. 2. The impulse per unit mass imparted to the Sun is then of order 0.1 km/s, and this directly affects the heliocentric motions of all the comets in the Oort cloud.

One consequence is a massive migration of comets between the different parts of the cloud. For instance, one easily finds that a

---

[3] Actually, very few (about 300) are lost by reaching heliocentric distances larger than 4×10^5 AU. This is possible, since the dynamics of a tides only model is not strictly integrable, and consequently the orbital energy may undergo some variations.

Table 1
The first row gives the initial population of the Oort cloud and the fraction of comets in each of its parts. Then, for each model, the "tot" column gives the total final population of the cloud, and columns "inner", "central" and "outer" the fraction, in percent, of comets in each part. The "loss" columns give the decreases (in percent) of each population separately. The "qd" and "out" columns provide a split-up of the total losses according to the end state reached (see text for details).

Model initial	Tot	(Loss – qd – out)	Inner	(Loss)	Central	(Loss)	Outer	(Loss)
	4×10^6		74.1		17.2		8.7	
T	3.74×10^6	(6.6–6.6–0.0)	74.3	(6.4)	17.1	(7.3)	8.6	(7.0)
TS_1	2.97×10^6	(25.7–11.4–14.4)	83.0	(16.8)	11.6	(50.2)	5.4	(53.5)
TS_2	2.79×10^6	(30.1–11.4–18.8)	83.7	(21.1)	10.7	(56.4)	5.5	(55.4)
TS_3	2.33×10^6	(41.8–12.6–29.1)	80.3	(36.9)	11.6	(60.9)	8.2	(45.2)
TS_4	2.67×10^6	(33.2–12.0–21.1)	83.5	(24.7)	10.7	(58.6)	5.9	(54.8)
TP	3.75×10^6	(6.3–1.7–4.6)	73.1	(7.6)	17.6	(4.4)	9.3	(−1.1)
TS_1P	3.04×10^6	(24.0–2.2–21.8)	80.8	(17.1)	12.6	(44.3)	6.5	(42.8)
TS_2P	2.86×10^6	(28.5–2.2–26.3)	81.6	(21.3)	11.8	(51.1)	6.6	(45.5)
TS_3P	2.37×10^9	(40.8–2.4–38.4)	78.8	(37.1)	12.3	(57.8)	9.0	(38.1)
TS_4P	2.73×10^6	(31.6–2.3–29.4)	81.5	(24.9)	11.7	(53.7)	6.9	(45.7)

comet of the inner core with $a = 10000$ AU may even be ejected from the Solar System, if it is moving in the inner part of its orbit and the heliocentric impulse due to the star is favorably oriented. In more typical situations, the comet is likely to be moved most of the way, or all the way, into the central part by increasing its orbital energy. Comets belonging to the central or outer parts are even more vulnerable.

It is thus clear that an instantaneous, large-scale migration of individual comets and rearrangement of the orbital energy distribution of the Oort cloud must occur at each of the extreme stellar encounters. Less extreme encounters, of the kind that is expected to happen several times during the age of the Solar System, will have large effects as well. Since there is always an associated loss of comets into interstellar space, and the outward migration from the densely populated inner part of the cloud must dominate over the return flow from the other parts, the features seen in Table 1 are easily understood.

We remind the reader that the quantitative results found in this Section are specific to the assumption made as to the initial energy distribution of the Oort cloud. Changing the initial fraction of comets in the inner part of the cloud would lead to changes in the loss rates and amounts of transferred comets. However, the migration phenomenon itself also leads to a certain loss of memory of the initial conditions that tends to reduce the sensitivity to those.

5. Dynamics of decoupling

5.1. General results

We now turn to the decoupled comets, i.e., the ones that reach semi-major axes less than 1000 AU and as a consequence have their integrations stopped. Among the three perturbing agents that we consider, the Galactic tide is integrable for this range of semi-major axis and hence cannot contribute to the decoupling. Only two processes remain: either a planetary perturbation that kicks the comet across the border close to perihelion passage, or a stellar encounter that can occur anywhere in the orbit but acts like an impulsive kick in a similar way.

In each of these two cases, the size of the decoupling kick is in principle arbitrary, but it carries interesting information on the nature of the decoupling process, and thus we will consider this as a diagnostic parameter. On one side of the spectrum, the comet may diffuse smoothly across the border, and on the other side, it may suffer a major energy perturbation that kicks its orbit a long way, thereby passing the border.

The number of planetary perturbations applied to the comet before it gets decoupled offers a supplementary parameter with a similar bearing, since a decoupling process characterized by large planetary perturbations will in general require fewer orbits than one where the perturbations are small. A stellar decoupling, on the other hand, may in fact occur without any previous planetary perturbation.

Consequently, we will pay attention to both the last energy kick suffered by a decoupled comet and the number of planetary perturbations applied to the comet before it gets decoupled. This is equal to the number of perihelion passages at less than 50 AU, when planetary perturbations are modeled (TP and TSP models).

For classification purpose, we use the decrease of the orbital energy at the last planetary perturbation in the TP and TSP models, or between the last perihelion passage before and the first one after the decoupling in the TS model. Table 2 lists, for each model, the total number of decoupled comets (n_d), the numbers (and corresponding fractions) of decoupled comets for which this decrease in orbital energy exceeds 10^{-5} AU^{-1} (n_5), 10^{-4} AU^{-1} (n_4) and 10^{-3} AU^{-1} (n_3), and the number of decoupled comets with orbital period less than 200 yrs (n_{SP}). These are just the general statistics, and further information on how the decouplings are distributed over q and $\cos i$ is given in the next subsections.

Table 2
Statistics of the strength of decouplings. For each model, described in the first column, the next column gives the total number of decoupled comets n_d, and the following columns are described in the text. All fractions are given with respect to the relevant n_d.

Model	n_d	n_5	(frac %)	n_4	(frac %)	n_3	(frac %)	n_{SP}
T	0	0	(–)	0	(–)	0	(–)	0
TS_1	5	5	(100.0)	5	(100.0)	0	(0.0)	0
TS_2	9	9	(100.0)	9	(100.0)	1	(11.1)	0
TS_3	138	137	(99.3)	129	(93.5)	25	(18.1)	0
TS_4	105	102	(97.1)	99	(94.3)	31	(29.5)	0
TP	68478	54263	(79.2)	32532	(47.5)	7416	(10.8)	8
TS_1P	87851	74810	(85.2)	50729	(57.7)	11777	(13.4)	12
TS_2P	89032	76025	(85.4)	51182	(57.5)	11840	(13.3)	4
TS_3P	94549	83148	(87.9)	58028	(61.4)	13844	(14.6)	19
TS_4P	90386	78679	(87.0)	54623	(60.4)	12815	(14.2)	14

As already noted, the T model is unable to produce any decoupled comets. In the TS model, very small numbers of decoupled comets are found, and as noticed in Section 3, these comets are decoupled via close stellar encounters[4]. The stellar perturbations causing decouplings are almost always larger than 10^{-4} AU^{-1} but smaller than 10^{-3} AU^{-1} in at least 70% of the cases. They are hence likely to be generally in the range of several times 10^{-4} AU^{-1}, so at the last perihelia before the comets were decoupled, their semi-major axes were likely about 2000 AU or less. Thus they have typically undergone an evolution of orbital energy caused by stellar perturbations before the final, decoupling star appeared.

In the TP model the number of decoupled comets is significant. For about 20% of them, the decoupling occurs via a smooth diffusion in orbital energy, since they do not even contribute to n_5. We will call these *smoothly decoupled comets*. But for almost half of the decoupled comets the reason is a significant planetary kick (larger than 10^{-4} AU^{-1}), so we refer to them as *strongly decoupled comets*. For 11% of the decoupled comets the decoupling kick is even larger than 10^{-3} AU^{-1}. Remarkably, eight short-period comets are produced in this model. All of these have periods larger than 20 yrs, but three have a Tisserand parameter[5] larger than 2. They have very small inclinations and perihelion distances beyond 2.6 AU.

In the TSP model the fraction of smoothly decoupled comets is less than 15%, and about 60% are strongly decoupled. Comparing to the TP model, the number of decoupled comets has increased by 28% (TS$_1$P) to 38% (TS$_3$P). One can also see that the number of smoothly decoupled comets decreases by 8% (TS$_1$P) to 20% (TS$_3$P), while the number of strongly decoupled comets increases by 56% (TS$_1$P) to 78% (TS$_3$P).

Since the number of stellar decouplings is very small in the TS model, it must be very small in the TSP model too. Consequently, in both TP and TSP models, the decouplings are essentially caused by the planets. Thus, strong decouplings are favored by the presence of strong perturbations, when the perihelion distance is close to or inside the orbit of Saturn, while smooth decouplings should dominate at larger values of q. This will be shown graphically below. At this point, we may conclude that the presence of stars in the TSP model helps to bring comets into orbits with small perihelion distances. This, too, will be shown graphically below.

There are two ways, in which this may happen. One is the presence of comet showers in the TSP model with consequences illustrated in Fig. 2, and the other is the continuous TAZ filling that helps the tide to inject comets into low-q orbits from the central part of the Oort cloud. This favors the appearance of strong decouplings rather than smooth ones. Indeed, for a typical, smoothly decoupled comet the perihelion has to stay for a long time in the outer part of the planetary system in order for the energy diffusion to take place.

The decoupling of an Oort cloud comet typically requires, first, that the perihelion is brought into the realm of the planets, and then, that the planets perform the decoupling by perturbing the orbital energy. This dynamics is similar to, though acting opposite to, the one whereby the Oort cloud was initially formed by the outward scattering of planetesimals by planets and storage into high-q orbits by external perturbers. Understanding this is aided by considering the basic time scales introduced by Duncan et al. (1987), namely, that of energy diffusion caused by planetary perturbations (t_D) and that of changing the perihelion distance by Galactic tides (t_q). Further discussion of these time scales was given by Kaib et al. (2009).

Duncan et al. (1987) showed that, for semi-major axes less than several thousand AU and perihelion distances in the range between the orbits of Uranus and Neptune, t_D is less than t_q. Thus, in our TP model, comets from the inner core of the Oort cloud with $a < 10000$ AU will typically be subject to energy diffusion by Neptune or Uranus before their perihelia reach into the Jupiter–Saturn region. In the model used in Paper I involving only planetary perturbations (P model), t_q was artificially set to infinity, and planetary diffusion acted to decouple the comets at a rate that only depended on their initial perihelion distance. As we now introduce the Galactic tide, the decouplings are shifted to lower perihelion distances, increasing the importance of strong decouplings. And when we also introduce the stellar perturbations as in the TSP model, this trend is further accentuated.

On the other hand, comets from the outer parts of the Oort cloud – especially with $a > 20000$ AU – will quickly descend into low-q orbits and thereafter take some extra time to get decoupled. In Paper II we discussed the importance of "creepers" for the Oort spike and the struggle between tidal/stellar and planetary perturbations that such comets have to undergo. While in that case the goal was to reach a certain range of semi-major axis (relevant for injection into observable orbits) before the planets caused hyperbolic ejection, in the present case the issue is about reaching a rather far away limit of negative orbital energy before any excursion into positive values. The smaller the perihelion distance, the larger the typical step size of energy diffusion, and the larger the chance of reaching the decoupling limit, but the success rate is always limited by the risk of hyperbolic ejection.

Thus, comparing the TP and TSP models, we expect that the stellar perturbations help to decouple comets by decreasing their perihelion distances into the range, where the planetary perturbations are efficient. This contributes to the difference of decoupling rate shown in Table 2.

We may crudely estimate the importance of the major showers in this process by noting in Fig. 1 that the background level of the decoupled comet flux in the TSP models is of the order of 10% larger than the flux of the TP model. According to Table 2, this would mean that the difference of slightly more than 20000 between the n_d values of the TSP and TP models has a contribution of about 7000 from this elevated background, while the rest would come from the shower peaks. Those peaks are hence seen to be quite important in relative terms, but except for the highest peaks, the difference of the decoupled comet flux between TSP and TP is small compared to the flux of the TP model.

In Table 3 we show data regarding the provenance of the decoupled comets in the TP and TSP models together with their range of perihelion distance as the decouplings occur (less than or larger than 10 AU). The first thing to note is that most of the decoupled comets stem from the innermost region of the Oort cloud with $a_i < 10000$ AU, and less than 20% have their origin at $a_i > 20000$ AU. This is similar to, but even more extreme than, the case for quiescent observable comets during the last 3 Gyr as found in Paper II. In that case, 73% came initially from orbits with $a_i < 20000$ AU. The reason why we now find an even larger fraction may be connected with the inclusion of shower comets. The comets from the innermost region mostly get decoupled with $q > 10$ AU, while a vast majority of the decoupled comets from the outer part of the cloud have $q < 10$ AU.

In fact, the TSP models bring an increased fraction of decoupled comets from the outer part, showing that TAZ filling must be a contributing phenomenon. At the same time, these models also show an increased fraction of low-q decouplings for the comets from the

---

[4] For simple geometrical reasons, the stellar encounters have to be very close. Since the resulting comet aphelion distance is less than 2000 AU, the culprit stars have to penetrate within this distance from the Sun and preferably much closer. Hence the expected number of passages during 5 Gyr is very small, and it is easy to understand why different realizations of our TS model yield very different results.

[5] The distinction between Halley type and Jupiter family comets is usually made by means of the Tisserand parameter T. If $T > 2$, a short-period comet is considered as a Jupiter family comet, and otherwise it is a Halley type comet (Carusi et al., 1987). Another distinction is sometimes made by means of the orbital period, such that a Jupiter family comet has $P < 20$ yr.

Table 3
Statistics on the provenance and perihelion distance of decoupled comets. For the TP and TSP models, we list the total number of decoupled comets (the same as in Table 2) and, in the following three pairs of columns, the fractions of those numbers in three different ranges of a_i (left) and the fractions thereof with perihelion distances less than 10 AU at the moment of decoupling (right).

Model	n_d	$<1 \times 10^4$ AU	$q < 10$ AU	$(1-2) \times 10^4$ AU	$q < 10$ AU	$>2 \times 10^4$ AU	$q < 10$ AU
TP	68478	0.724	0.279	0.133	0.692	0.143	0.910
TS_1P	87851	0.606	0.344	0.199	0.789	0.195	0.928
TS_2P	89032	0.629	0.364	0.202	0.789	0.169	0.924
TS_3P	94549	0.637	0.433	0.202	0.803	0.161	0.924
TS_4P	90386	0.619	0.404	0.207	0.792	0.174	0.925

innermost part. This is a clear sign of the importance of comet showers, which is also borne out by the quite large differences in those numbers between the quiescent and dramatic versions of the TSP model – cf. Fig. 1, where the excess number of decouplings in the TSP models is seen to be mostly concentrated to the shower periods.

Consequently, it appears that the synergy between the stars and the planets for the production of decoupled comets is caused by both the few strongest and closest stellar encounters and the long-term TAZ filling provided by more normal encounters. These mechanisms easily account for the increase seen in the number of strong decouplings by bringing comets efficiently into the hands of Jupiter and Saturn, but this will happen at the expense of smooth decouplings by Uranus and Neptune, which are indeed seen to decrease in number. In that sense, the smooth decouplings rather suffer an anti-synergy between stars and planets.

Once more, we have to emphasize that the statistics shown here are specific to our choice of the initial energy distribution of the Oort cloud. A less populated inner part would have reduced the importance of shower comets as well as the overall number of decoupled comets.

5.2. The decoupled comets in the TP model

Let us now discuss in more detail the sample of decoupled comets, beginning with the TP model. Fig. 3 shows the number of decoupled comets over the entire period of 5 Gyr for this model in the (q, a) and $(q, \cos i)$ planes using color coding, and versus q, a and $\cos i$ individually. The positions of the short-period comets are highlighted in the color plots.

The effects of diffusion in orbital energy are similar to what we observed in Paper I: (i) a large-step evolution that is particularly evident for perihelia close to the semi-major axes of the planets; (ii) a very weak diffusion outside the planetary region ($q > 30$ AU), where all the decoupled comets pile up near the 1000 AU limit. Hence, the number of strongly decoupled comets peaks along the planetary semi-major axes, but the comets that are not strongly decoupled (large numbers occurring close to $a = 1000$ AU) show a more uniform q distribution.

As regards the inclination, in the region inside Saturn's orbit ($q < 10$ AU), there is no apparent preference, but in the range $10 < q < 30$ AU the decoupled comets are preferentially prograde. Beyond 30 AU we mainly note a paucity of strongly retrograde or

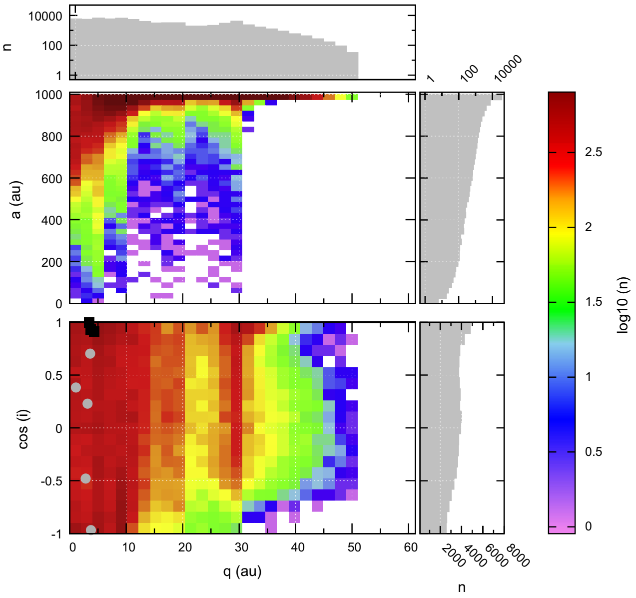

Fig. 3. Number of decoupled comets (color-coded with scale to the right) over all 5 Gyr for the TP model in the (q, a) plane (top color panel) and the $(q, \cos i)$ plane (bottom color panel). Histograms show marginal distributions of q (top), a (top right) and $\cos i$ (bottom right). By gray circles we indicate the positions of Halley type comets and by black squares those of Jupiter family comets (distinguished using the Tisserand parameter). (For interpretation of the references to color in this figure legend, the reader is referred to the web version of this article.)

prograde comets. The short-period comets have perihelion distances less than 5 AU, and the majority (six out of eight) have prograde orbits. The Jupiter family comets are extreme in this regard.

Fig. 4 shows the median number of planetary perturbations $\overline{n_{pp}}$ experienced by the decoupled comets and the median absolute value $\overline{|\Delta z|}$ of the last planetary perturbation of the orbital energy (the one actually decoupling the comets) in each cell of the $(q, \cos i)$ plane. As expected, $\overline{n_{pp}}$ and $\overline{|\Delta z|}$ show patterns of similar shape but opposite in color. Indeed, the smaller the typical planetary perturbations acting on the comets, the higher is the probability for the comets to return. Remarkably, even inside Jupiter's orbit $\overline{n_{pp}}$ is larger than 10, and it grows to values larger than 100 between Jupiter and Saturn except at low inclination. This was noticed for the case of shower comets in the discussion of Fig. 2. Between Uranus and Neptune for retrograde orbits, $\overline{n_{pp}}$ grows beyond 4000, and beyond Neptune, it may be even larger than 10000.

The $\overline{|\Delta z|}$ diagram in Fig. 4 illustrates the point already made, that the strongly decoupled comets mainly have perihelia inside Saturn's orbit. We also see that the smoothly decoupled comets are limited to orbits beyond Neptune except for retrograde orbits with perihelia between Uranus and Neptune.

Let us also illustrate in some more detail our findings about the provenance of decoupled comets, presented in Table 3 above. We now split the initial Oort cloud into four parts: the *innermost* part that contains comets with semi-major axis less than 10000 AU, the *inner* part containing comets with semi-major axis in the range [10000, 20000 AU], and the *central* and *outer* parts, where the comets have semi-major axis in the ranges [20000, 50000 AU] and larger than 50000 AU, respectively.

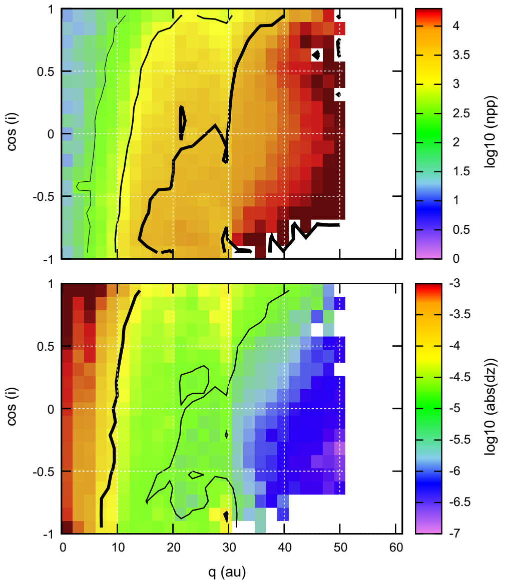

Fig. 4. For the TP model, the upper panel shows the median number of planetary perturbations ($\overline{n_{pp}}$) experienced by decoupled comets until their time of decoupling (the log-scale of color coding is indicated to the right, and brown color denotes the largest values) in each cell of the $(q, \cos i)$ plane. The three black level curves trace $\overline{n_{pp}} = 100$, 1000 and 4000 from the thinnest (left) to the thickest (right). The lower panel shows the median absolute value ($\overline{|\Delta z|}$), expressed in AU^{-1}, of the last planetary perturbation of the orbital energy (log-scale indicated to the right, with brown color denoting the largest values), suffered by the decoupled comets in each cell of the $(q, \cos i)$ plane. The two black level curves trace $\overline{|\Delta z|} = 10^{-5}$ and 10^{-4} AU^{-1} from the thinner (right) to the thicker (left). (For interpretation of the references to color in this figure legend, the reader is referred to the web version of this article.)

Fig. 5 shows the fraction of decoupled comets (in percent) coming initially from each part of the Oort cloud versus the perihelion distance upon decoupling. The total number of decoupled comets is also shown versus this perihelion distance in the figure. Note the log scale used in this case, meaning that the number of decouplings falls off very rapidly outside Neptune's orbit. Of the four Oort cloud regions, the innermost dominates at all values of q. The other regions are of some importance only for perihelia close to or inside the orbit of Saturn, and they become marginal already before Uranus' orbit is reached. Obviously the smoothly decoupled comets tend to occupy only orbits, where the innermost part of the initial Oort cloud dominates.

5.3. Decoupled comets in the TSP models

In Fig. 6 we show the number of decoupled comets in the (q, a) and $(q, \cos i)$ planes and versus q, a and $\cos i$ for the TS$_3$P and TS$_4$P models – the most dramatic ones among the TSP variants. At first glance, the same features are seen as for the TP model in Fig. 3. A new feature of all TSP variants is the presence of decoupled comets with perihelia beyond 50.5 AU (6, 10, 144, 103 for the TS$_i$P models with $i = 1, \ldots, 4$, respectively) and strongly decoupled comets with $q > 32$ AU (3, 7, 145, 104 for the same four models). Note that many of these comets are not seen in Fig. 6, since they extend to perihelion distances much larger than 60 AU. They are decoupled by stellar perturbations on their own, since the planets do not affect them or are too inefficient. An interesting question is whether these decouplings lead to Sedna-type orbits, and the answer is yes. However, from the numbers just given, we can see that they are very few and strongly dependent on the presence or absence of the strongest stellar encounters that we have found in all our simulations. Even in the TS$_3$P and TS$_4$P models, the efficiency of creating Sednas is only $\sim 10^{-5}$, which means that even the existence of one object as large as Sedna is unlikely to arise from stellar decouplings. Finally, the short-period comets are somewhat more numerous for the two plotted models than for TP (cf. Table 2), still showing some preference for prograde orbits.

The influence of the stars is illustrated in Fig. 7, where the fractional excess (or deficiency) in the number of decoupled comets obtained with each TS$_i$P variant compared to the number obtained

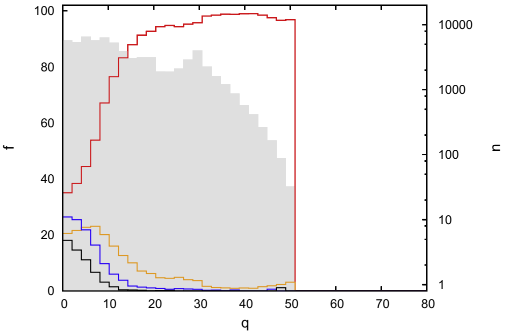

Fig. 5. Fraction of decoupled comets, in percent, for the TP model initially coming from the innermost (red line), inner (orange line), central (blue line) and outer (black line) parts of the Oort cloud versus the perihelion distance when the comets get decoupled (see text for the definitions of the parts). The gray histogram gives the total number of decoupled comets versus this perihelion distance in log scale (given on the right axis). (For interpretation of the references to color in this figure legend, the reader is referred to the web version of this article.)

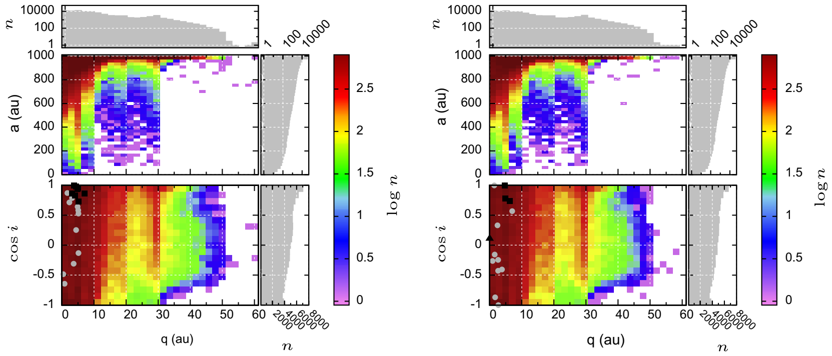

Fig. 6. Same as Fig. 3 for the TS$_3$P (left) and TS$_4$P (right) models. The black triangle in the right panel shows the only comet with period less than 20 yr. It is a high-inclination Halley type comet.

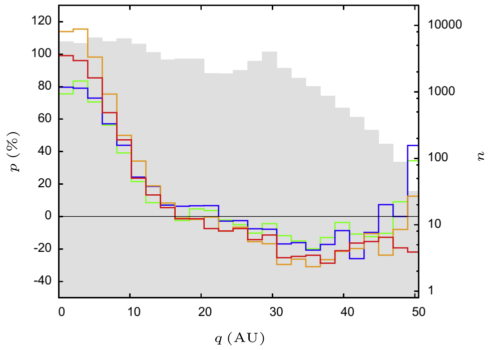

Fig. 7. Excess or deficiency, in percent, of the number of decoupled comets in the TS$_i$P models (green, blue, orange and red lines for $i = 1, \ldots, 4$, respectively) with respect to the number found in the TP model (gray histogram with scale to the right) versus the perihelion distance. (For interpretation of the references to color in this figure legend, the reader is referred to the web version of this article.)

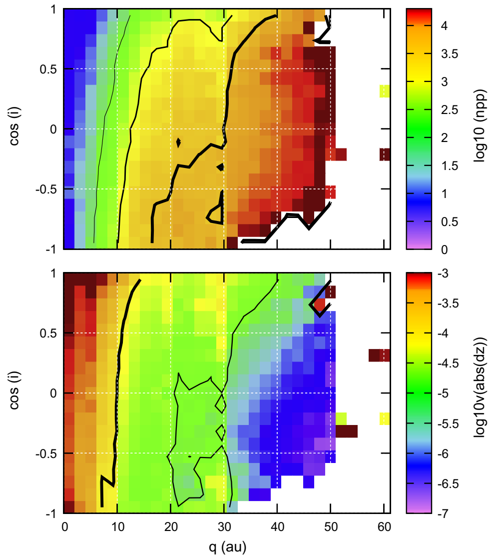

Fig. 8. Same as Fig. 4 for the TS$_3$P model.

with the TP model is shown versus perihelion distance. In confirmation of the arguments given above, the synergy between stellar and planetary perturbations is seen to be at its maximum for $q < 15$ AU, with more than 80% more comets decoupled below 5 AU, whereas an anti-synergy may be noted for $q > 23$ AU. Comparing the different TSP variants, we note that the stronger the synergy below 15 AU, the stronger is the anti-synergy above 23 AU. Thus, the maximum synergy occurs for orbits, where strongly decoupled comets dominate, and the anti-synergy occurs, where comets tend to be smoothly decoupled. Finally, at the edge of 50 AU, the synergy returns to positive, since the planets become very inefficient in decoupling comets, so that the decoupled comets are mainly due to the stars.

Fig. 8 shows the same as Fig. 4 for the TS$_3$P model, which is the model with the strongest synergy. While no clear difference is seen in the $\overline{|\Delta z|}$ diagram, it appears that the values of $\overline{n}_{pp}$ are globally smaller than in the TP model. This is a confirmation that it is more difficult for comets to keep their perihelia inside the planetary region in the TSP models than in the TP model, which is also the reason for the anti-synergy noted for smoothly decoupled comets.

Finally, looking at the initial semi-major axis of the decoupled comets in the TS$_3$P model, we see from Fig. 9 that the behavior is very similar to that of the TP model, shown in Fig. 5. The main difference concerns decoupled comets with $q > 50$ AU, which were not produced by the TP model. All these comets come from the innermost part of the initial Oort cloud. This is consistent with the fact that the stellar decouplings are mainly due to very close encounters with the Sun, which principally perturb comets in the innermost part of the cloud.

6. Summary and conclusions

We have produced several dynamical models for a large sample of Oort cloud comets affected by the Galactic tides, passing stars and giant planets over the age of the Solar System. The models differ in the kind of perturbers taken into account, or the sequence of passing stars used. Attention was paid to the decoupled comets obtaining a semi-major axis less than 1000 AU (upon which the

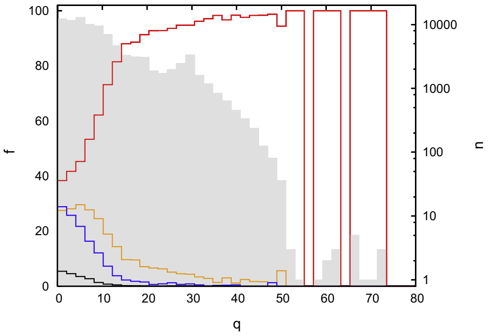

Fig. 9. Same as Fig. 5 for the TS_3P model.

integrations are stopped) and the long-term evolution of the Oort cloud resulting from the combined action of the perturbers.

The picture of the long-term evolution of the Oort cloud that emerges from our TSP model simulations is a very dynamic one, where two phenomena stand out. We typically expect one or a few very strong comet showers to occur during the 5 Gyr interval under consideration, which lead to a massive reshuffling in the cloud and the loss of an important fraction of its members. This is like a small-scale version of the effects expected from GMC encounters (Biermann, 1978; Hut and Tremaine, 1985), implying large consequences for the cloud. The classical Oort cloud ($a > 20000$ AU) is mostly lost to interstellar space but is replenished by outward migration from the inner core. To this comes a leakage from the cloud that occurs all the time but peaks during the showers, because comets get injected into the planetary region (and sometimes they become observable), and they are mostly ejected on hyperbolic orbits by the planets.

We divide the decoupled comets into three classes: the smoothly decoupled comets, where the orbital energy jumps across the limit by less than 10^{-5} AU^{-1}, the strongly decoupled comets whose jumps are larger than 10^{-4} AU^{-1}, and the rest which are intermediate as to the size of the jump. Smooth decouplings are characteristic of perihelia in the outermost parts of the planetary system, especially for large inclinations, while strong decouplings characterize the region close to Saturn's orbit and inside, as well as all perihelion-tangent orbits. Smoothly decoupled comets mainly come from the innermost part of the Oort cloud, while strongly decoupled ones probe the whole cloud.

Two agents provide decoupled comets: planetary and stellar perturbations. We find in the full model that the planetary decouplings contribute close to 100%. However, they need the help of the Galactic tide or stellar encounters in order to bring the cometary perihelia into the realm of the planets. In this sense, the tide is the main contributor – the stars accounting for an additional 25% as a long term average. This addition is largely due to the major comet showers, and during quiescent periods we estimate the stellar contribution at $\sim$10%. Thus, given that the Solar System is unlikely to be experiencing one of these very rare showers currently, the production rate of decoupled comets is not sensitive to whether or not there is a minor shower going on.

We find that 30% of the decouplings lead to orbits with $q < 5$ AU, forming a likely source for Halley type comets, while the rest is obviously a potential source for centaurs. The Halley type progenitors come from two main sources: a continuous flux of Oort spike comets, and intermittent, major comet showers. The centaur progenitors usually come from the inner parts of the Oort cloud via a slow, mainly tidal evolution of the perihelion distance, and they are mostly decoupled in the smooth way by Uranus or Neptune – though some manage to approach Saturn too. The showers are important, because they bring lots of comets into orbits with perihelia in the Uranus–Neptune region. Due to the long scattering time scale of those planets, such comets get decoupled nearly continuously, although they originate from intermittent showers.

In addition, we have direct stellar decouplings as another consequence of the shower-producing stars, involving perihelia well beyond the planetary system. These are always of the strong type. Apparently, even though Sedna type orbits may be produced by this mechanism, such events are likely too rare to offer a viable scenario for the origin of Sedna.

On the other hand, decoupled Oort cloud comets do form a source of other, more nearby objects. For centaurs it is likely important, especially concerning the ones on high inclination (Brasser et al., 2012) or large semi-major axis orbits (Emel'yanenko et al., 2005; Kaib et al., 2009). The low inclination part involves some that evolve into Jupiter family comets as well. This said, we have to emphasize that the Kuiper belt and scattered disk are additional sources of centaurs, which may dominate among the low-inclination objects with small semi-major axes that feed the Jupiter Family (Duncan and Levison, 1997; Levison and Duncan, 1997). In addition, we naturally see the decouplings of many comets on observable orbits. As far as dynamics is concerned, these will often lead into Halley type comets, although issues remain about their physical survivability (Levison et al., 2002).

Finally, we emphasize that a quantitative study of these problems should await a more realistic modeling of the Oort cloud, allowing for different possibilities as to its initial energy and inclination distributions as well as the possibility of a recent major perturbation (see also Paper II).

For instance, our result that Halley type progenitors have a flat $\cos i$ distribution and large-q centaur progenitors are concentrated to prograde orbits is clearly dependent on our assumption that the initial Oort cloud is altogether isotropic. Thus, modeling the inclination distributions of Halley types and centaurs requires attention to the issue of potentially flattened sources like the Oort cloud inner core (Levison et al., 2001) or the scattered disk (Levison et al., 2006).

Acknowledgements

We are grateful to both referees of a submitted paper that joined this paper and its companion paper, an anonymous referee and Ramon Brasser, for very valuable advice that gave us essential input in order to produce the two papers in a much improved shape. We are also grateful to the two referees of the present version of the paper Nathan Kaib and Julio Fernández. H.R. is indebted to Grant No. 74/10:2 of the Swedish National Space Board and Grant No. 2011/01/B/ST9/05442 of the Polish National Science Center.

References

Biermann, L., 1978. Dense interstellar clouds and comets. Astronomical Papers Dedicated to Bengt Stromgren, 327–336.
Brasser, R., Schwamb, M.E., Lykawka, P.S., Gomes, R.S., 2012. An Oort cloud origin for the high-inclination, high-perihelion Centaurs. Mon. Not. R. Astron. Soc. 420, 3396–3402.
Carusi, A., Kresák, L., Perozzi, E., Valsecchi, G.B., 1987. High-order librations of Halley-type comets. Astron. Astrophys. 187, 899–905.
Duncan, M.J., Levison, H.F., 1997. A scattered comet disk and the origin of Jupiter family comets. Science 276, 1670–1672.
Duncan, M., Quinn, T., Tremaine, S., 1987. The formation and extent of the Solar System comet cloud. Astron. J. 94, 1330–1338.
Emel'yanenko, V.V., Asher, D.J., Bailey, M.E., 2005. Centaurs from the Oort cloud and the origin of Jupiter-family comets. Mon. Not. R. Astron. Soc. 361, 1345–1351.

Fernández, J.A., Ip, W.-H., 1981. Dynamical evolution of a cometary swarm in the outer planetary region. Icarus 47, 470–479.

Fouchard, M., Rickman, H., Froeschlé, Ch., Valsecchi, G.B., 2013a. Planetary perturbations for Oort Cloud comets. I. Distributions and dynamics. Icarus 222, 20–31.

Fouchard, M., Rickman, H., Froeschlé, Ch., Valsecchi, G.B., 2013b. Planetary perturbations for Oort Cloud comets. II. Implication for the flux of observable comets, Icarus, in press.

Hut, P., Tremaine, S., 1985. Have interstellar clouds disrupted the Oort comet cloud? Astron. J. 90, 1548–1557.

Kaib, N.A. et al., 2009. 2006 SQ_{372}: A likely long-period comet from the inner Oort cloud. Astrophys. J. 695, 268–275.

Levison, H.F., Duncan, M.J., 1997. From the Kuiper belt to Jupiter-family comets: The spatial distribution of ecliptic comets. Icarus 127, 13–32.

Levison, H.F., Dones, L., Duncan, M.J., 2001. The origin of Halley-type comets: Probing the inner Oort cloud. Astron. J. 121, 2253–2267.

Levison, H.F., Morbidelli, A., Dones, L., Jedicke, R., Wiegert, P.A., Bottke, W.F., 2002. The mass disruption of Oort cloud comets. Science 296, 2212–2215.

Levison, H.F., Duncan, M.J., Dones, L., Gladman, B.J., 2006. The scattered disk as a source of Halley-type comets. Icarus 184, 619–633.

Rickman, H., Fouchard, M., Froeschlé, Ch., Valsecchi, G.B., 2008. Injection of Oort Cloud comets: The fundamental role of stellar perturbations. Celest. Mech. Dynam. Astron. 102, 111–132.

Wiegert, P., Tremaine, S., 1999. The evolution of long-period comets. Icarus 137, 84–121.

Chapitre 4

Conclusion et perspectives

Le modèle numérique pour la dynamique des comètes du nuage de Oort que j'ai conçu s'est révélé particulièrement efficace et fiable pour effectuer des simulations à très long terme d'un grand ensemble de comètes initialement dans le nuage de Oort. On a pu obtenir des résultats qui ont changé significativement notre compréhension de cette dynamique comme, *(i)* la synergie entre les marées galactiques et les effets des étoiles passantes, *(ii)* les effets des perturbations planétaires qui sont loin de l'image de loss cone souvent utilisée avec un système solaire interne plus transparent que ce que l'on pouvait croire, et enfin *(iii)* on a obtenu des résultats sur la quantification des routes dynamiques menant du nuage de Oort vers la région d'observabilité lorsque marées galactiques, étoiles et planètes sont à l'œuvre.

Nous ne sommes finalement qu'au début de l'exploitation de ce modèle. En effet, à court terme on devrait pouvoir mettre en place des simulations massives permettant de reproduire de manière précise un pic de Oort après 4.5 milliard d'années. Ceci nous permettra alors de mieux contraindre la distribution de comètes dans le nuage à l'instant présent mais aussi à l'instant initial. De même, en tenant compte le plus possible des observations, on devrait pouvoir établir des lois d'extinction pour les comètes du nuage de Oort. L'établissement de telles lois est déterminant dans l'évaluation du flux de comètes et permettra aussi de discuter du problème de fading des comètes à longue période.

Par la suite, le modèle peut et doit être amélioré sur deux points :

- prise en compte plus réaliste de la trajectoire du Soleil autour de la Galaxie, comme dans Gardner et al. (2011) ;
- modélisation des effets de la rencontre du système solaire avec un nuage moléculaire géant.

D'autre part, la dynamique des comètes ayant des demi-grands axes inférieurs à 1 000 UA, nest pas encore implémentée dans le modèle. Ceci constitue un des objectifs principaux à court terme. En effet, ce sont ces comètes qui vont nous permettre de faire le lien entre le nuage de Oort initial et la production de comètes de type Halley, de centaures, d'objets du disque étendu, voire même de comètes de la famille de Jupiter. L'analyse de l'évolution orbitale de ces comètes est donc une priorité.

Enfin, le 29 septembre 2013, le satellite GAIA aura été envoyé (sauf catastrophe !) pour commencer sa mission de 5 ans d'observations. Ce satellite sera une source d'informations précieuses pour la dynamique des comètes et en particulier celles venant du nuage de Oort. En effet, dans Fouchard et al. (2011b) et Rickman et al. (2012) on a mis en évidence le fait que GAIA observera 80% des étoiles qui auront eu un effet sur la trajectoire des comètes observées pendant leur dernière période orbitale. Même si les observations de GAIA devront être complétées par d'autres observations pour déterminer de manière précise la vitesse radiale de certaines de ces étoiles, il n'en reste pas moins que cet apport sera décisif pour pouvoir reconstruire de manière fiable la dernière période orbitale des comètes observées. Cette reconstruction nous permettra alors de mieux comprendre la dynamique de ces comètes et donc de préciser les contraintes sur la forme et la population du nuage de Oort.

GAIA ne devrait pas découvrir de nombreuses comètes, quelque soit leur famille, mais en revanche ses observations non biaisées de comètes, une loi de balayage de la voûte céleste parfaitement connue, une astrométrie de très haute précision et le fait que toutes les observations sont effectuées par un même instrument permettront entre autres :

- de mieux évaluer les populations des différentes familles de comètes, et on a vu combien ceci est important pour contraindre la formation du nuage de Oort ;
- d'améliorer la détermination des forces non-gravitationelles, en particulier pour les comètes à longue période pour lesquelles ces forces peuvent être déterminantes pour la détermination du demi-grand axe original.

Annexe A

Autres travaux de recherche et publications

A.1 Un modèle statistique de perturbations planétaires

Dans les années 80 des méthodes de Monte Carlo ont été mises en place pour modéliser la dynamique à long terme d'ensemble de comètes (Rickman et Vaghi, 1976; Froeschlé et Rickman, 1980, 1981). Ces méthodes consistaient essentiellement à calculer au préalable un ensemble de perturbations planétaires recouvrant tout l'espace d'étude. L'espace d'étude était ensuite divisé en cellules, et chaque cellule se voyait attribuer un ensemble de perturbations planétaires. Ensuite l'évolution de l'ensemble de comètes fictives était effectuée en appliquant une perturbation planétaire choisie au hasard dans l'ensemble de perturbations associé à la cellule dans laquelle se trouve la comète. Cette perturbation planétaire se traduisant par une variation de tous les éléments orbitaux de la comète considérée. Fouchard et al. (2003) ont montré qu'une telle méthode ne peut pas rendre compte des résonances, puisque les perturbations successives appliquées à une comète sont décorrélées. Ainsi une telle méthode n'était pas appropriée à l'étude de la dynamique des comètes de la famille de Jupiter.

En revanche, pour les comètes se trouvant sur des trajectoires presque paraboliques, comme celles qui viennent du nuage de Oort, leur période orbitale est telle qu'il ne peut y avoir de résonances affectant leur mouvements, donc une méthode de Monte Carlo du type décrit précédemment redevient applicable.

Cependant, on a vu dans Fouchard et al. (2003) que le nombre de perturbations pré-calculées doit être suffisamment grand pour que les perturbations les plus fortes mais aussi les plus rares soient bien représentées. D'autre part, l'espace d'étude est relativement vaste, ainsi le nombre de perturbations à calculer au préalable et à stocker peut devenir considérable, nécessitant l'utilisation de tableaux de taille prohibitive.

Une solution serait donc de remplacer les échantillons de perturbations pré-calculées par des lois de probabilité dont les paramètres dépendent de la localisation dans l'espace d'étude. Ceci constitue l'objectif d'une collaboration en cours avec Radu S. Stoica du laboratoire Painlevé de l'université de Lille 1.

Le premier article publié (Stoica et al., 2010) correspond à une première ébauche de cette étude. On a pu mettre en évidence le fait que les distributions de perturbations planétaires correspondent bien à des distributions à "queue lourde" et donc non gaussiennes. L'évaluation de certains paramètres statistiques caractéristiques de ce genre de distributions (comme le calcul de percentils) faisait apparaître les mêmes structures que celles obtenues par la bien connue théorie de Öpik.

Le modèle utilisé dans ce premier travail était un modèle "complet" dans lequel les quatre planètes géantes affectaient un objet de masse négligeable sur une orbite presque parabolique. Il s'avéra alors que l'espace d'étude était trop complexe et la quantité de perturbations calculées était loin d'être suffisante pour obtenir une bonne fiabilité sur l'estimation des paramètres de loi de probabilité.

Ce travail est donc repris, mais en considérant le modèle dynamique le plus simple possible, i.e. une seule planète géante sur une orbite circulaire qui perturbe des objets sur des trajectoires initialement paraboliques. Ce travail est en cours.

Article publié :

Is the dynamics of Jupiter family comets amenable to Monte Carlo modelling ?

Fouchard, M. ; Froeschlé, Ch. ; Valsecchi, G. B.

MNRAS, *2003*, **344**, 1283-1295.

abstract

In order to explore the range of applicability of Monte Carlo modelling, we reconsider in depth the Monte Carlo simulations of Froeschlé & Rickman aimed at the study of the orbital evolution of Jupiter family comets. We first analyse the computation of perturbation distributions, and find that to get statistically significant results, the sample size of these distributions must be larger than several times 10^5. We then show the necessity of introducing a procedure, referred to as the Spurious Perturbations Removal (SPR) procedure, to clean the perturbation distribution of any spurious contribution due to comets undergoing a close encounter with Jupiter at the beginning or/and the end of the perturbation computations. The partition of element space into 30 boxes in the (Q, q) plane ($4 \leq Q \leq 13$ au and $0 \leq q \leq 7$ au) does not lead to dynamically homogeneous boxes, as is required for Monte Carlo simulations ; these inhomogeneities are due to various reasons. Different ways to make such a partition are discussed. The strong influence of mean motion resonances on the dynamics of Jupiter family comets implies that resonances must be taken into account in any Monte Carlo simulation.

Article publié :

Order statistics and heavy-tail distributions for planetary perturbations on Oort cloud comets

Stoica, R.S. and Liu, S. and Davydov, Y. and Fouchard, M. and Vienne, A. and Valsecchi, G.B.

A&A, *2010*, **513**, A14.

abstract

Aims. This paper tackles important aspects of comet dynamics from a statistical point of view. Existing methodology uses numerical integration to compute planetary perturbations to simulate such dynamics. This operation is highly computational. It is reasonable to investigate a way in which a statistical simulation of the perturbations can be handled more easily. Methods. The first step to answer such a question is to provide a statistical study of these perturbations in order to determine their main features. The statistical tools used are order statistics and heavy-tailed distributions. Results. The study carried out indicated a general pattern exhibited by the perturbations around the orbits of the planets. These characteristics were validated through statistical testing and a theoretical study based on the Öpik theory.

A.2 Satellites irréguliers de Jupiter

Le travail de recherche concernant les satellites irréguliers de Jupiter a été mené par Julien Frouard dans le cadre de sa thèse de doctorat que j'ai co-dirigée avec Alain Vienne. Les satellites irréguliers sont des satellites qui se trouvent très éloignés de la planète sur des trajectoires généralement bien plus excentriques et inclinées que celle des satellites plus proches. Ces caractéristiques font que ces satellites ont très probablement été capturés par la planète au cours de l'évolution du système solaire.

La résonance d'évection correspond à une commensurabilité entre le mouvement moyen d'une planète et le mouvement de la longitude du péricentre d'un satellite de cette planète. Cette région représente la région de stabilité la plus lointaine pour des satellites d'une planète. Dans Frouard et al. (2010), cette résonance est étudiée, tant d'un point de vue analytique que d'un point de vue numérique. Un modèle analytique de la résonance y est développé. Ce modèle constitue une amélioration notable de modèles précédents, notament parce qu'il est valable à n'importe quelles excentricités. Cependant, pour Jupiter, il ne permet pas de rendre compte de manière précise de la localisation de la résonance à cause de la moyennisation des équations effectuée pour obtenir le modèle et de la grande valeur du demi-grand axe des satellites se trouvant au voisinage de la résonance. Une étude précise de la résonance est effectuée de manière numérique en utilisant des indicateurs de type Lyapunov pour la stabilité et par le biais de surface de section pour la localisation. De plus, la localisation de la résonance d'évection induite par l'applatissement d'une planète est aussi étudiée de manière analytique.

Dans Frouard et al. (2011) une étude à long terme de la stabilité des satellites irréguliers de Jupiter est effectuée. Cette étude est faite par le biais de cartes de stabilité faisant aparaître le réseau de résonances autour des satellites. Il a été montré que la majorité des satellites ont un comportement chaotique, bien que deux familles de satellites (*Ananke* et *Carme*) le sont faiblement.

Les cartes de stabilité ont permis de mettre en évidence le rôle important que semble jouer la grande inégalité entre Jupiter et Saturne. En particulier les familles *Ananke* et *Carme* se trouve au voisinage d'une résonance faisant intervenir la grande inégalité, ce qui a pu avoir jouer un rôle dans l'histoire dynamique passée de ces familles.

Article publié :

About the dynamics of the evection resonance

J. Frouard, M. Fouchard, and A. Vienne

2010, *A&A*, **515**, A54.

abstract

Context. The evection resonance appears to be the outermost region of stability for A prograde satellite orbiting a planet, the critical argument of the resonance indeed being found librating in regions surrounded only by chaotic orbits. The dynamics of the resonance itself is thus of great interest for the stability of satellites, but its analysis by means of an analytical model is not straightforward because of the high perturbations acting on the dynamical region of interest.

Aims. It is thus important to show the results and the limits inherent in analytical models. We use numerical methods to test the validity of the models and analyze the dynamics of the resonance.

Methods. We use an analytical method based on a classical averaged expansion of the disturbing function valid for all eccentricities as well as numerical integrations of the motion and surfaces of section.

Results. By comparing analytical and numerical methods, we show that aspects of the true resonant dynamic can be represented by our analytical model in a more accurate way than previous approximations, and with the help of the surfaces of section we present the exact location and dynamics of the resonance. We also show the additional region of libration of the resonance that can be found much closer to the planet due to its oblateness.

Article publié :

The long-term dynamics of the Jovian irregular satellites

J. Frouard, A. Vienne, and M. Fouchard

2011, *A&A*, **532**, A44.

abstract

Context. The dynamical region of the Jovian irregular satellites presents an interesting web of resonances that are not yet fully understood. Of particular interest is the influence of the resonances on the stochasticity of the individual orbits of the satellites, as well as on the long-term chaotic diffusion of the different families of satellites.

Aims. We make a systematic numerical study of the satellite region to determine the important resonances for the dynamics, to search for the chaotic zones, and to determine their influences on the dynamics of the satellites. We also compare these numerical results to previous analytical works.

Methods. Using extensive numerical integrations of the satellites along with an indicator of chaos (MEGNO), we show global and detailed views of the retrograde and prograde regions for various dynamical models of increasing complexity and indicate the appearance of the different types of resonances and the implied chaos.

Results. Along with secular and mean motion resonances that shape the dynamical regions of the satellites, we report a number of resonances involving the Great Inequality, and which are present in the system thanks to the wide range of the values of frequencies of the pericenter available for the satellites. The chaotic diffusion of the satellites is also studied and shows the long-term stability of the Ananke and Carme families, in contrast to the Pasiphae family.

A.3 Travaux de recherche reliés à la genèse du modèle dynamique pour les comètes du nuage de Oort

La construction du modèle de marées galactiques s'est faite en plusieurs étapes. La première a eu lieu en fin de thèse. Dans ce premier travail (Fouchard, 2004) un modèle de marées galactiques sous forme de *mapping*, c'est-à-dire d'une application qui permettait de modéliser les effets des marées galactiques sur une période orbitale de la comète, a été construit. En fait il s'agit d'une série de mappings dont la précision peut être arbitrairement grande, pourvu que le demi-grand axe des comètes reste modéré.

Ce modèle a ensuite été amélioré dans Fouchard et al. (2005). En effet, les mappings construits dans Fouchard (2004) utilisaient les variables hamiltoniennes de Delaunay, et avait une singularité. Un autre ensemble de variables hamiltoniennes, appelées variable de Matese dans Fouchard et al. (2005), a permis de déplacer cette singularité mais pas de l'éliminer.

Un premier modèle hybride de marée a été utilisé dans Fouchard et al. (2006) afin d'étudier les effets à long terme des marées galactiques, et en particulier du choix des paramètres intervenant dans la modélisation de la marée.

Finalement c'est dans le cadre d'une collaboration avec Sławomir Breiter de l'observatoire de Poznan (Pologne) que le modèle hybride final de marées galactiques a été construit (Breiter et al., 2007).

Article publié :

New fast models of the Galactic tide

M. Fouchard

2004, *Mon. Not. R. Astron. Soc.*, **349**, 347-356.

abstract

New models of the action of the Galactic tide on the motion of the Oort Cloud comets are investigated. The first one consists of the Hamiltonian form of the equations of motion which are averaged over the mean anomaly including the radial component of the tide. The second is a series of mappings which allows a noticeable reduction of the computer time. These models are checked in three different frames, and some of them turn out to be reliable for a wide range of initial conditions. In the last experiment we simulate the transport of 10^5 Oort Cloud comets to the inner Solar system under the Galactic tide impulse alone. For such a simulation, the best compromise between reliability and computer time is given by a mapping of order 3 which is more than 500 times faster than the usual numerical integrations and may be safely used when the comet semimajor axes $a < 30\,000$ au. The present study highlights the qualitative effects of the radial component of the Galactic tide. The models built here will be used in a forthcoming paper for a more realistic study of the transport of long-period comets including planetary perturbations.

Article publié :

Comparison Between Different Models of Galactic Tidal Effects on Cometary Orbit

M. Fouchard, Ch. Froeschlé, J. J. Matese and G. B. Valsecchi

2005, *Celestial Mechanics and Dynamical Astronomy*, **93**, 229-262.

abstract

Different models of the action of the galactic tide are compared. Each model is a substitute for direct numerical integrations allowing a drastic decrease of the computation time. The models are built using two different techniques, (i) averaging of the fast variable (the mean anomaly) over one cometary period and (ii) fixing the comet in its aphelion direction. Moreover, we consider two different formalisms (Lagrangian and Hamiltonian) and also two different sets of variables. As expected, we find that the model results are independent of the formalism and the set of variables considered, and are highly accurate, whereas mathematical technique (ii) leads to poor results. In order to further reduce the computation time, mappings are built from the development of the solution of the models. We show that for these mappings, the set of variables giving the most accurate results is strongly dependent on the cometary eccentricity, e, and semimajor axis, a.

Article publié :

Long-term effects of the Galactic tide on cometary dynamics

M. Fouchard, Ch. Froeschlé, G. B. Valsecchi and H. Rickman

2006, *Celestial Mechanics and Dynamical Astronomy*, **95**, 299-326.

abstract

We introduce a model for integrating the effects of Galactic tides on Oort cloud comets, which involves two procedures, according to the values of the osculating semi-major axis a and eccentricity e. Ten simulations of the dynamics of 10^6 comets over 5 Gyr are performed using this model. We thus investigate the long-term effects of the Galactic tide with and without a radial component, the effects of the local density of the Galactic disk, and those of the Oort constants. Most of the results may be understood in terms of the integrability or non-integrability of the system. For an integrable system, which occurs for moderate semi-major axes with or without radial component, the dynamics is explained by periodic variation of the cometary perihelion, inducing the depletion of the outer region of the Oort cloud, a constant flux from the inner region after 500 Myr, and the quick formation of a reservoir of comets with argument of perihelion near 26.6°. When the system is non-integrable, the efficiency of the tide in reducing the cometary perihelion distance is enhanced both by replenishing the Oort cloud domain from which comets are sent toward the planetary system, and by reducing the minimal value that the perihelion distance may reach. No effects of varying the Oort constants were observed, showing that the flat rotation curve is a satisfactory approximation in Oort cloud dynamics.

Article publié :

Two fast integrators for the Galactic tide effects in the Oort Cloud

S. Breiter, M. Fouchard,R. Ratajczak, W. Borczyk

2007, *Mon. Not. R. Astron. Soc.*, **377**, 1151-1162.

abstract

Two fast and reliable numerical integrators for the motion of the Oort Cloud comets in the Galactic tidal potential are presented. Both integrators are constructed as Hamiltonian splitting methods. The first integrator is based upon the canonical Hamiltonian equations split into the Keplerian part and a time-dependent perturbation. The system is regularized by the application of the Kuustanheimo-Stiefel variables. The composition rule of Laskar and Robutel with a symplectic corrector is applied. The second integrator is based on the approximate, averaged Hamiltonian. Non-canonical Lie-Poisson bracket is applied allowing the use of non-singular vectorial elements. Both methods prove superior when compared to their previously published counterparts.

Article publié :

Algorithms for Stellar Perturbation Computations on Oort Cloud Comets

H. Rickman, M. Fouchard, G. B. Valsecchi and Ch. Froeschlé

2005, *Earth Moon and Planets*, **97**, 411-434.

abstract

We investigate different approximate methods of computing the perturbations on the orbits of Oort cloud comets caused by passing stars, by checking them against an accurate numerical integration using Everhart's RA15 code. The scenario under study is the one relevant for long-term simulations of the clouds response to a predefined set of stellar passages. Our sample of stellar encounters simulates those experienced by the Solar System currently, but extrapolated over a time of 10^{10} years. We measure the errors of perihelion distance perturbations for high-eccentricity orbits introduced by several estimators including the classical impulse approximation and Dybczyński's (1994, *Celest. Mech. Dynam. Astron.* 58, 1330-1338) method and we study how they depend on the encounter parameters (approach distance and relative velocity). We introduce a sequential variant of Dybczynśki's approach, cutting the encounter into several steps whereby the heliocentric motion of the comet is taken into account. For the scenario at hand this is found to offer an efficient means to obtain accurate results for practically any domain of the parameter space.

A.4 Résultats complémentaires autour des comètes du nuage de Oort

A.4.1 Complément sur la dynamique générée par les marées seules

---

Article publié :

Stationary orbits of comets perturbed by Galactic tides

S. Breiter, M. Fouchard and R. Ratajczak

MNRAS, *2008*, **383**, 200-208.

abstract

Using the first-order normalized equations describing the heliocentric cometary motion perturbed by the Galactic tides, we identify 'stationary solutions' with constant values of the eccentricity, inclination, argument of perihelion and longitude of the ascending node in the reference frame rotating with the Galaxy. The families found involve circular orbits, orbits in the Galactic equatorial plane, rectilinear orbits normal to the equatorial plane, elliptic orbits symmetric with respect to the direction to the Galactic Centre or to its perpendicular, and asymmetrically oriented elliptic orbits. Linear stability of the stationary solution is studied analytically and confirmed by numerical experiments. Most, but not all, of the unstable solutions prove chaotic with the Lyapunov times at least 100 Myr.

A.4.2 Complément sur la synergie à court terme

Article publié :

Gaia and the new comets from the Oort cloud

H. Rickman, M. Fouchard, Ch. Froeschlé, G.B. Valsecchi
2012, *Planetary and Space Science*, **73**, 124-129.

abstract

We use Oort cloud simulations covering a time span of 5 Gyr, including the Galactic tides and stellar encounters and focussing on the last revolution of comets as they get injected into observable orbits, in order to analyze in detail the role of stars in those injections. We find this role to be very important in all parts of the cloud, so that most injected comets require the intervention of a star. Characterizing the stellar influence by the decrease of the perihelion distance, projected to the time of the next perihelion by means of tidal evolution, we identify the most efficient stars and study the properties of the corresponding encounters. We also judge the detectability of the culprit stars, responsible for the current arrival of new comets, by the Hipparcos and Gaia missions based on the magnitudes of the stars. Our main result is that the chances to detect and identify those culprits will be revolutionized by the Gaia data independent of which region of the cloud the comets come from.

A.5 Cours ou article de revue

Article publié :

Dynamical Features of the Oort Cloud Comets

M. Fouchard, C. Froeschl ?e, H. Rickman, and G. B. Valsecchi
Lect. Notes Phys., *2010*, **790**, 401-430.

abstract

The Oort cloud which corresponds to the outer boundary of our Solar system, is considered to be the main reservoir of long period comets. At such distance from the Sun (several times 10 000 AU), the comet trajectories are affected by the galactical environment of the Solar System. Two main effects contribute to inject comets from the Oort cloud to the inner Solar system where comets may become observable : the Galactic tide which is due to the difference of the gravitational attraction of the entire Galaxy on the Sun and on the comets, and the gravitational effects of stars passing close to the Sun. In this lecture the characteristics and the long term effects of these two mechanisms, taken independently and simultaneously, will be illustrated.

Article publié :

Galactic environment and cometary flux from the Oort cloud

M. Fouchard

Icy Bodies of the Solar System, J.A. Fernandez, D. Lazzaro, D. Prialnik, & R. Schulz, eds., *2010*, **Proceedings IAU Symposium No. 263**, 57-66.

abstract

The Oort cloud, which corresponds to the furthest boundary of our Solar System, is considered as the main reservoir of long period comets. This cloud is likely a residual of the Solar System formation due to the gravitational effects of the young planets on the remaining planetesimals. Given that the cloud extends to large distances from the Sun (several times 10 000 AU), the bodies in this region have their trajectories affected by the Galactic environment of the Solar System. This environment is responsible for the re-injection of the Oort cloud comets into the planetary region of the Solar System. Such comets, also called 'new comets', are the best candidates to become Halley type or 'old' long period comets under the influence of the planetary gravitational attractions. Consequently, the flux of new comets represents the first stage of the long trip from the Oort cloud to the observable populations of comets. This is why so many studies are still devoted to this flux. The different perturbers related to the Galactic environment of the Solar System, which have to be taken into account to explain the flux are reviewed. Special attention will be paid to the gravitational effects of stars passing close to the Sun and to the Galactic tides resulting from the difference of the gravitational attraction of the Galaxy on the Sun and on a comet. The synergy which takes place between these two perturbers is also described.

A.6 Activité de recherche sur les indicateurs de chaoticité

Ces travaux concernent essentiellement le travail de recherche effectué pendant ma thèse de doctorat. Cependant l'utilisation de ces indicateurs, en particulier du Fast Lyapunov Indicator, a été faite dans le cadre de la thèse de doctorat de Julien Frouard ainsi que dans le cadre d'une collaboration en développement avec Jérôme Daquin et Florent Deleflie.

Article publié :

On the Relationship Between Fast Lyapunov Indicator and Periodic Orbits for Continuous Flows

Fouchard, Marc ; Lega, Elena ; Froeschlé, Christiane ; Froeschlé, Claude

Celestial Mechanics and Dynamical Astronomy, *2002*, **83**, 205-222.

abstract

It is already known (Froeschlé et al., 1997a) that the fast Lyapunov indicator (hereafter FLI), i.e. the computation on a relatively short time of a quantity related to the largest Lyapunov indicator, allows us to discriminate between ordered and weak chaotic motion. Using the FLI many results have been obtained on the standard map taken as a model problem. On this model we are not only able to discriminate between a short time weak chaotic motion and an ordered one, but also among regular motion between non resonant and resonant orbits. Moreover, periodic orbits are characterised by constant FLI values which appear to be related to the order of periodic orbits (Lega and Froeschlé, 2001). In the present paper we extend all these results to the case of continuous dynamical systems (the Hénon and Heiles system and the restricted three-body problem). Especially for the periodic orbits we need to introduce a new value : the orthogonal FLI in order to fully recover the results obtained for mappings.

Annexe B

Curriculum vitae

Déroulement de carrière

1 Septembre 2006 : Maître de conférences à l'Université de Lille I.

20 Mars 2005 : Obtention d'une bourse externe de l'ESA pour travailler à l'Istituto di Astrofisica Spaziale e Fisica Cosmica de Rome.

20 Février 2004 : Obtention d'une thèse de doctorat sous la direction de Ch. Froeschlé et G.B. Valsecchi. Titre de la thèse : "Contribution à l'étude de la dynamique des comètes". Mention très honorable.

1998 : Agrégation de mathématiques (option mécanique).

1997 : Capes de mathématiques et admissible à l'agrégation de mathématiques.

1996 : DEA de Turbulences et Systèmes Dynamiques de l'Université de Nice Sophia Antipolis.

1995 : Maîtrise de mécanique à l'Université d'Aix-Marseille II.

Enseignement

depuis 2010 : responsable (depuis 2011) et animateur d'un service d'observation à la lunette de l'observatoire de Lille pour un public universitaire.

depuis 2009 : chargé de TD/colles en licence de Mathématiques, Science Physique et Science pour l'Ingénieur (analyse et algèbre), à raison de 40h par an en moyenne.

2007-2011 ; 2012-2013 : participation dans le cadre d'UNISCIEL au développement d'un site consacré à l'astronomie dans l'apprentissage des mathématiques au niveau licence.

depuis 2006 : Chargé de TD pour une option astronomie en 2ème année de licence (mathématiques, physiques, ingénierie). L'option est consacrée principalement à la géométrie sphérique et aux différents systèmes de coordonnées sphériques utilisés en astronomie.

depuis 2006 : responsable d'un cours d'introduction à l'astronomie en première année de licence (mathématiques, physique, ingénierie).

depuis 2006 : participation à un groupe de travail de l'IREM sur l'utilisation de l'astronomie pour l'enseignement des mathématiques dans le secondaire.

depuis 2006 : formateur pour les enseignants du second degré dans le cadre de stage sur l'enseignement de l'astronomie dans le secondaire.

2010-2011 : cours/TD en M1 (mathématiques, physiques). Il s'agit de la partie d'un cours de mécanique hamiltonienne (20h).

2006-2007 : chargé de TD pour une option en astronomie en 3ème année de licence de mathématiques. L'option consistait en une introduction à la mécanique céleste.

2003-28 Février 2005 : titulaire d'un poste d'enseignant au collège Paul Eluard (Nanterre, académie de Versailles).

1999-2002 : titulaire d'un poste d'enseignant au Lycée polyvalent Jacques Vaucanson classé en ZEP (Les Mureaux, académie de Versailles).

Investissements divers

avril 2013 : Rapporteur pour une demande de financement à hauteur de 70 000 € pour un projet de recherche soumis à une agence gouvernementale polonaise (National Science Centre).

2012 : Membre de l'UAI Division I Commission 7 "Celestial Mechanics & Dynamical Astronomy" et Division III Commission 15 "Physical Study of Comets & Minor Planets".

2011 : organisation d'un atelier international sur la dynamique et la formation du nuage de Oort du 27 au 30 Septembre 2011 à l'Observatoire de Lille (financement : université de Lille, observatoire de Paris).

2011 : Membre du Jury en tant qu'examinateur de la thèse de doctorat de Carlo Comito (cotutelle Université de Nice Sophia-Antipolis / Università degli Studi di Torino).

2010 : porteur d'une demande de BQR pour un achat de matériel informatique pour l'observatoire de Lille. La justification du matériel s'est faite, entre autre, dans le cadre d'un projet de recherche commun avec le laboratoire Painlevé de l'université de Lille 1 sur la dynamique des comètes.

Mai 2010 : participation en tant que membre externe au comité de sélection pour un poste de Maître de conférences en section 34 à l'université Paris VII.

depuis 2009 : responsable de la sécurité incendie à l'observatoire de Lille.

2009 : élu dans le vivier pour les comités de sélections pour les sections 25-26-34 à l'UFR de mathématiques de l'Université de Lille 1.

2008 et 2009 : porteur d'un projet scientifique international dans le cadre du BQR sur la dynamique des comètes (deux ateliers organisés).

2007 : porteur d'une demande conjointe de l'UFR de mathématiques et de l'UFR de physique pour l'achat d'un spectrographe par la cellule formation de l'USTL.

2007-2011 : élu du conseil d'institut de l'IMCCE.

depuis 2006 : participation à la préparation de la mission GAIA de l'Agence Spatiale Européenne. Contribution sur les apports potentiels de GAIA à notre compréhension de la dynamique des comètes.

depuis 2005 : participation à des comités de lectures pour les revues internationales suivantes : Monthly Notices of the Royal Astronomical Society, Contributions of the Astronomical Observatory Skalnaté Pleso, Planetary and Space Science, Celestial Mechanics and Dynamical Astronomy, Astronomy and Astrophysics, Icarus.

Encadrement de stagiaires hors thèse de doctorat

23 Mai 2011 - 22 Juillet 2011 : S3, Ecole Normale de Lyon, Ilyas Djafer-Cherif : "relever d'étoiles avec le spectrographe de l'observatoire de Lille"

15 Septembre 2009 - 15 Novembre 2009 : M1, Université de Lille 1, Vivien Scottez (co. Denis Duflot, Stefan Renner) : "relever du spectre du Soleil avec le spectrographe de l'observatoire de Lille"

15 Juin 2008 - 15 Juillet 2008 : M1, Université de Lille 1, Zheng Liu (co. Denis Duflot) : "Premières mesures avec le spectrographe de l'observatoire de Lille"

15 Juin 2008 - 15 Juillet 2008 : M1, Université de Lille 1, Gerald Ndong (co. Denis Duflot) : "Premières mesures avec le spectrographe de l'observatoire de Lille"

3 Mars 2008 - 2 Mai 2008 : M1, Université de Lille 1, Kamal Machto (co. Alain Vienne) : "Détermination d'orbites d'étoiles doubles"

1er Avril 2007 - 1er Juillet 2007 : M2 recherche, Observatoire de Paris, Julien Frouard (co. Alain Vienne) : “Etude des processus de capture de satellites des planètes”

7 Mai 2007 - 7 Aout 2007 : M1, Université Paris 11, Thomas Lemée (co. Alain Vienne) : “Outils de détection du chaos dans les systèmes planétaires”

1er Juillet 2007 - 15 Juillet 2007, 1er Sept. 2007 - 15 Sept. 2007 : L2, Université de Lille 1, Narei Lorenzo Martinez (co. Alain Vienne) : “Etude des trajectoires d’étoiles doubles”

Collaborations internationales et projets scientifiques

20 Avril-20 Mai 2009 : invitation de Hans Rickman (Centrum Badan Kosmicznych Polska Akademia Nauk, Varsovie, Pologne) par l’Université de Lille I pour collaboration scientifique.

Janvier 2008-Mars 2011 : participation à un projet financé par une bourse polonaise sur la dynamique du nuage de Oort et le disque étendu. Le projet concerne les personnes suivantes : Slawomir Breiter (Observatoire de Poznan, Pologne), Piotr A. Dybczynski (Observatoire de Poznan, Pologne), Christiane Froeschlé (Laboratoire Cassiopée, OCA, Nice), Ryszard Gabryszewski, (Centrum Badan Kosmicznych Polskiej Akademii Nauk, Pologne) Malgorzata Krolikowska-Soltan (Centrum Badan Kosmicznych Polska Akademia Nauk, Varsovie, Pologne) Hans Rickman, (Centrum Badan Kosmicznych Polska Akademia Nauk, Varsovie, Pologne), Slawomira Szutowicz(Centrum Badan Kosmicznych Polska Akademia Nauk, Varsovie, Pologne), Giovanni Valsecchi, (IASF-INAF, Rome, Italie).

2006-2010 : collaboration avec Slawomir Breiter de l’observatoire de Poznan, Pologne. Thème de recherche : étude de la dynamique engendrée par la marée galactique (trajectoires périodiques, stabilité, etc).

Depuis Janvier 2004 : collaboration avec Hans Rickman (Université de Uppsala, Suède), Giovanni Valsecchi (IASF-INAF, Rome, Italie) et Christiane Froeschlé sur l’étude à long terme de la dynamique des comètes du nuage de Oort.

Participations à des colloques / écoles / congrès

Octobre 2010 (Pasadena, USA) : DPS, présentation orale sur la dernière période des comètes “nouvelles”.

Août 2009 (Rio de Janeiro, Brésil) : review talk **invité** sur "Galactic environment and cometary flux from the Oort cloud", Assemblée Générale de l'Union Astronomique Internationale (IAU).

Juin 2009 (Aussois, France) : cours **invité** pour une Ecole Thématique du CNRS " La dynamique des systèmes gravitationnels : défis et perspectives.", intitulé du cours : "Oort cloud comets dynamics and planetary perturbations".

Juillet 2008 (Baltimore, USA) : ACM. Présentation sur l'importance de la masse de l'étoile sur la synergie marée-étoile.

Juin 2008 (Litohoro, Grèce) : Colloque en l'honneur de Prof. John D. Hadjidemetriou. Présentation sur l'influence de passage stellaire sur la dynamique des comètes du nuage de Oort

Juin 2007 (Spoleto, Italie) : Colloque en l'honneur de Claude Froeschlé. Présentation **invitée** sur la synergie entre les effets des perturbations stellaires et ceux de la marée galactique sur la dynamique des comètes du nuage de Oort.

Mars 2007 (Bad Hofgastein, Autriche) : cours **invité** pour une Ecole Thématique du CNRS "Récentes Investigations en Dynamique des Corps Célestes dans les Systèmes Solaire et Extra-solaires". Cours sur les différents aspects de la dynamique des comètes du nuage de Oort.

Mars 2006 (Aussois, France) : cours **invité** pour un Atelier de mécanique céleste : les derniers développements en mécanique céleste. Cours sur la modélisation de la dynamique des comètes du nuage de Oort.

Sept. 2005 (Viterbo, Italie) : CELMEC IV. Présentation sur les nouveaux modèles de marée galactique.

Activité grand-public

2013 Ecriture d'un paragraphe pour l'agenda 2014 de l'IMCCE sur le nuage de Oort.

2011 Interview pour un article de Science et Avenir sur le nuage de Oort.

2011 Témoignages pour le blog vidéo de Lille 1 dans le cadre du projet "Demain, l'Université".

2009 Intervenant dans le cadre de Lillosciences et présentation d'un atelier "Carte du Ciel".

2007 intervenant à la journée Jeunes Chercheurs organisée par le forum des sciences de Villeneuve d'Ascq.

Publications dans des revues internationales avec comité de lecture

- Fouchard, M. and Rickman, H. and Froeschlé, Ch. and Valsecchi, G.B., " Planetary perturbations for Oort cloud comets. I. Distributions and dynamics ", Icarus, 222, p. 20-31, 2013.
- Rickman, H. and Fouchard, M. and Froeschlé, Ch. and Valsecchi, G.B., " Gaia and the new comets from the Oort cloud", PSS, 73, p. 124-129, 2012.
- Fouchard, M. and Rickman, H. and Froeschlé, Ch. and Valsecchi, G.B., "The last revolution of new comets : the role of stars and their detectability", A&A, **535**, 1-13, 2011.
- Fouchard, M. and Froeschlé, Ch. and Rickman, H. and Valsecchi, G.B., " The key role of massive stars in Oort cloud comet dynamics", Icarus, **214**, 334-347, 2011.
- Frouard, J. and Vienne, A., and Fouchard, M., "The long-term dynamics of the Jovian irregular satellites", A&A, 532, id.A44, 15 pp., 2011.
- Frouard, J. and Fouchard, M. and Vienne, A., "About the dynamics of the evection resonance", *A&A*, 2010,**515**, 54.
- Stoica, R.S. and Liu, S. and Davydov, Y. and Fouchard, M. and Vienne, A. and Valsecchi, G.B., "Order statistics and heavy-tail distributions for planetary perturbations on Oort cloud comets", *A&A*, 2010, **513**, 14.
- Fouchard, M. and Froeschlé, Ch. and Rickman, H. and Valsecchi, G., "Dynamical features of the Oort cloud comets", *Lecture Notes in Physics, Berlin Springer Verlag*, 2010, **790**, 401-430.
- Rickman, H. and Fouchard, M. and Froeschlé, Ch. and Valsecchi, G. B., "Injection of Oort Cloud Comets : The Fundamental Role of Stellar Perturbations", *Celestial Mechanics and Dynamical Astronomy*, 2008, **102**,111-132.
- Breiter, S. and Fouchard, M. and Ratajczak, R., "Stationary orbits of comets perturbed by Galactic tides",MNRAS, 2008,**383**,200-208.
- Fouchard, M. and Froeschlé, Ch. and Rickman, H. and Valsecchi, G., "Methods to Study the Dynamics of the Oort Cloud Comets I : Modelling the Stellar Perturbations", Topics in Gravitational dynamics, 2007, *Lectures Notes in Physics, Berlin Springer Verlag*, **729**, Benest, D. Froeschlé, Cl. and Lega, E. eds., 255-270.
- Fouchard, M. and Froeschlé, Ch. and Breiter, S. and Ratajczak, R. and and Valsecchi, G. Rickman, H. , "Methods to Study the Dynamics of the

Oort Cloud Comets II : Modelling the Galactic Tide", Topics in Gravitational dynamics, 2007, *Lectures Notes in Physics, Berlin Springer Verlag*, **729**, Benest, D. Froeschlé, Cl. and Lega, E. eds., 271-293.

- Breiter, S. and Fouchard, M. and Ratajczak, R. and Borczyk, W. , "Two fast integrators for the Galactic tide effects in the Oort Cloud",MNRAS, 2007,**377**, 1151-1162.
- Fouchard, M. and Froeschlé, Ch. and Valsecchi, G. and Rickman, H., "Long-term effects of the Galactic tide on cometary dynamics", *Celestial Mechanics and Dynamical Astronomy*, 2006, **95**, 299-326.
- Rickman, H. and Fouchard, M. and Valsecchi, G. B. and Froeschlé, Ch., "Algorithms for Stellar Perturbation Computations on Oort Cloud Comets", *Earth Moon and Planets*, 2005, **97**, 411-434.
- Fouchard, M. and Froeschlé, Ch. and Matese, J. J. and Valsecchi, G., "Comparison between Different Models of Galactic Tidal Effects on Cometary Orbits", *Celestial Mechanics and Dynamical Astronomy*, 2005, **93**, 229-262.
- Fouchard, M., "New fast models of the Galactic tide", MNRAS, 2004, **349**, 347-356.
- Fouchard, M. and Froeschlé, Ch. and Valsecchi, G. B., "Is the dynamics of Jupiter family comets amenable to Monte Carlo modelling ?", *MNRAS*, 2003, **344**, 1283-1295.
- Fouchard, M. and Lega, E. and Froeschlé, Ch. and Froeschlé, Cl., "On the Relationship Between Fast Lyapunov Indicator and Periodic Orbits for Continuous Flows", *Celestial Mechanics and Dynamical Astronomy*, 2002, **83**, 205-222.

Autres publications

- Fouchard, M., "*Galactic environment and cometary flux from the Oort cloud*", IAU Symposium, 2010, 263, edts. Fernandez, J. A. and Lazzaro, D. and Prialnik, D. and Schulz, R., pp 57-66
- Frouard, J. and Fouchard, M. and Vienne, A., "*The evection resonance : solar and oblateness perturbations*", SF2A-2010 : Proceedings of the Annual meeting of the French Society of Astronomy and Astrophysics, 2010, edts. Boissier, S. and Heydari-Malayeri, M. and Samadi, R. and Valls-Gabaud, D., p 127
- Fouchard, M. and Rickman, H. and Valsecchi, G. B. and Froeschlé, Ch., "*The Last Orbital Period of "new Comets""*", AAS/Division for Planetary Sciences Meeting Abstracts #42, 2010, Bulletin of the American Astronomical Society, **42**, 950

- Weiler, M. and Babusiaux, S. M. C. and Fouchard, M. and Mignot, S., "*Comet observations with Gaia*", European Planetary Science Congress 2010, 2010, 339
- Frouard, J. and Fouchard, M. and Vienne, A., "*The Long-term Evolution of the Jovian Irregular Satellites*", AAS/Division of Dynamical Astronomy Meeting #41, 2010, series = Bulletin of the American Astronomical Society, **42**, 936
- Frouard, J. and Fouchard, M. and Vienne, A., "*Chaoticity of the Jovian Irregular Satellites*", AAS/Division for Planetary Sciences Meeting Abstracts #41, 2009, AAS/Division for Planetary Sciences Meeting Abstracts, **41**, #38.08
- Frouard, J. and Fouchard, M. and Vienne, A., "*Comparison of fast Lyapunov chaos indicators for Celestial Mechanics*", SF2A-2008, 2008, edts. Charbonnel, C. and Combes, F. and Samadi, R., 121
- Gauchez, D. and Fouchard, M. and Souchay, J., "*Inter-Comparisons Between Numerical Integrations and Analytical Theory for the Solar System*", 2002, Modern Celestial Mechanics : from theory to applications (A. Celletti, S.Ferraz-Mello, J. Henrard eds), Kluwer A.P., 393-396.

Bibliographie

Bailey M.E. 1983. The structure and evolution of the Solar System comet cloud. *MNRAS*, **204**, 603–633.

Biermann L. 1978. Dense interstellar clouds and comets. In Reiz A. and Andersen T., editors, *Astronomical Papers Dedicated to Bengt Stromgren*, pages 327–336.

Brasser R. 2008. A two-stage formation process for the Oort comet cloud and its implications. *AAP*, **492**, 251–255.

Brasser R., Duncan M. J., and Levison H. F. September 2006. Embedded star clusters and the formation of the Oort Cloud. *Icarus*, **184**, 59–82.

Brasser R., Duncan M. J., and Levison H. F. 2007. Embedded star clusters and the formation of the Oort Cloud II. The effect of the primordial solar nebula. *Icarus*, **191**, 413–433.

Brasser R., Duncan M. J., and Levison H. F. 2008. Embedded star clusters and the formation of the Oort cloud. III. Evolution of the inner cloud during the Galactic phase. *Icarus*, **196**, 274–284.

Brasser R. and Morbidelli A. 2013. Oort cloud and Scattered Disc formation during a late dynamical instability in the Solar System. *Icarus*, **225**, 40–49.

Brasser R., Schwamb M. E., Lykawka P. S., and Gomes R. S. 2012. An Oort cloud origin for the high-inclination, high-perihelion Centaurs. *MNRAS*, **420**, 3396–3402.

Breiter S., Fouchard M., Ratajczak R., and Borczyk W. 2007. Two fast integrators for the Galactic tide effects in the Oort Cloud. *MNRAS*, **377**, 1151–1162.

Byl J. 1983. Galactic perturbations on nearly-parabolic cometary orbits. *Moon and Planets*, **29**, 121–137.

Byl J. 1986. The effect of the Galaxy on cometary orbits. *Earth Moon and Planets*, **36**, 263–273.

Carusi A., Kresak L., Perozzi E., and Valsecchi G. B. 1987. High-Order Librations of Halley-Type Comets. *AAP*, **187**, 899.

Charnoz S. and Morbidelli A. 2007. Coupling dynamical and collisional evolution of small bodies II. Forming the Kuiper belt, the Scattered Disk and the Oort cloud. *Icarus*, **188**, 468–480.

Chebotarev G. A. 1966. Cometary Motion in the Outer Solar System. *SvA*, **10**, 341–344.

Clube S. V. M. and Napier W. M. 1982. Spiral Arms, Comets and Terrestrial Catastrophism. *QJRAS*, **23**, 45–66.

Delsemme A. H. 1987. Galactic Tides Affect the Oort Cloud - an Observational Confirmation. *AAP*, **187**, 913–918.

Dones L., Weissman P. R., Levison H. F., and Duncan M. J. 2004. Oort cloud formation and dynamics. In Kronk G. W., editor, *Comets II*, pages 153–174.

Duncan M., Quinn T., and Tremaine S. 1987. The formation and extent of the solar system comet cloud. *AJ*, **94**, 1330–1338.

Duncan M. J. and Levison H. F. 1997. A scattered comet disk and the origin of Jupiter family comets. *Science*, **276**, 1670–1672.

Dybczynski P. A. 1994. Impulse approximation improved. *Celestial Mechanics and Dynamical Astronomy*, **58**, 139–150.

Dybczyński P. A. 2002. Simulating observable comets. I. The effects of a single stellar passage through or near the Oort cometary cloud. *AAP*, **396**, 283–292.

Dybczyński P. A. and Królikowska M. 2011. Where do long-period comets come from ? Moving through the Jupiter-Saturn barrier. *MNRAS*, **416**, 51–69.

Emel'yanenko V. V., Asher D. J., and Bailey M. E. October 2007. The fundamental role of the Oort cloud in determining the flux of comets through the planetary system. *MNRAS*, **381**, 779–789.

Emel'yanenko V. V., Asher D. J., and Bailey M. E. 2013. A Model for the Common Origin of Jupiter Family and Halley Type Comets. *Earth Moon and Planets*, **110**, 105–130.

Everhart E. 1967. Intrinsic distributions of cometary perihelia and magnitudes. *AJ*, **72**, 1002.

Everhart E. 1972. The origin of short-period comets. *Astrophys. Lett.*, **10**, 131–135.

Everhart E. 1985. An efficient integrator that uses Gauss-Radau spacings. In Carusi A. and Valsecchi G. B., editors, *ASSL Vol. 115 : IAU Colloq. 83 : Dynamics of Comets : Their Origin and Evolution*, page 185.

Fernández J. A. 1980. Evolution of comet orbits under the perturbing influence of the giant planets and nearby stars. *Icarus*, **42**, 406–421.

Fernandez J. A. 1981. New and evolved comets in the solar system. *AAP*, **96**, 26–35.

Fernandez J. A. 1997. The Formation of the Oort Cloud and the Primitive Galactic Environment. *Icarus*, **129**, 106–119.

Fernández J. A. and Brunini A. 2000. The buildup of a tightly bound comet cloud around an early Sun immersed in a dense Galactic environment : Numerical experiments. *Icarus*, **145**, 580–590.

Fernández J. A. and Sosa A. 2012. Magnitude and size distribution of long-period comets in Earth-crossing or approaching orbits. *MNRAS*, **423**, 1674–1690.

Fernández J. A., Tancredi G., Rickman H., and Licandro J. 1999. The population,magnitudes, and sizes of Jupiter family comets. *Astron. Astrophys.*, **352**, 327–340.

Fouchard M. 2004. New fast models of the Galactic tide. *MNRAS*, **349**, 347–356.

Fouchard M., Froeschlé Ch., Breiter S., Ratajczak R., and Valsecchi H., G.B. Rickman. 2007a. Methods to Study the Dynamics of the Oort Cloud Comets II : Modelling the Galactic Tide. In Benest D., Froeschlé Cl., and Lega E., editors, *Topics in Gravitational dynamics*, volume 729 of *Lecture Notes in Physics, Berlin Springer Verlag,*, pages 271–293.

Fouchard M., Froeschlé Ch., Matese J. J., and Valsecchi G. 2005. Comparison between Different Models of Galactic Tidal Effects on Cometary Orbits. *Celestial Mechanics and Dynamical Astronomy*, **93**, 229–262.

Fouchard M., Froeschlé Ch., Rickman H., and Valsecchi G. 2007b. Methods to Study the Dynamics of the Oort Cloud Comets I : Modelling the Stellar Perturbations. In Benest D., Froeschlé Cl., and Lega E., editors, *Topics in Gravitational dynamics*, volume 729 of *Lecture Notes in Physics, Berlin Springer Verlag, in press*, pages 255–270.

Fouchard M., Froeschlé Ch., Rickman H., and Valsecchi G. B. 2010. Dynamical Features of the Oort Cloud Comets. In J. Souchay & R. Dvorak , editor, *Lecture Notes in Physics, Berlin Springer Verlag*, volume 790 of *Lecture Notes in Physics, Berlin Springer Verlag*, pages 401–430.

Fouchard M., Froeschlé Ch., Rickman H., and Valsecchi G. B. 2011a. The key role of massive stars in Oort cloud comet dynamics. *Icarus*, **214**, 334–347.

Fouchard M., Froeschlé Ch., Valsecchi G., and Rickman H. 2006. Long-term effects of the Galactic tide on cometary dynamics. *Celestial Mechanics and Dynamical Astronomy*, **95**, 299–326.

Fouchard M., Froeschlé Ch., and Valsecchi G. B. 2003. Is the dynamics of Jupiter family comets amenable to Monte Carlo modelling ? *MNRAS*, **344**, 1283–1295.

Fouchard M., Rickman H., Froeschlé Ch., and Valsecchi G. B. 2011b. The last revolution of new comets : the role of stars and their detectability. *AAP*, **535**, A86.

Fouchard M., Rickman H., Froeschlé Ch., and Valsecchi G. B. 2013. Planetary perturbations for Oort cloud comets. I. Distributions and dynamics. *Icarus*, **222**, 20–31.

Fouchard M., Rickman H., Froeschlé Ch., and Valsecchi G. B. 2014a. Planetary perturbations for Oort cloud comets. II. Implications for the origin of observable comets. *Icarus*, **231**, 110–121.

Fouchard M., Rickman H., Froeschlé Ch., and Valsecchi G. B. 2014b. Planetary perturbations for Oort cloud comets. III. Evolution of the cloud and production of centaurs and Halley type comets. *Icarus*, **231**, 99–109.

Francis P. J. 2005. The Demographics of Long-Period Comets. *APJ*, **635**, 1348–1361.

Froeschlé Cl. and Rickman H. 1980. New Monte Carlo Simulations of the Orbital Evolution of Short-period Comets and Comparison with Observations. **82**, 183–194.

Froeschlé Cl. and Rickman H. 1981. A Monte Carlo Investigation of Jovian Perturbations on Short-Period Comet Orbits. *Icarus*, **46**, 400–414.

Frouard J., Fouchard M., and Vienne A. 2010. About the dynamics of the evection resonance. *AAP*, **515**, A54.

Frouard J., Vienne A., and Fouchard M. 2011. The long-term dynamics of the Jovian irregular satellites. *AAP*, **532**, A44.

Gardner E., Nurmi P., Flynn C., and Mikkola S. 2011. The effect of the solar motion on the flux of long-period comets. *MNRAS*, **411**, 947–954.

Gladman B., Marsden B. G., and Vanlaerhoven C. 2008. Nomenclature in the Outer Solar System. In Barucci M. A., Boehnhardt H., Cruikshank D. P., Morbidelli A., and Dotson R., editors, *The Solar System Beyond Neptune*, pages 43–57.

Gomes Levison H.F. Tsiganis K. Morbidelli A., R. 2005. Origin of the cataclysmic Late Heavy Bombardment period of the terrestrial planets. *Nature*, **435**, 466–469.

Hahn J. M. and Malhotra R. 1999. Orbital Evolution of Planets Embedded in a Planetesimal Disk. *AJ*, **117**, 3041–3053.

Heisler J. and Tremaine S. 1986. The influence of the galactic tidal field on the Oort comet cloud. *Icarus*, **65**, 13–26.

Heisler J., Tremaine S., and Alcock C. 1987. The Frequency and Intensity of Comet Showers from the Oort Cloud. *Icarus*, **70**, 269–288.

Hills J. G. 1981. Comet showers and the steady-state infall of comets from the Oort cloud. *AJ*, **86**, 1730–1740.

Hughes D. W. 2001. The magnitude distribution, perihelion distribution and flux of long-period comets. *MNRAS*, **326**, 515–523.

Jakubík M. and Neslušan L. 2008. The dynamics of the Oort cloud during a passage through a spherical giant interstellar cloud with the Gaussian-density profile. *Contributions of the Astronomical Observatory Skalnate Pleso*, **38**, 33–46.

Kaib N. A. and Quinn T. 2008. The formation of the Oort cloud in open cluster environments. *Icarus*, **197**, 221–238.

Kaib N. A. and Quinn T. 2009. Reassessing the Source of Long-Period Comets. *Science*, **325**, 1234–.

Królikowska M. 2006. Non-Gravitational Effects in Long-Period Comets and the Size of the Oort Cloud. *Acta Astronomica*, **56**, 385–412.

Królikowska M. and Dybczyński P. A. 2010. Where do long-period comets come from ? 26 comets from the non-gravitational Oort spike. *MNRAS*, **404**, 1886–1902.

Levison H. F., Dones L., and Duncan M. J. 2001. The Origin of Halley-Type Comets : Probing the Inner Oort Cloud. *Astron. J*, **121**, 2253–2267.

Levison H. F., Duncan M. J., Dones L., and Gladman B. J. 2006. The scattered disk as a source of Halley-type comets. *Icarus*, **184**, 619–633.

Levison H. F., Morbidelli A., Vokrouhlický D., and Bottke W. F. 2008. On a Scattered-Disk Origin for the 2003 EL_{61} Collisional Family-An Example of the Importance of Collisions on the Dynamics of Small Bodies. *AJ*, **136**, 1079–1088.

Levison H.F., Duncan M.J., Brasser R., and Kaufmann D.E. 2010. Capture of the Sun ? Oort cloud from stars in its birth cluster. *Science*, **329**, 187–191.

Marsden B. G. and Sekanina Z. December 1973. On the distribution of "original" orbits of comets of large perihelion distance. *AJ*, **78**, 1118–+.

Matese J. J. and Whitman P. G. 1992. A model of the galactic tidal interaction with the Oort comet cloud. *Celest. Mech. Dynam. Astron.*, **54**, 13–35.

Matese J. J. and Whitmire D. P. 2011. Persistent evidence of a jovian mass solar companion in the Oort cloud. *Icarus*, **211**, 926–938.

Napier, W.M., and Staniucha, M. . 1982. Interstellar planetesimals. I - Dissipation of a primordial cloud of comets by tidal encounters with massive nebulae. *MNRAS*, **198**, 723–735.

Oort J. H. 1950. The structure of the cloud of comets surrounding the Solar System and a hypothesis concerning its origin. *Bull. Astron. Inst. Neth.*, **11**, 91–110.

Öpik E. 1932. Note on Stellar Perturbations of Nearby Parabolic Orbit. *Proceedings of the American Academy of Arts and Science.*

Remy F. and Mignard F. 1985. Dynamical evolution of the Oort cloud. I - A Monte Carlo simulation. II - A theoretical approach. *Icarus*, **63**, 1–30.

Rickman H. 1976. Stellar perturbations of orbits of long-period comets and their significance for cometary capture. *Bulletin of the Astronomical Institutes of Czechoslovakia*, **27**, 92–105.

Rickman H., Fouchard M., Froeschlé C., and Valsecchi G. B. 2012. Gaia and the new comets from the Oort cloud. *PSS*, **73**, 124–129.

Rickman H., Fouchard M., Froeschlé Ch., and Valsecchi G. B. 2008. Injection of Oort Cloud comets : the fundamental role of stellar perturbations. *Celestial Mechanics and Dynamical Astronomy*, **102**, 111–132.

Rickman H., Fouchard M., Valsecchi G. B., and Froeschlé Ch. 2005. Algorithms for Stellar Perturbation Computations on Oort Cloud Comets. *Earth Moon and Planets*, **97**, 411–434.

Rickman H. and Vaghi S. 1976. A Monte Carlo Simulation of the Orbital Evolution of Comets in the Inner Planetary Region. **51**, 327–342.

Smoluchowski R. and Torbett M. 1984. The boundary of the solar system. *nature*, **311**, 38–+.

Sosa Fernández J.A., A. 2011. Masses of long-period comets derived from non- gravitational effects-analysis of the computed results and the consistency and reliability of the non-gravitational parameters. *MNRAS*, **416**, 767–782.

Stagg C.R. and Bailey M.E. 1989. Stochastic capture of short-period comets. *MNRAS*, **241**, 507–541.

Stoica R. S., Liu S., Davydov Y., Fouchard M., Vienne A., and Valsecchi G. B. 2010. Order statistics and heavy-tailed distributions for planetary perturbations on Oort cloud comets. *AAP*, **513**, A14+.

Weissman P. R. 1979. Physical and dynamical evolution of long-period comets. In Duncombe R. L., editor, *Dynamics of the Solar System*, volume 81 of *IAU Symposium*, pages 277–282.

Weissman P. R. 1980. Stellar perturbations of the cometary cloud. *Nature*, **288**, 242–243.

Weissman P. R. 1996. The Oort Cloud. In Rettig T. and Hahn J. M., editors, *Completing the Inventory of the Solar System*, volume 107 of *Astronomical Society of the Pacific Conference Series*, pages 265–288.

Weissman P. R. 2011. The Problem of Cometary Fading is Not a Problem. In *EPSC-DPS Joint Meeting 2011*, page 1598.

Wiegert P. and Tremaine S. 1999. The Evolution of Long-Period Comets. *Icarus*, **137**, 84–121.

Yabushita S., Hasegawa I., and Kobayashi K. 1982. The stellar perturbations of orbital elements of long-period comets. *MNRAS*, **200**, 661–671.